Time-Sequenced Optical Nuclear Magnetic Resonance of Gallium Arsenide

Thesis by

Steven Keith Buratto

In Partial Fulfillment of the Requirements

for the Degree of

Doctor of Philosophy

California Institute of Technology

Pasadena, California

1993

(Submitted September 3, 1992)

to Laura and my family

Acknowledgements

I would like to thank my thesis advisor Prof. Dan Weitekamp for giving me the opportunity to work on this project which has provided many interesting challenges. His leadership and guidance have been invaluable, and I have learned a great deal working with him. It has been my pleasure to collaborate with several talented scientists: David Shykind, Narayanan "KD" Kurur, and Jack Hwang. Special thanks goes out to David Shykind who was instrumental in making the experiments described in this thesis work. I wish Jack Hwang and Michael Miller the best of luck as they continue work in TSONMR.

I also acknowledge the remaining members of the Weitekamp group: Dan Jones, Pedro Pizarro, Herman Cho, Margat Werner, Russ Bowers, Paul Carson, John Marohn, and Len Mueller, for their support both in and out of lab. I have benefited from working with each of them. Special thanks to Dan Jones who, for one year, had to put up with me as a roomate as well as a labmate.

I would also like to thank several (past and present) members of the groups of Prof. Ahmed Zewail and Prof. Nate Lewis: Jack Breen, Bob Bowman, Dean Willberg, Earl Potter, and Martin Gruebele of the Zewail group for many fruitful discussions concerning optical spectroscopy, and Gail Ryba of the Lewis group for GaAs samples and helpful discussions on photoluminescence.

I acknowledge AT&T Bell Laboratories for a graduate fellowship the last three years here at Caltech.

I would also like to thank Mike Rock, Gary Guthart, Todd Richmond, Marc Hillmyer, and Wayne Larson for their friendship. I have enjoyed the softball, basketball, and golf over the years. I wish them all best of luck in their future plans.

Finally, none of this would have been possible without the love and support of my wife Laura. She was always there to help no matter what the task, from listening to my problems to helping make figures for this manuscript. Her dedication was well beyond the call of duty. Special thanks to my mother, Beth Buratto, and my sisters Jill and Dina for all of their love and support. I also thank my mother for her constant encouragement as well as personal sacrifice in helping me achieve this goal. Thanks also to my father, Steve Buratto, for his love, support, and encouragement. I also thank my grandparents, Bill and Blanche Anderson, with whom I've shared a close relationship and who were always there to support me. I would also like to thank Laura's parents Fran and Bob Oliver, for taking me into their family and making me feel at home.

Abstract

This dissertation describes the development of a new method of optical NMR, time–sequenced optical NMR (TSONMR), of GaAs for which both sensitivity and resolution are optimized. In this method, the three processes of optical nuclear polarization (ONP), nuclear magnetic resonance (NMR), and optical detection (OD) occur in distinct sequential periods achieving order–of–magnitude improvements in sensitivity and resolution relative to the earlier quasi–steady–state methods. The TSONMR experiment is also flexible, allowing both continuous wave (CW) and time–domain TSONMR experiments to be performed. The underlying physics is used to develop a quantitative theory of sensitivity which is in good agreement with experiment.

Applications to epitaxial p–type GaAs samples show that the CW and Fourier transform (FT) versions of TSONMR are sensitive to different nuclear sites. The locus of the method is an unknown optically relevant defect (ORD) present at $\leq 10^{15}/\mathrm{cm}^3$. The CW experiment is sensitive to the more numerous bulk spins far from the ORD, while the FT experiment is sensitive to the low abundance sites which are quadrupole–perturbed by proximity to the ORD. The difference between the two experiments can be understood by accounting for and manipulating the role of spin diffusion. Nutation experiments and the dependence on sample orientation rule out the alternative interpretation that only strongly perturbed sites are seen. Thus, the range of the optically–induced hyperfine coupling at the ORD far exceeds that of valence–band electric field perturbations.

The FT–TSONMR experiment is sample specific as is demonstrated for two electrically–equivalent p–type samples (both containing 10^{17} Zn atoms/cm^3). One

sample exhibits much stronger electric field gradient perturbations than the other indicating differences at the atomic level in the defects responsible for localization.

It is also shown on a bulk sample that the method allows high–resolution measurement of the optically–induced Knight shift which is proportional to the electron density at the nucleus. Extensions of these observations to quantum wells are proposed. For a GaAs/$Ga_{1-x}Al_xAs$ ($x \simeq 0.3$) quantum well, sample calculations show that the optical Knight shift will provide spectral resolution of individual atomic layers. Optical–rf multiple–pulse sequences are described to minimize other contributions to the linewidth. It should therefore be possible to map out the electron probability across the GaAs layer of a quantum well and give great insight into the electronic wavefunction near the interface as well as the center of the well.

Contents

List of Figures

Chapter 1

Overview

Since its inception nuclear magnetic resonance (NMR) spectroscopy has been a powerful tool in the determination of structure in crystalline solids. Its ability to report on both static and dynamic structural properties at the atomic level makes its application to the study of defects and nanostructures in GaAs semiconductors very attractive. As an example of the information obtainable through NMR consider the GaAs lattice shown in Figure 1.1. Even though each of the major isotopes in GaAs (^{69}Ga, ^{71}Ga, and ^{75}As) is quadrupolar (I = 3/2), the cubic symmetry of the ideal lattice causes the quadrupole interaction to vanish at each site. The NMR spectrum in this case consists of a single line for each isotope. If, however, a defect is placed at position A in Fig. 1.1, then the nuclei surrounding this site have reduced symmetry and the quadrupole interaction for these nuclei is nonzero. By measuring the range of quadrupole splittings observed in the NMR spectrum of the sites around the defect, the local strain induced by the defect can be mapped.

Additional information comes from the NMR spectrum of the defect itself. The chemical specificity of NMR provides the means for identifying unknown defects. As mentioned, the lattice sites surrounding the defect in Fig. 1.1 have reduced symmetry, but the defect site has cubic symmetry (see Fig 1.1). If the defect is a quadrupolar nucleus, a measured quadrupole splitting in the NMR spectrum of the defect indicates the presence of another defect nearby. Measuring the quadrupole splittings of the defect yields information about defect clustering.

Such structural information is important to understanding the local electrical

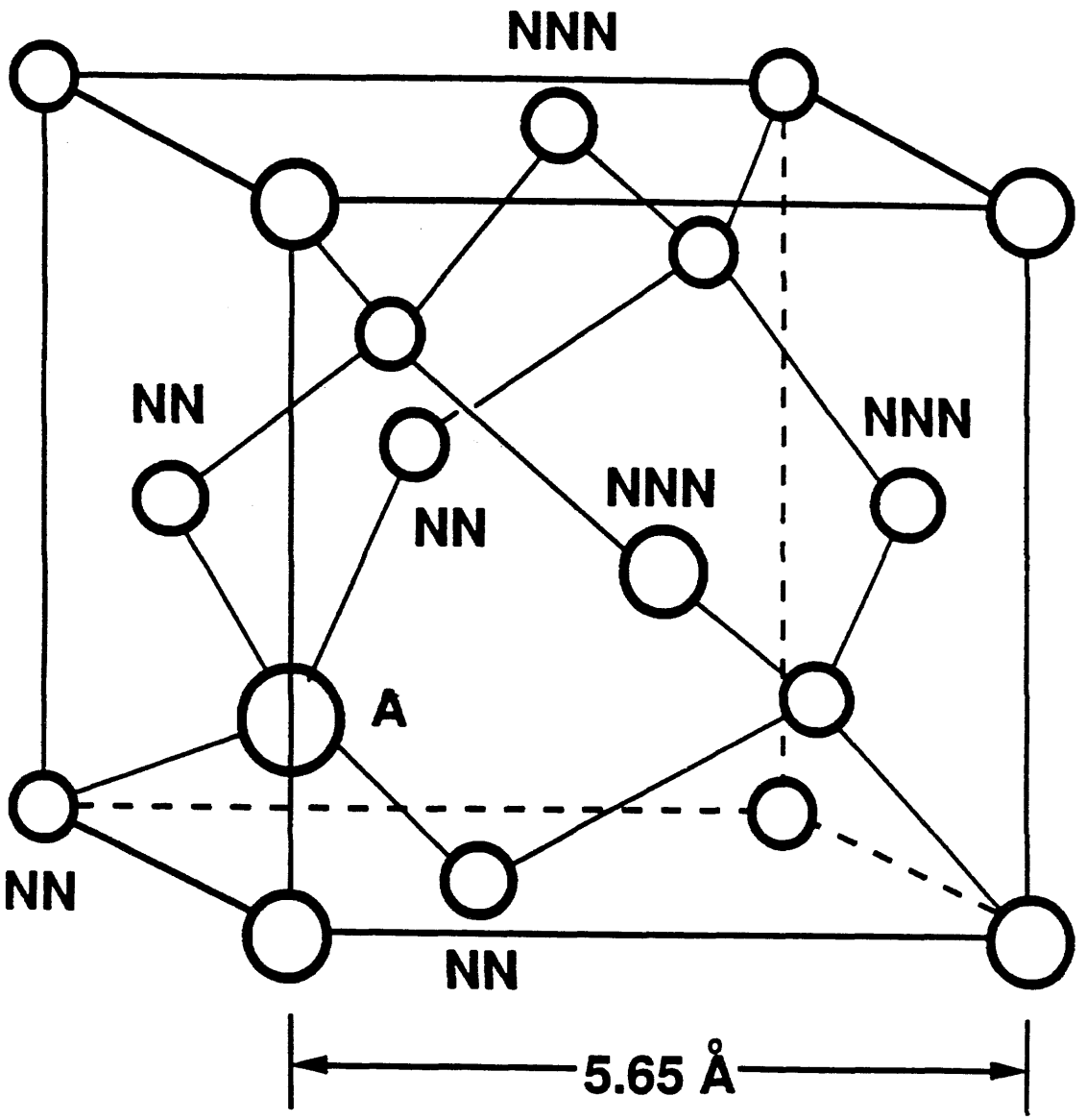

Figure 1.1: The GaAs unit cell. Each site in the zincblende lattice depicted in the figure has cubic symmetry. Starting from the nucleus at position A, the nearest neighbors are represented by NN and the next–nearest neighbors are represented by NNN. If the site A is a Ga atom then the NN sites are As atoms and the NNN sites are Ga atoms.

and optical properties of these materials. The conventional method of NMR is too insensitive to be useful for studying device–quality epitaxial material where the sample volume is small and defect concentrations are low ($\lesssim 10^{17}/cm^3$). The sensitivity problem in conventional NMR stems from the small energy differences of the nuclear spin sublevels. The minuteness of the radiofrequency (rf) quantum affects the sensitivity in two distinct ways. First, the nuclear polarization is low due to the small fractional population differences that exist between the spin sublevels in thermal equilibrium. Second, the detection of rf photons is difficult due to the appreciable thermal noise present at these frequencies. The combined result of these limitations is that conventional solid–state NMR requires large sample volumes ($\gtrsim$ 0.1 cm^3) and many spins ($\gtrsim 10^{18}$). The low sensitivity inherent to conventional NMR, however, can be circumvented for III–V semiconductors by coupling optical degrees of freedom with nuclear spin.

For over a decade it has been known that irradiating III–V semiconductors with circularly–polarized light near the band gap results in nuclear polarizations on the order of 10%. [1–18] This process, known as optical nuclear polarization (ONP), occurs through two transfers of angular momentum: one from the circularly–polarized photon to the excited conduction electron (optical pumping [5,19]), and the other from the excited electron to the lattice nuclei (the Overhauser effect [20]). The nuclear polarization resulting from ONP is also optically–detectable through the back–action of the nuclear spin angular momentum on the spin angular momentum of the excited electrons. [1–18] The physics of the feedback of the nuclear polarization on the conduction electrons will be explained in detail in chapter 2. The optical observable is the angular momentum (circular–polarization) of the recombination luminescence ρ which is related to the electron polarization by

$$\rho = \frac{(I_+ - I_-)}{(I_+ + I_-)} = C\frac{(N_+ - N_-)}{(N_+ + N_-)} \qquad (1.1)$$

where $I_\pm$ are the intensities of right–hand and left–hand circularly–polarized light, respectively, and $N_\pm$ are the number of excited electrons in the $\pm$ 1/2 spin states, respectively. The proportionality constant C, of order unity, depends on optical selection rules as described in section 2.1. Combining the ONP and OD processes with NMR, results in a high–sensitivity optical NMR experiment. A simplified schematic of optical NMR in GaAs is shown in Figure 1.2. The optical detection of NMR is recorded as a change in ρ on resonance.

Prior to the work described here, experiments using the above phenomena were performed with the ONP, NMR, and OD processes occurring simultaneously. The circular–polarization of the luminescence ρ was monitored as the rf frequency was swept through resonance in a quasi steady–state fashion. [9–18] An NMR resonance was detected as a depolarization of ρ. Quasi steady–state ODNMR experiments have been demonstrated in a variety of GaAs samples including bulk $Ga_{1-x}Al_xAs$ [9–11,14,15], bulk GaAs [12–15], and GaAs/$Ga_{1-x}Al_xAs$ quantum wells [16,17] and heterojunctions. [18] While these quasi steady–state ODNMR experiments showed at least a factor 10^5 improvement in sensitivity over conventional NMR methods, the observed lineshapes were distorted by the presence of spin polarized photocarriers during NMR and by the high rf powers needed to observe a signal. [9–18] The best lineshape resulting from quasi steady–state ODNMR [9] was still a factor of 20 larger than expected from spin–spin couplings alone. [21,22]

By considering ONP, NMR, and OD as three distinct processes, we have developed a new method of optical NMR, called time–sequenced optical NMR (TSONMR), which separates the three processes in time. The time–sequencing also allows each process to be separately optimized. By time–sequencing, the NMR part

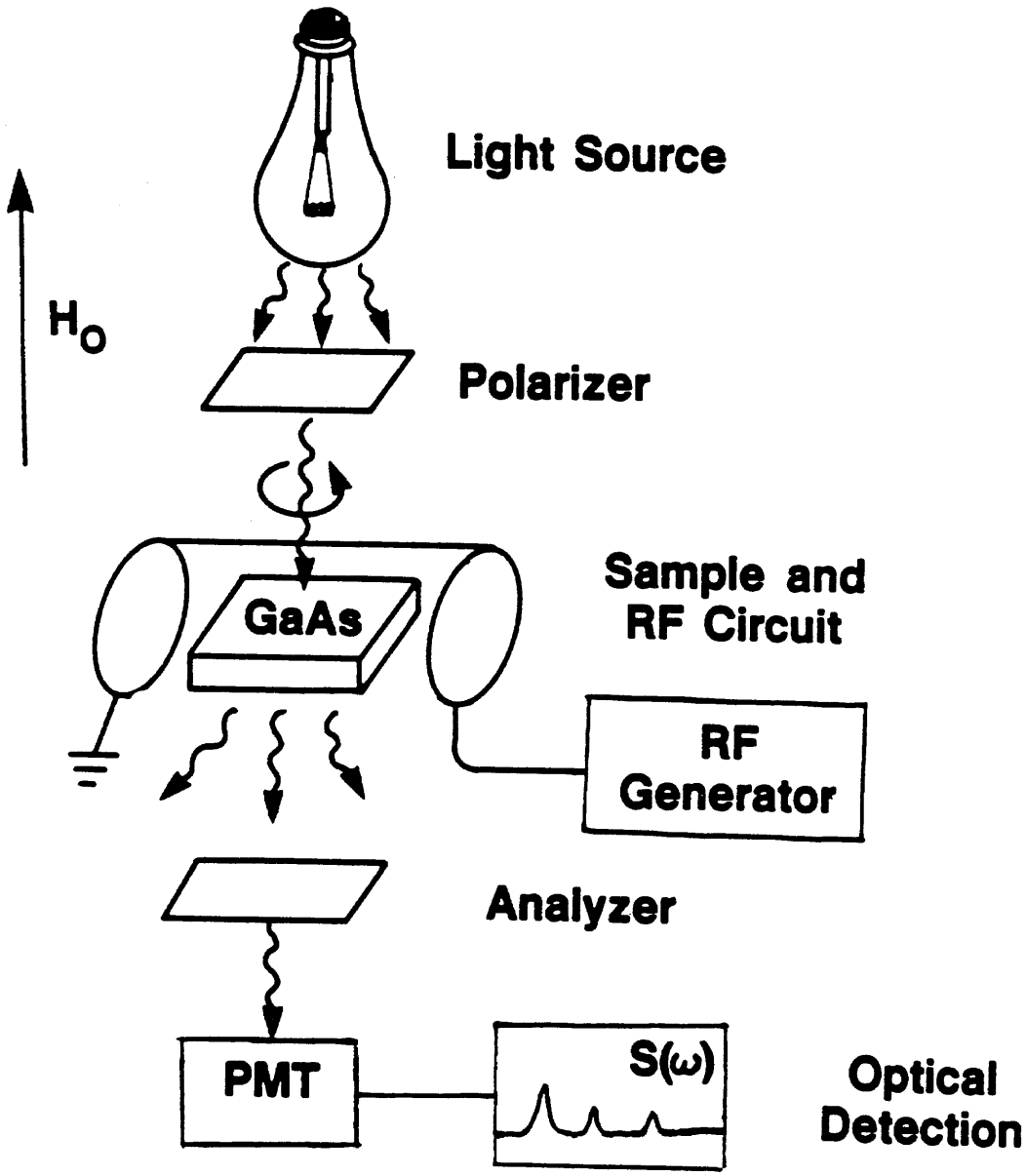

Figure 1.2 Simple scheme for optical NMR in GaAs. The sample is irradiated with the band gap light in a magnetic field H_0. The light is circularly–polarized for ONP (see text). The luminescence is collected in transmission and analyzed for circular–polarization ρ. The rf frequency ω is swept and the NMR is detected as a change in ρ.

of the TSONMR experiment can be performed in the dark, obviating the deleterious affects of the spin polarized carriers on the resolution. [23] We have also shown that the method not only has better resolution than the previous quasi–steady–state method but also better sensitivity. [23] Thus, the TSONMR technique reconciles the sensitivity and resolution of optical NMR, and results in a high–sensitivity, high–resolution technique for application to the study of bulk defects and interfaces in GaAs materials. [23–26] Another consequence of the TSONMR method is that the NMR part of the experiment is general to any NMR experiment including time–domain spectroscopy. [25,26] The remainder of this thesis will dicuss the theoretical and experimental foundations of TSONMR in much greater detail, and the application of TSONMR to shallow donors in p–type GaAs present at concentrations of 1 part–per–million or less ($\leq 10^{16}/\mathrm{cm}^3$).

1.1 Outline

In chapter 2 the basic theoretical concepts underlying optical NMR (optical pumping, optical nuclear polarization (ONP), and optical detection (OD)) are discussed. The locus of ONP and OD, the chemically unknown optically relevant defect (ORD), is described. This chapter also includes a review of the previous method of optical NMR, quasi–steady–state optically–detected NMR (ODNMR), and explains the need for an alternative method. The last section of chapter 2 introduces our method of time–sequenced optical NMR (TSONMR) which maximizes both sensitivity and resolution.

Chapter 3 describes in detail the development of the TSONMR spectrometer. The spectrometer combines technology from both magnetic resonance and optical spectroscopies and is "homebuilt." A detailed discussion of the fully automated spectrometer and its data acquisition software is given in Appendix A including a

copy of the source code written in the C programming language.

In chapter 4 the experimental foundations of the TSONMR technique (the complete Hanle effect, time–sequencing, and field cycling for detection) are developed. The physics of the field cycling transient and its incorporation in the detection period of a time–sequenced experiment is thoroughly discussed. An expression for the sensitivity of a TSONMR experiment is derived and shown to depend on readily measurable material properties. Chapter 4 also includes a discussion of the different samples used in our experiments.

The application of the TSONMR technique to the study of p–type GaAs is presented in chapter 5. The NMR spectra of nuclei perturbed by ORD's present at the part–per–billion level are recorded. It is demonstrated that the Fourier transform version of the method has enhanced sensitivity to sites of electron localization relative to the continuous wave experiment. The use of multiple–pulse and 2D extensions of TSONMR in determining nuclear spin parameters for the perturbed nuclei is presented, and attempts to determine the identity of the ORD by double resonance TSONMR are discussed. The spin dynamics of nuclei near the ORD are also examined.

The technique is shown to be very sample specific. The ability to discriminate between different samples is demonstrated for the case of two electrically–equivalent p–type samples (10^{17} Zn atoms/cm^3) that exhibit very different TSONMR spectra.

Electron properties are also measured by TSONMR. The square of the electron wavefunction is measured through the optical Knight shift. The resulting Knight shift is shown to be inhomogeneous due to the spatially varying wavefunction of the localized electron. The possibility for using an rf–optical multiple–pulse double resonance technique to resolve this inhomogeneity for both bulk and quantum well samples is discussed. Estimates of the results of such

experiments for quantum wells is presented. A step toward such experiments is demonstrated in the form of multiple–pulse line–narrowing TSONMR experiments which yielded further resolution enhancement by over an order of magnitude.

1.2 References

[1] M.I. Dyakonov and V.I. Perel, Zh. Eksp. Teor. Fiz. **60**, 1954 (1971) [Sov. Phys.–JETP **33**, 1053 (1971)].

[2] M.I. Dyakonov and V.I. Perel, Zh. Eksp. Teor. Fiz. **63**, 1883 (1972) [Sov. Phys.–JETP **36**, 995 (1973)].

[3] M.I. Dyakonov and V.I. Perel, Zh. Eksp. Teor. Fiz. **65**, 362 (1973) [Sov. Phys.–JETP **38**, 177 (1974)].

[4] D. Paget, G. Lampel, B. Sapoval, and V.I. Safarov, Phys. Rev. B **15**, 5780 (1977).

[5] M.I. Dyakonov and V. I. Perel in: *Optical Orientation* ed. F. Meier and B.P. Zakharchenya (North Holland, Amsterdam, 1984) p. 11.

[6] D. Paget, and V.L. Berkovits *ibid* p. 381.

[7] V.G. Fleisher and I.A. Merkulov *ibid* p. 173.

[8] V.K. Kalevich, V.D. Kul'kov, and V.G. Fleisher, Pis'ma Zh. Eksp. Teor. Fiz. **35**, 17 (1982) [JETP Lett. **35**, 20 (1982)].

[9] A.I. Ekimov and V.I. Safarov, ZhETF Pis. Red. **15**, 453 (1972) [JETP Lett. **15**, 319 (1972)].

[10] V.L. Berkovits, A.I. Ekimov, and V.I. Safarov, Zh. Eksp. Teor. Fiz. **65**, 346 (1973) [Sov. Phys.–JETP **38**, 169 (1974)].

[11] M.I. Dyakonov, V. I. Perel, V.L. Berkovits and V.I. Safarov, Zh. Eksp. Teor. Fiz. **67**, 1912 (1974) [Sov. Phys.–JETP **40**, 950 (1975)].

[12] D. Paget, Phys. Rev. B **24**, 3776 (1981).

[13] D. Paget, Phys. Rev. B **25**, 4444 (1982).

[14] V.K. Kalevich, V.D. Kul'kov, I.A. Merkulov, and V.G. Fleisher, Fiz. Tverd. Tela **24**, 2098 (1982) [Sov. Phys. Solid State **24**, 1195 (1982)].

[15] V.K. Kalevich, V.L. Korenev, and V.G. Fleisher, Izvest. Akad. Nauk SSSR. Ser. Fiz. **52**, 434 (1988).

[16] G.P. Flinn, R.T. Harley, M.J. Snelling, A.C. Tropper, and T.M. Kerr, J. of Lumines. **45**, 218 (1990).

[17] G.P. Flinn, R.T. Harley, M.J. Snelling, A.C. Tropper, and T.M. Kerr, Semicond. Sci. Technol. **5**, 533 (1990).

[18] M. Krapf, G. Denninger, H. Pascher, G. Weimann, and W. Schlapp, Solid State Comm. **78**, 459 (1991).

[19] R. Bernheim, *Optical Pumping* (Benjamin, New York, 1965).

[20] A.W. Overhauser, Phys. Rev. **92**, 411 (1958).

[21] R.G. Shulman, B.J. Wyluda, and H.J. Hrotowski, Phys. Rev. **109**, 808 (1958).

[22] O.H. Han, H.K.C. Timken, and E. Oldfield, J. Chem. Phys. **89**, 6046 (1988).

[23] S.K. Buratto, D.N. Shykind, and D.P. Weitekamp, Phys. Rev. B **44**, 9035 (1991).

[24] C.R. Bowers, S.K. Buratto, P.J. Carson, H.M. Cho, J.Y. Hwang, L.J. Mueller, P.J. Pizarro, D.N. Shykind, D.P. Weitekamp, SPIE Proc. **1435**, 36 (1991).

[25] S.K. Buratto, N.D. Kurur, D.N. Shykind, and D.P. Weitekamp, Bull. Am. Phys. Soc., **37**, 253 (1992).

[26] S.K. Buratto, D.N. Shykind, and D.P. Weitekamp, J. Vac. Sci. Technol. B 10, 1740 (1992).

Chapter 2

Theory of Optical NMR in GaAs

In this chapter the theoretical background for optical pumping, optical nuclear polarization (ONP), and optical detection (OD) of NMR in GaAs semiconductors will be discussed. Two research groups, one at the A.F. Ioffe Physico–Technical Institute in St. Petersburg, Russia, and the other at the Ecole Polytechnique in Paris, dominated the early theoretical [1–8] and experimental [9–15] work in optical NMR of GaAs through the 1970's and early 1980's. The first few sections will draw heavily from their work. Section 2.4 describes the quasi steady–state optically–detected NMR (ODNMR) experiment which, until our work, was the only method for optical NMR in GaAs. This section also describes the shortcomings of this experiment as an analytical method, motivating the need for an alternative technique. Finally, section 2.5 introduces our method of time–sequenced optical NMR (TSONMR), and demonstrates the superiority of TSONMR to quasi steady–state ODNMR in both resolution and sensitivity.

2.1 Optical Pumping in GaAs

The band structure of gallium arsenide is depicted in Figure 2.1. At the point k=0 the valence band has three subbands [16], the light–hole band, the heavy–hole band, and the split–off band. In the bulk lattice the light–hole band and the heavy–hole band are degenerate at k=0, and the split–off band is at energy Δ lower than the bands of light and heavy holes. The conduction band is at an energy E_g higher than the top of the valence band. At liquid nitrogen (LN_2) temperature 77

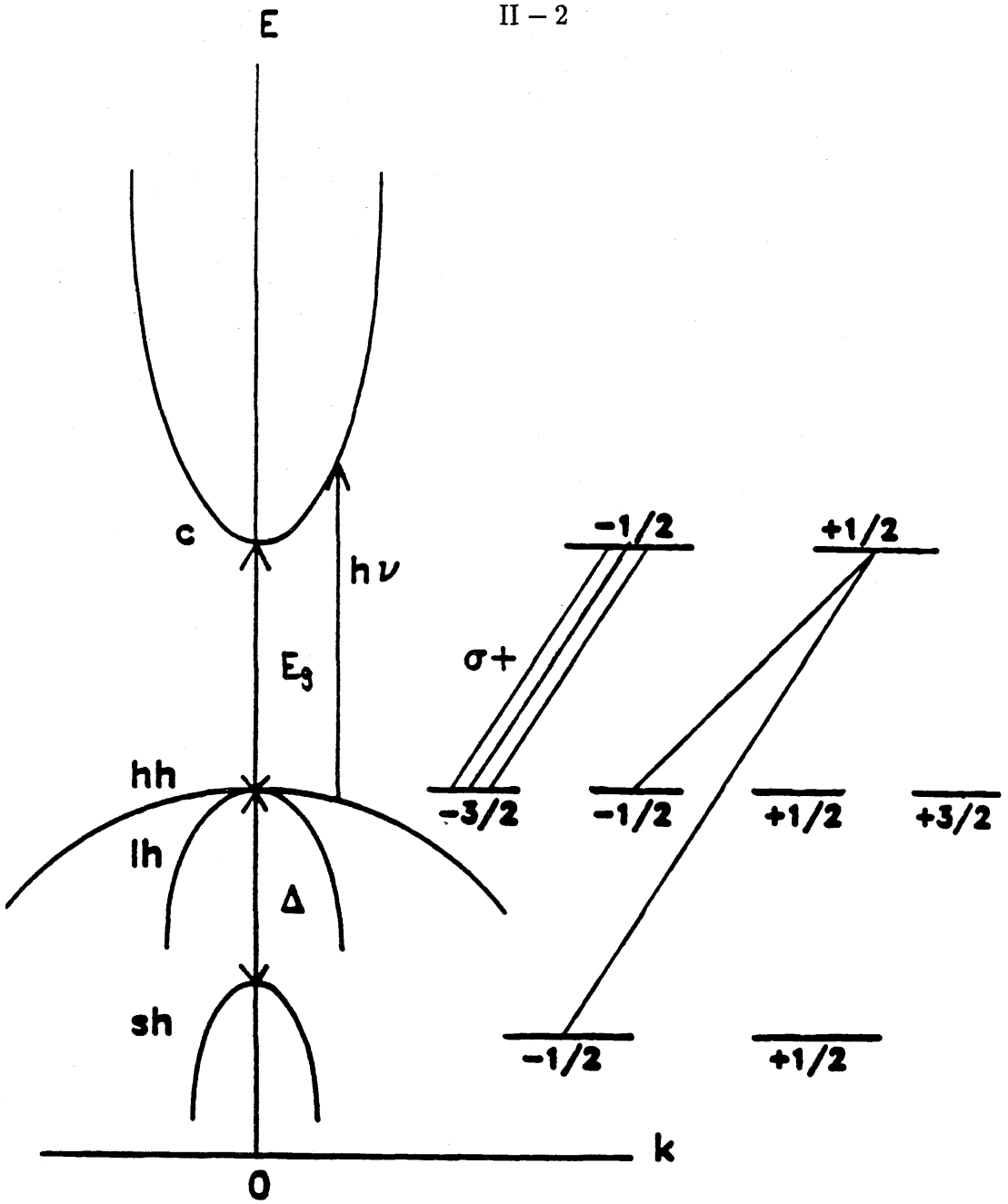

Figure 2.1: GaAs band structure and selection rules for interband absorption. *Left*: Band structure of GaAs. In this figure, hh, lh, and sh represent the heavy–hole, light–hole and split–off bands, respectively. E_g is the band gap energy, Δ is the spin–orbit coupling, and $h\nu$ is the laser energy. *Right*: Allowed transitions for the absorption of right–hand circularly–polarized light.

K, the band gap energy E_g for GaAs is 1.50 eV (828 nm) and $\Delta \simeq 0.30$ eV.

2.1.1 Selection Rules

The optical selection rules for the GaAs band structure are given in Fig. 2.1 For interband transitions at k = 0 from the top of the valence band to the bottom of the conduction band, the selection rules are the same as for atomic transitions between levels with angular momenta J = 3/2 ($^2P_{3/2}$) and J = 1/2 ($^2S_{1/2}$) [1]. Fig. 2.1 shows the allowed transitions for absorption of right–hand circularly–polarized light σ^+. The absorption can be described as the transfer of the angular momentum of the circularly–polarized photon to the total angular momentum of the excited electron. Since the excited electron is in a state analogous to an S–state, L = 0 and the angular momentum transfer is to the spin angular momentum of the electron. As depicted in Fig. 2.1, the allowed transitions are from the lower state with magnetic quantum number $m_j = -3/2$ to the upper state with $m_s = -1/2$, and from the lower state with $m_j = -1/2$ to the upper state with $m_s = 1/2$. The probabilities of these transitions are in a ratio of 3:1, respectively. Defining the polarization,

$$P_e = \frac{n_+ - n_-}{n_+ + n_-}, \tag{2.1}$$

where n_+ and n_- are the number of electrons in the conduction band with $m_s = 1/2$ and $m_s = -1/2$, respectively, $P_e = -0.5$ for excitation by σ^+ light, and the polarization direction is parallel to the propagation direction of the exciting light. For an electron spin, S = 1/2, and light propagating in the z–direction, the total electron spin polarization $\langle S \rangle = \langle S_z \rangle = 1/2 P_e = -0.25$ for σ^+ light. For σ^- light the polarization is reversed and $\langle S_z \rangle = 0.25$.

This degree of polarization is possible only if $E_g \leq h\nu \leq E_g + \Delta$. The

symmetry of the split–off sub–band is such that J = 1/2, and for a σ^+ photon the allowed transition is from the state $m_s = -1/2$ in the split–off band to the state $m_s = 1/2$ in the conduction band as seen in Fig. 2.1. The net effect of this excitation is to decrease the polarization and becomes accessible once the photon energy exceeds $E_g+\Delta$. A transition from the split–off band results in a conduction electron with the opposite magnetic quantum number and decreases the polarization of the free carriers.

If the crystal is subject to strain such as occurs at a heterointerface, the light–hole and heavy–hole degeneracy is broken. [17] If the degeneracy is broken such that the heavy–hole transition (which is the top of the valence band) can be selected without excitation from the light–hole, the polarization is 100%. In a $GaAs/Ga_{1-x}Al_xAs$ (x = 0.3) quantum well structure, where the strain at the interface breaks the degeneracy of the light and heavy holes, tuning to the heavy–hole transition produced a steady–state polarization of 80%. [18,19] Further discussion concerning optical pumping of quantum wells is given in chapter 6.

Polarizations lower than predicted from the optical selection rules are due to spin–lattice relaxation of the electron which is discussed in the next subsection.

2.1.2 Polarization of the Luminescence

When the oriented electrons in the conduction band relax optically to the valence band, their spin angular momentum is transfered to the emitted photon. [1] This luminescence will be circularly–polarized to the same degree that the conduction band electrons are polarized. The degree of circular polarization is given by,

$$\rho = \frac{I_+ - I_-}{I_+ + I_-}, \tag{2.2}$$

where $I_{\pm}$ is the intensity of σ^+ and σ^- polarized light, respectively. The quantity ρ can be related to the average electron spin, $\langle \mathbf{S} \rangle$, ($\langle \mathbf{S} \rangle = \langle S_z \rangle \mathbf{k}$ for light propagating in the z–direction) by, [5]

$$\rho = - CP_e \mathbf{z} \cdot \langle \mathbf{n}_1 \rangle = - 2C \langle \mathbf{S} \rangle \cdot \langle \mathbf{n}_1 \rangle, \tag{2.3}$$

where $\mathbf{n}_1$ is a unit vector in the direction of the observation of the luminescence, and the constant C = 1/2 for the bulk or C = 1 for heterostructures. If spin–lattice relaxation of the electrons is neglected and a bulk sample is excited along the z–axis with σ^+ polarized light yielding $P_e = C = 1/2$, then $\langle S_z \rangle = - 0.25$, and the resultant luminescence polarization is – 0.25 for observation along **z**. In practice, however, the steady–state value of ρ is achieved through a competition between the recombination lifetime τ and the spin–lattice relaxation time of the electron τ_s. If an electron spin flip occurs before the recombination of the electron and hole, then the electron polarization decreases and, consequently, the polarization of the luminescence decreases. Defining T_1^e as lifetime of the oriented electron, one can relate T_1^e to, τ and τ_s by, [1,5]

$$1/T_1^e = 1/\tau + 1/\tau_s. \tag{2.4}$$

Thus, the average electron spin just before recombination is given by,

$$\langle S_z \rangle = \frac{1}{2} \frac{C}{1+\tau/\tau_s} = C \frac{T_1^e}{2\tau}. \tag{2.5}$$

The polarization of the luminescence is then given by,

$$\rho = - C^2 \frac{T_1^e}{\tau}. \tag{2.6}$$

2.1.3 Optical Pumping in n–Type GaAs

The arguments presented in the previous two subsections assumed that the only carriers present in the conduction band are oriented carriers. In the case of

n–type GaAs, carriers are present at equilibrium. Since these carriers can recombine with the holes with equal probability to that of the oriented photocarriers, the degree of electron spin polarization is reduced. If the electron spin–lattice relaxation is slow, then, eventually, all of the carriers will be oriented under continuous wave excitation. This situation is completely analogous to the situation that occurs in optical pumping of gas–phase alkali metal atoms in the hyperfine levels of the ground state. [20]

To predict the amount of electron spin orientation that results from optical pumping of n–type material, consider, the average spin polarization <S> for an n–type semiconductor given by, [5]

$$P_e = \frac{C}{(1 + \tau_J/\tau_s)}, \tag{2.7}$$

where the time constant τ_J is analogous to the recombination time of an electron in the conduction band (regardless of whether it is oriented or not). In steady–state the recombination time is equal to the photoexcitation time such that,

$$\tau_J = n/G. \tag{2.8}$$

where n is the electron concentration and G is the number of electron–hole pairs created per unit time. Using Eq. 2.7,

$$P_e = \frac{C}{(1 + n/G\tau_s)}. \tag{2.9}$$

The parameter G is directly proportional to the excitation light intensity. In the case where $n >> G\tau_s$ (i.e. low light powers),

$$P_e \simeq CG\tau_s/n, \tag{2.10}$$

and the electron polarization is linear in the light intensity. In the case of $G\tau_s >> n$,

$$P_e \simeq C(1 - n/G\tau_s), \tag{2.11}$$

and the contribution of the equilibrium carriers has little effect on P_e. At very high light powers the electron polarization saturates at $P_e = C$. The physical insight into

optical pumping of n–type material is that a non–zero P_e is not accomplished by adding oriented carriers to the equilibrium ones, but by replacing equilibrium carriers with oriented ones. [5] In order to achieve electron spin orientation in n–type material one needs the combination of a favorably long τ_s and high light powers. [21,22]

2.2 Optical Nuclear Polarization

The spin polarized electrons in the conduction band are able to polarize the lattice nuclei through the Fermi–contact hyperfine interaction given by, [23]

$$\mathcal{H}_{HF} = 2/3\ \mu_0 g_0 \mu_\beta \gamma \hbar \mathbf{I}\cdot\mathbf{S}|\Psi(0)|^2 \tag{2.12}$$

or more simply,

$$\mathcal{H}_{HF} = A\mathbf{I}\cdot\mathbf{S}|\Psi(0)|^2 \tag{2.13}$$

where g_0 is free electron g–factor, μ_β is the Bohr magneton taken as positive, γ is the nuclear gyromagnetic ratio, and $\Psi(0)$ is the value of the electron wavefunction at the position of the nucleus. Since the excited electrons that create the hyperfine interaction are undergoing recombination and excitation at a rate of $1/\tau$ ($\tau \simeq 1$ ns), the nuclei see a rapidly fluctuating interaction. If we assume $\tau << (A|\Psi(0)|^2)^{-1}$, then the Hamiltonian in Eq. 2.12 can be replaced by a static average, [23,4]

$$\mathcal{H}_{HF} = \sum_i A_i \mathbf{I}_i \cdot \sum_q <\mathbf{S}_q> |\Psi_q(\mathbf{r}_i)|^2 \tag{2.14}$$

where i indexes the nucleus, q indexes the electronic state denoted Ψ_q, and $\mathbf{r}_i$ denotes the position of nucleus i. Eq. 2.14 implies that a given nucleus i sees an effective field from the excited electrons $\mathbf{B}_e^i$ which has the value, [4]

$$\mathbf{B}_e^i = (A_i/\gamma_i)\sum_q <\mathbf{S}_q> |\Psi_q(\mathbf{r}_i)|^2. \tag{2.15}$$

This field as will be described in section 2.5 is responsible for the optical Knight shift of the nuclear resonance line. [12] The field defined in Eq. 2.15 has another

role. The fluctations in this field act as a mechanism for nuclear spin–lattice relaxation which creates nuclear spin polarization, the process of optical nuclear polarization (ONP). [2–4]

The nuclei relax via the modulation of their hyperfine interaction with the electron spins (as in the Overhauser effect) which are not in thermal equilibrium. This relaxation occurs with time constant $T_{1_{hf}}$ and is given by the weak collision expression, [2]

$$\frac{1}{T_{1hf}} = \tilde{\omega}^2 \tau_e, \tag{2.16}$$

where $\tilde{\omega}^2$ is the average of the square of the precession frequency of the nuclear spin in the fluctuating field created by the electrons, and τ_e is the correlation time of the fluctuations. The assumption $(A|\Psi(0)|^2)^{-1} >> \tau_e$ has been made. If there are no competing mechanisms for nuclear relaxation, the steady–state nuclear spin polarization <I> is given by the familiar form, [23]

$$<I> = \frac{I(I+1)}{S(S+1)} <S>, \tag{2.17}$$

provided that the electron spin polarization is small. If there are other forms of nuclear relaxation that compete with the relaxation due to the hyperfine interaction then the right side of Eq. 2.17 is multiplied by a leakage factor f given by, [3,4]

$$f = \frac{T_{1_u}}{T_{1_u} + T_{1_{hf}}} \tag{2.18}$$

where $T_{1_u}^{-1}$ represents the spin–lattice relaxation rate due to any mechanism other than the hyperfine interaction. The leakage factor will differ with nuclear isotope due to differences in gyromagnetic ratio and quadrupole moment. In chapter 5 the case is discussed where $T_{1_u}^{-1}$ is dominated by relaxation through the quadrupole interaction.

2.2.1 Nuclear Polarization via Localized Electrons

Theoretical estimates of $T_{1_{hf}}$ have been made for both free and localized electrons. [4,5] The principle difference between the hyperfine coupling for a localized electron and for a free electron is in the square of the electron wavefunction at the nucleus $|\Psi_q(\mathbf{r}_i)|^2$, the electron density at the nucleus. In the case of free electrons this electron density can be considered as distributed over many unit cells, [5] and its value at a given nucleus is small. For free electrons an estimate of the relaxation time $T_{1_{hf}}$ is on the order of 10^4s was obtained by assuming that the range of localization was the de Broglie wavelength. [5] As will be discussed, ONP and OD have only been observed when a mechanism for electron localization is present.

If the electron is localized the electron density at a given nucleus is larger than for a free electron, and the relaxation through the hyperfine interaction becomes more efficient. In bulk GaAs the sites of electron localization, referred to as the optically relevant defects (ORD's), are presumably shallow donor states. Paget *et al.* [4] have calculated the field $\mathbf{B}_e^{\alpha}$ at a distance r from a shallow donor for a nucleus of type α ($\alpha = {}^{69}\text{Ga}, {}^{71}\text{Ga}, {}^{75}\text{As}$),

$$\mathbf{B}_e^{\alpha}(r) = \Gamma_t b_e^{\alpha}(0)\, \mathbf{S} \exp(-2r/a_0^*) \tag{2.19}$$

where Γ_t is the occupation probability of the donor state (taken as 1 in the calculation), a_0^* is the effective Bohr radius of the localized state ($\simeq 100\text{Å}$), $b_e^{\alpha}(0) = -2/3\mu_0 g_0 \mu_\beta (\Omega/\pi a_0^{*3}) d_\alpha$, Ω is the unit cell volume, and d_α is the electron density of a delocalized electron at the nucleus α. For each of the isotopes of GaAs, $b_e^{({}^{75}\text{As})}(0) \simeq -220\text{G}$, $b_e^{({}^{69}\text{Ga})}(0) = b_e^{({}^{71}\text{Ga})}(0) \simeq -130\text{G}$. An estimate using Eqs. 2.16 and 2.19 of the relaxation time $T_{1_{hf}}$ for nuclei near the ORD is on the order of 1s for $\tau_c \simeq 10^{-8}$ 10^{-9} s. [4,5] The polarization time (which is a combination of the relaxation times

$T_{1_{hf}}$ and T_{1_u}) has been measured experimentally in GaAs by several groups [10,15,16] and in each case was found to be on the order of 10 s indicating that the nuclei are predominantly polarized by electrons localized at defects.

The nuclear spin polarization rate resulting from localized electrons is ,therefore. predicted to fall as $\exp(-4r/a_0^*)$. [2,4] If the distance between ORD's is much greater than a_0^*, then the ONP process is localized to a fraction of the irradiated volume. In this case, the remaining nuclear spins can be polarized only by spin diffusion which turns out to have a similar range ($\simeq$ 100 Å) as a_0^* over a time T_1 ($\sim$ 1 s) during which the spins are isolated from the lattice. [5,13] Spin diffusion is a spin–energy conserving process driven by the nuclear spin–spin couplings. [24] A polarized nucleus near the ORD flips its spin simultaneously with a spin flip of opposite sign in a coupled nucleus. This flip–flop process occurs in a cascading action that carries spin polarization from the spins near the ORD to spins far from the ORD. Spin diffusion rates determine to what extent nuclei outside the influence of the ORD are polarized. The spin diffusion constant has been calculated and measured for ^{75}As to be 10^{-13} cm^2/s. [13] Spin diffusion turns out to be an important process in a time–sequenced optical NMR experiments as will be explained in chapter 5.

2.3 The Nuclear Field

Once the nuclei have been polarized by ONP they create an effective hyperfine field, called the nuclear field B_n, which is analogous to the electron field B_e and acts on the excited electrons. [3,4] The magnitude of the nuclear field felt by an electron in state Ψ_q is found by summing the Hamiltonian of Eq. (2.12) over all the nuclei, [3,4]

$$B_n^q = (2/3)\mu_0(g_0/g^*)\hbar\sum_i \gamma_i I_i |\Psi_q(r_i)|^2, \qquad (2.20)$$

where g^* is the effective electron g–factor. The field of Eq. (2.20) is the sum of the contributions from all isotopes. Defining B_α^q as the nuclear field of species α felt by the electron in state Ψ_q, and assuming a uniform polarization yields,

$$B_\alpha^q = (2/3)\mu_0(g_0/g^*)\hbar\gamma_\alpha\sum_{i\in\alpha} I_i |\Psi_q(r_i)|^2. \qquad (2.21)$$

The total nuclear field created by a uniform nuclear polarization is,

$$B_\alpha = (2/3)\mu_0(g_0/g^*)\hbar\gamma_\alpha\chi_\alpha d_\alpha \langle I_\alpha\rangle = b_\alpha\langle I_\alpha\rangle, \qquad (2.22)$$

where χ_α is the natural abundance of the nuclear species α. For GaAs (using $g^* = -0.44$) $b_{(^{75}As)} \simeq -18.4$kG, $b_{(^{69}Ga)} \simeq -9.1$kG, and $b_{(^{71}Ga)} \simeq -7.8$kG. [4] If the polarization of the nuclei by the oriented electrons is considered nonuniform (because only the nuclei close to defects are rapidly polarized) a free electron sees only a weak nuclear field because only a small number of nuclei in Eq. 2.20 contribute to the sum. [4] An electron localized at an ORD, however, sees a strong nuclear field because the values of $|\Psi_q(r_i)|^2$ near the defect are large.

It would appear from the above argument that the conduction electrons do not feel the effects of B_n. Paget [12], however, has shown experimentally and theoretically that even though the free electrons experience a small nuclear field directly, the nuclear field can still influence the free electrons to the same degree as the trapped electrons because of efficient spin exchange. The spin exchange process averages the effect of the nuclear field because it occurs on the time scale of picoseconds compared to the nanosecond lifetime of T_1^e. This implies that exchange occurs many times before an electron recombines with a hole.

2.3.1 The Magnitude of B_n

Before discussing the feedback of the nuclear field on the excited electrons

the question of the magnitude of the nuclear field will be examined in this subsection. Two cases are considered. First, the nuclear field in a large applied field parallel to the direction of the light will be calculated, and, second, the nuclear field in a small applied field of arbitrary direction will be calculated.

During the course of the calculations it will be convenient to invoke the concept of a spin temperature. [25] The heart of spin temperature theory is based on the assumption that the nuclear spin systems behave like the systems described by thermodynamics. According to Goldman [25], the spin temperature hypothesis can be stated, "A spin system isolated from the lattice and subjected to spin–spin interactions proceeds toward a state of internal equilibrium such that the probabilities of finding the system in any of its energy levels are given by a Boltzmann distribution $\exp(-E_i/k\theta_t)$. This distribution defines the spin temperature θ_t of the system."

For a nuclear spin system in the presence of an externally applied magnetic field **B** the energy of the system (neglecting quadrupolar effects which will be discussed in a later section) is described by the Hamiltonian,

$$\mathcal{H} = \mathcal{H}_Z + \mathcal{H}_D. \tag{2.23}$$

The Zeeman energy, $\mathcal{H}_Z = -\hbar\sum_i \gamma_i(\mathbf{B}+\langle\mathbf{B}_e^i\rangle)\cdot\mathbf{I}_i$, is the interaction with the external field **B** and the electronic field, $\langle\mathbf{B}_e^i\rangle$. The spin–spin energy is the interaction between nuclear spins:

$$\mathcal{H}_D = \sum_{i>k}\left(-\frac{\gamma_i\gamma_k\hbar^2}{r_{ik}^3}\right)\left[\frac{3(\mathbf{I}_i\cdot\mathbf{r}_{ik})(\mathbf{I}_k\cdot\mathbf{r}_{ik})}{r_{ik}^2} - \mathbf{I}_i\cdot\mathbf{I}_k\right], \tag{2.24}$$

where $\mathbf{r_{ik}}$ is the vector connecting spin i and spin k. The field felt by a nucleus due to this dipolar interaction is called the local field B_L, and is defined by,

$$B_L^2 = \frac{\mathrm{Tr}(\mathcal{H}_D^2)}{1/3\ \mathrm{Tr}(\sum_\alpha n_\alpha I_\alpha(I_\alpha+1)\gamma_\alpha^2)\hbar^2} \tag{2.25}$$

where n_α is number of spins of nuclear species α. The local field is a measure of the strength of $\mathcal{H}_D$, and in GaAs was calculated to be $B_L^2 = 2.1 \pm 0.1$G. [4] The density operator for the spin system described by $\mathcal{H}$ is given by,

$$\sigma = \exp(-\mathcal{H}/k\theta_t)/\mathrm{Tr}[\exp(-\mathcal{H}/k\theta_t)]. \tag{2.26}$$

If we assume that the ratio $\mathcal{H}/k\theta_t << 1$ then Eq. 2.26 reduces to the familiar high temperature approximation for σ,

$$\sigma = (1 - \mathcal{H}/k\theta)/\mathrm{Tr}(1). \tag{2.27}$$

The average nuclear spin, $<I_\alpha>$, can now be obtained as,

$$<I_\alpha> = \mathrm{Tr}(\sigma I_\alpha). \tag{2.28}$$

In the case of high field, $B >> B_L$, the time of the exchange of energy between $\mathcal{H}_Z$ and $\mathcal{H}_D$ becomes large and the Zeeman and dipolar reservoirs can be described by different spin temperatures [25]. The Zeeman reservoir dominates the heat capacity and the dipolar reservoir can be neglected in determining the spin temperature under conditions of ONP. The polarization that results from the hyperfine interaction is then given by Eqs. 2.17 and 2.18,

$$<I_\alpha> = f_\alpha \frac{I_\alpha(I_\alpha + 1)}{S(S+1)} <S>, \tag{2.29}$$

and the direction of this polarization is parallel to B,

$$<I_\alpha> = (4/3)I_\alpha(I_\alpha + 1)f_\alpha \frac{<S>\cdot B}{B^2} B. \tag{2.30}$$

The total nuclear field B_n in the direction of **B** is then given by, [3,4]

$$B_n = 4/3<S>\sum_\alpha f_\alpha I_\alpha(I_\alpha + 1)b_\alpha. \tag{2.31}$$

In the case of $B \simeq B_L$, the dipolar reservoir cannot be neglected, and obtaining a value for B_n becomes more complicated. [3,4] In this case the nuclear spin system is described by a single spin temperature θ_t, and the energy of the system is partitioned between the Zeeman and dipolar energies. This partitioning depends on the relative strengths of $B_T = |B + <B_e^i>|$ and B_L. To determine the partitioning two processes must be taken into account. First, we must consider the

thermalization of the nuclear spin system along the magnetic field $\mathbf{B}_T = \mathbf{B} + \langle \mathbf{B}_e^i \rangle$, and second, the ONP which tends to polarize all the nuclei equally along the direction of the light. By solving the master equation of the density matrix describing the two processes, a solution for $\mathbf{B}_n$ can be obtained. The following result for the component of the nuclear field aligned along **B** has been obtained independently by Dyakonov and Perel [3] and by Paget *et al.* [4]

$$\mathbf{B}_n \simeq f b_n \frac{\langle \mathbf{S} \rangle \cdot (\mathbf{B} + \Gamma_t b_e \langle \mathbf{S} \rangle)}{B^2 + \xi B_L^2} \mathbf{B}, \tag{2.32}$$

where $\xi = T_1/T_{1d}$ represents the relative relaxation rates of the Zeeman and dipolar energies, and b_e and b_n are suitable averages over α for $b_e^\alpha(0)$ and b_α discussed earlier: $b_n = (4/3)\Sigma_\alpha I_\alpha(I_\alpha+1)b_\alpha$, and $b_e = (1/3)\Sigma_\alpha b_e^\alpha(0)$. For GaAs $b_n \simeq$ 170 kG, $\xi B_L^2 \simeq 4.6\ G^2$ and $b_e \simeq -170$ G. [4] There are two points to note regarding Eq. 2.32. First, even though each nuclear species α is aligned in a different direction $(\mathbf{B} + \Gamma_t b_e^\alpha \langle \mathbf{S} \rangle)$, in low field, the nuclear spin system as a whole behaves as one "equivalent" nuclear spin system described by $f b_n$, $\Gamma_t b_e$, and ξB_L. Second, the nuclear field can be established in a field **B** perpendicular to $\langle \mathbf{S} \rangle$ (the light direction) so long as $B \simeq \Gamma_t b_e \langle S \rangle$.

In either high or low field the nuclear field B_n is quite strong (depending, of course, on f) and can be on the order of 10 kG. [3–5] This nuclear polarization corresponds to a spin temperature on the order of 10^{-7} K in a field of 1 G. [4]

2.3.2 The Effect of B_n on the Electron T_1

We now turn our attention to the feedback mechanisms of the nuclear field on the oriented electrons. If the field **B** is oriented along the z–axis then a change in the electron spin polarization due to nuclear polarization is seen in the field

dependence of τ_s (see Eq. 2.5). In this situation $<S_z>$ depends on the field $B_T = B_z + B_n$ by the equation

$$<S_z>(B_T) = -\frac{1}{2}\frac{C}{1+\tau/\tau_s(B_T)}, \tag{2.33}$$

where $\tau_s(B)$ is given by, [5,26]

$$\tau_s(B) = \tau_s(0)(1 + \Omega_L^2\tau_c^2). \tag{2.34}$$

Here Ω_L is the Larmor frequency of the electron in the total field, $B_T = B_z \pm B_n$ for $\sigma^{\pm}$ exciting light (parallel and antiparallel polarization), and τ_c is the correlation time of the fluctuations in the total field. As the field increases, τ_s increases and $<S_z>$ approaches C/2.

Experiments by Berkovits et al. [10] have demonstrated the field dependence of τ_s by sweepin the applied field B_0 from zero field to 20 kG. The value of ρ is recorded immediately after the exciting light is turned on to obtain the value of $\rho(B_0)$. The value for $\rho(B_T)$ is recorded time once ONP has occurred and a steady–state value is reached. Figure 2.2 shows the results for both the parallel and antiparallel cases. The difference $\rho(0) - \rho(B_T)$ were then fitted using Eqs. 2.33 and 2.34 to obtain values for $B_n \simeq 4$ kG and $(g^*\mu_\beta\tau_c/\hbar)^{-1} = 600$ G.

The implication of these results is that it is possible to measure changes in the nuclear field B_n through the field dependence of τ_s. This feedback of B_n on $<S>$ is one method of optically–detecting NMR which will be explored further in section 2.4.1.

2.3.3 The Hanle Effect

In general, the motion of the oriented electrons in the conduction band in an external magnetic field **B** is given by the Bloch–like equation, [2,4]

$$\frac{d<S>}{dt} = -\frac{<S> - <S_z>(B_T)}{T_1^e} - g^*\mu_\beta/h(<S> \times B). \tag{2.35}$$

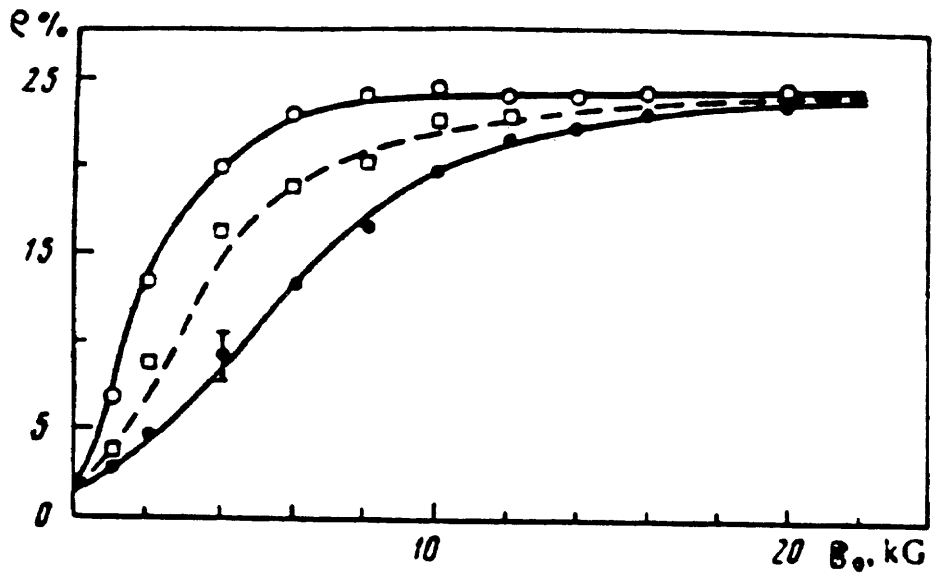

Figure 2.2: Longitudinal field dependence of ρ. Reproduced from [10]. The data points o and • correspond to the steady–state value of ρ upon excitation with σ^+ and σ^- light, respectively. The points □ correspond to the value of ρ before nuclear polarization is created. The data is fitted using Eqs. 2.33 and 2.34 with $\tau/\tau_s(0) = 24$ and $(g^* \mu_\beta \tau_c/\hbar)^{-1} = 600$ G. The dashed line yielded $B_n = 0$ as expected and the solid lines returned a maximum value of $B_n = 4$ kG.

The steady–state solution of Eq. 2.35 for the z–component of the average spin, $<S_z>$, is given by the Lorentzian,

$$<S_z> = <S>_0 \frac{\Delta B^2 + B_z^2}{\Delta B^2 + B^2}, \tag{2.36}$$

and the optical observation is $\rho = 2C<S_Z>$ where $<S>_0 = (1/2)C\tau_s(\tau + \tau_s)^{-1}$ allows for the decrease in C due to electron spin–lattice relaxation. The result of Eq. 2.36 is analogous to the magnetic depolarization of fluorescence in the gas phase explained by Hanle. [27] Figure 2.3 depicts the Hanle effect for optical pumping in an applied field **B** perpendicular to the light direction (excluding nuclear effects). The case illustrated in Fig. 2.4 where $B_z = 0$ is called the complete Hanle effect. The quantity ΔB is known as the Hanle width and is inverse electron spin lifetime expressed in field units i.e., $\Delta B = h(g^* \mu_\beta T_1^e)^{-1}$.

An interesting result occurs when the applied field is perpendicular to the pumping light and is swept from zero field to a field $B >> \Delta B$. In the small fields such that $B \leq B_L$, ONP occurs in the effective field $(\mathbf{B} + \Gamma_t b_e <\mathbf{S}>)$ as indicated by Eq. 2.32. [4,6,8] The resultant nuclear field is parallel to $(\mathbf{B} + \Gamma_t b_e <\mathbf{S}>)$ and has a magnitude much larger than B and B_L. The Hanle effect in this case is magnified by the presence of the nuclear field. Defining, [4]

$$K = f b_n <S>_0 \frac{(\mathbf{B} + \Gamma_t b_e <\mathbf{S}>)}{B^2 + \xi B_L^2} \cdot <\mathbf{S}> \tag{2.37}$$

and using the field defined by $(\mathbf{B} + K\mathbf{B})$ in Eq. 2.35, the steady–state value for $\rho = <S_z>$ is given by,

$$<S_z> = <S>_0 \frac{\Delta B^2 + B_z^2(1+K)^2}{\Delta B^2 + B^2(1+K)^2}. \tag{2.38}$$

The amplification of the Hanle effect is determined by the value of K which is large for B comparable to $\Gamma_t b_e <S>$, but tends to zero as B increases such that $B >> \Gamma_t b_e <S>$. The amplification manifests itself as a dip in the Hanle curve (the dotted

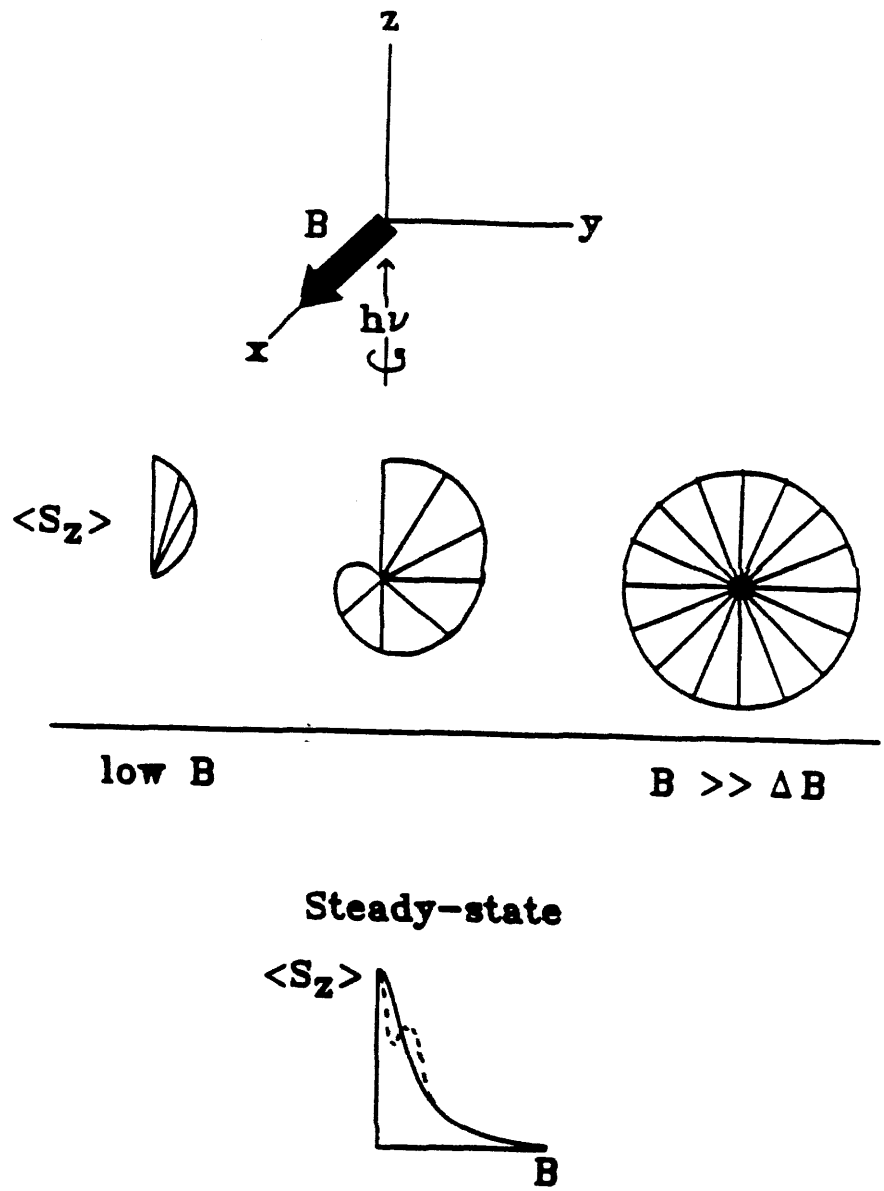

Figure 2.3: The Hanle effect. The electron spin polarization <S> undergoes damped precession about the transverse field B = B**x**. As B increases the z–component of <S>, $\langle S_z \rangle = \rho$, decreases. The steady–state solution for $\langle S_z \rangle$ (the solid trace) is a Lorentzian with half–width ΔB, the Hanle width. The dashed line indicates nuclear polarization in the field $(B + \Gamma_t b_e \langle S \rangle)$ by a characteristic dip in low field. The large nuclear field amplifies the depolarization of the Hanle effect (see text).

line in Fig. 2.3) for small B. [4,6,8] The importance of this dip is that it is a clear and experimentally simple indication of nuclear spin polarization. As will be discussed in chapter 4, this type of field sweep was used for preliminary measurement of the strength of the nuclear field by fitting the observed Hanle curve using Eq. 2.38

If ONP occurs in a field $\mathbf{B}_0$ parallel to the light direction (the z–axis) then the total field seen by the electrons $\mathbf{B}_T = \mathbf{B}_0 \pm \mathbf{B}_n$ is parallel to the z–axis and no Hanle effect is seen. If, however, the angle of the total field becomes oblique to the z–axis then a Hanle effect is seen. In this case, for σ^+ light, the steady–state solution of Eq. (2.35) for $<S_z>$ is given by,

$$<S_z> = <S>_0 \frac{\Delta B^2 + (B_z + \Sigma_\alpha B_{\alpha z})^2}{\Delta B^2 + (B + \Sigma_\alpha B_\alpha)^2} . \qquad (2.39)$$

Equation (2.39) describing the Hanle effect in the presence of an oblique total field also provides a means for measuring the nuclear field.

Resonance methods for obtaining the Hanle effect when ONP occurs in a parallel field $\mathbf{B}_0$ will be the subject of the next section. The next section will also compare the two feedback mechanims, the field dependence of τ_s and the Hanle effect, and how they are used to optically–detect NMR.

2.4 Optically–Detected NMR

The early optically–detected NMR (ODNMR) experiments were performed under quasi steady–state conditions. [9–15,18,19,28] The ONP process took place in a field $\mathbf{B}_0$ parallel to the light for a time long enough to establish a steady–state ρ_{ss} in the total field $\mathbf{B}_T = \mathbf{B}_0 + \mathbf{B}_n$. Once this steady–state was reached, the radiofrequency (rf) field was swept through the resonances of the major isotopes (^{69}Ga, ^{71}Ga, and ^{75}As) while the light remained on. The nuclear resonance was

seen as a deviation of ρ from $\rho_{ss} = 2C <S_z>(B_T)$. The steady–state ODNMR experiment has been performed on a number of GaAs materials including bulk $Ga_{1-x}Al_xAs$ ($x \simeq 0.3$) [9–11], bulk GaAs [12–15], and GaAs/$Ga_{1-x}Al_xAs$ ($x \simeq 0.3$) quantum wells [18,19] and heterojunctions [28]. While the results of these quasi steady–state ODNMR experiments clearly showed the sensitivity improvements of at least 10^5 over conventional NMR, the resulting lineshapes were not indicative of the unperturbed lattice. The detected lineshape strongly depends on the NMR conditions (sudden application of rf or adiabatic passage through resonance) [9,10,12] as well as on the presence of the polarized photocarriers during NMR. The following subsections describe the quasi steady–state ODNMR experiment and motivate the need for an alternative method.

2.4.1 The Field Dependence of τ_s and Steady–State ODNMR

As mentioned, the field dependence of τ_s can be used as a method of detection for quasi steady–state ODNMR. [9,10] The deviation from the steady–state value ρ_{ss} under magnetic resonance conditions is found by combining Eqs. 2.33 and 2.34 and differentiating with respect to B_n,

$$\frac{d\rho_{ss}}{dB_n} = \frac{d\rho_{ss}}{dB_T} = 2C\left(\frac{\tau}{\tau_s(0)}\right)\frac{\left[\frac{g^*\beta\tau_c}{h}\right]^2 B_T}{\left[1 + \left[\frac{g^*\beta\tau_c}{h}\right]^2 B_T^2 + \frac{\tau}{\tau_s(0)}\right]^2}, \qquad (2.40)$$

where $B_T = B_0 \pm B_n$ depending on the circular–polarization of the exciting light.

In a quasi steady–state ODNMR experiment, however, the mechanism of Eq. 2.40 due to the field dependence of τ_s is seen only as a secondary effect. [10] The majority of the change in ρ is due to the tilting of the nuclear contribution B_n of the total field B_T on resonance, an effect called the incomplete Hanle effect expressed in Eq. 2.36.

2.4.2 The Incomplete Hanle Effect and Steady–State ODNMR

The incomplete Hanle effect occurs when the total field B_T becomes oblique to the light direction **z**. The tilting of the total field is illustrated vectorally in Figure 2.4a and can be understood using the concept of spin temperature in the rotating frame. [29] If we consider a spin system being irradiated with rf, the rotating–frame Hamiltonian (considering only the secular spin–spin inteaction) is time–independent and given by,

$$\mathscr{H}' = \Delta\omega I_z + \mathscr{H}'_D + \omega_1 I_x, \tag{2.41}$$

where $\Delta\omega$ is the resonance offset and ω_1 is the rf field amplitude. The effective field $\mathbf{B_{eff}}$ in the rotating frame has magnitude,

$$\gamma B_{eff} = (\Delta\omega^2 + \omega_1^2)^{1/2}, \tag{2.42}$$

and is oriented at angle φ from the z–axis given by,

$$\varphi = \tan^{-1}\left[\frac{\omega_1}{\Delta\omega}\right]. \tag{2.43}$$

The Hamiltonian of Eq. 2.41 can now be rewritten in the form,

$$\mathscr{H}' = \mathscr{H}'_Z + \mathscr{H}'_D = \gamma \mathbf{B_{eff}} \cdot \mathbf{I} + \mathscr{H}'_D. \tag{2.44}$$

The spin temperature hypothesis applied to the Hamiltonian of Eq. 2.44 implies that, eventually, the system will come to equilibrium with the nuclei aligned along the effective field $\mathbf{B_{eff}}$, an effect called spin–locking.

It is the spin–locked component of the resonant nuclear field that causes the tilting of the total field away from **z** and initiates the incomplete Hanle effect. If the rf field is applied suddenly in a time short compared to the spin–spin relaxation time T_2 and a spin temperature is established in the rotating frame (in a time $\simeq T_2$), then the resulting Hanle effect can be calculated from the vector picture of Fig. 2.4a. The spin–locked component of B_α (B'_α) lies along the effective field at angle

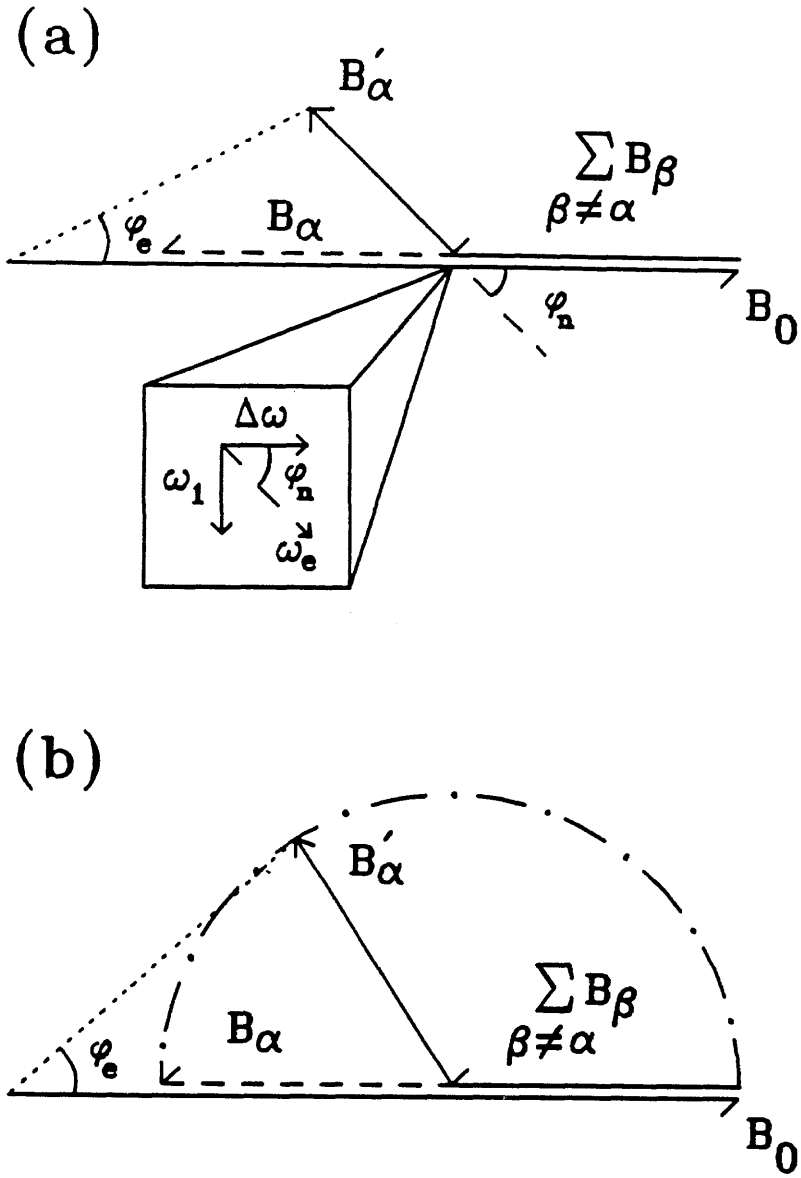

Figure 2.4: Vector picture for quasi steady–state ODNMR using sudden application of rf, part (a), and adiabatic passage, part (b). Both figures show the anti–parallel geometry ($B_T = B_0 - B_n$) with $B_0 > B_n$. In the sudden approximation the spin–locked component $B'_\alpha = B_\alpha \cos(\varphi_n)$ where φ_n is the direction of the effective field ω_e (shown in the inset). The field responsible for the Hanle effect B_T is given by $B_T = B_T \cos(\varphi_e)$. In adiabatic passage (part (b)) the field B_α follows the effective field (follows the dash/dot semicircle) as the rf sweeps through resonance. The spin–locked component in high field ω_1 is equal to $B_{\alpha'}$.

$\varphi_n = \tan^{-1}(\omega_1/\Delta\omega)$. The total field seen by the oriented electrons is then given by the vector sum, [12]

$$\mathbf{B}_T' = \mathbf{B}_0 + \sum_{\beta \neq \alpha} \mathbf{B}_\beta + \mathbf{B}_\alpha' \tag{2.45}$$

where the sum is over the nuclear field contributions of the nonresonant spins. The value of the spin–locked component is just the projection of $\mathbf{B}_\alpha$ on the effective field $B_\alpha' = B_\alpha \cos(\varphi_n)$. [12] Using this result we find the projections of B_α' on the z and x–axes,

$B_{\alpha_z}' = B_\alpha \cos^2(\varphi_n)$ and $B_{\alpha_x}' = B_\alpha \cos(\varphi_n)\sin(\varphi_n)$, respectively. The total tilt angle φ_e of B_T is then given by,

$$\cot(\varphi_e) = \frac{B_T - B_\alpha \sin^2(\varphi_n)}{B_\alpha \cos(\varphi_n)\sin(\varphi_n)}. \tag{2.46}$$

The resulting Hanle effect is found from Eq. 2.35,

$$\rho = 2C \langle S \rangle_0 \frac{\Delta B^2 + (B_T)^2 \cos^2(\varphi_e)}{\Delta B^2 + (B_T)^2}. \tag{2.47}$$

The change $\partial\rho$ in ρ due to the incomplete Hanle effect is given by,

$$\partial\rho = 2C \langle S \rangle_0 \sin^2(\varphi_e). \tag{2.48}$$

An important consequence of Eqs. 2.46 and 2.47 is that there is a null in the signal $\partial\rho$ at the resonance position $\Delta\omega = 0$ ($\varphi_n = 90^\circ$). The reason for the null can be explained using a simple geometric argument. [30] On resonance, the effective field is equal to the rf field B_1 oriented along the x–axis. The nuclear spins precess about the effective field in the yz–plane. The projection of B_α on the x–axis is thus zero and no magnetization is spin–locked. In this situation the nuclei are said to be at an infinite spin temperature. [25] A steady–state ODNMR experiment performed under these conditions yields a lineshape with a doublet structure ("W" shaped). [9,12] The null is a direct result of the sudden application of the rf field, and if the steady–state ODNMR experiment is performed using adiabatic processes, the null is not observed. [3,10]

A Hanle effect also occurs if the rf is applied adiabatically. [3,10] In the case of adiabatic fast passage where the rate is fast enough to neglect spin–lattice relaxation, but slow enough to allow a spin temperature in the rotating frame to be established ($\leq 1/T_2$). The trajectory of the resonant nuclear field is depicted by the dotted line in Fig. 2.4b. As mentioned the signal that results from adiabatic fast passage does not contain the same null that occurs from sudden application of rf. The magnetization follows the effective field in the rotating frame [30] during the rf field sweep, and the Hanle effect has a maximum on resonance. [3,10]

The nuclear field of the resonant nucleus is now given by, [30]

$$B'_{\alpha} = B_{\alpha} \frac{B_{eff}}{\sqrt{B_{eff}^2 + B_L^2}}, \tag{2.49}$$

and has the same magnitude as it started with if $B_{eff} >> B_L$ (i.e. $B_1 >> B_L$). The total field can be calculated by Eq. 2.45 with a simple vector model that follows the trajectory shown in Fig. 2.4b. The signal on resonance is governed by Eqs. 2.47 and 2.48 with φ_e following from $\varphi_n = \varphi$ of Eq. 2.43.

2.4.3 Problems With Steady–State ODNMR

The steady–state ODNMR technique has several drawbacks in its use as a way of increasing the sensitivity of conventional solid–state NMR for application to GaAs defects and surfaces. The signal derived in the previous section is valid only for saturation conditions $B_1 >> B_L$ where the irradiated spin system reaches a quasi–steady–state in the rotating frame in a time short compared to T_1. [25,31] The consequence of such high–power rf experiments is that the nuclear resonance lineshape is broadened by the rf field. [26] The rf power can be lowered only at the expense of signal–to–noise as indicated by Eq. 2.49. Once the rf power is lowered to $B_1 \leq B_L$ (linear response regime) the spin–locked component is only a fraction of its

initial value. The tilting angle of B_T becomes smaller, and the signal is reduced.

Eq. 2.49 is valid only if the spin system reaches a quasi–steady–state for each rf frequency. The time it takes to reach this state for low B_1 regime can be calculated by solving the dynamics of the spin system including effects of the local field B_L (the Provotorov equations of partial saturation). [25] The important implication here is that if the sweep rate is faster than the effective time constant, the spin–locked component is even smaller than indicated by Eq. 2.49. A quantitative description of the lineshape in this case would be a cumbersome task.

Another problem with the steady–state ODNMR technique is its inherent inflexibility. One is limited to NMR experiments in the continuous wave (cw) regime. The advances in conventional solid–state NMR spectroscopy over the past 30 years (FT spectroscopy, multiple–pulse experiments, 2D spectroscopy, etc.) are not possible in conjunction with steady–state ODNMR.

Finally, the resolution of the steady–state ODNMR experiment is further compromised by the presence of the excited electrons during NMR. If the light remains on during NMR, then the Zeeman Hamiltonian has the form,

$$H_Z^\alpha = \gamma_\alpha(B_0 + \Gamma_t b_e^\alpha \langle S_z \rangle) I_z^\alpha, \tag{2.50}$$

where the term $\Gamma_t b_e^\alpha \langle S_z \rangle$ is the average hyperfine field defined in Eq. 2.19. The position of the resonance line is shifted by this field (the optical Knight shift). [12,28,31] Using the TSONMR technique (discussed in the next section), we have determined that the field is spatially inhomogeneous. The field originates predominantly from localized electrons at ORD's and the inhomogeneity is due the Knight shift falling off for nuclear sites in more distant shells. This inhomogeieity is unresolved and results in a broadening of the nuclear resonance line.

Based on the successes and failures of the steady–state ODNMR technique, we have developed a new method of optical NMR, time–sequenced optical NMR (TSONMR), that separates the three processes of optical NMR (ONP, NMR, and

OD) in time and allows them to be separately optimized. The resulting technique maximizes the resolution and sensitivity of optical NMR while at the same time adds versatility to the NMR part of the experiment. The following section describes the theory behind TSONMR.

2.5 Time–Sequenced Optical NMR

The subject of this section, the TSONMR experiment, is the focus of the rest of this thesis. This section is designed as an introduction to the TSONMR method using the theoretical basis established in the previous sections. Experimental evidence for the enhanced sensitivity and resolution of the technique as well as its versatility will be presented, and comparisons to the quasi steady–state ODNMR method will be made. Considerable effort has gone into the development of the experimental apparatus, and a detailed discussion of it is given in chapter 3. The experimental foundations of the TSONMR technique and applications to GaAs materials are given in chapters 4 and 5, respectively.

2.5.1 Time–Sequencing

An optical NMR experiment can be viewed in terms of three physical processes, ONP, NMR, and OD. In the TSONMR method these processes occur in distinct intervals as depicted in Figure 2.5. In the first step ONP is induced in the usual manner by irradiation with circularly–polarized light near the band gap in an external magnetic field B_0^p parallel to the direction of light propagation. This leads to a steady–state B_n which is approached with time constant $T_{1_{on}}$ (a combination of the $T_{1_{hf}}$ defined earlier in Eq. 2.16 and all other relaxation processes). The subscript denotes spin–lattice relaxation with the band–gap light on. As discussed

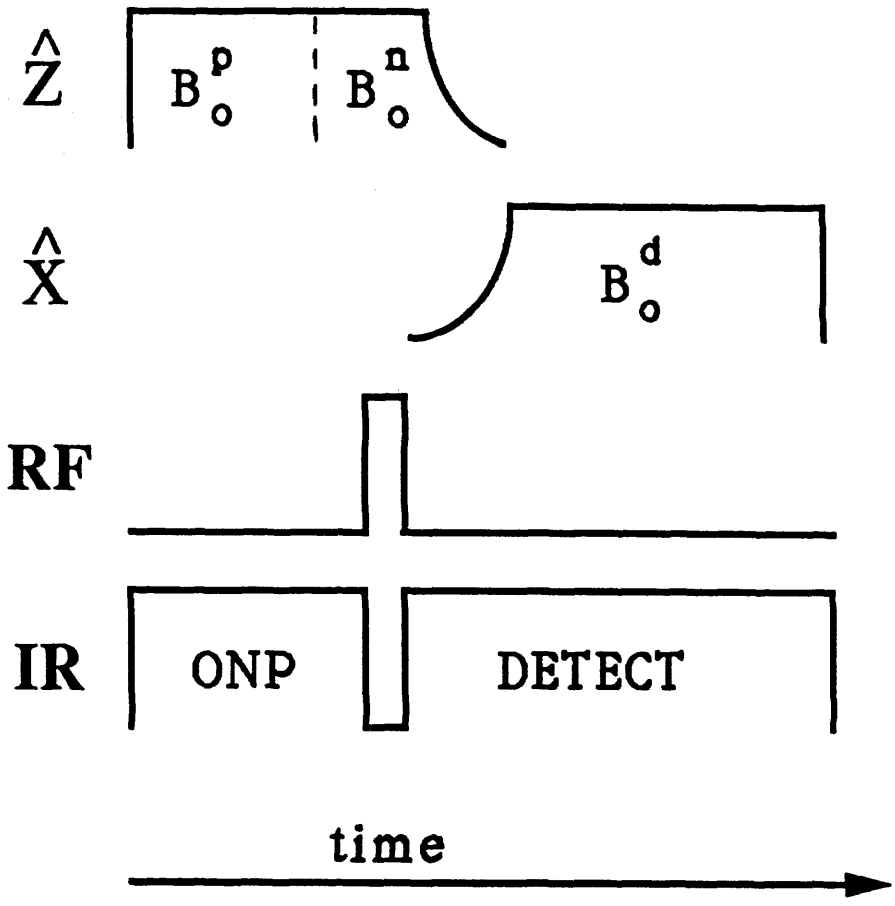

Figure 2.5: General timing diagram for TSONMR. The ONP period is carried out in a field B_0^p for a period of seconds to minutes. The field may then be adiabatically cycled to a new field B_0^n for NMR. The NMR part of the experiment is carried out in the dark and can consist of continuous irradiation at frequency ω or a sequence of high power rf pulses. The field B_0^n is cycled to the field B_0^d perpendicular to **z** and the light is restored for detection via the complete Hanle effect. The sequence is repeated for each frequency ω or for each pulse cycle time t_1 to obtain the full spectrum.

in section 2.3, this process only requires B_0^p to be greater than the internuclear spin–spin couplings, but will typically be optimum in high field [3,10,11], where the electron spin lattice relaxation rate $1/\tau_s$ falls well below the decay rate $1/\tau$ of the optically excited states.

In the second step the light is turned off and the nuclei are irradiated as in any NMR or NQR experiment. The cw variant of the TSONMR experiment is discussed here using a single rf frequency variable ω to distinguish successive repetitions of the sequence, but multiple resonance and time–domain experiments could be treated identically (see chapter 5). Since T_{1off} is at least as long as T_{1on} and can be many minutes,[10,13] it is practical to cycle adiabatically to any field $\mathbf{B_0^n}$, possibly different from $\mathbf{B_0^p}$, appropriate for the nuclear resonance. The absence of the light during the rf irradiation step will be shown to be crucial to spectral resolution and interpretation.

The third step is optical detection of the remaining nuclear polarization by the complete Hanle effect. By using the complete Hanle effect for detection in the time–sequenced experiment the incompatibility between sensitivity and resolution is reconciled. In the complete Hanle effect $\mathbf{B_0}$ and $\mathbf{B_n}$ are collinear (parallel or antiparallel) and perpendicular to the **z** direction of light propagation **z**. This is achieved by rotation of $\mathbf{B_0}$ into the **x** direction with $\mathbf{B_n}$ following adiabatically as illustrated vectorally in Figure 2.6. The observed transient determined by the quasi–steady–state Hanle effect subsequent to restoring the light at $t_d = 0$ is found using Eq. 2.36,

$$\rho(\omega,t_d) = 2C \langle S \rangle_0 \frac{\Delta B^2}{\Delta B^2 + B_T^2(\omega,t_d)} . \qquad (2.51)$$

The time dependence [8] is due to the approach to a new steady–state nuclear field B_n^d under the influence of the OD period applied field $\mathbf{B_0^d} = B_0^d\mathbf{x}$, the optical irradiation and other spin–lattice mechanisms. [4,32] The new nuclear field is

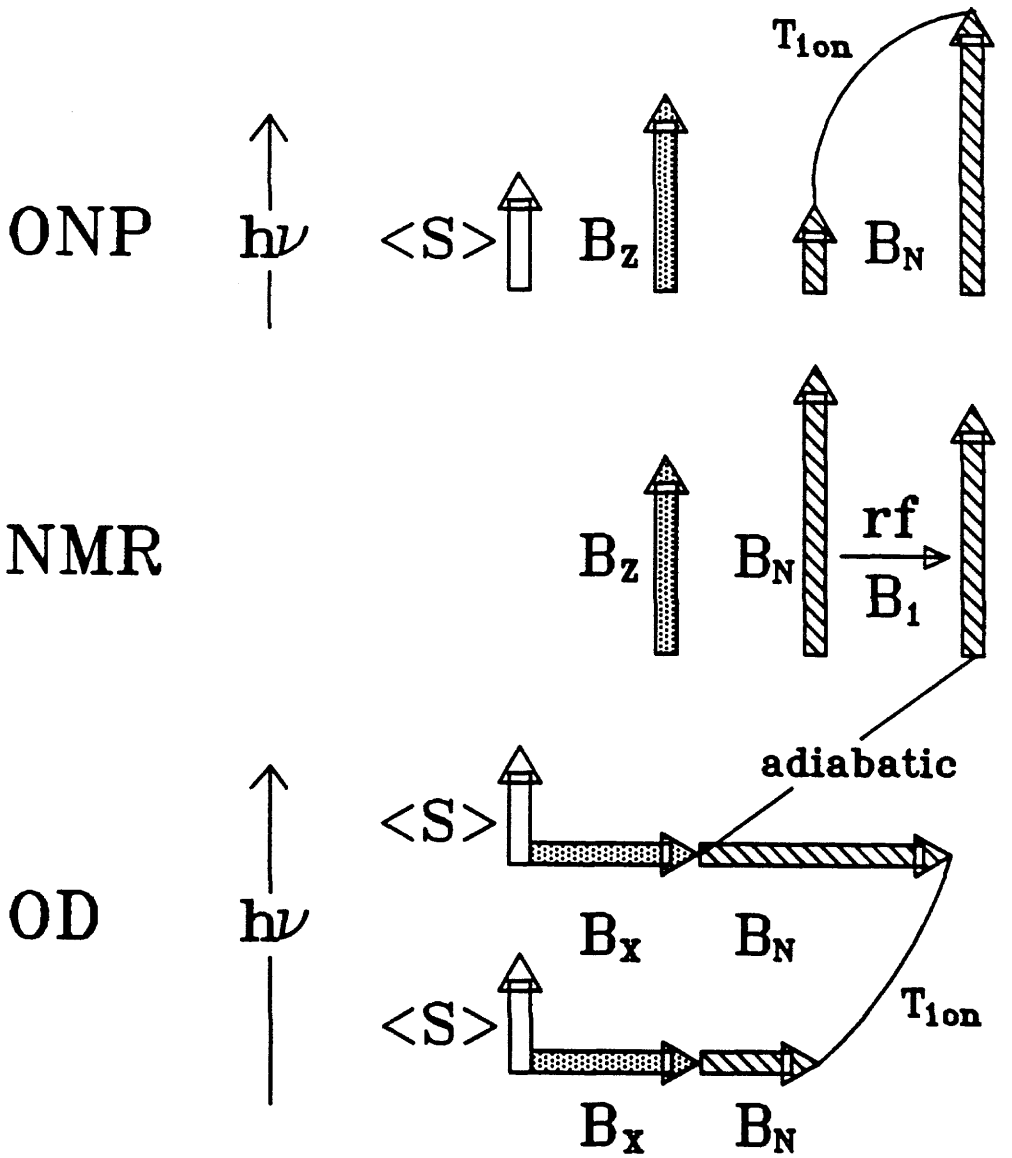

Figure 2.6: Vector picture of TSONMR. This figure shows the orientation of the electron spin polarization <S>, the applied fields $B_0^p = B_z$ and $B_0^d = B_x$, and the nuclear field B_N during a TSONMR experiment. Note that the light is off during NMR which is essential for high resolution.

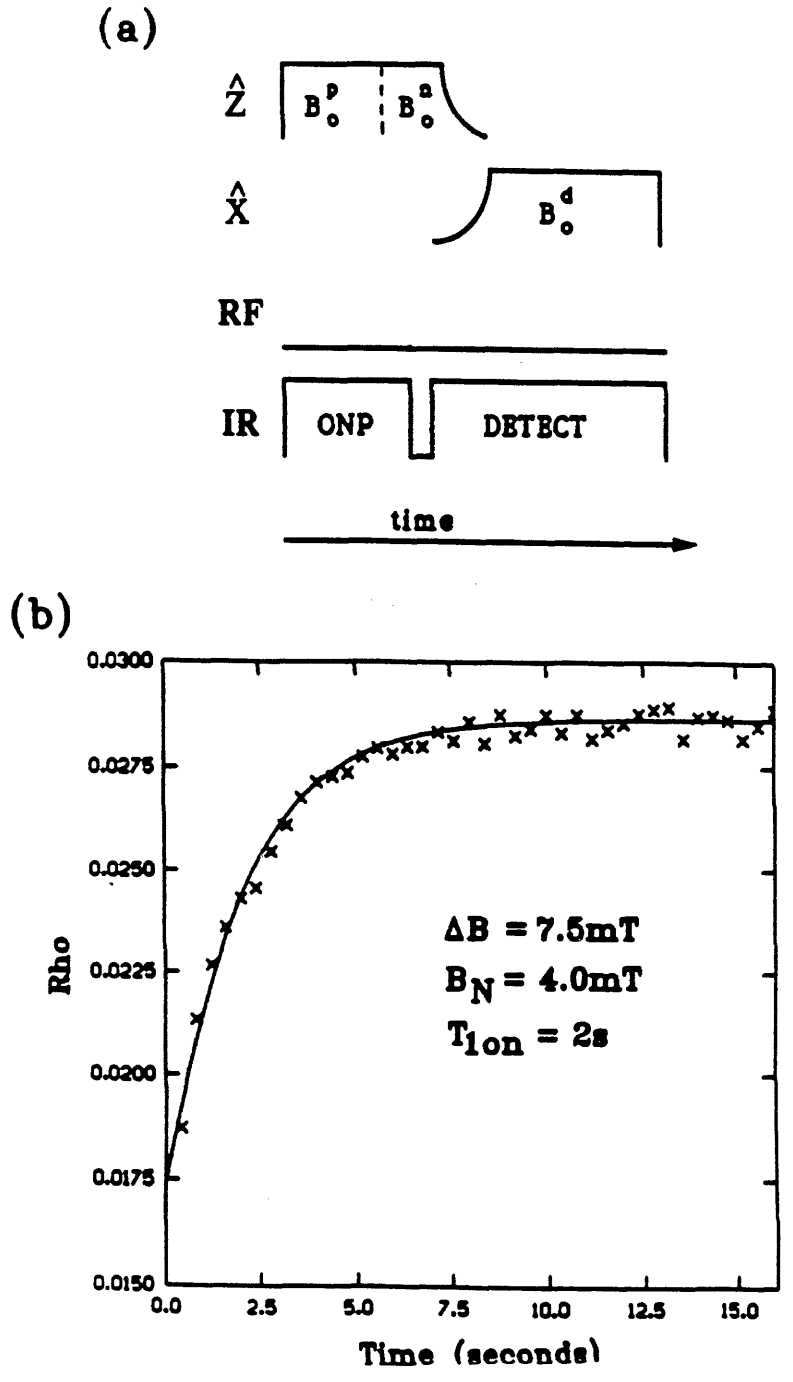

Figure 2.7: The timing diagram for the null experiment (no rf) part (a), and the detected transient $\rho^{null}(t_d)$, part (b). The x's represent the data obtained from the experiment described in (a) omitting the rf irradiation. The solid line represents a theoretical fit, and the resulting parameters are given in the inset of (b).

approached exponentially starting from the value $B_n(\omega)$ which survives the NMR irradiation at frequency ω in the dark. Thus, insertion of $B_T(\omega,t_d) = B_0^d + B_n^d + (B_n(\omega) - B_n^d)\exp(-t_d/T_{1_{on}})$ into Eq. 2.51 specifies the transient.

Figure 2.7b is an experimental example of this procedure performed on a p–type GaAs sample doped with Zn acceptors at a concentration of $4x10^{17}/cm^3$. The experiment was done omitting the rf irradiation and serves as a null for the NMR experiment. The fit according to Eq. 2.51 provides the parameters $\Delta B = 7.5$ mT, $B_n^{null} = 4.0$ mT, $B_n^d = 0.0$, and $T_{1_{on}} = 2.0$ s. The time–sequenced NMR signal $S(\omega)$ is the frequency–dependent modulation in the area of the transient $\rho(t_d)$. Figure 2.6 shows a vector diagram for the TSONMR experiment.

2.5.2 Sensitivity and Resolution of TSONMR

Figure 2.8a is a demonstration of time–sequenced optical NMR on the ^{69}Ga resonance of the p–type sample described in the previous section. The rf field strength was $\cong$ 1 μT and lower values gave the same linewidth of 2 ± 0.5 kHz. This is a factor of $\cong$ 20 narrower than the highest resolution ^{69}Ga spectrum previously obtained with steady–state optical methods [9,10] as shown in Figure 2.9. Figure 2.10 compares the observed linewidth with that obtained from conventional NMR detection. [33] The width is identical to the conventional NMR linewidth and is explicable as due to nuclear spin–spin coupling. [34,35]

The spectrum of Fig. 2.8b shows the same ^{69}Ga cw–TSONMR spectrum with the light remaining on during NMR. The spectrum exhibits both an optical Knight shift and broadening of the resonance line. This result is consistent with the interpretation that the strongest hyperfine coupling occurs near centers of electron localization, but sharpens it in a way that is encouraging for analytical uses of the method. While the "light on" spectrum of Fig. 2.8b shows that the signal is

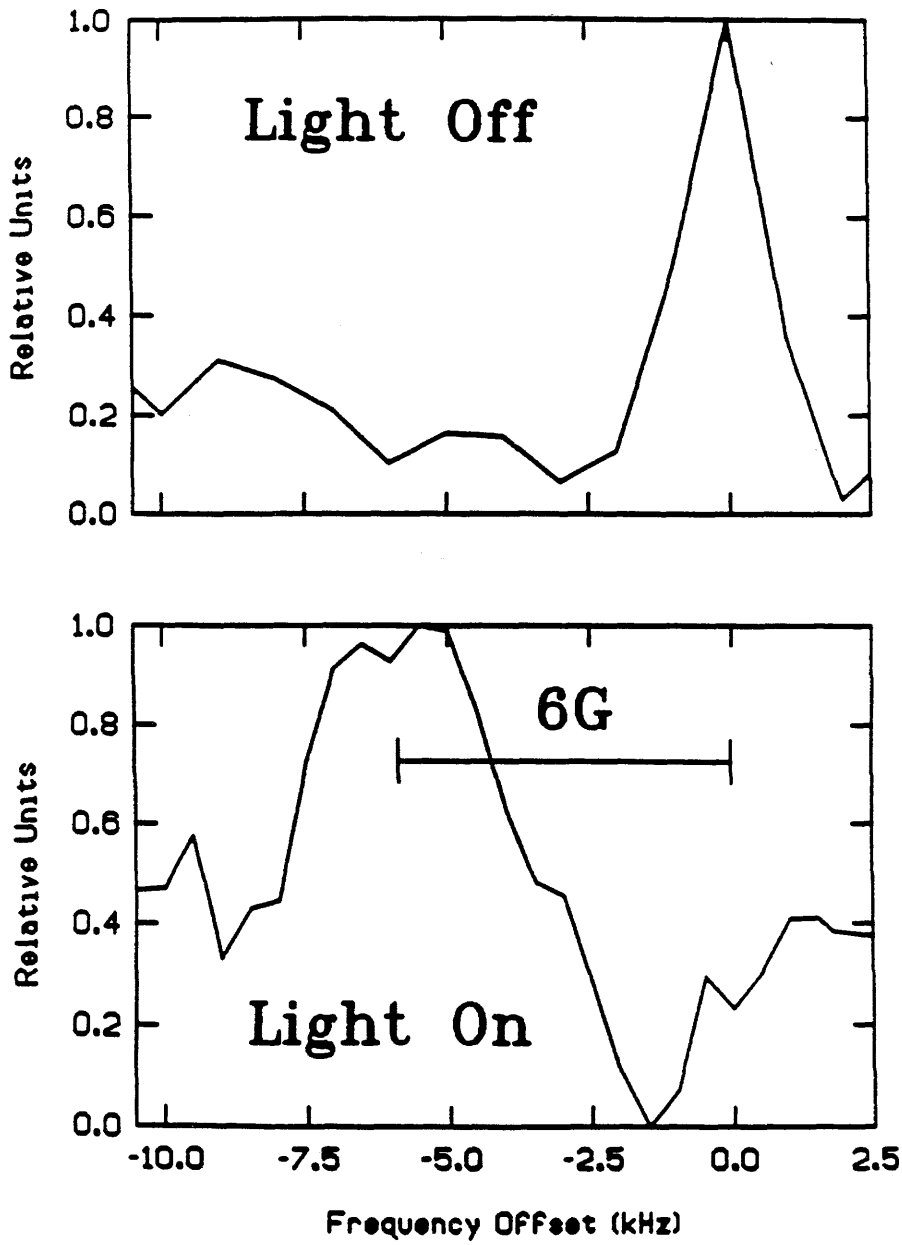

Figure 2.8: Time–sequenced optical NMR of ^{69}Ga in GaAs. The spectra in (a) and (b) were obtained with the light off and the light on during NMR, respectively. The x–axis in (a) is identical to and aligned with the x–axis in (b). The difference in the resonance frequency for the two spectra is due to the optical Knight shift of $\simeq$ 6 kHz. The broadening of the resonance in (b) is due to inhomogeneities of the electron field B_e.

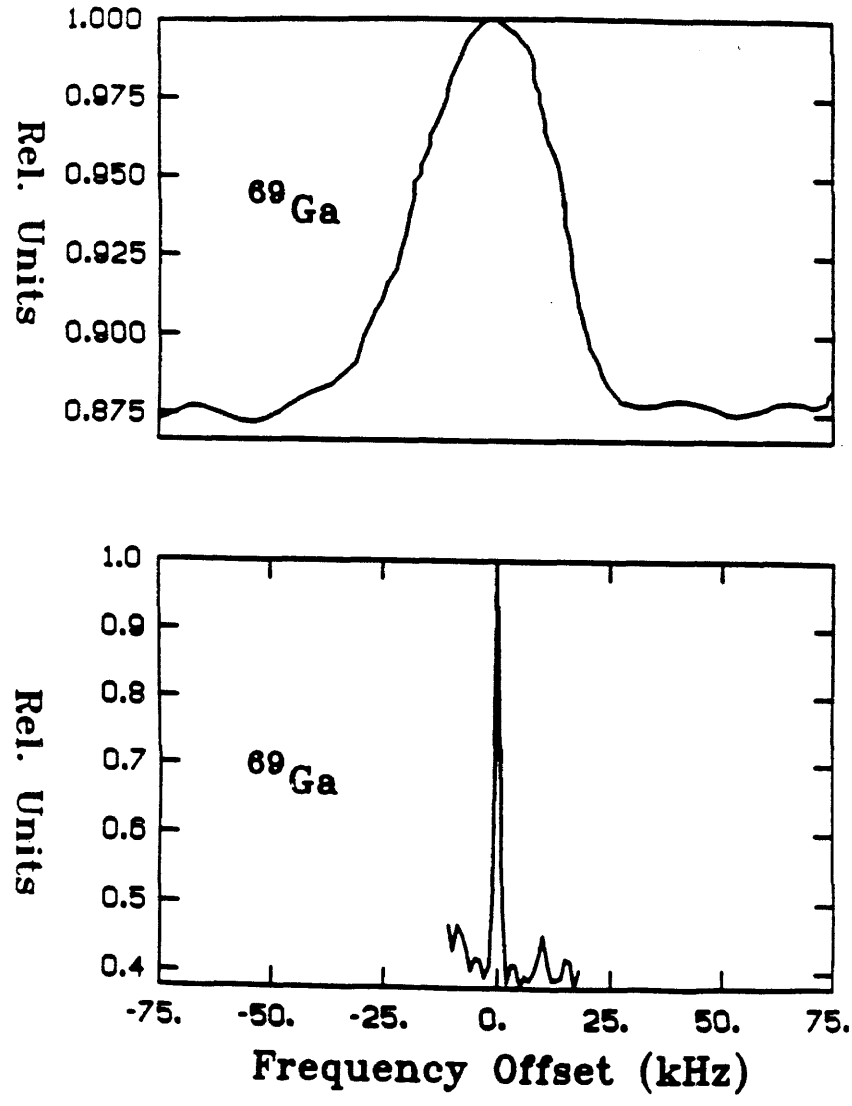

Figure 2.9: TSONMR vs. quasi steady–state ODNMR. The upper trace is reproduced from [9]. This spectrum is the ^{69}Ga resonance from a $Ga_{1-x}Al_xAs$ ($x \simeq 0.3$) and was taken in a field $B_z = 1.5$ kG. The spectrum represents the best lineshape recorded by steady–state ODNMR. The lower trace is a ^{69}Ga TSONMR spectrum of a p–type GaAs sample with $B_0^p = B_0^n = 150$ G, $B_0^d = 30$ G, and 10 s ONP. The TSONR linewidth is narrower by a factor of 20 than the ODNMR linewidth. The sensitivity is also better since our sample has a nuclear field only 10^{-3} of that of the upper trace.

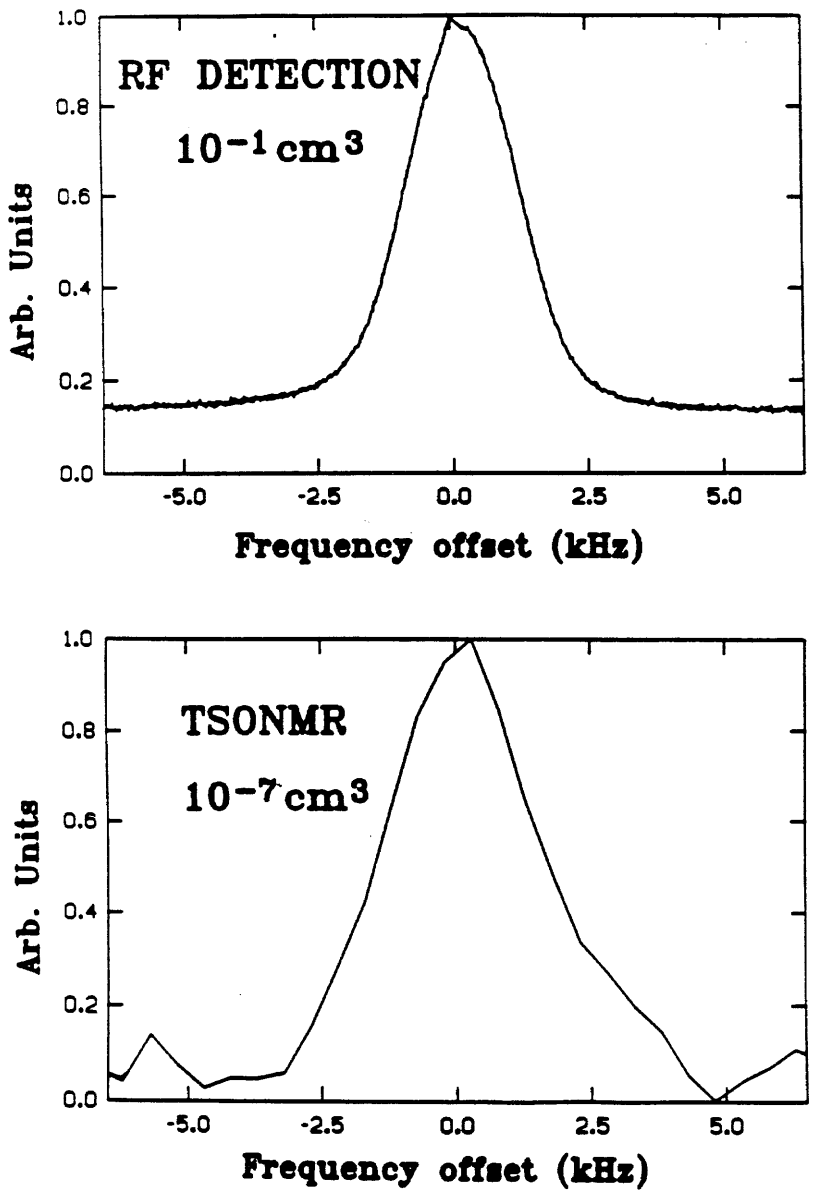

Figure 2.10: Radiofrequency detection vs. TSONMR. The upper trace is an rf–detected ^{69}Ga NMR spectrum of sample 1 at 4.7 T. [34] The ^{69}Ga TSONMR spectrum (lower trace) is from sample A. The sample volume is 10^6 times smaller in the lower trace (TSONMR). Allowing for the difference in S/N between the spectra, the TSONMR technique is more sensitive by a factor of at least 10^5. The linewidth of the TSONMR spectrum is equal to that of the rf–detected spectrum which indicates that the TSONMR spectrum is dominated by the bulk spins.

dominated by nuclear spins that experience the optical Knight shift, the "light off" resonance shows that these spins have a spectrum that in the absence of photocarriers is not measureably perturbed by the optically relevant defect. Thus it is anticipated that the method will be applicable to randomly distributed defects and that the necessary proximity to a localization site will not unduly degrade the resolution. A similar situation might be expected to hold in quantum wells, [18,19] where the interfacial barrier provides the necessary electron localization and point defects are presumably unnecessary (see chapter 5).

The signal–to–noise ratio in Fig. 2.8 is consistent with quantum–limited detection (see chapter 3) and a change in the nuclear field $\delta B_n(\omega) = (B_n(\omega) - B_n^{null}) \cong 0.02\ B_n$ by the NMR irradiation at resonance. It corresponds to a volume of $\cong 10^{-7}$ cm^3 implying sensitivity about five orders of magnitude better than conventional NMR. This estimate is self–consistent in that it represents a destruction of $\cong$ 8% of the ^{69}Ga polarization, and a significantly higher percent destruction would be expected to be associated with power broadening and overtone transitions, [14] which were indeed seen at higher rf field strength. Also, in separate measurements in which the rf frequency was not incremented, the variance in the observed signal was that expected from the photon statistics and this value is indicated by the error bar in Fig. 2.8a. A more detailed description of the signal–to–noise ratio will be given in chapter 4.

2.6 References

[1] M.I. Dyakonov and V.I. Perel, Zh. Eksp. Teor. Fiz. **60**, 1954 (1971) [Sov. Phys.–JETP **33**, 1053 (1971)].

[2] M.I. Dyakonov and V.I. Perel, Zh. Eksp. Teor. Fiz. **63**, 1883 (1972) [Sov. Phys.–JETP **36**, 995 (1973)].

[3] M.I. Dyakonov and V.I. Perel, Zh. Eksp. Teor. Fiz. **65**, 362 (1973) [Sov. Phys.–JETP **38**, 177 (1974)].

[4] D. Paget, G. Lampel, B. Sapoval, and V.I. Safarov, Phys. Rev. B **15**, 5780 (1977).

[5] M.I. Dyakonov and V. I. Perel in: *Optical Orientation* ed. F. Meier and B.P. Zakharchenya (North Holland, Amsterdam, 1984) p. 11.

[6] V.G. Fleisher and I.A. Merkulov *ibid* p. 173.

[7] D. Paget, and V.L. Berkovits *ibid* p. 381.

[8] V.K. Kalevich, V.D. Kul'kov, and V.G. Fleisher, Pis'ma Zh. Eksp. Teor. Fiz. **35**, 17 (1982) [JETP Lett. **35**, 20 (1982)].

[9] A.I. Ekimov and V.I. Safarov, ZhETF Pis. Red. **15**, 453 (1972) [JETP Lett. **15**, 319 (1972)], and *Proc. XI Int. Conf. on the Physics of Semiconductors, Warsaw, 1972*, ed. M. Miasek (PWN Polish Scientific, Warsaw, 1972).

[10] V.L. Berkovits, A.I. Ekimov, and V.I. Safarov, Zh. Eksp. Teor. Fiz. **65**, 346 (1973) [Sov. Phys.–JETP **38**, 169 (1974)].

[11] M.I. Dyakonov, V. I. Perel, V.L. Berkovits and V.I. Safarov, Zh. Eksp. Teor. Fiz. **67**, 1912 (1974) [Sov. Phys.–JETP **40**, 950 (1975)].

[12] D. Paget, Phys. Rev. B **24**, 3776 (1981).

[13] D. Paget, Phys. Rev. B **25**, 4444 (1982).

[14] V.K. Kalevich, V.D. Kul'kov, I.A. Merkulov, and V.G. Fleisher, Fiz. Tverd. Tela **24**, 2098 (1982) [Sov. Phys. Solid State **24**, 1195 (1982)].

[15] V.K. Kalevich, V.L. Korenev, and V.G. Fleisher, Izvest. Akad. Nauk SSSR. Ser. Fiz. **52**, 434 (1988).

[16] N.W. Ashcroft and N.D. Mermin, *Solid State Physics* (Saunders College, Philadelphia, 1976), p. 566.

[17] E.O. Kane, J. Phys. Chem. Solids **1**, 249 (1957)

[18] G.P. Flinn, R.T. Harley, M.J. Snelling, A.C. Tropper, and T.M. Kerr, J. of Lumines. **45**, 218 (1990).

[19] G.P. Flinn, R.T. Harley, M.J. Snelling, A.C. Tropper, and T.M. Kerr, Semicond. Sci. Technol. **5**, 533 (1990).

[20] C. Cohen–Tannoudji and A. Kastler, in: *Progress in Optics, Vol. 5*, ed. E. Wolf (North Holland, Amsterdam, 1966) p. 33.

[21] A.I. Ekimov and V.I. Safarov, Zh. Eksp. Teor. Fiz. Pis'ma **13**, 251 (1971).

[22] V.L. Vekua, R.I. Dzhioev, B.P. Zakharchenya, and V.G. Fleisher, Fiz. Tekhn. Poluprovodn. **10**, 354 (1976).

[23] A. Abragam, *Principles of Nuclear Magnetism*, (Oxford, London, 1961), Chp. VI.

[24] *ibid*, Chp. IX.

[25] M. Goldman, *Spin Temperature and Nuclear Magnetic Resonance in Solids* (Oxford, London, 1970).

[26] Reference 23, Chp. VIII.

[27] W. Hanle, Z. Phys. **30**, 93 (1924).

[28] M. Krapf, G. Denninger, H. Pascher, G. Weimann, and W. Schlapp, Solid State Comm. **78**, 459 (1991).

[29] A.G. Redfield, Phys. Rev. **98**, 1787 (1955).

[30] C.P. Slichter, *Principles of Magnetic Resonance 3rd Ed.* (Springer–Verlag, Berlin, 1990), Chp. 6.

[31] S.K. Buratto, D.N. Shykind, and D.P. Weitekamp, Phys. Rev. B **44**, 9035 (1991).

[32] A.G. Aronov, G.E. Pikus, and A.N. Titkov, Zh. Eksp. Teor. Fiz. **84**, 1170 (1983) [Sov. Phys. – JETP 57, 680 (1983)].

[33] H.M. Cho, J.Y. Hwang, and D.P. Weitekamp, in preparation.

[34] R.G. Shulman, B.J. Wyluda, and H.J. Hrotowski, Phys. Rev. **109**, 808 (1958).

[35] O.H. Han, H.K.C. Timken, and E. Oldfield, J. Chem. Phys. **89**, 6046 (1988).

Chapter 3

The TSONMR Spectrometer

The apparatus used in the TSONMR experiment was designed and constructed in the Weitekamp lab at Caltech. The TSONMR spectrometer incorporates a wide variety of technologies from the fields of magnetic resonance and optical spectroscopy. An overall picture of the spectrometer is given in Figure 3.1. The optics were completely enclosed in a 122 cm by 186 cm by 100 cm black hut. The hut was constructed in order to isolate the spectrometer from the room lights which have significant power at the near infrared frequencies detected. The spectrometer was assembled on a homebuilt laser table and includes a cryostat to cool the sample, two orthogonal DC magnetic field coils (one for ONP and one for OD), a radiofrequency coil for NMR, optics for band–gap laser excitation, and optics for detecting the circular polarization of the luminescence ρ.

This chapter describes each of the components of the apparatus in detail as well as how they fit together to form the TSONMR spectrometer. Particular emphasis is paid to the photodetector where state–of–the–art technology facilitated our application. The chapter also includes a description of the software which controls the spectrometer. The source code for this program can be found in Appendix A.

3.1. The Laser Table

The homebuilt laser table (114 cm x 76 cm) consisted of 3/4" particle board,

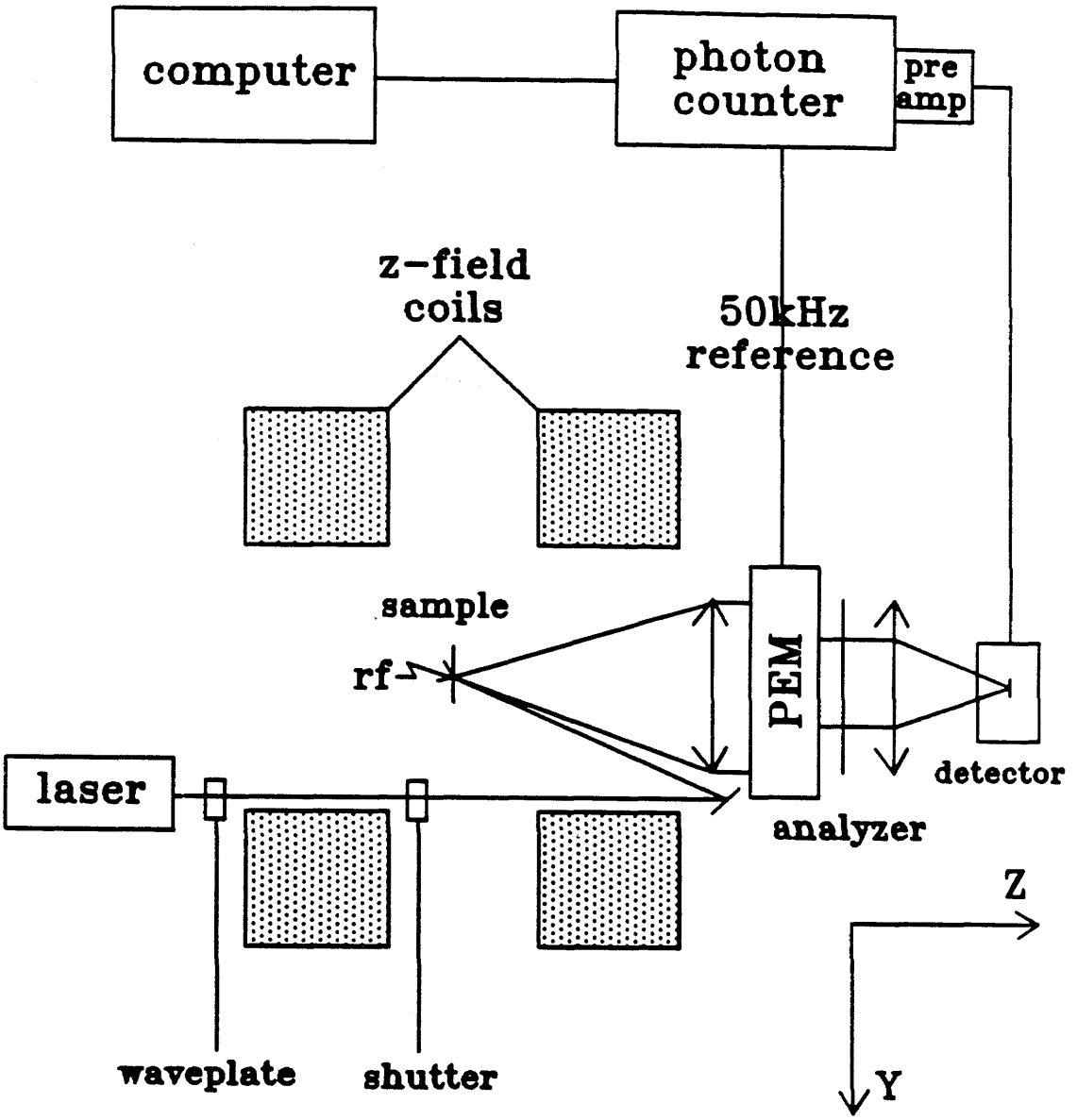

Figure 3.1: The TSONMR Spectrometer. The figure shows the yz–cross section. The sample is held at a temperature of 77 K in an optical cryostat not shown. The Hanle coil, which creates the x–axis field, is also not shown.

two layers of felt, and 1/4" aluminum as the top. The table was then placed on four legs made up of two cinder blocks with two layers of felt at each interface. The total height of the table was 42 cm. The felt and the particle board were used to provide vibrational isolation. Figure 3.2 shows a side–on view of the laser table.

3.2 Optical Cryostats

All of the experiments described in this thesis were done with the sample held at liquid nitrogen (LN_2) temperature (77 K). Two different cryostats have been used for this purpose; a commercial, stainless steel cryostat from Adonian Associates, Inc. model O–24/7M–H (circa 1964) that was restored for this application, and a homebuilt glass dewar.

3.2.1 The Stainless Steel Cryostat

Although the stainless steel cryostat was originally designed as a variable temperature cryostat capable of temperatures between 1.7 K and 80 K, it was used only at 77 K due to a prohibitive boil–off rate for liquid helium. The sample holder was redesigned to include a semi–rigid coaxial cable down its center which ended in a four–turn Helmholtz coil terminated with a 50 Ω resistor. This coil was used to supply the radiofrequency (rf) field to the sample. The sample was mounted to a rectangular piece of Delrin with masking tape. The sample mount was screwed into threads cut in the end of the sample holder such that the sample sat in the center of the Helmholtz coil. Figure 3.3 shows the dimensions of the cryostat as well as an enlargement of the sample chamber. In order to maximize the hold time, the vacuum space was maintained at a pressure of approximately 10^{-5} Torr by continuous pumping. The pumping system consisted of a mechanical vacuum pump,

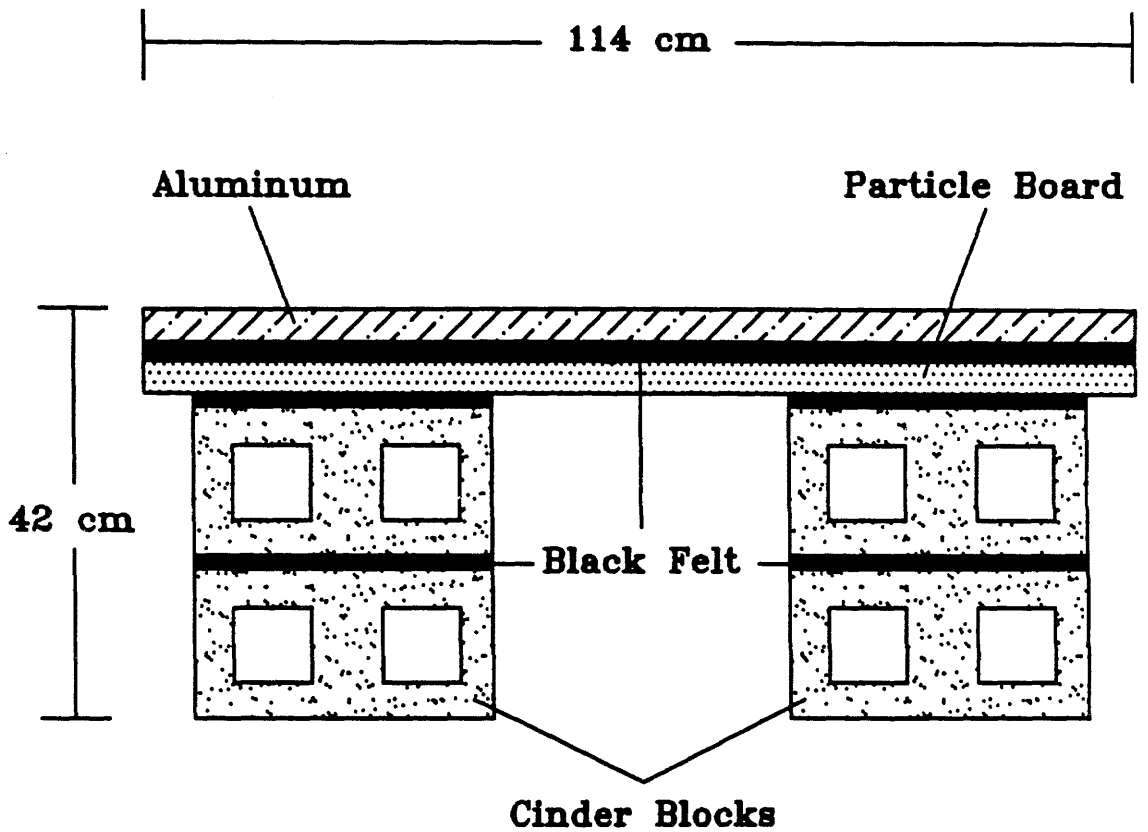

Figure 3.2: The Laser Table. The combination of aluminum, felt, and particle board provides vibrational isolation. The table is raised to a height of 42 cm by placing it on top of two cinder blocks. Felt is placed in between the two cinder blocks as well as between the cinder blocks and the table. The table is leveled by adjusting the felt between the table and the cinder blocks. The optical rail, cryostat stand, and both magnet stands are attached to the table by tapping holes in the aluminum.

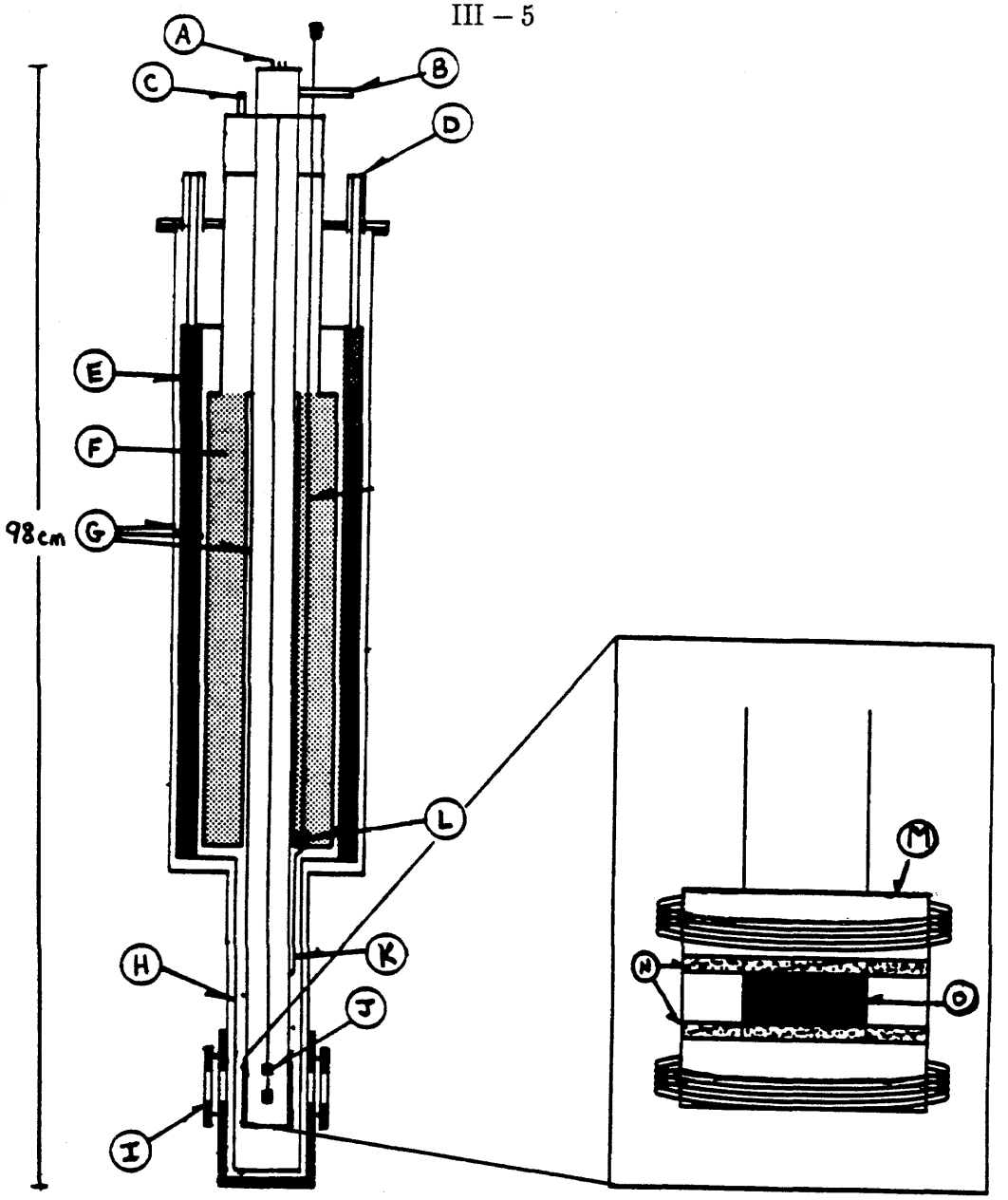

Figure 3.3: The Stainless Steel Cryostat. The insert shows the rf coil, the sample mount, and the sample. (A) BNC connection for the rf coil. (B) Sample vent. (C) Inner reservoir fill and vent tubes. (D) Outer reservoir fill and vent tubes. (E) Outer reservoir. (F) Inner reservoir. (G) Vacuum Space. (H) Radiation Shield. (I) Windows. (J) Sample holder and rf coil. (K) Capillary tube. (L) Needle valve. (M) Delrin mount. (N) Masking tape. (O) Sample.

a small diffusion pump, an LN_2 trap, and an ion vacuum gauge. The system was connected together using rubber vacuum hose with a wall thickness of 1 cm. At a pressure of 10^{-5} Torr and both reservoirs full of LN_2, the hold time was approximately 30 hrs. Liquid nitrogen from the inner reservoir was given access to the sample chamber by opening the needle valve (see Fig. 3.3). The liquid nitrogen level was maintained at approximately 12 cm above the sample so that the nitrogen bubbles near the sample vanished and the boil–off rate was minimized.

There were several drawbacks to using the stainless steel cryostat. The cryostat was too large in the tail section which limited the solid angle of the luminescence collected from the sample. It also required 6 L of LN_2 to fill each reservoir, but only 3 L were used to cool the sample. We attempted to use only the inner reservoir for LN_2 and to leave the nitrogen jacket empty, but the hold time decreased by almost a factor of two. Because of the age of the cryostat, most of the o–ring seals failed during its tenure in the apparatus which created a large amount of down time. The two seals around the LN_2 fill and vent tubes (see Fig. 3.3) required extensive modification in order for them to hold vacuum. These seals consisted of teflon o–rings that were compressed around the tubes and tightened as the nitrogen jacket cooled. These seals were remachined to incorporate Viton o–rings, but the repeated tightening eventually led to irreparable damage of the fill and vent tubes. Rather than replace these tubes, a new dewar was made by of the glass shop which had a single nitrogen reservoir and was considerably smaller than the stainless steel cryostat.

3.2.2 The Glass Dewar

The glass dewar is illustrated Figure 3.4. Once the dewar was delivered from the glass shop, the vacuum space was silvered using the following Brashear's method

of silvering. [1] Care was taken to insure that the silvering solution did not penetrate the tail section. Once the silver had coated both sides of the vacuum space the dewar was washed thoroughly with water and methanol and then annealled at 200°C for 2 hrs. The lid for the dewar was made of plexiglass with a rubber seal (see Fig. 3.4) and had holes for the fill and vent tubes as well as a center hole for the sample holder. The sample holder consists of a glass rod with coaxial cable down the center ending in a 40–turn Helmholtz coil for the rf field. The coil was soldered to the coaxial cable and taped to the glass rod. The sample was mounted on a rectangular piece of plastic with masking tape and pressed into the coil. The sample remained in place at liquid nitrogen temperature by the contraction of the copper wire around the plastic. In order to suppress nitrogen bubbling in the sample chamber, a boiling chip was placed just above the top of the coil which had the effect of creating a better spot for nitrogen bubbles to nucleate than near the sample. The glass rod was held rigid in two places. First, a piece of cloth netting was pressed into the neck of the sample chamber around the sample holder. The netting also stopped any ice formed at the top of the dewar from getting into the sample chamber. The glass sample holder was also held at the top of the dewar by teflon tape. The vacuum space was held at 10^{-5} Torr by continuous pumping. At this pressure the hold time for the 4 L glass cryostat was approximately 24 hrs, but was generally filled every 12 hrs to insure a high level of nitrogen in the belly and to prevent ice formation.

3.3 The Static and Oscillating Magnetic Fields

The magnet system in the TSONMR spectrometer included two orthogonal electromagnets. One electromagnet supplied the z–axis ONP and NMR fields approximately parallel ($\sim 15^{\circ}$) to the direction of light propagation, and the other

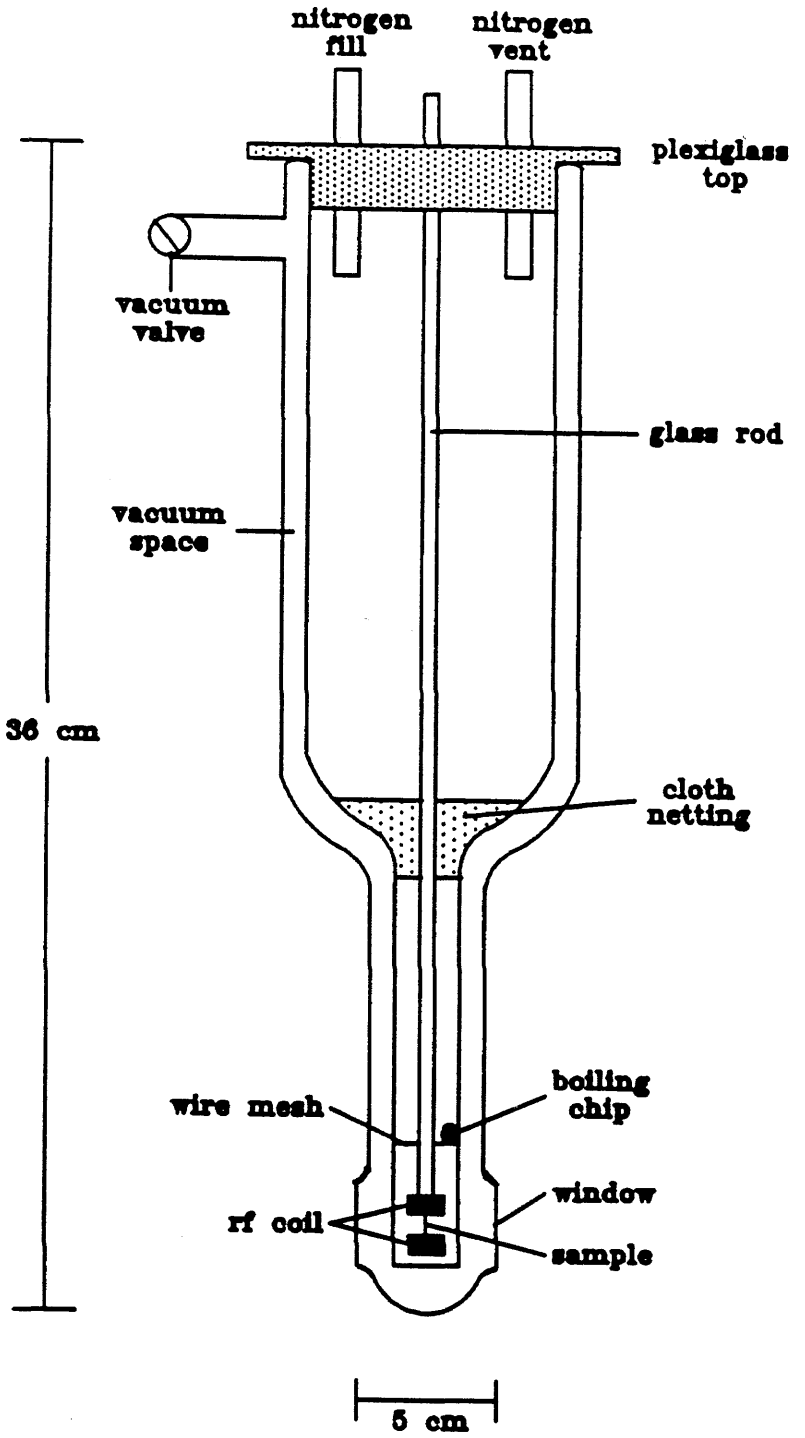

Figure 3.4: The Glass Dewar. The inner portion of the tail section is made of square quartz tubing so no inner window is needed. The glass rod contains the coaxial cable which is soldered to the rf coil. The rf coil is attached to the glass rod with masking tape.

electromagnet supplied the detection (Hanle) field along the x–axis perpendicular to the direction of light propagation. Since the effective sample defined by the optical excitation was quite small ($10^{-3}cm^2$ x 10^{-4}cm penetration), shim coils were not needed to enhance the homogeneity of the magnets.

3.3.1 The Z–Field Magnet

The z–field magnet consisted of a Helmholtz pair of coils, each with 400 turns of 14 gauge polyurethane–nylon insulated wire. The magnet was wound on a plexiglass form with a 24 cm diameter and required no active cooling. Each coil was 4 cm wide with 24 layers (5 cm) of wire, and the two coils were separated by 12 cm (measured from the middle of each coil) in accordance with the Helmholtz configuration. The room temperature resistance of the magnet was 6 Ω, and the driving current was supplied by a 1 kW (20 A, 50 V) power supply. In order to maintain a stable current through the magnet, a current regulator (0–10 A) was designed and built. The current regulator was stable to within 0.5%, and was capable of being programmed by a modulation input voltage. The modulation input voltage was supplied by the programmable analog outputs of either the photon counter or the lock–in amplifier (see section 3.8) to allow for computer control of the field strength. Resistive heating limited the usable range to ± 200 G. A graph of field strength versus modulation voltage is shown in Figure 3.5. The measurement of field was done by placing a gauss meter at the center of the coils. Since the TSONMR experiment requires the field to be cycled, the switching time was an important experimental parameter. An oscilloscope trace of the voltage across the sensing resistor of the current regulator during field cycling showed a switching time of 100 ms (150 G to 0 G). This time proved to be adequate for adiabatic demagnetization, yielding a negligible loss in total magnetization due to nuclear

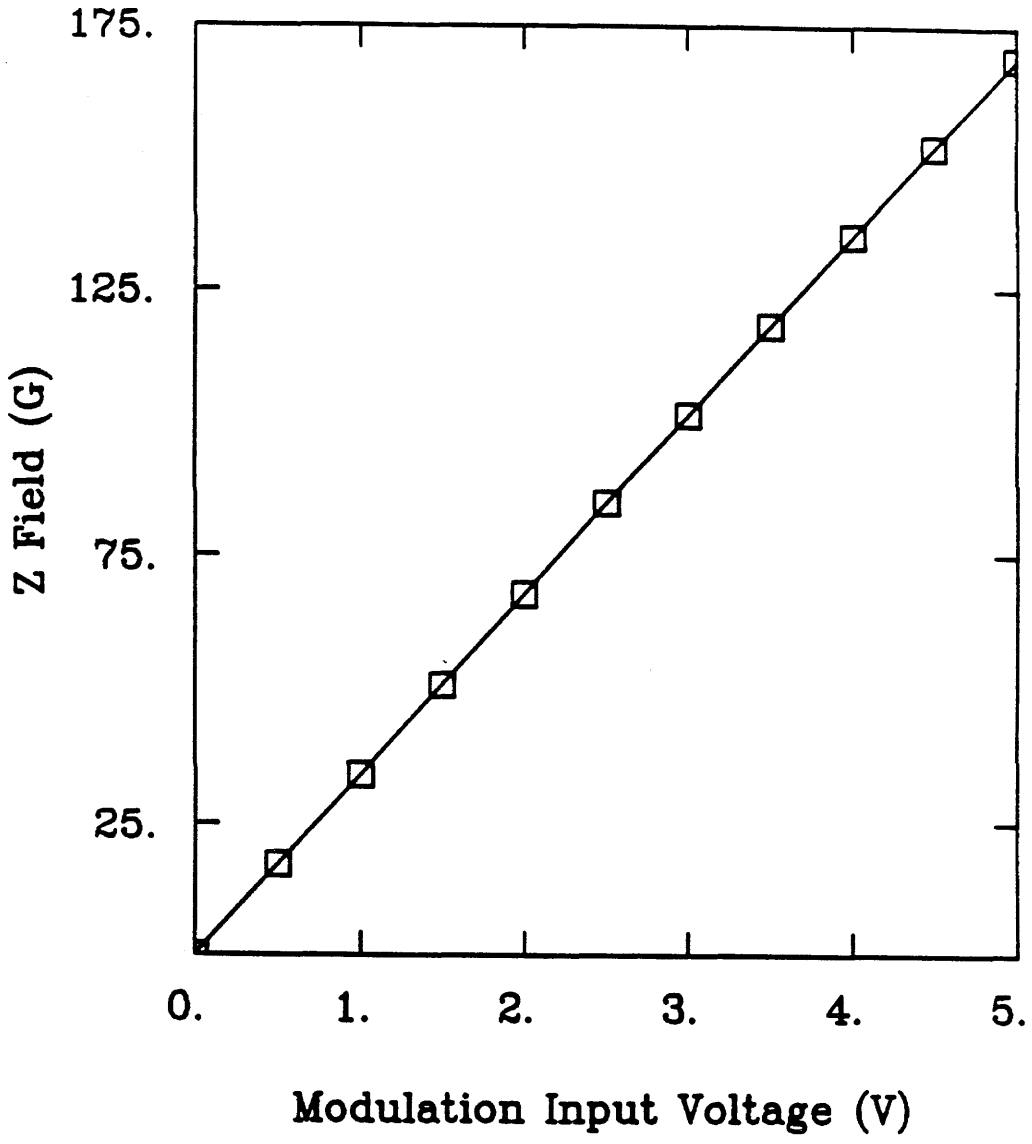

Figure 3.5: The Z Field Strength vs. Modulation Input Voltage. The modulation input voltage of the z–field current regulator is supplied by the analog output port P1 of the SR400 photon counter. The curve is linear with slope 33.4 G/V. The current regulator is set such that 1.0 V = 1.1 A.

relaxation ($T_1 \geq 5$ s for all the major isotopes) during field cycling.

3.3.2 The Hanle Field

The Hanle field was also produced with a Helmholtz pair of coils. For experiments done with the stainless steel cryostat, the Hanle coil was wrapped on the 5 cm diameter radiation shield (made of aluminum) of the sample chamber. The shield was heat sinked to the outer LN_2 reservoir which kept the coil at a resistance of less than 1 Ω. Each coil was 10 cm wide with 50 turns of 22 gauge copper wire (1 layer thick). The spacing between the coils was 4 cm measured from the beginning of each solenoid. A 400 W (20 V, 20 A) power supply provided the driving current for this magnet, and a replica of the z–field current regulator controlled the current (0 to 10 A). The field strength of the Hanle field versus modulation input voltage is shown in Figure 3.6. The usable range for the Hanle coil was 0 G to 90 G, and the switching time from 90 G to zero field was measured to be less than 50 ms. Therefore, cycling the field from the z–field to the Hanle field could be done in 100 ms by ramping the z–field to zero while simultaneously charging the Hanle field.

When the glass dewar was installed in the spectrometer, a new Hanle coil was designed to be placed outside the dewar. The new coil was designed to keep the same usable range of field strengths as the previous coil. Since this coil was no longer cooled, it was necessary to increase the number of turns from 50 to 100 for each solenoid to compensate for the loss in driving current due to a higher resistance (3 Ω). This Hanle coil was wound on a 5 cm diameter aluminum support to provide a heat sink, and each coil was wound 8 cm wide and consisted of 3 layers of 22 gauge copper wire. The switching time was increased by approximately 20 ms (to just less than 70 ms) due to the higher inductance. This increase, however, did not affect the time for field cycling from the z–field to the Hanle field since the z–field switching

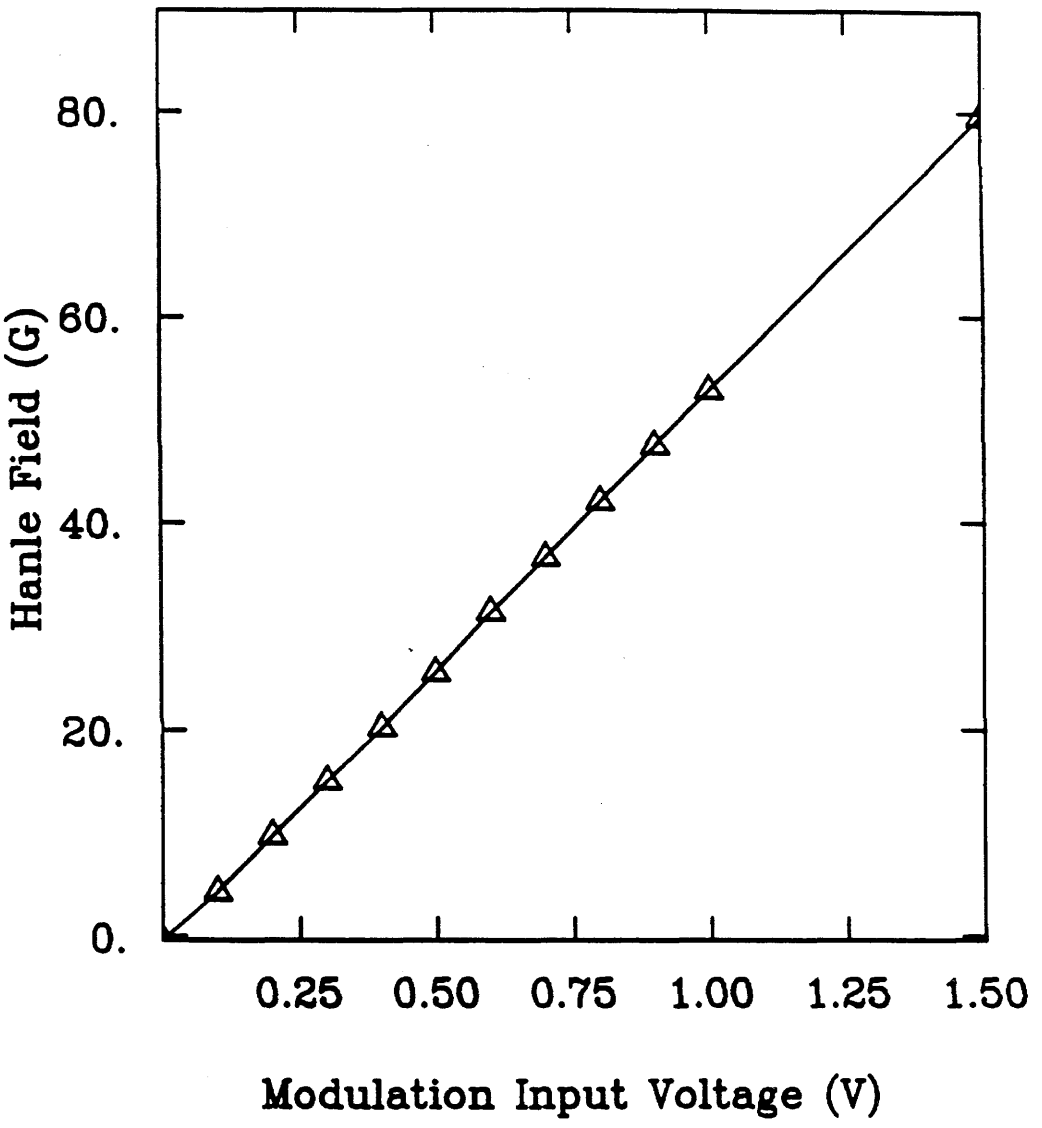

Figure 3.6: Hanle Field Strength vs. Modulation Input Voltage. The modulation input voltage of the Hanle field current regulator is supplied by the analog output port P2 of the SR400. The slope of the curve is 51.8 G/V, and the current regulator is set such that 1.0 V = 4.7A.

time remained the bottleneck.

3.3.3 The Radiofrequency Field

Since the magnetic resonance signal is optically–detected, the rf electronics for the TSONMR spectrometer were much simpler than for a conventional NMR spectrometer. The rf coil used in TSONMR experiments was a 1.0 μm diameter Helmholtz coil designed to fit inside the sample chamber of the cryostat, and wound with 40 turns of 30 AWG wire. The rf circuit was matched using a 50Ω resistor and no tuning elements were needed. The reflected power for the 40–turn Helmholtz rf coil (measured with a directional coupler) versus frequency is listed in Table 3.1.

TABLE 3.1: Reflected Power vs. Frequency

Frequency (MHz)	Forward Voltage (mV)	Reflected Voltage (mV)	Reflected Amplitude (%)
0.150	46.0	6.3	13.7
0.300	47.8	6.5	13.5
0.600	48.2	6.5	13.5
1.00	48.8	6.5	13.5
5.00	53.2	7.4	13.3
10.0	58.4	8.6	14.7
20.0	51.2	10.5	20.5

Thus this single circuit could be used to supply rf over the entire frequency range of interest.

A Hewlett Packard (HP) model 3335A frequency synthesizer was used as the primary frequency source. This synthesizer was equipped with an IEEE–488 (GPIB) interface for computer control of both frequency and amplitude. For experiments which required phased rf (such as a multiple–pulse experiment), a homebuilt quadrature phase shifter, which is described in detail elsewhere [2], supplied 30MHz

rf in 90° phase steps which was down–converted to give the desired frequency and phase (see Figure 3.7). A PTS model 500 frequency synthesizer supplied both the 30 MHz LO to the phase shifter and the RF frequency. The resulting IF difference frequency rf field was then amplified by an Electronic Navigation Industries (ENI), Inc. broadband 100 W power amplifier. The ENI amplifier had a nominal low frequency cutoff of 250 kHz but was useable at the frequencies used in most experiments (80 kHz – 200 kHz), where it supplied a maximum of 20 W. At this power the B_1 field was 15 G for the 40–turn Helmholtz coil. The rf pulses were controlled using a 40 MHz digital word generator (Interface Technology, Inc. (ITI) model RS–670). The pulse sequences were down loaded to the ITI through an IEEE–488 interface which was also used to trigger the ITI.

3.4 The Excitation Optics

A semiconductor laser, a $\lambda/4$ waveplate, an optical chopper, a 45 cm focal length lens, and a shutter comprised the excitation optics as depicted in Figure 3.8. The laser was a Spindler and Hoyer, Inc. model DL25C single mode GaAs/GaAlAs laser diode which provided up to 30 mW of continuous wave (cw) power at a center wavelength of 780 nm. The power setting was placed at 30 mW and neutral density (ND) filters were used to obtain lower powers. The spectrum of the laser diode output showed several spectral lines at 780±3 nm as well as a narrow line at 806±0.6 nm which was lower in power by a factor of 10^3 from the signal at 780 nm. The output of the laser diode was collimated with an elliptical beam (3 mm x 5 mm) and was linearly polarized along the large axis with a 500:1 ratio. The linearly polarized beam was circularly–polarized by a Newport Corp. zero–order $\lambda/4$ waveplate with an efficiency of greater than 95%. A 500 Hz optical chopper was used for lock–in detection of the total luminescence. For experiments using photon counting

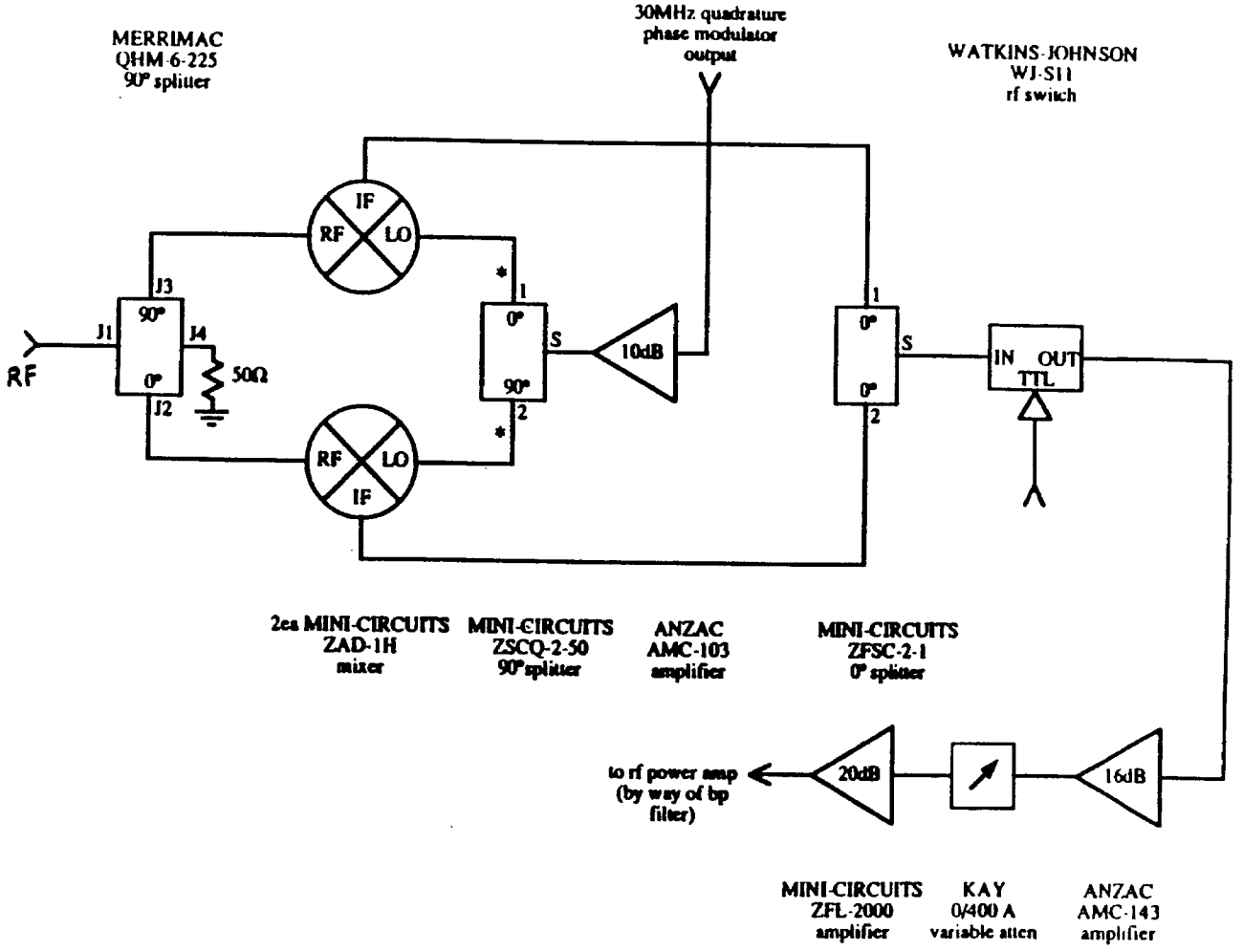

Figure 3.7: Quadrature RF Transmitter. The components of the transmitter are given in the figure. The lower sideband of the IF signal (RF – LO) is selected after the mixing stage. The phased LO (30 MHz) comes from the output of the quadrature phase modulator (ref. [2]), and the RF comes from the PTS synthesizer. The output of the transmitter is filtered with a band pass filter before being amplified by the ENI amplifier.

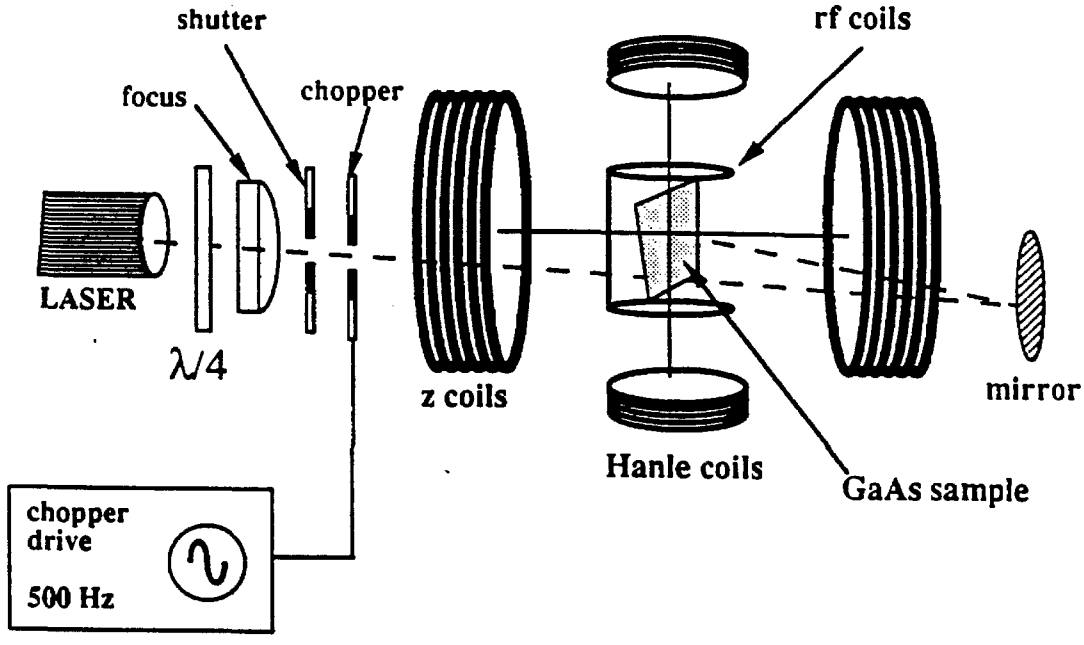

Figure 3.8: The excitation optics. The excitation optics begin with a 780 nm, 30 mw continuous wave AlGaAs/GaAs quantum well laser. The output beam is elliptical (3 mm x 5 mm) and linearly polarized in a 500:1 ratio. The quartz $\lambda/4$ retarder converts the linear polarization to circular polarization. The circularly–polarized beam then passes through a focusing lens, an electrically actuated mechanical shutter, and a 500 Hz optical chopper wheel. Finally, the beam is reflected on to the sample using a multilayer dielectric mirror. The laser light impinges on the sample at a slight angle (15°) to the applied field along the z–axis.

detection, the chopper was removed from the experiment. The lens was used to focus the elliptical beam on the sample surface to a spot size of approximately 0.1 mm^2 (the penetration depth is approximately 1 μm), and the angle between the z–field direction and the excitation beam is approximately 15°. The shutter was a Newport Corp. model 846HP capable of handling cw powers of up to 5 W. This shutter was designed to hold its blade in both the open and closed positions such that no power was required to maintain it in either position. This was accomplished by using a 13 Ω solenoid to control the shutter blade. A 20 ms pulse of +5 V opens the shutter where as a –5 V pulse closes the shutter. A homebuilt switching circuit controls the shutter. In this circuit the shutter was opened/closed with a 18 ms pulse of ±12 V, respectively. The actual opening and closing times were both measured by an oscilloscope trace to be 7 ms. The voltage pulses for opening and closing the shutter were supplied by two lines of a 32–bit digital output board resident in the IBM PS/2 model 80 computer which acted as the master control for the experiment.

3.5 The Detection Optics

The collecting optics were oriented parallel to the z–field and consisted of a collecting lens, a photoelastic modulator (PEM), a linear polarizer, a focusing lens for the detector, an interference filter, and an avalanche photodiode detector. The detection optics are shown in Figure 3.9. The 5 cm diameter, 10 cm focal length collecting lens collimated the luminescence for polarization analysis. The circular polarization of the luminescence was analyzed using the combination of a Hinds International, Inc. series 1 model 80 PEM and a linear polarizer oriented at an angle of 45° to the PEM's axis. The PEM is a tuned circuit containing a birefringent fused silica crystal that is periodically strained at a frequency of 50 kHz to provide

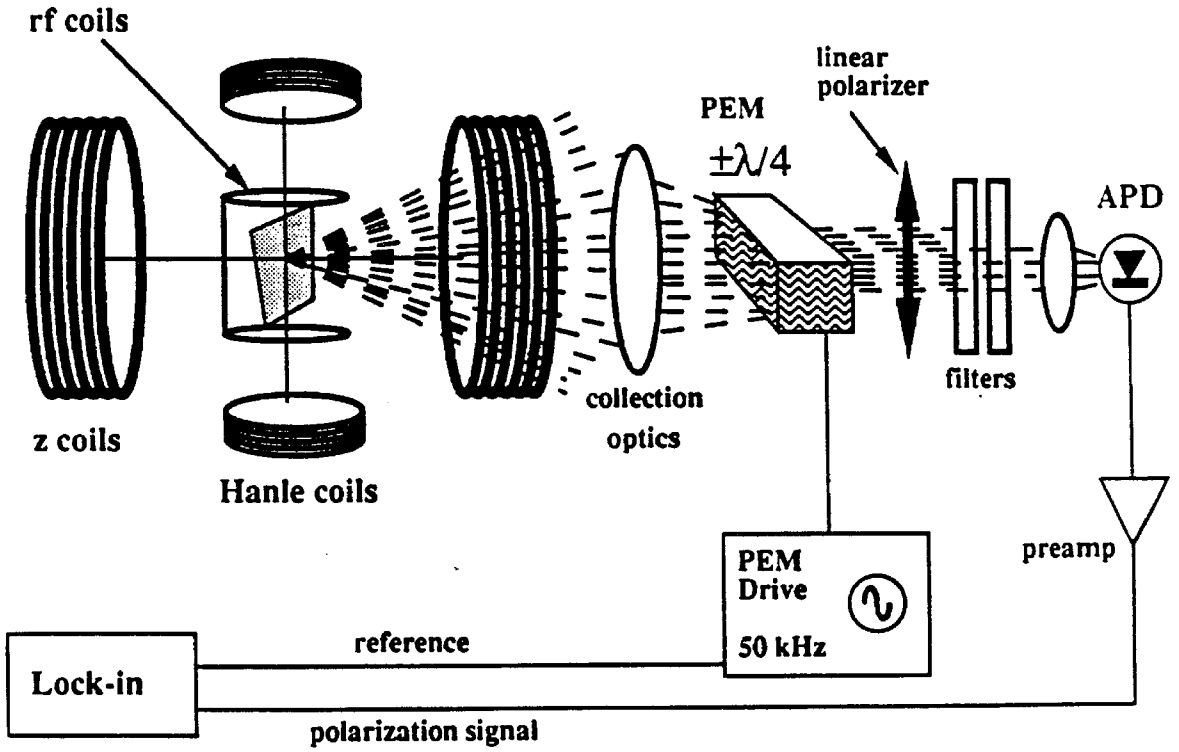

Figure 3.9: The detection optics. The luminescence was collected in a reflection geometry using a 5.0 cm diameter, 10.0 cm focal length lens. The circular–polarization was analyzed by the combination of the PEM and the 45° polarizer combination resulting in a 50 kHz–modulated signal proportional to ($I_+ - I_-$). Stray laser light is filtered with one or two 870 nm bandpass filters. The luminescence is then focused on the avalanche photodiode detector (APD). The 50 kHz–modulated photocurrent is converted into a voltage using a transconductance amplifier and synchronously detected.

oscillating retardation. The signal obtained from this analyzer combination is described in the next subsection.

3.5.1 Analyzing Circular Polarization of the Luminescence

The electromagnetic wave with electric field **E** incident on the polarization analyzer is shown schematically in Figure 3.10. In general, the wave **E** is given by,

$$\mathbf{E} = (a\mathbf{i} + b\mathbf{j})\exp(-i\omega t) \tag{3.1}$$

where a and b are complex constants, **i** and **j** are unit vectors along the x and y axes, respectively, and ω is the frequency. The two refractive indices of the PEM are periodically strained along these axes denoted by n_x and n_y. The phase shift $\Delta\varphi(t)$ is given by [3],

$$\Delta\varphi(t) = \frac{2\pi d}{\lambda}(n_x - n_y)(t) = A_0\cos(\Omega t), \tag{3.2}$$

where A_0 is the retardation amplitude and Ω is the fused silica resonance frequency (50 kHz). The resulting wave $\mathbf{E}'$ modulated by the PEM can be found using Eq 3.2 and is

$$\mathbf{E}' = [a\mathbf{i}\exp(i\Delta\varphi(t)/2) + b\mathbf{j}\exp(-i\Delta\varphi(t)/2)]\exp(-i\omega t). \tag{3.3}$$

The wave $\mathbf{E}''$ is found by projecting $\mathbf{E}'$ on the axis of the linear polarizer,

$$\mathbf{E}'' = \frac{1}{\sqrt{2}}(\mathbf{i} + \mathbf{j})\cdot\mathbf{E}'\frac{1}{\sqrt{2}}(\mathbf{i} + \mathbf{j}), \tag{3.4}$$

and

$$\mathbf{E}'' = \frac{1}{\sqrt{2}}[a\exp(i\Delta\varphi(t)/2) + b\exp(-i\Delta\varphi(t)/2)]\exp(-i\omega t)(\mathbf{i} + \mathbf{j}). \tag{3.5}$$

The output intensity $I'' = |\mathbf{E}''|^2$ is then given by,

$$I'' = \frac{1}{2}|a\exp(i\Delta\varphi(t)/2) + b\exp(-1\Delta\varphi(t)/2)|^2. \tag{3.6}$$

If the incident wave is right–hand circularly polarized

$$\mathbf{E}_+ = \frac{1}{\sqrt{2}}(\mathbf{i} + i\mathbf{j})\exp(-i\omega t), \tag{3.7}$$

then

$$I_+'' = \frac{1}{2} + \frac{1}{2}\sin(\Delta\varphi(t)) = \frac{1}{2} + \frac{1}{2}\sin(A_0\cos(\Omega t)). \tag{3.8}$$

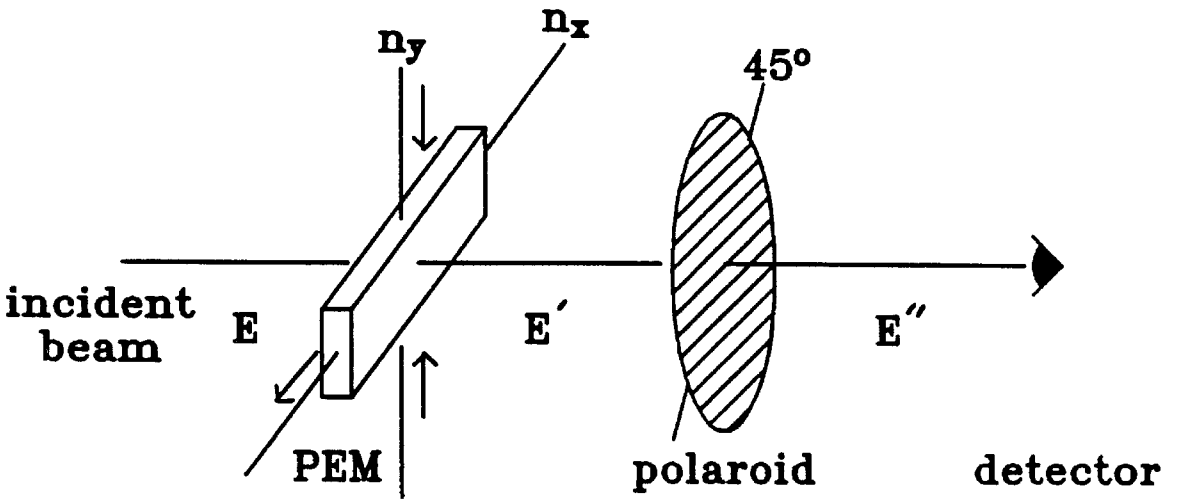

Figure 3.10: The PEM/45° Polarizer Combination. The fused silica crystal which is the tuned element of the PEM is periodically strained in the direction of the arrows at a frequency of 50 kHz. The resulting 50 kHz signal $I'' = |E''|^2$ is proportional to the signal $(I_+ - I_-)$. See text for details.

Equation 3.8 has the form [3],

$$I_+'' = \frac{1}{2} + J_1(A_0)\cos(\Omega t) - J_3(A_0)\cos(3\Omega t) + \ldots \qquad (3.9)$$

where $J_1(A_0)$ and $J_3(A_0)$ are the Bessel–function coefficients for the fundamental and third harmonic signals, respectively. Thus, right–hand circularly–polarized light gives a leading signal $J_1(A_0)$ at the fundamental PEM frequency with a maximum of about 0.58 at $A_0 \simeq 1.85$, slightly more than "quarter wave" operation ($A_0 = \pi/2 = 1.57$). Similarly, for left–hand circularly–polarized light, one finds

$$I_-'' = \frac{1}{2} - \frac{1}{2}\sin(A_0\cos(\Omega t)), \qquad (3.10)$$

which is 180° phase–shifted from the right–hand signal. Thus, for incident light consisting of a mixture of right–hand and left–hand circularly polarized light and quater–wave retardation, the signal synchronous with the fundamental PEM frequency will be proportional to $(I_+ - I_-)$. The $(I_+ - I_-)$ signal can then be synchronously detected using a lock–in amplifier or a gated photon counter and the PEM's 50 kHz reference.

3.5.2 Wavelength Selection

Once the circular–polarization of the luminescence was analyzed, the resulting signal was focused onto the detector by a 5 cm diameter, 10 cm focal length lens. Before hitting the detector, the light had to be filtered to remove scattered laser light. This was accomplished by a bandpass filter (Corion Corp. model $S10 - 870 - F$) centered at the luminescence frequency. Most experiments were done using a filter centered at 870 nm. A monochromator was not necessary for wavelength selection for bulk GaAs because all of the luminescence lines contain the same electron spin information as described in chapter 1. The UV–visible spectrum of each filter was taken and the results showed the peak transmittance to be 70% at

870 nm with a FWHM of 10 nm. The transmittance at the laser wavelength of 780 nm was 0.1%, which provided adequate isolation from laser scatter for all but the lowest luminescent samples. For samples with a luminescence flux corresponding to less than 300 counts/sec in the photon counting setup of section 3.6, two interference filters were used.

3.6 The Avalanche Photodiode Detector

The photodetector was an RCA model C30902 avalanche photodiode. This detector was chosen because of its high quantum efficiency in the near infrared ($\simeq$ 80%), and its ability to be used as either a linear detector or a single photon counter.

An avalanche photodiode is a specific type of p–n junction where, when biased, the photoinduced carrier gains enough kinetic energy in the depletion layer (the avalanche region) to excite other electron–hole pairs [4]. These newly–formed carriers can, in turn, create even more electron–hole pairs in a cascading process. The sensitivity of an avalanche photodiode in both linear and photon–counting (Geiger) modes is, of course, dependent on the bias voltage. The operation of the photodiode in both linear and Geiger modes is described in detail in the following subsections.

Because of the small active area (0.5 mm diameter) of the photodiode, the luminescence needed to be tightly focused. Aligning the detector to the focal point of the lens was accomplished by mounting the photodiode to an xyz translation stage made by Newport Corp. and capable of positioning in each direction with 10 μm resolution.

3.6.1 Linear Mode Operation

Using the avalanche photodiode in linear mode was straightforward. The photodiode was back–biased with a voltage V_R near the breakdown voltage V_{BR} of the photodiode. At a voltage difference $(V_{BR} - V_R) = 5$ V the photodiode was maximized with respect to signal–to–noise with a gain of 150. The resulting photocurrent was converted to a voltage by a homebuilt transconductance amplifier of standard design [5] with a 100 kΩ resistance making the voltage response of the photodiode/transconductance amplifier equivalent circuit equal to 7.4×10^7 V/W. This voltage was then split and synchronously detected at the PEM's 50 kHz frequency and at the chopper's 500 Hz frequency. The 50 kHz frequency was detected using a Stanford Research Systems (SRS) model SR530 dual–channel lock–in amplifier resulting in the $(I_+ - I\_)$ signal. The total luminescence signal $(I_+ + I\_)$ was obtained by synchronous detection with the 500 Hz reference of the optical chopper using an SRS model SR510 single channel lock–in amplifier. When necessary, an SRS model SR552 preamplifier was used to amplify the photovoltage before synchronous detection by the two lock–ins.

The analog output of the SR510 signal was sent to one of the four A/D converters of the SR530. Both the $(I_+ - I\_)$ and $(I_+ + I\_)$ signals were digitized simultaneously by the SR530 to avoid timing errors and sent to the PS/2 computer via an IEEE–488 interface. The two signals were subsequently ratioed by software to obtain the photoluminescence polarization $\rho = (I_+ - I\_)/(I_+ + I\_)$.

3.6.2 Theory of Geiger Mode Operation

It was also possible to use the same photodiode as a single–photon counter by putting the photodiode in Geiger mode. This mode was achieved by reverse

biasing the photodiode with a $V_R > V_{BR}$. Once the bias voltage reaches the breakdown voltage, the photodiode begins to conduct as expected. However, if the current is limited to less than 50 μA (called the latch current) the current in the photodiode is unstable and can switch off by itself [6]. This effect is due to the small number of electrons in the avalanche region fluctuating rapidly and eventually reaching zero at which point conduction stops. A photon incident on the active surface of the diode (or a thermally–generated electron) induces conduction by creating an avalanche current pulse that discharges the diode from V_R to a voltage slightly below V_{BR}. This current pulse is passively discharged through a load resistor R_L. In order for the photodiode to achieve Geiger mode, $(V_R - V_{BR})/R_L$ < 50 μA [6] which insures a small enough concentration of electrons in the avalanche region to fluctuate to zero. The photodiode is then recharged with a time constant $R_L C$, where C = 1.6 pF is the capacitance of the diode. With $R_L = 200$ kΩ the photodiode is recharged and ready to detect another photon within 1 μs. For our applications it was necessary to buffer the photodiode pulses so that the pulses could drive a 50 Ω line. The pulses were also amplified by a homebuilt preamplifier with a gain of 100 to allow easier positioning of the discriminator level of the photon counter. A model of a current pulse resulting from the passive quenching circuit (see Figure 3.11a) is shown in Fig. 3.11b.

3.6.3 Geiger Mode Quantum Efficiency

The efficiency of the photodiode in Geiger mode, the detected quantum efficiency (DQE), is found by multiplying the linear quantum efficiency (80% at 870 nm) with the probability that a photoelectron generates an avalanche current pulse. The probability that a photoelectron creates an avalanche is dependent on the

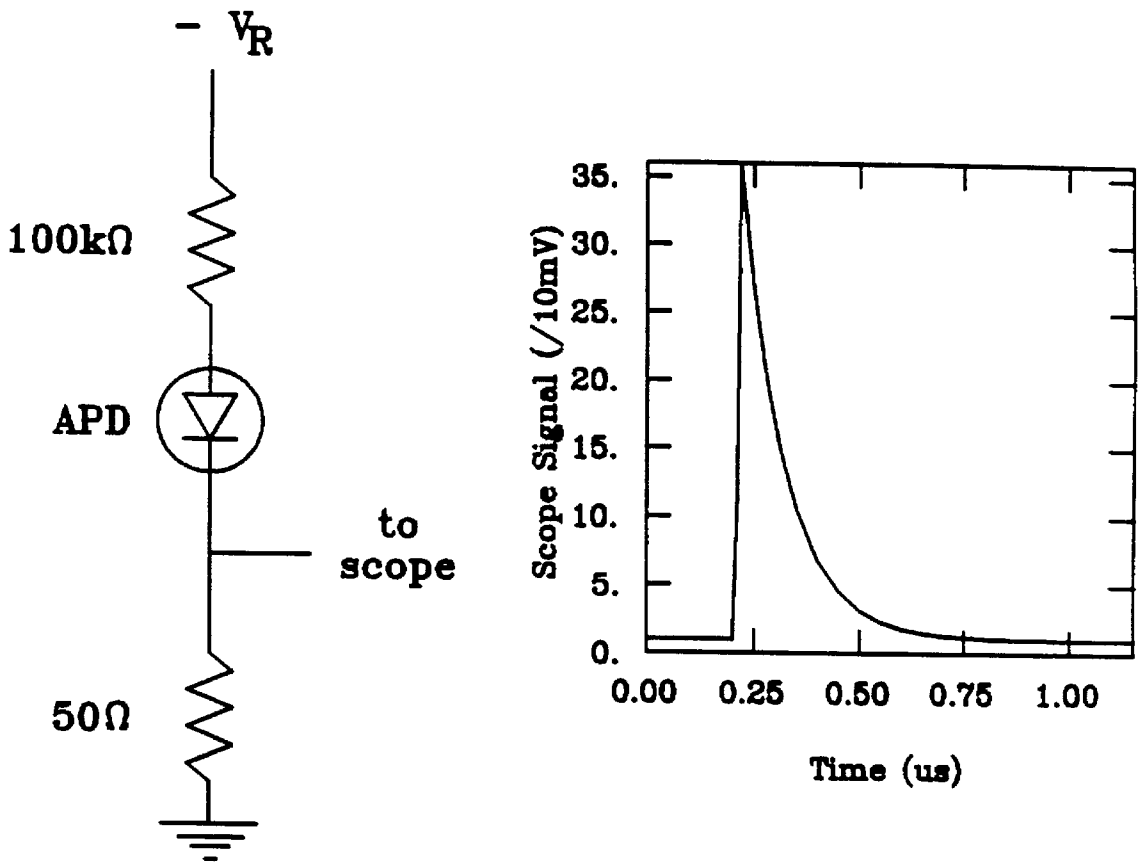

Figure 3.11: The Avalanche Pulse. The passive quenching circuit is shown on the left side of the figure. The output of this circuit is buffered and amplified by a factor of 100. A model of the avalanche pulse is shown on the right side of the figure. The photodiode is ready to detect another photon in approximately 1 μs.

overvoltage ($V_R - V_{BR}$). The increase in probability is approximately linear up to an overvoltage of 10 V after which the increase is less than linear and saturates at an overvoltage of 20 V. The voltage V_R was applied using an HP model 6209B power supply which maintained the bias voltage to within 0.02%.

The dark count rate for Geiger mode photodiodes is due to thermally–generated electrons creating avalanche pulses. A simple way to decrease the dark count rate is to lower the temperature. By decreasing the temperature from 300 K down to 77 K the dark count rate can be reduced from 50 kHz to less than 1 Hz, a significant reduction. In principle the sensitivity of the Geiger photodiode is maximized when the photodiode is cooled and the overvoltage is such that $(V_R - V_{BR})/R_L \simeq 50\mu A$. [6]

In practice, however, optimizing sensitivity by adjusting the operating temperature and overvoltage is made complex by the existence of after–pulsing [7]. After–pulsing occurs when electrons in the avalanche region become trapped at defect sites, and decay at some time after the completion of the avalanche pulse. If the trapped electron decays after the photodiode is recharged, then the resulting avalanche of this electron is detected above the discriminator level of the photon counter. Letting Z be the probability of an after–pulse, n be the number of photoinduced avalanches and G be the average number of avalanches per photon ($G \geq 1$ due to echo avalanches), the total number of counts N is given by,

$$N = n + nZ + (nZ)Z + [(nZ)Z]Z + \ldots \tag{3.11}$$

and, by simplifying,

$$N = n\frac{1}{1 - Z} = nG. \tag{3.12}$$

Therefore, the average number of avalanche pulses per photon $G = 1/(1 - Z)$. If G fluctuates then these fluctuations will degrade the signal–to–noise ratio (S/N) of the Geiger photodiode. Considering G as an ideal multiplier and adopting the statistical

model of Personick [8], the second moment $<G^2>$ is given by,

$$<G^2> = \frac{1}{(1 - Z)^3}, \tag{3.13}$$

and the variance in G, $<\Delta G^2> = <G^2> - <G>^2$ is given by,

$$<\Delta G^2> = \frac{1}{(1 - Z)^3} - \frac{1}{(1 - Z)^2} = \frac{Z}{(1 - Z)^3}. \tag{3.14}$$

Using Eq.3.12, the variance in N is given by,

$$<\Delta N^2> = <n>^2<\Delta G^2> + <G>^2<\Delta n^2> + <\Delta G^2><\Delta n^2>, \tag{3.15}$$

and from Eq 3.14

$$<\Delta N^2> = \frac{<n>^2 Z + <\Delta n^2>}{(1 - Z)^3}. \tag{3.16}$$

Considering the variance in N for a single photocarrier (n = 1),

$$<\Delta N^2>_{\text{single}} = \frac{1 + Z}{(1 - Z)^3}. \tag{3.17}$$

For a total of n photoinduced carriers,

$$<\Delta N^2>_n = n<\Delta N^2>_{\text{single}} = n\left[\frac{1 + Z}{(1 - Z)^3}\right]. \tag{3.18}$$

The S/N is then given by,

$$S/N = \left[\frac{<N>^2}{<\Delta N^2>}\right]^{1/2} = \left[\frac{<n><G>}{<\Delta N^2>}\right]^{1/2}. \tag{3.19}$$

Using Eqs. 3.12 and 3.13 one finds,

$$S/N = \sqrt{\bar{n}}\left[\frac{1 - Z}{1 + Z}\right]^{1/2}. \tag{3.20}$$

The number of photoinduced avalanches n is modelled by counting statistics (a Poisson process), and in the absence of any after–pulsing, $S/N = \sqrt{\bar{n}}$. Hence, the effect of the after–pulsing is to decrease the S/N by a factor of $[(1 - Z)/(1 + Z)]^{1/2}$. Equivalently, the effect of the after–pulsing can be expressed as a decrease in the DQE by a factor of $[(1 - Z)/(1 + Z)]$, yielding an effective quantum efficiency (EQE) given by,

$$EQE = DQE\left[\frac{1 - Z}{1 + Z}\right]. \tag{3.21}$$

Several models have been proposed for predicting the probability of after–pulsing Z [7,9–11]. These models have included a dependence on a number of factors including the number of defects available for trapping, the population of these traps, the temperature, and the overvoltage. None of the theories, however, have been successful in predicting the after–pulsing behavior of the photodiodes. The best way of determining the amount of after–pulsing and the DQE is to measure the total counts in the presence of a source of known light flux. One can then calculate Z and n from Eqs. 3.12 and 3.13 and determine the DQE. We have made these measurements at varying temperature and overvoltage to determine the optimum operating conditions. The results of these experimental tests are given in subsection 3.7.2.

3.6.4 Temperature Regulation

The temperature of the photodiode was regulated for two reasons. First, the linear dependence of the breakdown voltage on temperature (0.7 V/°C) required that the temperature be kept constant during Geiger mode operation to insure a constant DQE. Second, the dark count rate is kept stable by regulating the temperature. The designs used for regulating the temperature are described below.

The first design for temperature regulation utilized cold N_2 gas to cool the photodiode and a resistive heating element to regulate the temperature of the gas. Figure 3.12a shows the design of this cooling system. The photodiode was mounted on a Delrin ring positioned 1 cm away from a Delrin plug with two screws. A small glass dewar, evacuated to a pressure of 10^{-5} Torr, was placed on the outside of the Delrin plug to isolate the photodiode from the atmosphere. The N_2 gas was cooled by passing it through a 20–turn coil of 1/4" inner diameter copper tubing sitting in an ice bath. The cold gas was transferred to the glass dewar containing the Delrin

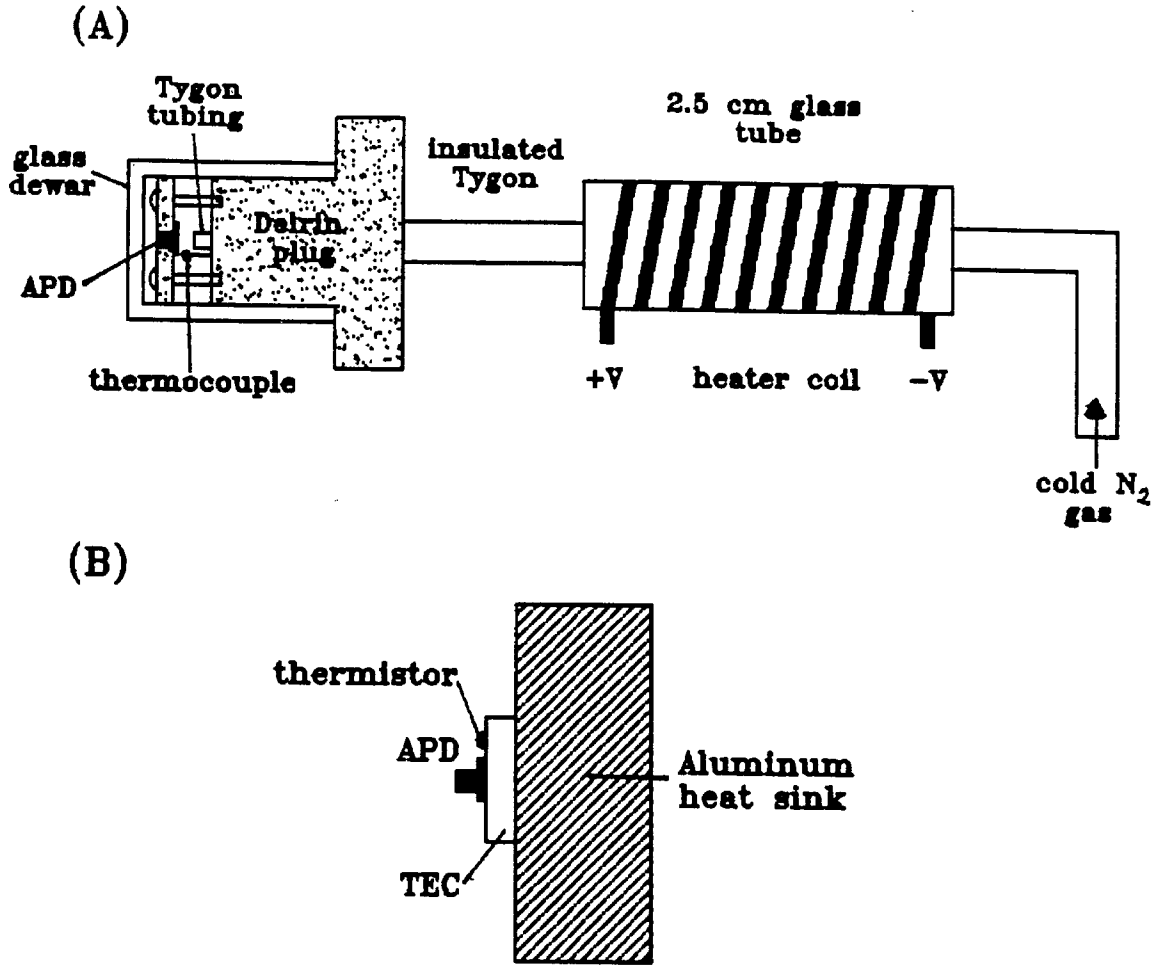

Figure 3.12: Temperature Regulation of the APD. (A) Cold N_2 gas passes through heater coils of length 10 cm. The cold gas is transferred to the photodiode by an insulated piece of Tygon tubing. The thermocouple is the sensing element for the switching network of the Omega Temperature Controller (not shown). When the temperature dipped below the set point of the controller, the heater was turned on until the temperature raised above the set point. The temperature regulation was good to 1°C. (B) The thermoelectric cooler (TEC) cools the APD. The thermistor is the sensing element for the proportional controller. The aluminum heat sink dissipates the resistive heating of the TEC. The temperature regulation of this design was good to 0.08°C.

plug. In between the copper coil and the insulated transfer line the cold gas passed across a 100–turn coil of 14 gauge copper wire. This coil acted as a resistive heating element to regulate the temperature of the gas. The temperature near the diode was measured with a thermocouple and read by an Omega temperature controller model CN 9000. If the gas temperature dipped below the set point of the controller, the controller's relay was tripped and the power to the heater was switched on. Once the gas temperature rises above the controller's set point, the relay switches off the power supply. This type of temperature regulation was good to approximately 1°C about an average temperature of 10°C. This regulation, however, proved to be inadequate for most applications. The number of counts for a constant light flux still fluctuated with temperature changes of less than 1°C.

The second design for regulating the temperature of the photodiode used a *thermoelectric cooler* (TEC) *from Marlow Industries model MI1063T* (see Fig. 3.12b). The TEC was equipped with a 10 kΩ thermistor which was used as the feedback element in the regulating circuit. The temperature regulation was achieved by a proportional controller of standard design. [5] The temperature was set by adjusting the resistance across a Wheatstone bridge containing the thermistor. The photodiode was mounted on the TEC with thermally conductive epoxy next to the thermistor. As the temperature at the thermistor increases, the resistance of the thermistor drops, unbalancing the bridge. The voltage difference across the bridge was amplified by a high precision instrumentation amplifier, and the resulting voltage was used to turn on the transistor which provided power to the TEC. The amount of current reaching the TEC was proportional to the voltage difference across the bridge. Once the thermistor was cooled and the bridge became balanced, the power to the TEC was turned off. This circuit was able to regulate the temperature of the photodiode to within approximately 0.2°C, which proved to be adequate for the experiments performed by photon counting.

3.6.5 Obtaining ρ by Photon Counting

The buffered pulses from the photodiode were counted by an SRS model SR400 200 MHz gated photon counter. The 50 kHz reference signal from the PEM was used to trigger the two gates of the SR400. First, the rising edge of the reference signal triggers the A–gate, then the gate was delayed for a time $t_d = 2.5\ \mu s$, and finally the A–gate was counted for a time $2t_d$ [12]. The B–gate was counted in analogous fashion for the negative half of the sinusoid. Figure 3.13 illustrates the counting mechanism. The total counts in the A and B channels (N_A and N_B, respectively) were transferred to the PS/2 computer through an IEEE–488 interface, and the photoluminescence polarization $\rho = (N_A - N_B)/(N_A + N_B)$ was calculated by software.

3.7 Performance of the Three Photodiodes

We have used three different RCA avalanche photodiodes in the course of our experiments. Two of the photodiodes are model C30902E and will be denoted E#1 and E#2. The last photodiode is a model C30902S which is a specially–selected photodiode for its low noise, but is essentially the same as the C30902E photodiode. This model will be denoted S#1. Each of the three photodiodes were tested for their performance in the following categories: (i) linear mode responsivity, (ii) Geiger mode pulse shape, (iii) Geiger mode dark count rate, (iv) Geiger mode pulse height distribution, (v) Geiger mode quantum efficiency, and (vi) maximum Geiger mode count rate.

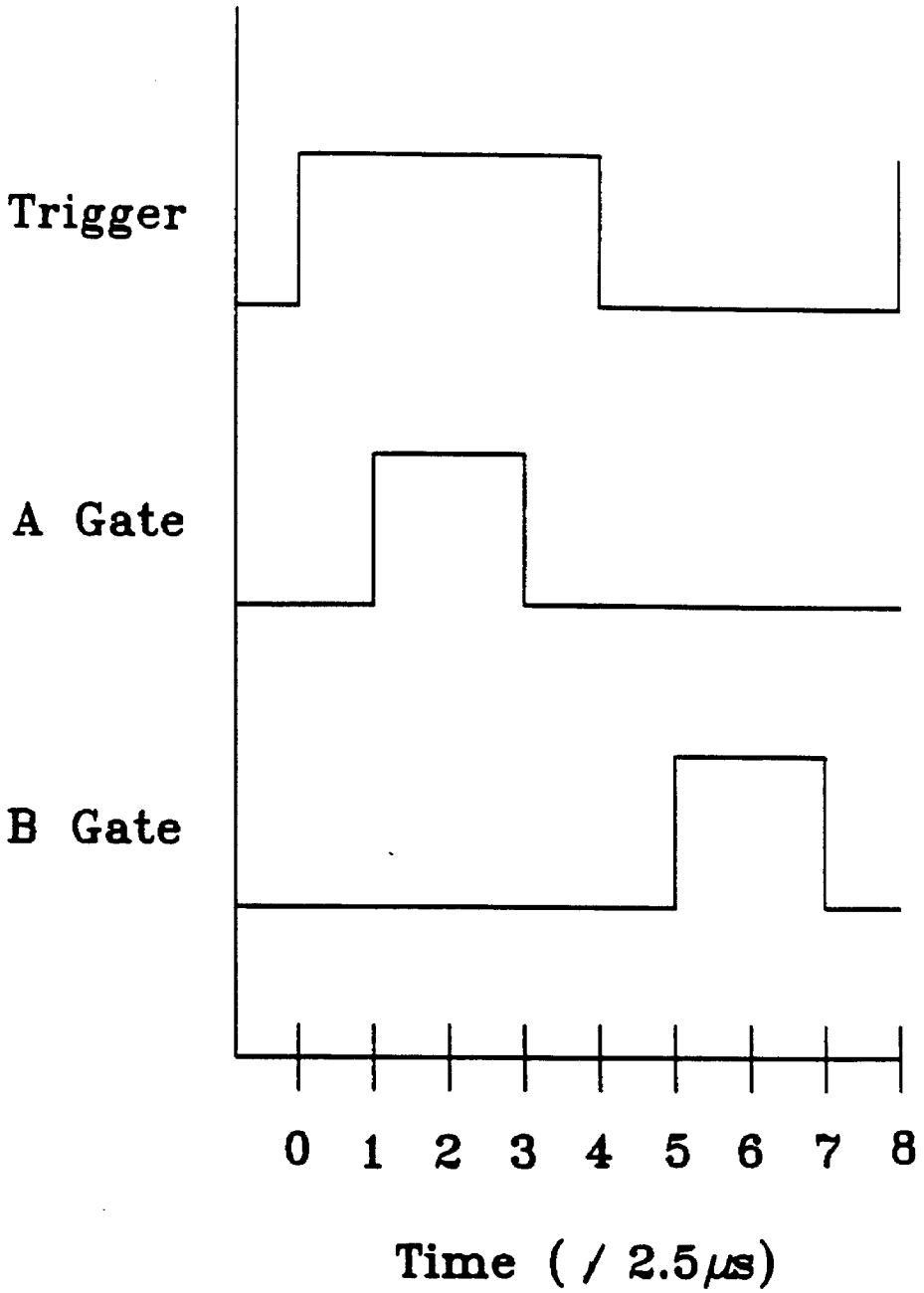

Figure 3.13: Gated Photon Counting. The PEM's 50 kHz reference supplied the trigger frequency. The rising edge of this signal initiates both gates. Gate A delays 2.5 μs and then counts for 5.0 μs. Gate B delays 12.5 μs and then counts for 5.0μs. The counts in gate A (N_A) and the counts in gate B (N_B) form $\rho = (N_A - N_B)/(N_A + N_B)$.

3.7.1 Linear Mode Performance

The linear mode characteristics are given in Table 3.2. The results for photodiodes E#1 and S#1 were quite similar while E#2 had the worst performance. The light source used for comparing responsivities was the luminescence of sample B (see Chapter 3). There was little dependence of the responsivity on temperature as indicated in Table 3.2. The dependence of the responsivity on the bias voltage is also shown in Table 3.2.

TABLE 3.2: Linear Mode Comparison
[SR530 Signal (mV)]

T (°C)	$V_{BR} - V_R$ (V)	E#1	E#2	S#1
20	3	38.3	16.3	30.1
20	5	27.9	12.8	21.6
20	7	20.8	9.9	16.3
20	10	9.5	4.6	7.5
20	20	5.3	2.0	4.2
10	5	20.5	9.7	16.2
10	10	10.2	4.6	7.9
10	20	4.6	2.6	4.0

In all categories the photodidode E#1 had the superior performance, and was used for all linear mode applications. All linear mode applications were performed at room temperature with the bias voltage such that $(V_{BR} - V_R) = 5$ V. The sensitivity in measuring the observable ρ with the linear photodiode and its equivalent circuit is discussed in section 3.9.

3.7.2 Geiger Mode Performance

Operating the photodiode in Geiger mode was not as straightforward as

operating the photodiode in linear mode. In Geiger mode the photodiode was sensitive to a single photon, and care was taken to shield the photodiode from the room lights. This was accomplished by enclosing the photodiode in a light–proof housing with an interference filter covering the opening.

Because there was a desire to measure the absolute DQE, the laser was used as the light source. In order to perform photon counting on the laser light, the laser was attenuated using 5 ND filters of optical density 1.0 (10% transmittance), two 870 nm bandpass interference filters (0.1% transmittance at 780 nm), and one 780 nm bandpass filter (1% transmittance at 806 nm). The 780 nm filter was used to remove the small laser light centered at 806 nm mentioned in section 3.4. The 30mW laser diode produces $1x10^{17}$ photons/s, and after passing through the ND filters and the bandpass filters, only $9.5x10^{5}$ photons/s remain.

The pulse shapes of the photodiodes were identical (see Fig. 3.11). Table 3.3 shows the dark count rate for each of the photodiodes at three different temperatures.

TABLE 3.3: Dark Count Rate Comparison (kHz)

Temp (°C)	E#1	E#2	S#1
20	3.62	57.8	29.3
10	0.305	7.37	3.66
5	0.018	2.26	0.95
- 196	0.00052	-	-

Photodiode E#1 was also tested for dark counts in LN_2 where the dark count rate was $\simeq$ 0.5 Hz. A pulse height distribution (PHD) was measured for each of the photodiodes in the dark in order to determine the appropriate discriminator level for the photon counter. This experiment was done by using the two gates of the SR400 to form a 10mV window. Gate A was set initially with a discriminator level of 2 mV, and gate B was set initially with a discriminator level of 12 mV. Both gates

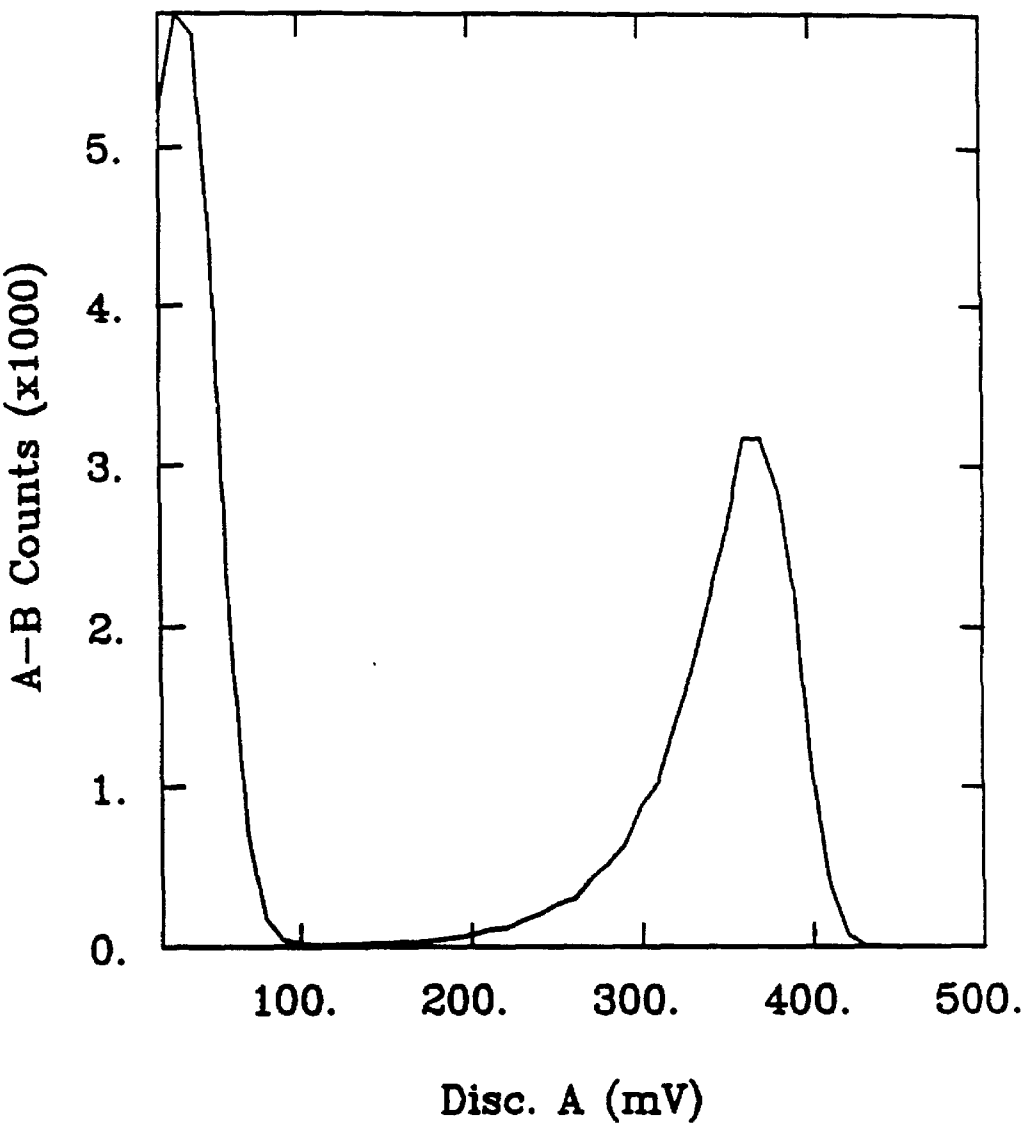

Figure 3.14: Pulse Height Distribution. The figure shows the pulse heights for the room temperature dark counts of photodiode E#1. The overvoltage was set to 7 V. The first peak corresponds to noise pulses, and the second peak (350 mV) corresponds to the avalanche pulses.

were counted for 10 s. The discriminator levels were then increased by 10 mV, and another point was taken. The resulting signal was plotted as (counts in A – counts in B) versus discriminator level A. Figure 3.14 shows a PHD plot for E#1 at room temperature. This PHD is characteristic for any photon counter. The initial counts represent the noise pulses due to the ringing of the buffer, preamp, and cable. The peak at 350 mV, well separated from the noise, represents the avalanche pulses. Based on the data of Fig. 3.14, the discriminator level of the SR400 should be placed at approximately 110 mV where no noise pulses will be counted, but all of the avalanche pulses will be counted. All three photodiodes showed similar PHD's.

Table 3.4 shows the results of photon counting performed on the attenuated laser light at 10°C. The discriminator level was set at 110 mV, photons were counted for 10 s for each point, and 500 total points were taken.

TABLE 3.4: DQE Comparison

Photodiode	N	ΔN^2	Z	DQE (%)
E#1	7.75×10^4	7.91×10^4	0.03	8.0
E#2	3.65×10^4	4.67×10^4	0.12	3.3
S#1	5.27×10^4	5.85×10^4	0.05	5.2

Photodiode E#1 seemed to be superior to the other two, but the possibility of after–pulsing had to be explored. The probability of after–pulsing can be calculated from the data of Table 3.4 using Eqs. 3.12 and 3.13. Performing the calculations yields the corresponding values for Z and DQE given in Table 3.4. Thus, photodiode E#1 was superior for photon counting as well as for linear detection.

The remaining question which was addressed was that of the appropriate operating voltage and temperature. The same counting experiment described above was repeated for photodiode E#1 at varying temperature and overvoltage. No dependence of EQE on temperature was seen over a range – 10° C to 20° C. The

data of Table 3.5 taken at 10° C, however, indicate a sensitive dependence of EQE on the overvoltage.

TABLE 3.5: After-Pulsing vs. Overvoltage (photodiode E#1)

Overvoltage (V)	N	ΔN^2	Z	EQE (%)
5	7.75×10^4	7.91×10^4	0.03	7.5
6	8.83×10^4	9.01×10^4	0.03	9.0
7	1.05×10^5	1.07×10^5	0.04	10.3
8	1.21×10^5	1.31×10^5	0.07	10.0
9	1.58×10^5	1.99×10^5	0.21	8.5
10	3.31×10^5	7.78×10^5	0.57	4.0

As the overvoltage was changed from 5 V to 10 V the number of counts increased by a factor of 4, but the EQE dropped by a factor of 2 after going through a maximum at 7 V. In addition to the changes in EQE, there were also changes in the shape of the PHD. The peak associated with the avalanche pulses became less separated from the noise pulses. At an overvoltage of 10 V it was hard to tell the difference between the end of the noise pulses and the beginning of the avalanche pulses. This effect is due to *after–pulses decaying during the recharging time of the photodiode. If an* echo avalanche occurs before the photodiode is fully recharged then the resulting avalanche has a height less than that of the initial avalanche. If the probability of an after–pulse is high then the photodiode never becomes fully recharged, and the pulse height drops. The changes in total counts, EQE and PHD indicated that although the sensitivity of the Geiger photodiode increased with overvoltage, the after–pulsing destroyed the S/N at high overvoltage. The data of Table 3.5 indicates that the optimum overvoltage is 7 V. The temperature for the photon counting experiments was set at 10°C where the TEC controller was most efficient

and the dark count rate was low compared to the signal. At 10°C and an overvoltage of 7 V the EQE of photodiode E#1 ≃ 10%.

3.7.3 Maximum Geiger Mode Count Rate

The maximum count rate for photodiode E#1 was determined by counting the attenuated laser source and selectively removing the ND filters until the detector was saturated. The count rate for the attenuated laser source with 5 ND filters was 77.5 kHz at an operating temperature of 10°C and an overvoltage of 7V. When the incident power was increased by a factor of 10 the avalanche pulses became slightly smaller, but no change in EQE was detected. When the incident power was increased further by factor of 2, the pulse heights were almost too short to count properly. The separation between the noise pulses and the avalanche pulses was barely discernable, similar to the effect seen in the experiment of Table 3.5. The EQE showed a dramatic drop of a factor of 5. There are two causes for this drop in EQE. First, the photon flux is too high causing photons to arrive before the photodiode is fully recharged. This reason alone, however, is not enough to explain such a large drop in EQE. The other reason for the drop is an increase in after–pulsing. Increasing the photon flux has the same effect as increasing the sensitivity (overvoltage) on the after–pulsing. There is a higher electron concentration in the avalanche region when the overvoltage increases or when the photon flux increases, and an increase in the probability of occupying a trap follows. The maximum count rate for photodiode E#1 was found to be approximately 800kHz. It should be noted that references [7] and [9] claim a maximum count rate of only 400 kHz for their photodiodes.

If the photon flux is greater than 800 kHz an active quenching circuit could be employed [14,15]. Active quenching of the photodiode means that the photodiode

is driven back to its recharged state electronically and a factor of 2 improvement in dead–time can be obtained. Many different circuits have been implemented with great success, and maximum count rates of up to 2 MHz have been achieved [11,14,15]. This type of circuit, however, was not implemented in our lab. If the luminescence signal became higher than the maximum count rate of 800 kHz, linear detection was applied.

3.8 Data Acquisition Software

As mentioned, an IBM PS/2 model 80 computer controls the TSONMR spectrometer. The hardware used in interfacing the computer to the various instruments consists of a National Instruments multi–channel IEEE–488 GPIB bus and a National Instruments 32–bit digital input/output (DIO) board. There are a total of five instruments under direct control via the GPIB bus: the SR400 photon counter, the SR530 lock–in amplifier, the ITI word generator, the HP frequency synthesizer, and the PTS frequency synthesizer. The DIO board controlled the opening and closing of the shutter, and, at times, an rf switch. The magnetic fields were controlled indirectly by the GPIB bus. The analog voltage of the analog output port P1 of the SR400 was set via the GPIB bus and this voltage was then supplied to the modulation input of the current regulator of the z–field. The analog port P2 of the SR400 supplied the modulation input voltage for the current regulator of the Hanle field.

In this section a brief description of the data acquisition software is given. A more detailed discussion of interfacing with GPIB is presented in Appendix A. A copy of the source code written entirely in the C programming language is also included in Appendix A.

3.8.1 Program Specifics

The program for the TSONMR experiment (TSONMR.C) is broken up into four parts, the initialization period, the ONP period, the NMR period, and the OD period.

The initialization period initializes all variables and arrays, the GPIB bus, all GPIB devices, and the DIO board. The setup routines for the SR400, SR530, and ITI are also executed. The setup routines send each string of a setup file to the specific device. This is done for all device–specific parameters that do not change over the course of the experiment.

The ONP period is performed by setting the modulation input voltage of the z–field current regulator, nulling the modulation input voltage of the Hanle current regulator, opening the shutter, and delaying for the ONP time (an input parameter usually a period of seconds). The ONP delay is accomplished by continuously reading the PC clock until the delay time has elapsed. This method is useful for any delay higher than 10 ms with a resolution of approximately 10 ms. The shutter is then closed or left open at the end of the ONP period depending on the desired NMR experiment.

The NMR period begins with the PC triggering the ITI word generator which controls the timing of the rf pulse(s). Logic levels from the ITI are used to control the main rf switch, the phase of the rf, and an rf pulse–shaper depending on the type of NMR experiment. During the NMR period the computer delays until the ITI is finished. The length of this delay is input as a parameter at the start of the experiment.

After the NMR period, the magnetic fields are cycled in the dark by setting the modulation input voltage to the Hanle field current regulator, and nulling the

modulation input voltage to the z–field current regulator. The program delays 200 ms while the fields are cycled. Once the fields are cycled, the shutter is opened and the signal is detected. If the signal is acquired by photon counting, the detection period begins by triggering the SR400. The timing for the gates is done by the internal clock of the SR400 and the computer continuously polls the SR400 until the SR400 returns a flag indicating that it is finished counting. When this flag is set, the computer polls the SR400 for counts in both the A and B gates. The resulting data is then converted into the circular polarization $\rho = (N_A - N_B)/(N_A + N_B)$.

If the signal is acquired by lock–in detection then the detection period begins with the computer polling the SR530 for data in channel A ($I_+ - I\_$) and A/D port 1 ($I_+ + I\_$) simultaneously. The SR530 digitizes the two signals and the data is sent to the computer via the GPIB bus. If more than one data point is required, then the above process is repeated. The minimum time delay between points is 60 ms. The SR530 cannot send data faster than this limit. The two signals are then ratioed to obtain ρ.

In the detection period, the data is acquired at 60 ms intervals (or down to 10 ms intervals for photon counting) for 100 points. A single NMR data point is extracted from this transient by subtracting it from the null transient (a field cycling transient without an NMR period), multiplying each point by a weighting function (see chapter 4), and summing the resulting points. The entire spectrum is obtained by repeating the ONP, NMR, and OD periods for a different rf frequency, pulse width, or pulse delay.

3.9 Noise in Detecting the Circular–Polarization

This section will describe the noise associated with both linear and Geiger mode detection. The different sources of noise and how the sources influence the

noise $\Delta\rho$ will be explored. A full discussion of the signal–to–noise ratio will, however, be postponed until the next chapter where the signal of the TSONMR experiment is described.

3.9.1 Standard Deviation of the Circular Polarization of the Luminescence

The variance $\Delta\rho^2$ of the circular polarization ρ is given by, [16]

$$\Delta\rho^2 = \left[\frac{\partial\rho}{\partial(I_+ - I_-)}\right]^2 \Delta(I_+ - I_-)^2 + \left[\frac{\partial\rho}{\partial(I_+ + I_-)}\right]^2 \Delta(I_+ + I_-)^2 \qquad (3.22)$$

and, simplifying,

$$\Delta\rho^2 = \frac{1}{(I_+ + I_-)^2}\left[\Delta(I_+ - I_-)^2 + \rho^2\Delta(I_+ + I_-)^2\right] \qquad (3.23)$$

where $\Delta(I_+ - I_-)^2$ and $\Delta(I_+ + I_-)^2$ are the variances of the 50 kHz difference signal and the 500 Hz sum signal, respectively. If the noise of the two signals is shot noise limited, then the statistical fluctuations of the incident photons dominate the noise, and Eq. 3.23 can be replaced by,

$$\Delta\rho^2 = \frac{\Delta N_+^2 + \Delta N_-^2}{(N_+ + N_-)^2}(1 + \rho^2), \qquad (3.24)$$

where N_+ and N_- are the number of right–hand and left–hand photons counted, respectively. If $\rho << 1$ (as is the case with our samples) then $N_+ \simeq N_- = N$. Using Eq. 3.24 for Poisson counting statistics $\Delta\rho^2 = 1/(2N)$ and the standard deviation $\Delta\rho = 1/\sqrt{2N}$.

3.9.2 Noise in Photon Counting

For photon counting, the standard deviation $\Delta\rho$ will be shot–noise–limited if the counting statistics are described by a Poisson process. Table 3.5 clearly indicates that if the overvoltage is between 5 V and 7 V then the total counts is described by

a Poisson process. As long as the incident flux is less than 800 kHz, shot noise limited detection is achieved with photon counting.

3.9.3 Noise in Linear Detection

To determine the shot noise limit in the case of linear detection, the luminescence signal was collected at a bias voltage V_R such that $V_{BR} - V_R = 5$ V. The average photovoltage of the signal proportional to $(I_+ + I_-)$, was converted into photon counts using the known responsivity of the device. The square root of the result was taken and then inverted to give the shot noise limit for $\Delta\rho$. In this experiment the time constants of both lock–in amplifiers were set to 30ms and 500 points were acquired for the statistics. Table 3.6 shows the results of this experiment for different bias voltages.

TABLE 3.6: Shot Noise Test for Photodiode E#1

Undervoltage (V)	SR510 Signal (mV)	Measured Δρ (x 10^5)	Expected Δρ (x 10^5)
3	38.3	7.80	1.50
5	27.9	7.76	1.75
7	20.8	7.93	2.03
10	9.5	8.29	3..00
25	5.3	27.6	4.01

The measured standard deviation in ρ is larger than the shot noise limit by approximately a factor of 4. The deviation from the shot noise limit has been thoroughly investigated and described elsewhere. [17] They indicate that the noise at the present luminescence power is dominated by the Johnson noise of the equivalent circuit (photodiode, transconductance amplifier, and lock–in amplifier). Thus, although sensitivity is improved for bright samples by using linear detection,

there is a range of luminesence power ($\sim 10^6 - 10^{10}$ counts/sec) where detector improvement (CCD detector, faster counting, faster circuits) would help in approaching the shot–noise limit.

3.10 References

[1] B.K. Johnson, *Optics and Optical Instruments* (Dover, New York, 1960), p. 209.

[2] D.N. Shykind, G.C. Chingas, A. Pines, and A.J. Shaka, Rev. Sci. Inst. **61**, 1474 (1990).

[3] J.C. Kemp, J. Opt. Soc. **59**, 950 (1969); and J.C. Kemp, HINDS International Inc. Applications Notes.

[4] A. Yariv, *Optical Electronics 3rd Ed.* (Holt, Rinehart and Winston, New York, 1985) pg. 376.

[5] P. Horowitz and W. Hill, *The Art of Electronics 2nd Ed.* (Cambridge, Cambridge, 1989) pg. 105.

[6] RCA avalanche photodiodes models C30902E and C30902S applications notes.

[7] T.E. Ingerson, R.J. Kearney, and R.L. Coulter, Appl. Opt. **22**, 2013 (1983).

[8] S.D. Personick, Bell Syst. Tech. J. **50**, 167 (1971).

[9] P.A. Ekstrom, J. Appl. Phys. **52**, 6974 (1981).

[10] R.G.W. Brown, K.D. Ridley, and J.G. Rarity, Appl. Opt. **25**, 4122 (1986).

[11] A. Lightstone, A. MacGregor, D. MacSween, R. McIntyre, C. Trottier, and P. Webb, Elect. Eng. **XX**, 37 (October, 1989).

[12] A.P. Balatsyuk, V.A. Novikov, and V.G. Fleisher, Prib. Tekh. Eksp. **No. 1**, 171 (1976).

[13] B.H. Candy, Rev. Sci. Inst. **56**, 183 (1985).

[14] R.G.W. Brown, R. Jones, J.G. Rarity, and K.D. Ridley, Appl. Opt. **26**, 2383 (1987)

[15] A. Lacaita, S. Cova, and M. Ghioni, Rev. Sci. Inst. **59**, 1115 (1988).

[16] D. Skoog, *Principles of Instrumental Analysis 3rd Ed.* (Saunders, Philadelphia, 1984) pg. 16.

[17] N.D. Kurur, Ph.D. Thesis, California Institute of Technology, Pasadena, 1991.

Chapter 4

Experimental Foundations of TSONMR

The basic theoretical principles for optical NMR in GaAs were discussed in chapter 2. In section 2.5 the TSONMR experiment was introduced and shown to demonstrate high sensitivity and resolution. In this chapter the experimental principles of the TSONMR experiment are discussed in detail. A description of each of the samples used in our experiments is given and comparisons are made between them. The methods for obtaining material parameters pertinent to the signal–to–noise ratio of a TSONMR experiment are also discussed. The complete Hanle effect used in detection, the heart of the optimized sensitivity of TSONMR, is examined further. The physics of the field cycling transient and its use in measuring the nuclear field B_n is explored in detail. Finally, a sensitivity analysis for TSONMR is developed which describes how the signal depends on measurable material parameters. Throughout the course of this development, the process of optimizing the different periods of the TSONMR experiment is also described.

4.1 Samples

We have attempted experiments on eight different bulk GaAs samples of varying dopant, dopant concentration, and growth method. The samples obtained for our experiments were grown by three different techniques: molecular beam epitaxy (MBE), liquid phase epitaxy (LPE) and liquid–encapsulated Czochralski (LEC). The samples were first tested for luminescence and the results are

summarized in Table 4.1. The photoluminescence (PL) was measured by synchronous detection with the 500 Hz optical chopper unless indicated otherwise. The analog voltage was then converted into a photon flux.

Table 4.1: TSONMR Samples

Sample #	Dopant	Conc. (cm^{-3})	Growth Method	PL (counts/sec)	ρ_0
1	undoped	-	LEC	*3.0 x 10^2	0.008
2	In	10^{19}	LEC	none	-
3	Zn (p-type)	10^{16}	MBE	*2.3 x 10^6	0.021
4	Zn (p-type)	10^{17}	MBE	1.7 x 10^{10}	0.048
5	Zn (p-type)	10^{17}	MBE	1.5 x 10^{10}	0.033
6	Si (n-type)	10^{18}	LPE	8.6 x 10^{10}	0.000
7	Zn (p-type)	10^{18}	LPE	3.4 x 10^9	0.063
8	Zn (p-type)	10^{19}	LPE	2.7 x 10^9	0.051

* measured luminescence by photon counting

In general, the MBE and LPE–grown samples had the highest luminescence. For the LEC–grown samples 1 and 2 luminescence was weak presumably because of the large number of nonradiative traps created during the growth process. [1,2] The epitaxial methods have proven to produce low–defect samples since the growth process is more closely controlled. [3,4] Also, the surface of these samples was passivated with a thin film ($\simeq 1\ \mu m$) of $Ga_{1-x}Al_xAs$ ($x \simeq 0.3$) to insure an unreactive GaAs interface. This cap acts as a transparent window at our excitation wavelength of 790 nm due to its higher band gap. [5]

For the luminescent samples, 1 and 3 through 8, ρ in zero applied field also appears in Table 4.1. The measurement was taken for right–hand

circularly–polarized exciting light. Only the p–type samples exhibited an appreciable ρ. This result is understood based on the discussion in section 2.1.3. The n–type sample was highly–doped so the excitation power was inadequate given the short τ_s at 77 K to displace the unpolarized thermal carriers. It should be possible to orient the electrons in sample 6 either by cooling the sample to liquid helium (LHe) temperatures ($\lesssim$ 4 K) or by increasing the excitation power. By cooling the sample, the electron spin–lattice relaxation time τ_s increases and the ratio τ_J/τ_s decreases. By increasing the excitation power, the number of electron–hole pairs created per unit volume (parameter G in Eq. 2.8) increases and τ_J decreases. Both of these cases require changes to the apparatus described in chapter 3 (a LHe cryostat or a high power laser), and these improvements are currently underway.

4.2 Evidence for Nuclear Spin Polarization

We have employed three methods to test for the existence of a nonzero nuclear field prior to TSONMR: sweeping the z–field, [6] by sweeping the Hanle field, [7–9] or by quasi steady–state ODNMR. [10,11] We have performed all of these experiments on the samples from Table 4.1 which show a nonzero ρ.

In a z–field sweep the circular–polarization is measured as a function of the applied field. The dependence of ρ on the applied field parallel to the light manifests itself in the field dependence of τ_s in Eq. 2.33. If nuclear polarization is created, then the dependence of ρ on the applied field is enhanced or suppressed for right–hand and left–hand circularly–polarized light, respectively (see Fig. 2.2).

A Hanle field sweep is performed the same way as a z–field sweep. In this case, however, nuclear effects are seen as an enhancement of the Hanle effect in low field as described in section 2.3.2.

4.2.1 Z–Field Sweep

For a z–field sweep $\mathbf{B}_0^p$ and $\mathbf{B}_n$ are colinear, and the total field has magnitude $B_T = B_0^p \pm B_n$ for parallel and antiparallel ONP, respectively. Figure 4.1 shows a sweep of B_0^p for sample 4. The sweep rate was kept slow enough for steady–state to be reached at each point. In order to achieve both the parallel and antiparallel orientations, the direction of the applied field $\mathbf{B}_0^p$ was changed from + B_0^p to $-B_0^p$. The negative field values represent the antiparallel orientation $B_T = B_0^p - B_n$, and the positive field values represent the parallel orientation $B_T = B_0^p + B_n$. Samples 3 and 5 showed similar results, but samples 7 and 8 showed no change in ρ for any value of B_0^p. The difference in samples can be explained in terms of the nuclear field.

The most prominent feature of Fig. 4.1 is a dramatic increase in ρ in low field. As discussed in section 2.3.1 low field spin dynamics are described in terms of a thermalization between the dipolar and Zeeman heat capacities. Here the nuclear spin system acts as a single entity with spin temperature θ. The nuclear cooling resulting from ONP manifests itself as a combination of Zeeman and dipolar order. The nuclear field at values of B_0^p small compared to the local field B_L is a fraction of its high field value B_n. Once the applied field reaches the limit $B_0^p >> B_L$ ($B_L \simeq$ 3 G in GaAs), the Zeeman terms dominate and the nuclear field reaches its high field value. In sufficiently high field each spin reservoir (^{69}Ga, ^{71}Ga, and ^{75}As) is isolated from the others and the nuclear field is the sum of the contributions of the three nuclear species, the dipolar reservoirs being negligible. This competition between dipolar and Zeeman terms in the nuclear spin Hamiltonian magnifies the field dependence of τ_s. The interplay between the different spin reservoirs is evident in Fig. 4.1; the slope at low fields is greater than can be accounted for by the field dependence of τ_s as described by Eqs. 2.33 and

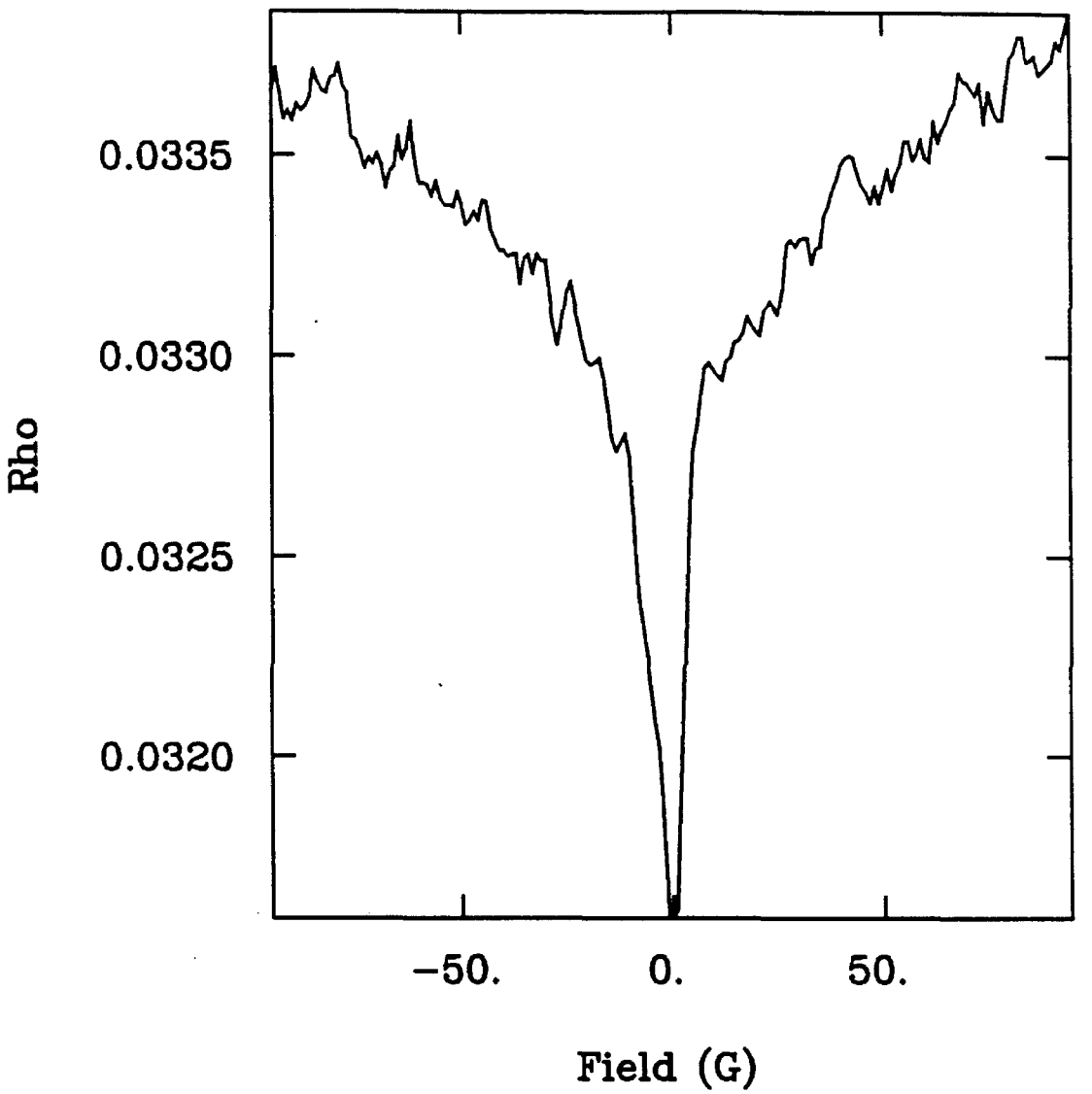

Figure 4.1: Z–field Sweep. The figure shows a z–field sweep at a rate of 1.3 G/10 s for sample 4. The sweep is performed from $-B_0^p$ to $+B_0^p$ in the presence of right–hand circularly–polarized light. The initial rise from zero field is due to the increase of B_n. The asymmetry around zero applied field is due to B_n opposing the applied field for negative B_0^p, and adding to the applied field for positive B_0^p.

2.34.

The asymmetry in Fig. 4.1 is also evidence of nuclear effects. On the antiparallel side of the trace the increase in ρ lags behind the increase in ρ on the parallel side because $|B_n - B_0^p| \leq |B_n + B_0^p|$ and the change in ρ is greater on the parallel side. At points beyond ±10 G the slope of the curve becomes less steep since the Zeeman quantization is complete and the gain in B_n with increasing B_0^p is smaller than in low field.

In the case of samples 7 and 8, either no nuclear field is achieved or the field dependence of τ_s is very small. The explanation of this observation will be clearer at the end of the next subsection.

In principle, the nuclear field could be found by fitting Fig. 4.1 to Eqs. 2.32 – 2.34, but such attempts failed to reproduce the rapidity of the drop in ρ in low field. Possible reasons for this are that a different mechanism for τ_s applies in low field, or that the increase in B_n with applied field is steeper than predicted by spin temperature theory.

4.2.2 Hanle Sweep

This experiment is identical to the experiment of Paget et al. [8] The field B_0^d, oriented perpendicular to the light, is incremented slowly enough for steady–state to be reached at each point (typically 10 s). Figure 4.2 shows the Hanle curve for sample 4. The enhancement in low B_0^d due to nuclear effects (see section 2.3.3) is indeed seen. The shape of the Hanle curve is also sample dependent as is indicated by Figures 4.3 and 4.4. No measurable dependence of ρ on B_0^d was seen for samples 7 and 8. This indicates not only that these samples lack substantial nuclear field, but that their Hanle widths are also large compared to the range of field accessible. This result is in agreement with Hanle effect experiments performed

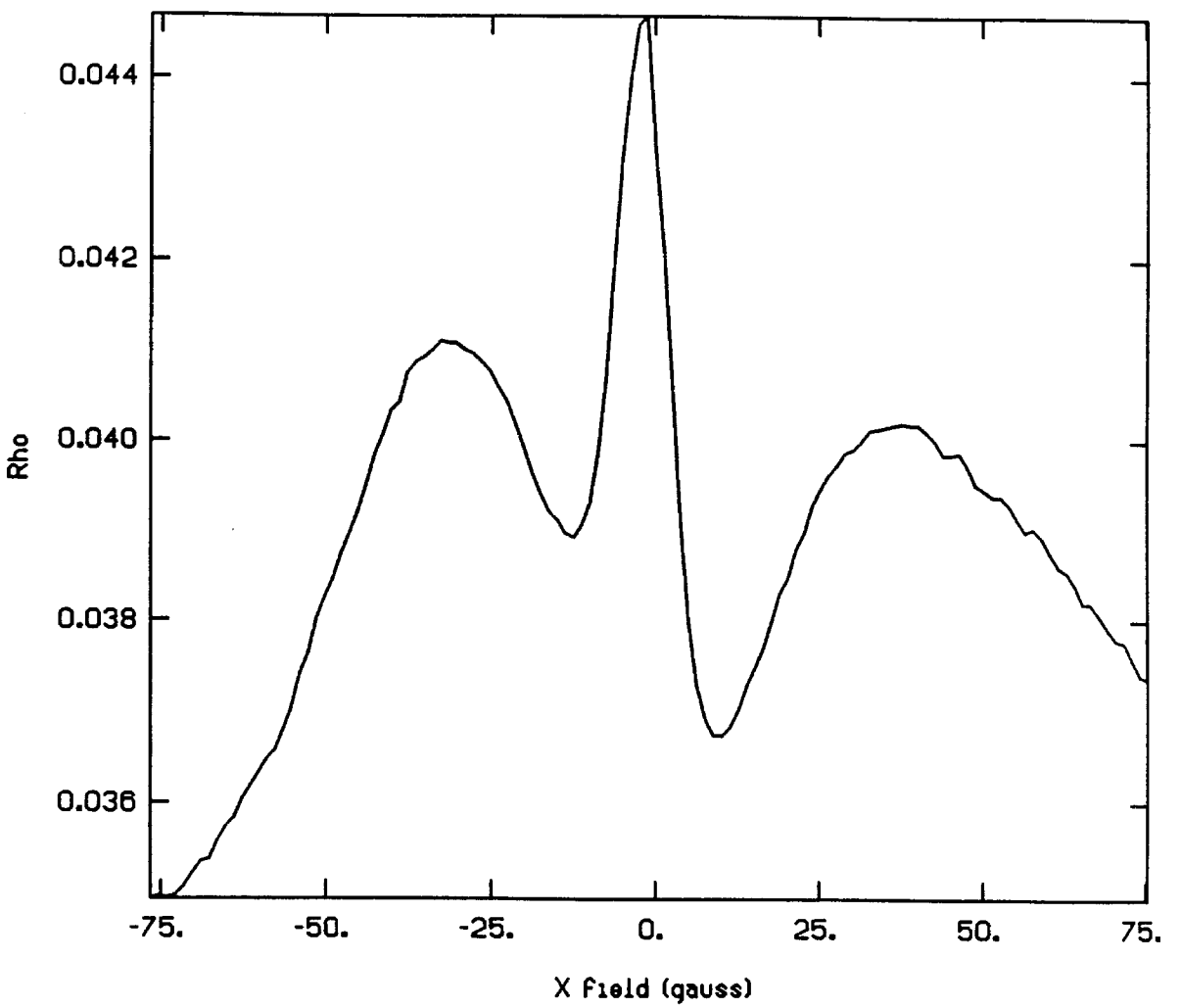

Figure 4.2: Hanle field sweep. The field B_0^d perpendicular to the light direction is swept at a rate of 1.9 G/10 s for sample 4. The sweep was performed from $-B_0^d$ to $+B_0^d$ in the presence of right–hand circularly–polarized light. The large depolarization near zero field is due to nuclear polarization aligned along the field $(B_0^d + \Gamma_t b_e \langle S \rangle)$.

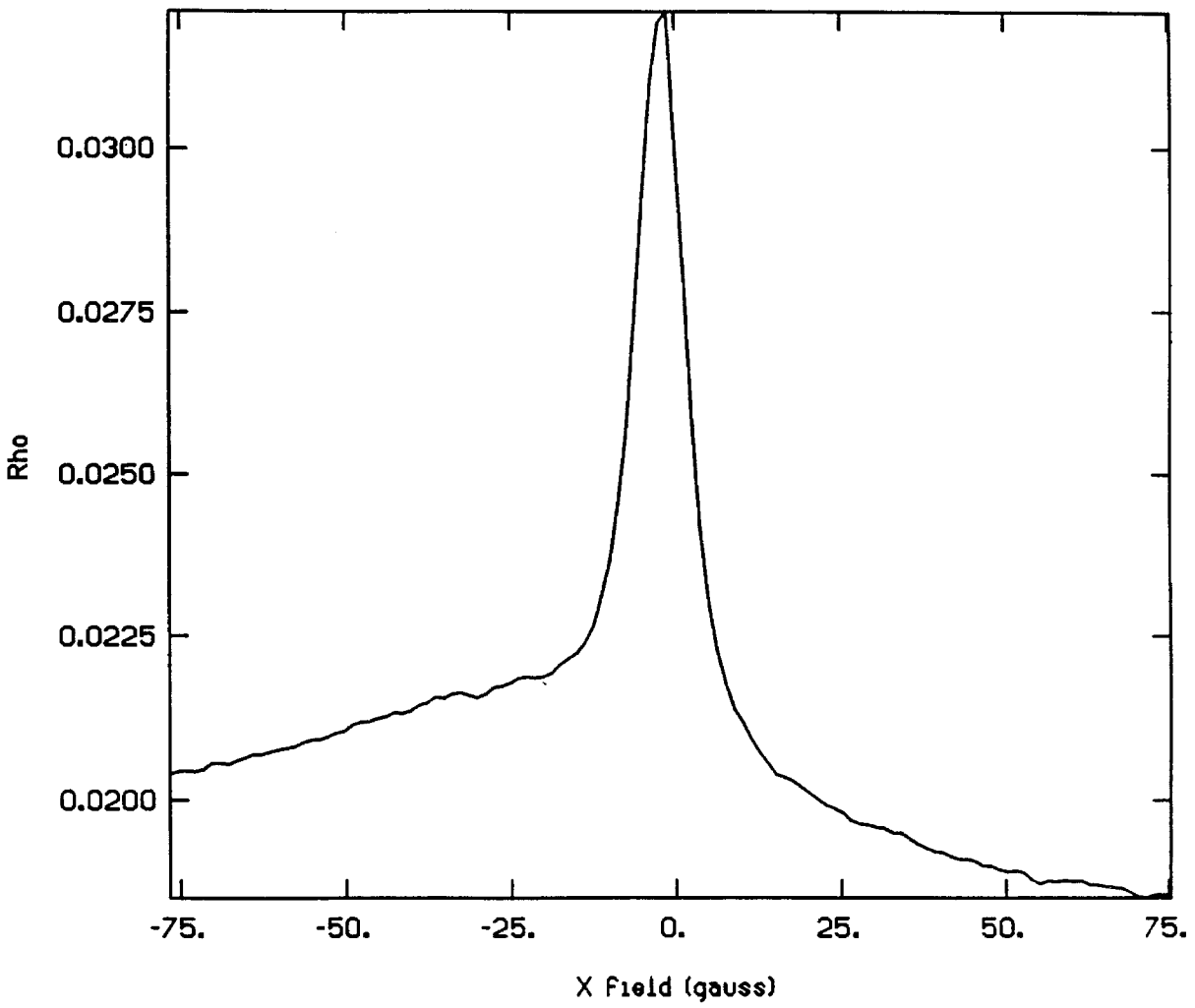

Figure 4.3: Hanle field sweep of sample 4. The conditions of this experiment were the same as in Fig. 4.2. The shape of the Hanle curve including nuclear effects is strongly dependent on the sample (see refs. [7–9]). The difference in the TSONMR spectra for samples 4 and 5 will be discussed in chapter 5.

on similar samples. [12]

The influence of the nuclear field on the Hanle curve is a sensitive function of sample orientation as indicated in Figure 4.5. In this experiment the angle between the light axis and the applied field $\mathbf{B}_0^{\mathbf{d}}$ was changed by less than five degrees by moving the laser, and illuminating the same spot on the sample.

The asymmetry in the Hanle curve in the presence of nuclear polarization has been widely studied. [7–9,13] The general equation of motion of the electron spin polarization is given in Eq. 2.35. If the external magnetic field is replaced by the total field $\mathbf{B}_T = \mathbf{B}_0^{\mathbf{d}} + \mathbf{B}_n$ and the dynamics of the nuclear spin system (including nuclear cooling in the field $\mathbf{B}_0^{\mathbf{d}} + \Gamma_t b_e \langle \mathbf{S} \rangle$) and the electron spin system are solved simultaneously, it is possible to obtain a fit to the Hanle curve in the general case of $\mathbf{B}_0^{\mathbf{d}}$ oblique to $\langle \mathbf{S} \rangle$. The special case of $\mathbf{B}_0^{\mathbf{d}} \perp \langle \mathbf{S} \rangle$ was solved by Dyakonov and Perel [2] and Paget [3] and was described in section 2.3.3. While the case of an arbitrary angle φ between $\mathbf{B}_0^{\mathbf{d}}$ and $\langle \mathbf{S} \rangle$ would require extensive computation to solve quantitatively, it is possible to describe the shape of the Hanle curve qualitatively by considering the positions of the extrema. [9] The extrema in the Hanle curve occur when the nuclear field (partially) compensates for the applied field B_0^d. Experimental results performed on GaAs have shown that for angle $\varphi < 87^0$, both maxima occur on the same side of zero field (a consequence of $g^* < 0$ for GaAs).[8,9] The maxima do not reach the value $\rho(0)$ because the decrease of B_n with increasing B_0^d is greater than the increase in B_0^d and complete compensation is not possible.

Although it is, in general, difficult to fit the Hanle curves theoretically. The solution is simplified in the case of $\varphi = 90^0$. In this case the steady–state solution is given by Eqs. 2.37 and 2.38. Using these equations a fit to the curve of Fig. 4.4 was obtained (the solid line) yielding the parameters $\xi B_L = 4.0$ G, $\Delta B = 75$ G, and $fb_n = 400$ G. Similar numbers were obtained for samples 4 and 5.

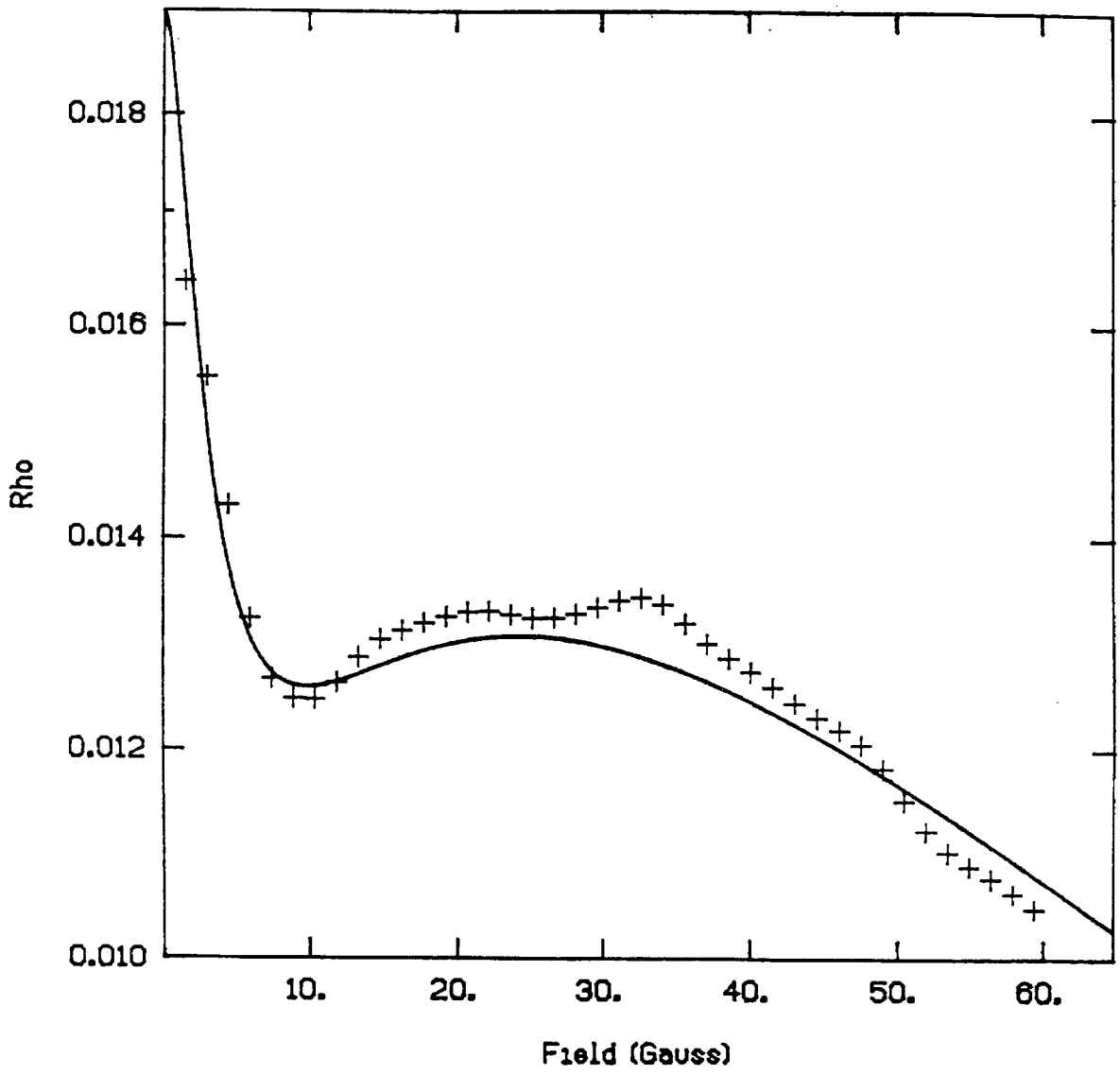

Figure 4.4: Hanle field sweep of sample 3. The sweep for this experiment was performed from zero field to $+B_0^d$ in steps of 1.9 G/10 s. The data (x's) was taken using gated photon counting. The fit to the data was obtained from Eqs. 2.37 and 2.38 yielding the parameters $\xi B_L = 4$ G, $\Delta B = 75$ G, and $fb_n = 400$ G.

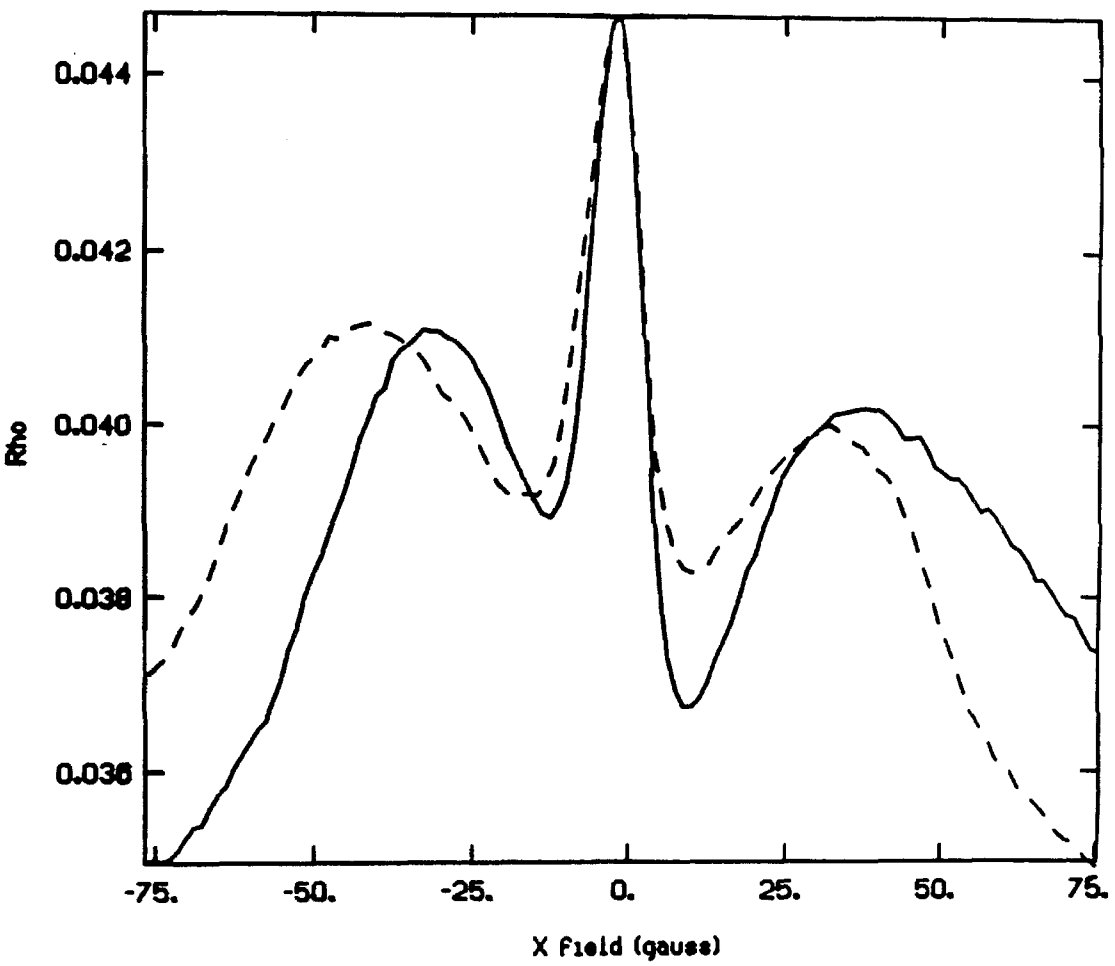

Figure 4.5: Asymmetry in the Hanle curve (sample 4). The solid trace is the same as Fig. 4.2. The dashed trace is obtained by changing the angle between the light direction and B_0^d by approximately 5°. The dependence of the Hanle effect on the angle between B_0^d and the light is described in the text.

4.2.3 Quasi Steady–State ODNMR

Although the quasi steady–state ODNMR technique was shown in chapter 2 to be inadequate for high–resolution and high–sensitivity spectroscopy, the ease of the technique makes it attractive for screening for nuclear spin effects, and as a point of reference for comparing techniques and samples. The quasi steady–state technique was attempted on samples 4, 5, 7, and 8. In this experiment the frequency was swept upward in 150 G in the antiparallel geometry. No signal was seen for any of the samples for rf field strengths $B_1 < 3$ G. If the rf field was increased to above 3 G, a small signal was seen for samples 4 and 5. Figure 4.6 shows the spectrum obtained for sample 5 which has a linewidth of $\simeq$ 18 kHz due to power broadening. No signal was detected for samples 7 and 8 which also exhibit no other nuclear effects.

Many factors determine the success of the steady–state experiment as was discussed in section 2.4. Although the existence of a signal is positive proof of nuclear spin polarization, the complex dependence of the signal on the conditions of resonance makes the technique awkward for quantifying the various nuclear spin effects.

4.3 The Field Cycling Transient

In this section the physics of the field cycling transient, introduced as the detection period of a TSONMR experiment in section 2.5.1, will be described in detail. Monitoring ρ once the nuclei are reoriented perpendicular to the light provides an efficient means of detecting the nuclear field B_n. A complete Hanle effect is observed due to the colinearity of the applied and nuclear fields. The effect

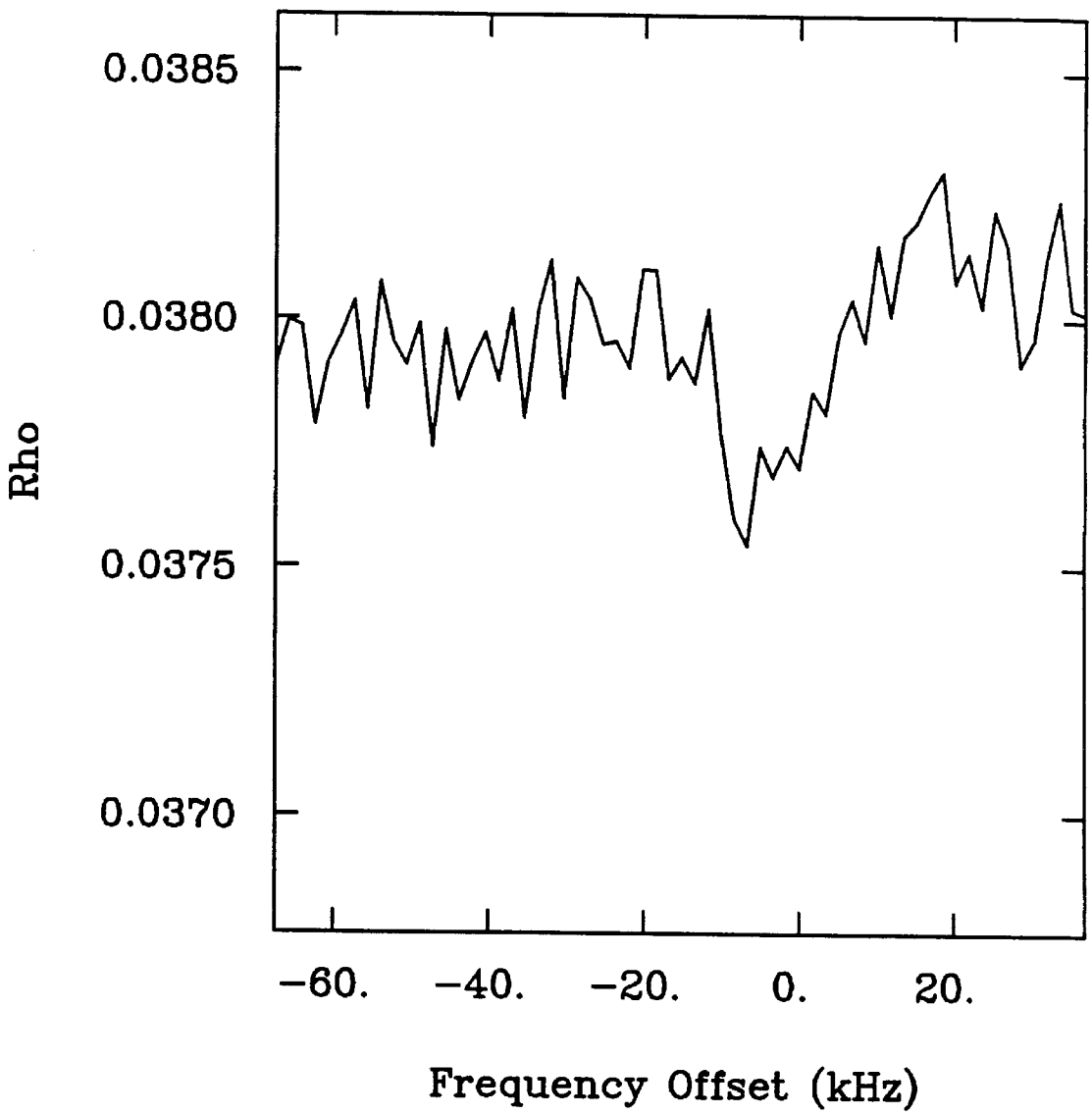

Figure 4.6: Quasi steady–state ODNMR (sample 4). The figure shows the ^{71}Ga resonance obtained in an external field B_0^p of 155 G. The rf ($B_1 \simeq 4$ G) was swept from high to low. The spectrum is the result of 100 averages, and the linewidth is $\simeq$ 18 kHz.

persists for a time of order $T_{1_{on}}$, the spin–lattice relaxation time in the exciting light. This time thus determines the period available for photon counting. In the present samples and fields the relaxation time was not significantly different in the dark. The role of $T_{1_{on}}$ in sensitivity and the ultimate use of field cycling as the detection period of a time–sequenced experiment will be developed in section 4.3.3.

4.3.1 Measuring B_n

The use of field cycling to detect the nuclear polarization was first described by Kalevich *et al.* although it was not used by those authors to map out NMR spectra. [14] In general, the experiment consists of first polarizing the nuclei in a longitudinal field parallel to the light direction **z** until steady–state is reached ($\simeq 3T_{1_{on}}$). The nuclear field is then adiabatically demagnetized and remagnetized along a transverse field $\mathbf{B_0^d} = B_0^d\mathbf{x}$ causing a Hanle effect in the total field $B_T = B_0^d + B_{n_x}$ along **x**, where B_{n_x} represents the nuclear field that survives the field cycling. The field cycling is illustrated graphically in Figure 4.7. A transient $\rho(t)$ is observed due to the relaxation of the nuclei in the exciting light which alters the Hanle effect.

There are several important points to note before deriving the equation for $\rho(t)$. The initial point $\rho(0)$ represents the Hanle effect due to the field $B_T = B_0^d + B_{n_x}(t=0)$. If $B_0^d >> B_L$ and the adiabatic field cycling is done fast enough to neglect spin–lattice relaxation of the nuclei, then $B_{n_x} = B_n$. In the original field cycling experiment [14], however, the applied field B_0^d was much smaller than the local field B_L. In this case nuclear field is lost to dipolar order and the Hanle effect (at $t = 0$) underestimates the largest attainable value of B_n. Charging the transverse magnet (Hanle coil) before fully discharging the longitudinal magnet (z–field coil) is also important. This keeps the magnitude of the applied field high

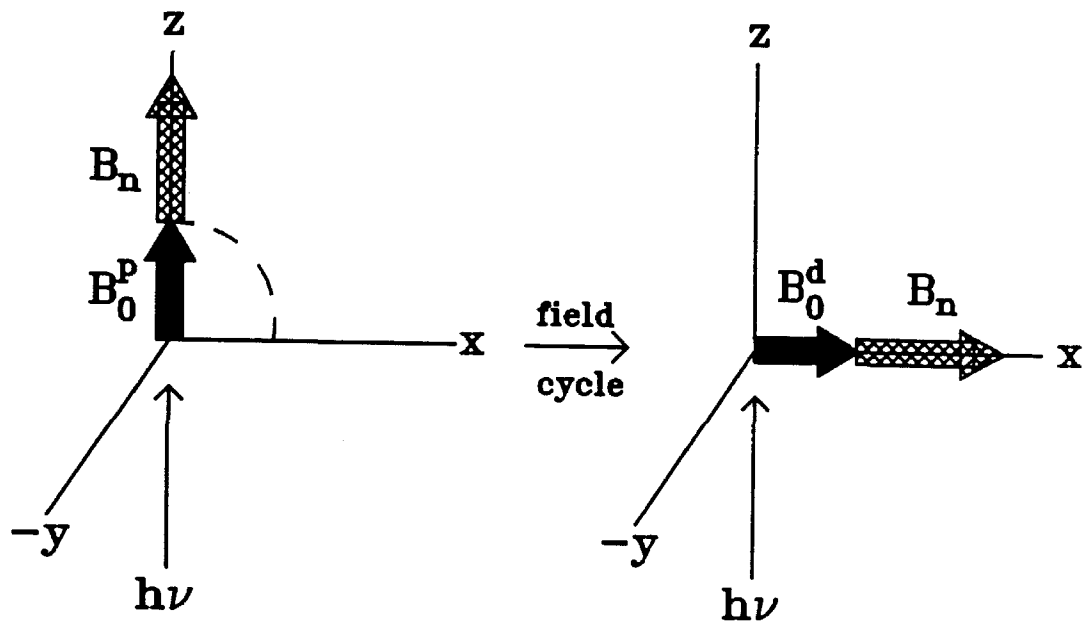

Figure 4.7: Vector picture of field cycling. The field cycling step is performed in the dark. The field B_0^d ($< B_0^p$) is ramped on as the the field B_0^p is ramped off, and the total field $B_0^p + B_0^d$ follows the dashed arc shown on the left. The total field cycling is performed in approximately 100 ms, and the nuclear field B_n becomes reoriented parallel (or antiparallel) to B_0^d. Once the field cycling is complete, the light is restored and the transient $\rho(t)$ is detected as B_n decays.

(the dashed line in Fig. 4.7) throughout the field cycling step and avoids nuclear relaxation through level crossing that can occur in low field. [15] The laser is shuttered during field cycling to insure no relaxation due to the light.

Since the Hanle effect reaches a quasi–steady–state (fixed B_n) on the time scale of T_1^e (~ 10 ns), Eq. 2.36 derived for fixed field is valid with $B = B_T(t)$, which is constant on this time scale. Once the field cycling is complete and the light is restored, the transient $\rho(t)$ is found by substituting $B_T(t)$ into Eq. 2.36

$$\rho(t) = C^2 \left[\frac{\tau_s(B_T(t))}{\tau + \tau_s(B_T(t))}\right]\left[\frac{\Delta B^2 + [B_n(t)]^2 \sin^2\varphi}{\Delta B^2 + [B_T(t)]^2}\right], \tag{4.1}$$

where $[B_n(t)]\sin\varphi$ is the z–component of $\mathbf{B_n}$ aligned along the field $(\mathbf{B_0^d} + \Gamma_t b_e \langle S\rangle) \equiv (\mathbf{B_0^d} + \mathbf{B_e})$ and

$$\sin\varphi = \frac{B_e}{[(B_0^d)^2 + B_e^2]^{1/2}}. \tag{4.2}$$

The time dependence of the total field $B_T(t)$ is due to the decay of the nuclear field in the light to a steady–state value B_n^d. Thus,

$$B_T(t) = B_0^d + B_n^d + (B_n - B_n^d)\exp(-t/T_{1_{on}}). \tag{4.3}$$

The transient of equation 4.1 is the product of two time–dependent functions f(t) and g(t) given by,

$$f(t) = C^2 \frac{\tau_s(B_T(t))}{\tau + \tau_s(B_T(t))}, \tag{4.4}$$

and

$$g(t) = \frac{\Delta B^2 + [B_n(t)]^2 \sin^2\varphi}{\Delta B^2 + [B_T(t)]^2}, \tag{4.5}$$

respectively. The function f(t) accounts for the effect of the field dependence of τ_s. Using the model of Dyakonov and Perel [16] given in section 2.3.1, f(t) is rewritten

$$f(t) = C^2 \frac{1 + (\frac{g\mu\beta}{\hbar})^2 \tau_c^2 [B_T(t)]^2}{1 + (\frac{g\mu\beta}{\hbar})^2 \tau_c^2 [B_T(t)]^2 + \frac{\tau}{\tau_s(B=0)}}. \tag{4.6}$$

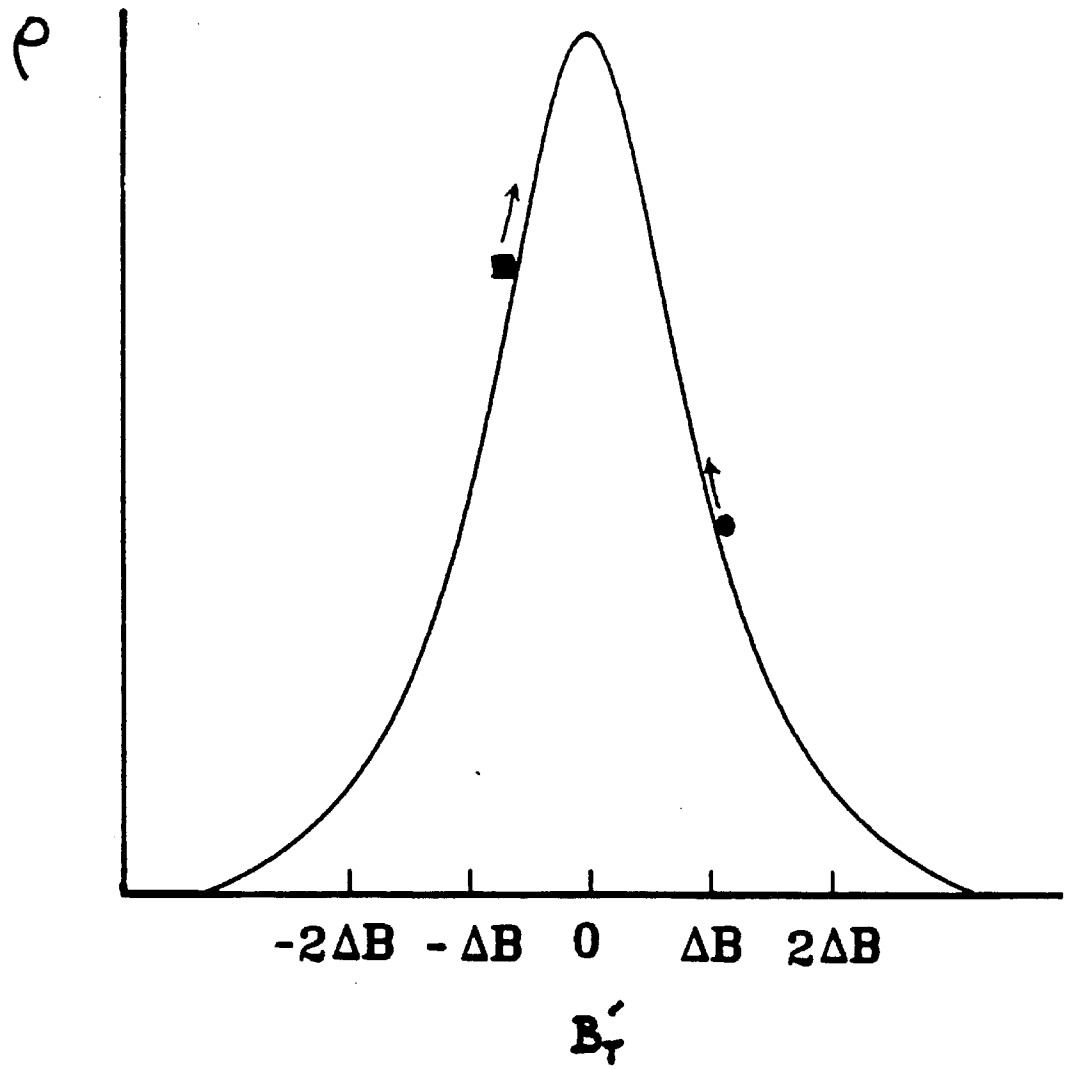

Figure 4.8: Simple description of the detection period transient. At t = 0, the Hanle effect is due to the field $B_T = B_0^d + B_n$ for parallel ONP, and is represented by the dot on the steady–state Hanle curve shown above. The antiparallel case is represented as the square. It is assumed initially that $|B_n| > |B_0^d|$. As the nuclear field decays, the system moves on the curve in the direction of the arrows. Both ρ and $d\rho/dB$ are diminished for the parallel case. For the antiparallel case, ρ reaches a maximum ($d\rho/dB = 0$) when the total field reaches zero. After this point $B_0^d > B_n$ and $d\rho/dB$ increases transiently as B_n decays.

A possible relaxation mechanism for localized electrons may be the hyperfine interaction, similar to nuclear relaxation through this interaction. [17] In this case the correlation time would be given by $\tau_c \simeq T_1^e$, and the quantity $(\hbar/g\mu_\beta T_1^e) \simeq \Delta B$. Thus, letting $A = (\tau/\tau_s(B=0))$ and simplifying, Eq. 4.6 becomes

$$f(t) = C^2 \frac{\Delta B^2 + [B_T(t)]^2}{(1+A)\Delta B^2 + [B_T(t)]^2}. \tag{4.7}$$

The transient $\rho(t) = f(t)g(t)$ is also simplified,

$$\rho(t) = C^2 \frac{\Delta B^2 + [B_n(t)]^2 \sin^2\varphi}{(1+A)\Delta B^2 + [B_T(t)]^2}. \tag{4.8}$$

Eq. 4.8 can be rewritten in a more familiar form

$$\rho(t) = \rho_0 \frac{\Delta B^2 + [B_n(t)]^2 \sin^2\varphi}{\Delta B^2 + [B_T'(t)]^2}, \tag{4.9}$$

where ρ_0 is the value of ρ in zero field given by $\rho_0 = C^2/(1 + A)$, and $B_T'(t) = B_T(t)/(1 + A)$.

Equation 4.9 is the equation of the Hanle effect in the field $B_T'(t)$. The effect of the function f(t) is to "spoil" the Hanle effect in the total field $B_T(t)$ by attenuating $B_T(t)$ by a factor of $(1 + A)$. A simple physical picture of the transient effect of Eq. 4.9 is that of the field $B_T'(t)$ traversing the steady–state Hanle curve depicted in Figure 4.8.

Figures 4.9 and 4.10 show detection period transients for sample 4 in the case of parallel and antiparallel polarization, respectively. Each experiment was fitted to Eq. 4.9. So far no distinction has been made between parallel and antiparallel ONP, but as is indicated in Figs. 4.9 and 4.10 the two cases are very different. In the parallel case the transient is monotonically increasing as expected from Fig. 4.8. The fit in this case is quite good yielding the parameters given in the figure caption and $B_n \simeq 100$ G. The antiparallel case, however, shows a sharp maximum near 1.0 ms followed by a decay to the same steady–state value seen in the parallel case. The

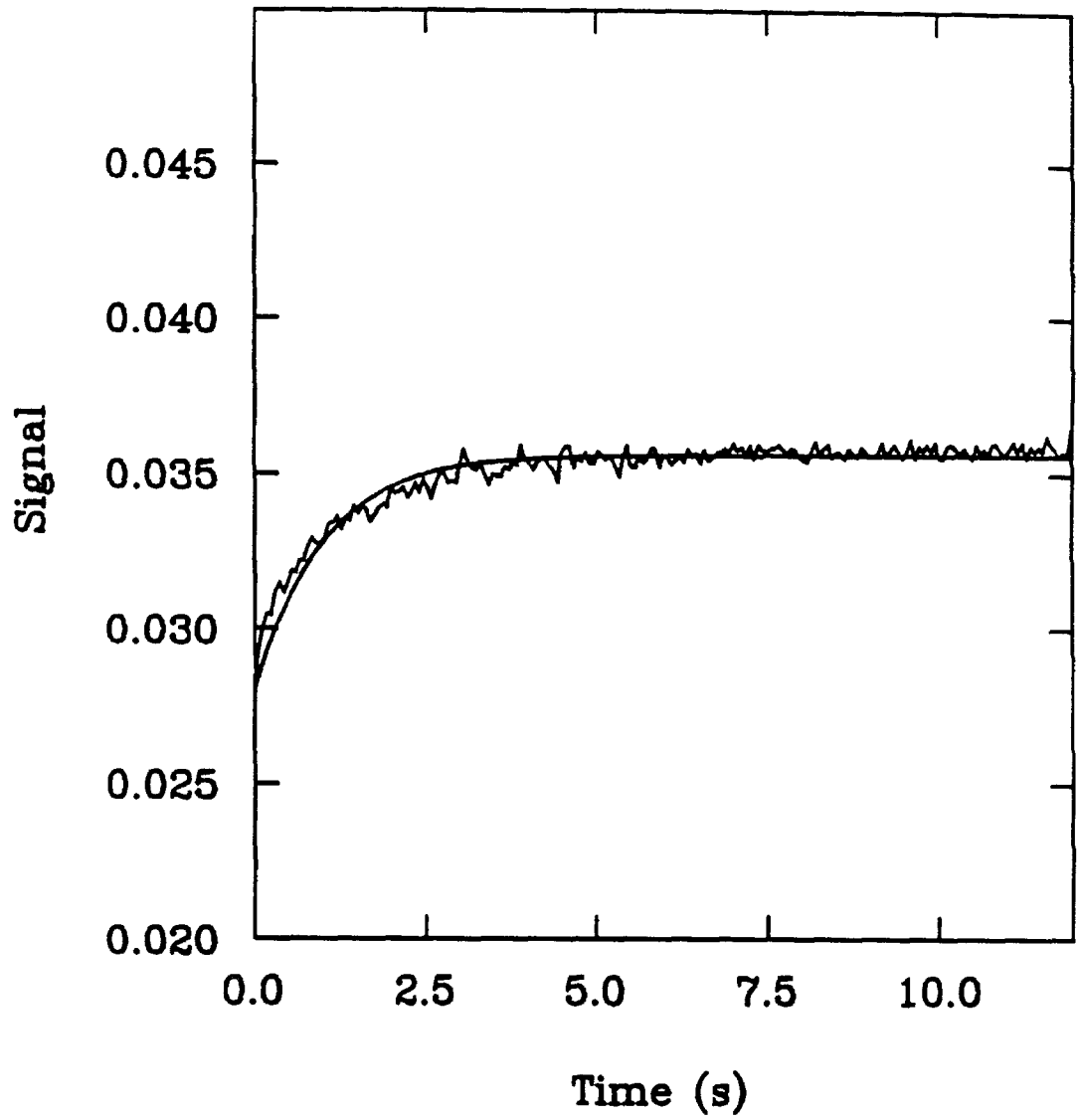

Figure 4.9: Detection period transient; parallel ONP. This data is from sample 4. The nuclei were first polarized for 10 s in a field $B_0^p = 155$ G with right–hand circularly–polarized light. This field is then cycled to a field $B_0^d = 30$ G and the transient is recorded. The fit to the data is obtained using Eq. 4.9 giving the parameters $\Delta B = 63$ G, $B_n = 120$ G, $B_n^d = 35$ G, and $T_{1_{on}} = 0.9$ s.

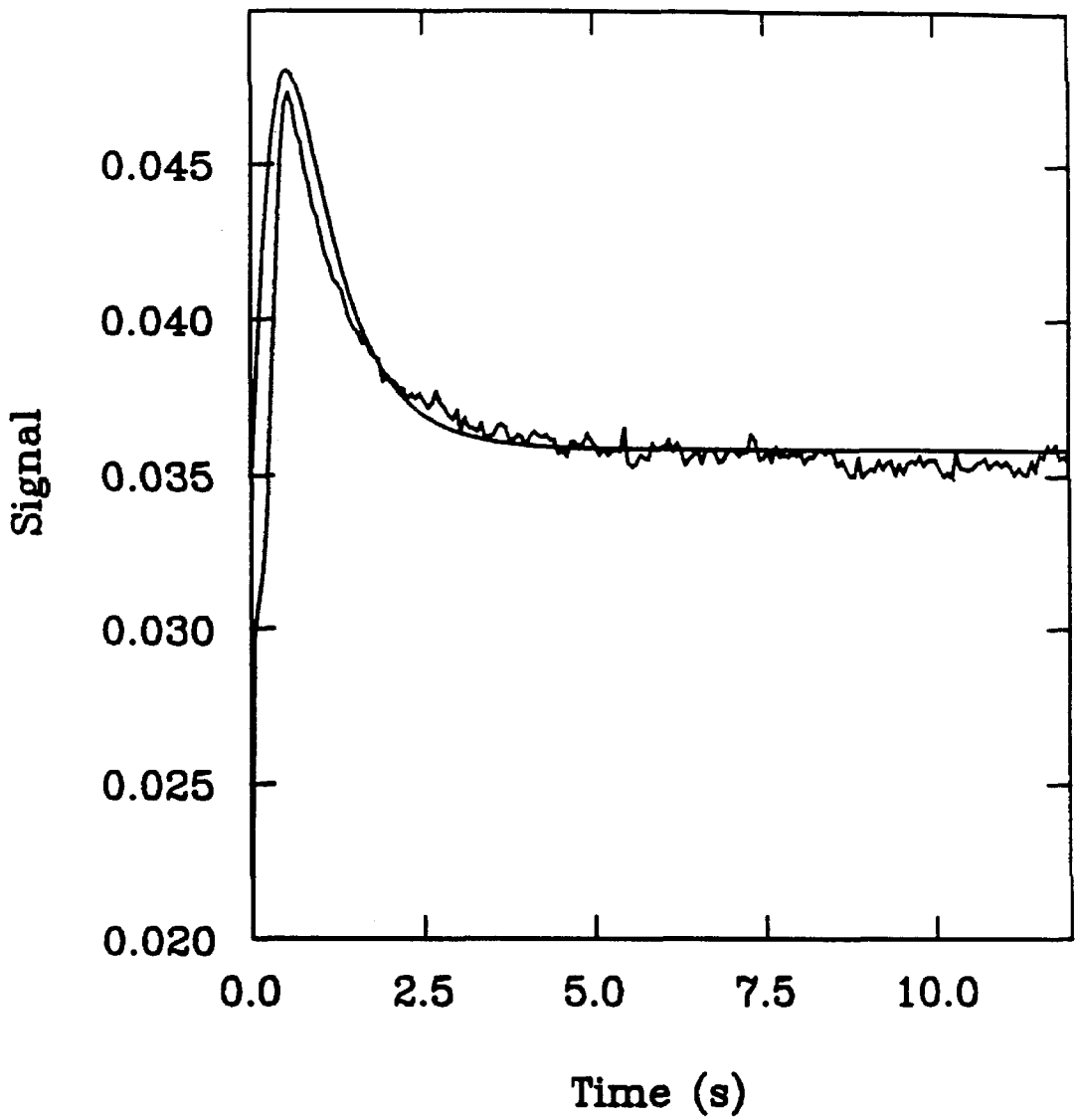

Figure 4.10: Detection period transient; antiparallel ONP. The conditions were the same for this experiment as for the experiment of Fig. 4.9 except $B_0^p = -155$ G for antiparallel polarization. The same paramteters given in Fig. 4.9 were used to fit this data.

maximum can be explained by considering the initial orientations of the applied and nuclear fields after field cycling. At point t = 0, B_n opposes B_0^d, having retained its negative spin temperature (obtained by ONP) during the adiabatic process. [18] If $B_n > B_0^d$ then there exists a point in the transient where B_n and B_0^d cancel each other and $B_T^{'} = 0$ yielding a maximum in $\rho(t) = \rho_0$. The fit for the antiparallel case is not as good as for the parallel case as seen in Fig. 4.10. The maximum in the observed transient does not reach $\rho_0 \simeq 0.048$ as expected from theory, and the early time points do not rise as fast as expected. One possible explanation of this is that the proposed theory for the field dependence of τ_s is not valid for points near $B_T^{'} = 0$. If electron spin relaxation is more efficient near zero field than the above theory suggests, then the rise and fall near $B_T^{'} = 0$ occur at lower values of ρ. Evidence for this hypothesis is seen in Figure 4.1 where there is a sharp minimum in ρ near zero field which is not predicted by the proposed theory.

4.3.2 Field Dependence of the Transient Signal

We have measured the transient signal for different periods of ONP time. A plot of the initial points of each transient versus ONP time is shown in Figure 4.11. The single exponential fit to the data in Fig.4.11 gives a value of 0.8 s for $T_{1_{on}}$ in the 155 G ONP field (B_0^p).

Figures 4.12 and 4.13 show detection period transients versus the applied field B_0^d for parallel and antiparallel ONP, respectively. The asymptotic points of both Figs 4.12 and 4.13 reproduce the Hanle curve shown in Figure 4.3 as expected. In both Fig. 4.12 and 4.13, a big change in the initial point from one transient to the next is seen for the first 20 G. Below $B_0^d = 20$ G, the nuclear field B_{n_x} that survives field cycling is less than B_n, and a steep dependence in the initial point of different transients is seen with increasing B_0^d as B_{n_x} approaches B_n. Once B_0^d becomes

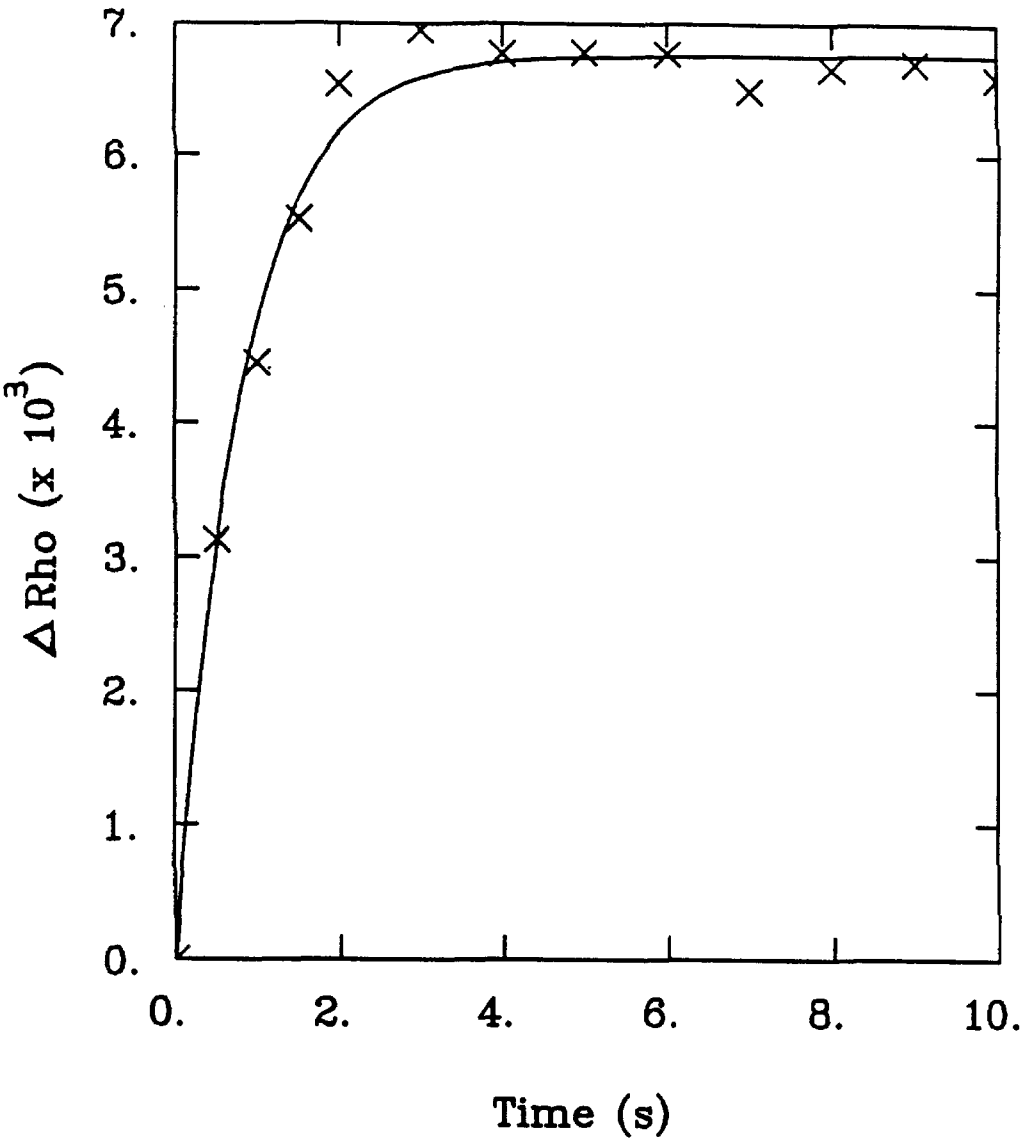

Figure 4.11: Measuring $T_{1_{on}}$. This data is from sample 4. The nuclei were polarized for a time t_{on} in a field $B_0^p = 150$ G. This field was cycled to $B_0^d = 30$ G and the transient was recorded. The difference in the initial detection period point (from zero ONP time) versus the ONP time t_{on} is given in the figure. The data was fitted to a single exponential yielding $T_{1_{on}} = 0.8$ s.

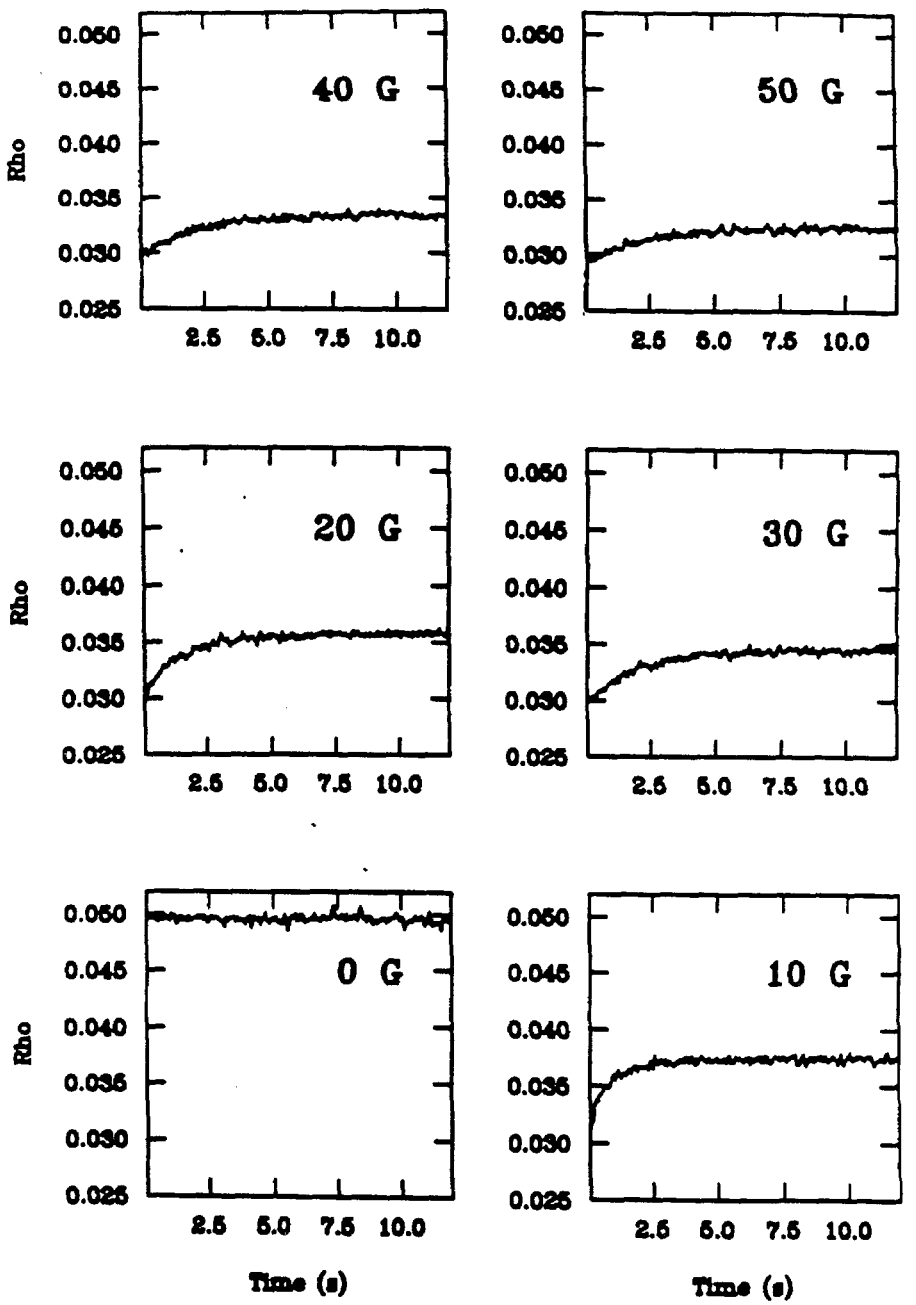

Figure 4.12: Detection period transients versus B_0^d; (parallel ONP). This data is from sample 4. The conditions of ONP are given in the caption of Fig. 4.9. The field B_0^d is inset in each spectrum. A noticeable increase in $T_{1_{on}}$ is seen with increasing B_0^d. The decrease in the initial point with increasing B_0^d saturates after 20 G which is unexplained by theory. A possible explanation for this behavior is given in the text.

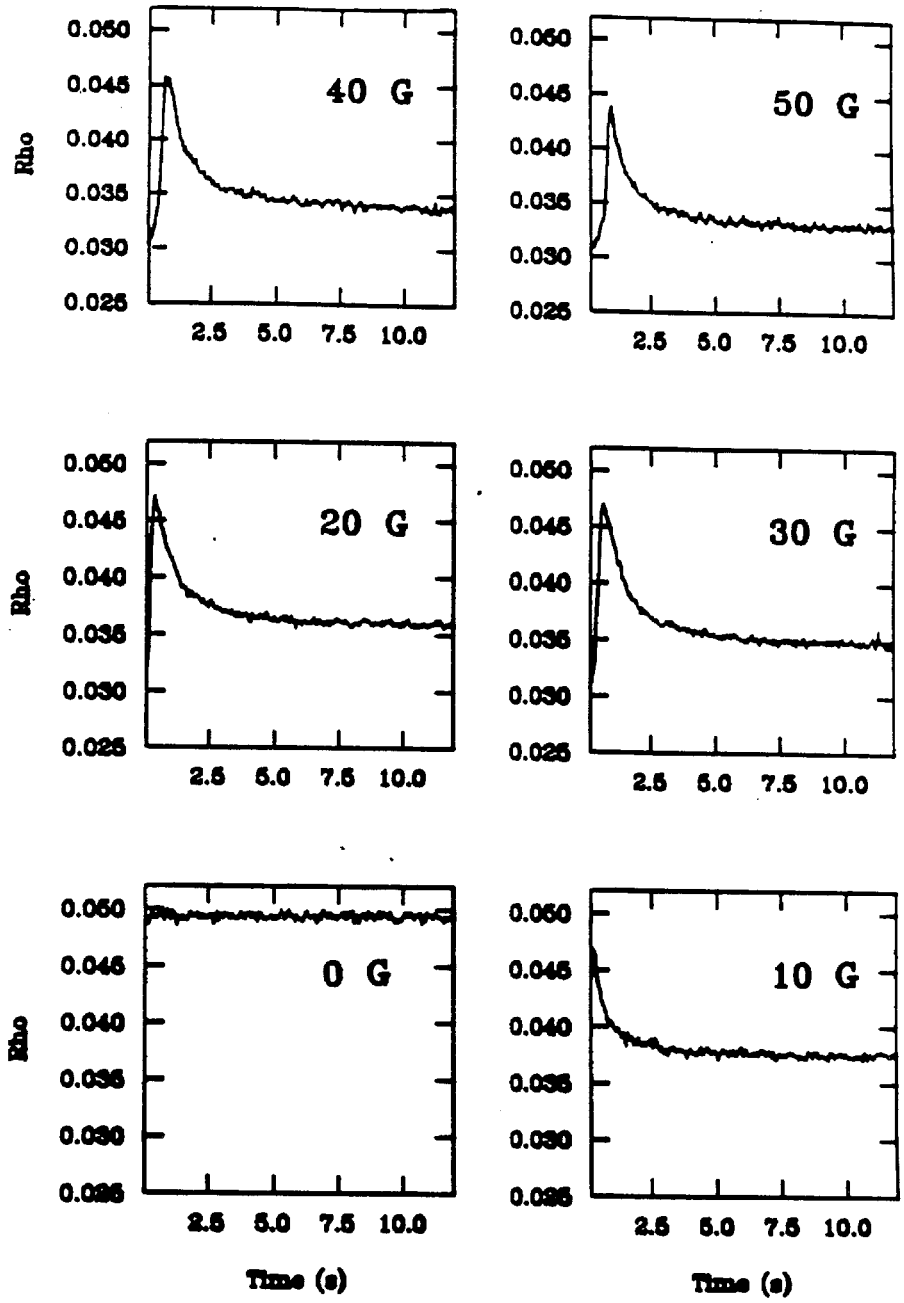

Figure 4.13: Detection period transient versus B_0^d; (antiparallel ONP). This data is from sample 4. The conditions for ONP are given in the caption of Fig. 4.10. As seen in the data of Fig. 4.12, $T_{1_{on}}$ increases with B_0^d, and the value of $\rho(t=0)$ saturates at 20 G. In addition to these observations, the maximum decreases and occurs later as B_0^d increases. A possible explanation for this behavior is given in the text.

greater than 20 G, the change in the initial point with B_0^d is less dramatic. For field values below 30 G, the parameters obtained in the fits of Figs. 4.9 and 4.10 can be used to fit the observed transients with a decrease in B_n^d and increase in $T_{1_{on}}$.

The results of Figs. 4.12 and 4.13 for applied field $B_0^d > 30$ G cannot be explained by the parameters obtained from Figs. 4.9 and 4.10. even allowing for the increase in $T_{1_{on}}$ with increasing B_0^d. In the case of parallel ONP the initial point occurs at a value of ρ higher than predicted by theory. In the case of antiparallel ONP the points near the maximum ρ are unexplained by theory. The value of the maximum decreases with increasing B_0^d, and the maximum is reached at a greater time than expected. One possible explanation for these deviations from theory is that two Hanle curves are responsible for the observed transients. In low field a narrow Hanle curve dictates the observed transient, but as B_0^d increases the transient behavior becomes dominated by a wide Hanle curve.

4.3.3 Field Cycling and Time–Sequenced Experiments

Whereas the focus of the previous subsection was the physics of the transient subsequent to field cycling, the focus of this subsection will be the incorporation of the field cycling transient into the detection period of a time–sequenced experiment. Figure 4.14 shows the detection scheme for using field cycling in a time–sequenced experiment. In general, a time–sequenced experiment can be viewed analogously to two–dimensional NMR as three separate periods: preparation, evolution, and detection. The nuclear spin system is first prepared by ONP establishing a steady–state B_n. The nuclear field then evolves under certain conditions (for example, during a delay time or under rf irradiation) which reduces it. Finally, the remaining B_n is measured after field cycling by a detection period transient. The timing sequence for TSONMR has already been shown (Fig. 2.5) and is obtained

(A)

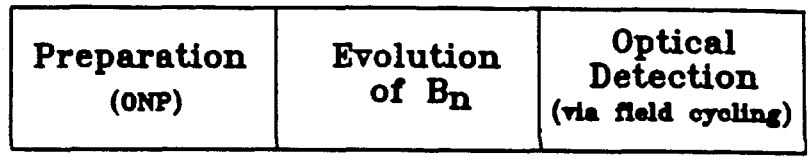

(B)

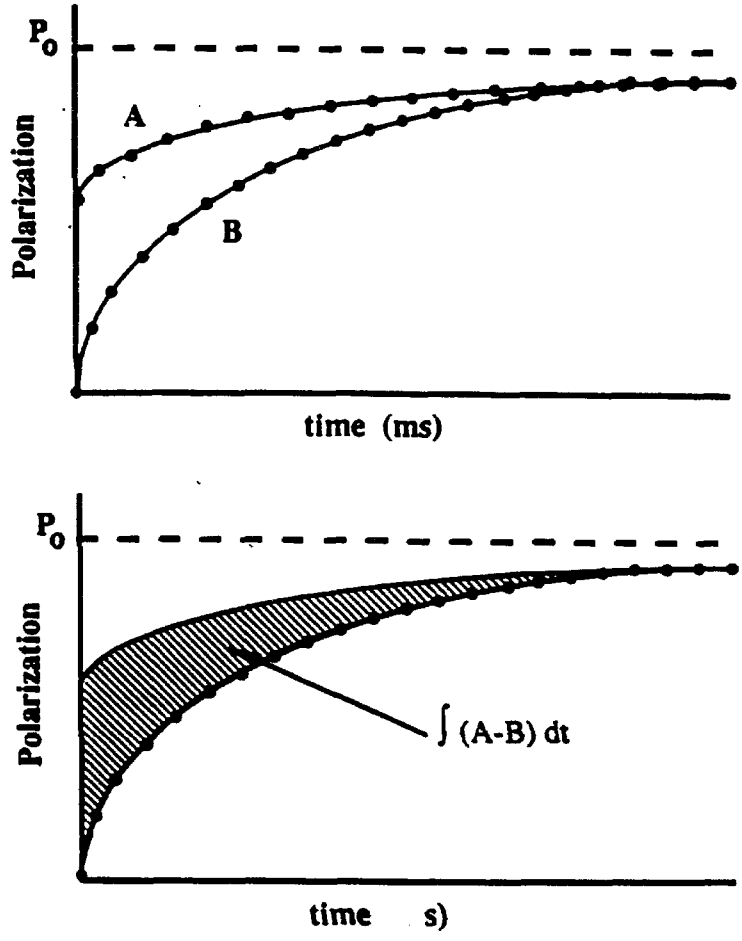

Figure 4.14: The general scheme for a time–sequenced experiment part (A), and field cycling detection part (B). The general scheme shown in (A) is analogous to 2D–NMR. The process of obtaining a data point by field cycling detection is shown in (B). Each data point is obtained from the difference in area between the detected transient A and the "null" experiment B as shown. The "null" experiment is acquired initially by omitting the evolution period.

from the general diagram by making evolution of B_n the result of rf irradiation. The time–sequenced experiment is performed point–by–point. The first point (point 0) is obtained by doing nothing in the evolution part of the experiment. The detected transient in this case serves as the "null" experiment for the remaining points. The timing steps are then repeated for each point (this time including the evolution) and the detected transient in each case is compared to the "null" transient. The signal for each point is the difference in the areas of the transients as shown in Fig. 4.14.

Our first time–sequenced experiments measured the spin lattice relaxation times of the entire nuclear spin system. Figure 4.15 shows a time–sequenced experiment designed to measure the nuclear spin–lattice relaxation time in the dark $T_{1_{off}}$. The nuclei relax in the dark during the delay time t_1, and the subsequent reduction in B_n is seen as a difference in the areas between the transients of each point and the "null" transient. Since it is assumed (at 150 G) that each nuclear spin reservoir is isolated from the other, the nuclear relaxation should be the sum of at least three exponentials (one for each of the major isotopes ^{69}Ga, ^{71}Ga, ^{75}As). The data, however, fits well to a single exponential indicating that either all of the spins have the similar $T_{1_{off}}$'s or they are acting collectively even at 150 G. A more thorough investigation of relaxation times is discussed in chapter 5.

Figure 4.16 shows a time–sequenced experiment designed to measure the spin–lattice relaxation time in zero field T_{1d}. In this experiment the applied field B_0^p is ramped adiabatically to zero after ONP, and the nuclear spin system is allowed to evolve for time t_1. The nuclei are then remagnetized along the field B_0^d for detection. The data is again given as the difference in area versus t_1. Since the entropy of the nuclear spin system is conserved during adiabatic demagnetization, the nuclear order resulting from ONP is transferred to the dipolar reservoir and is characterized by spin temperature θ. The thermalization of the dipolar order is measured by this experiment.

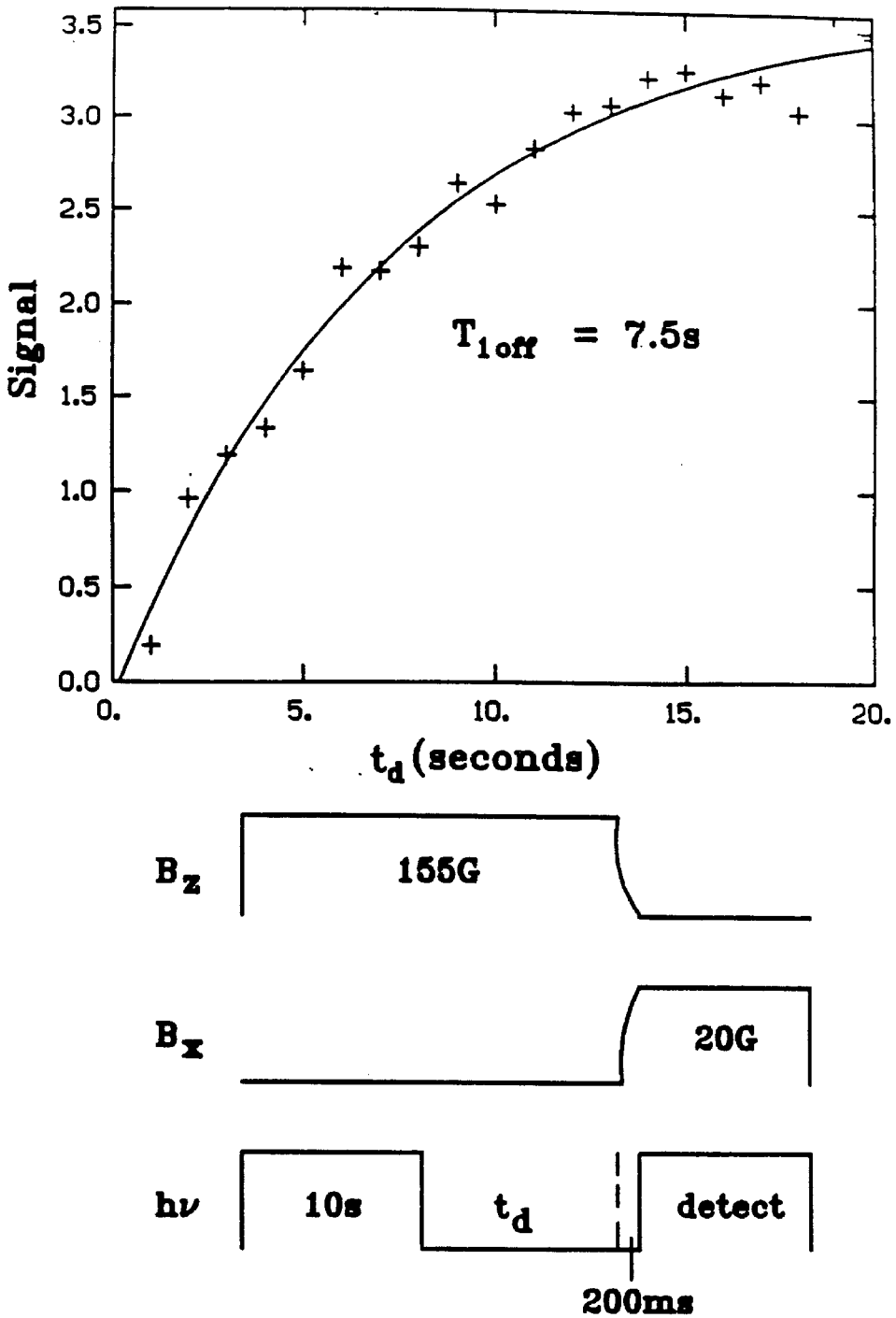

Figure 4.15: Spin–lattice relaxation. This data is from sample 4. The time–sequencing is shown in the lower half of the figure. The data fits well to a single exponanetial indicating that all of the nuclei have similar relaxation times.

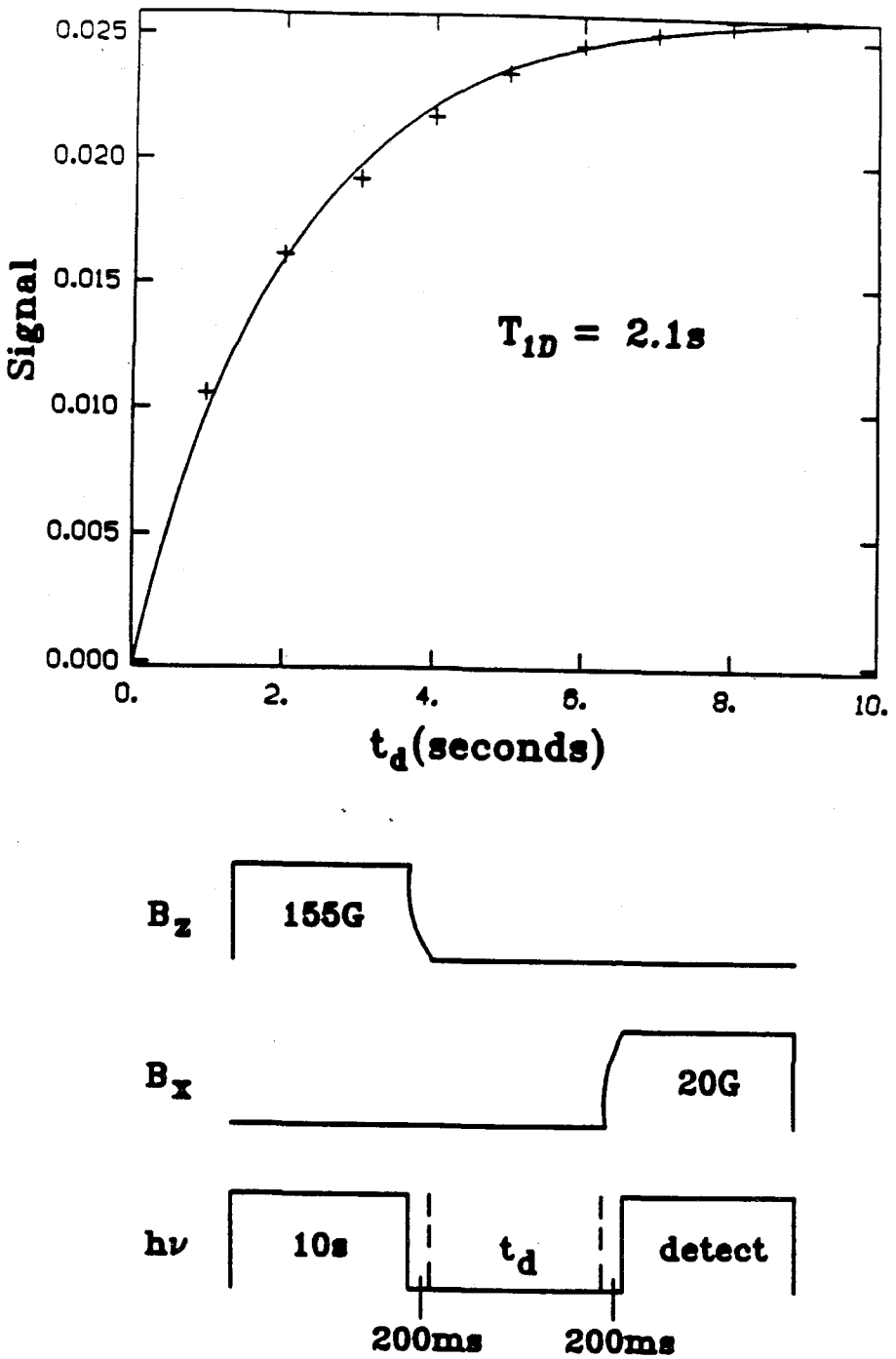

Figure 4.16: Spin–lattice relaxation in zero field. This data is from sample 4. The time–sequencing is shown in the lower half of the figure. The single exponential fit gives a value of T_{1d} = 2.1 s which is approximately 1/4 of T_1 in 155 G.

4.4 TSONMR Revisited

Now that both the theoretical and experimental foundations for TSONMR have been established, a more thorough discussion of the technique is possible. The application of the general time–sequenced experiment to TSONMR is straightforward. The timing–sequence includes (see Fig. 2.5): (i) ONP in a field B_0^p for a time $\simeq 3T_{1_{on}}$, (ii) NMR by continuous irradiation at frequency ω or a sequence of rf pulses in a field B_0^n possibly different from B_0^p, and (iii) field cycling detection for a period of $\simeq 3T_{1_{on}}$. The vector picture of TSONMR is shown in Figure 2.6, and an example of TSONMR is shown in Figure 2.8.

The signal–to–noise ratio of TSONMR will be derived in this section and shown to depend on the measurable material parameters ΔB, B_n, A, $T_{1_{on}}$, and the photon counting rate $\mathcal{N}$. The process of optimizing each period in the TSONMR experiment will also be described. This optimization includes choosing the optimum B_0^d as well as the optimum rf power and irradiation time for a continuous wave (CW) TSONMR experiment.

4.4.1 TSONMR Signal–to–Noise

Previously, the signal obtained from a time–sequenced experiment was introduced as the difference in area between the detected transient $\rho(t_d)$ and the "null" experiment $\rho_{null}(t_d)$, where t_d signifies the detection time. Letting $\mathcal{N}$ be the photon counting rate this signal S is given by

$$S = \mathcal{N}\int_0^\infty [\rho(t_d) - \rho_{null}(t_d)]dt_d \qquad (4.10)$$

Eq. 4.10, however, is not an optimum choice of signal because equal weighting is given to the integrand for all values of t_d. It is easily seen from Eq. 4.9 that the

largest signal $[\rho(t_d) - \rho_{null}(t_d)]$ for a change δB_n in the nuclear field occurs at $t_d = 0$. For subsequent points $[\rho(t_d) - \rho_{null}(t_d)]$ decays with t_d. A more useful definition of the signal includes a weighting function $W(t_d) = \exp(-t_d/T_{1_{on}})$ in the integrand of Eq. 4.10.

The TSONMR signal for rf irradiation at frequency ω can be defined as

$$S(\omega) = \mathcal{N}\int_0^\infty [\rho(\omega,t_d) - \rho_{null}(t_d)]W(t_d)dt_d. \qquad (4.11)$$

The difference in the integrand will be optimized when the magnitude of B_0^d and the relative sign of $B_n(\omega)$ have been chosen to maximize the slope $d\rho/dB_n$. The slope $d\rho/dB_n$ is found by differentiating Eq. 4.9 with respect to B_n. Performing the differentiation using the chain rule,

$$\frac{d\rho}{dB_n} = -2\,\rho_0 \frac{\Delta B^2 B_T'}{[\Delta B^2 + (B_T')^2]^2}\,\frac{1}{1+A}. \qquad (4.12)$$

Figure 4.17 shows plots of $d\rho/dB_n$ versus B_T' for various Hanle widths ΔB. The maximum of Eq. 4.12 occurs at the value $B_T' \simeq \Delta B/\sqrt{3}$. For $B_n >> \Delta B$, maintaining this condition will require that the detection field follow the decay of the nuclear field, i.e. $B_0^d = B_0^d(t_d = 0)\exp(-t_d/T_{1_{on}})$. With this substitution and the definition $d(\omega) \equiv \delta B_n(\omega)/B_n$ as the fractional destruction of the nuclear hyperfine field by the resonant irradiation, Eqs. 2.51 and 2.52 lead to

$$S_{max}(\omega) = -(\frac{3\sqrt{3}}{8})\,\mathcal{N}\rho_0\,(\frac{1}{1+A})\,(\frac{d(\omega)B_n}{\Delta B})T_{1_{on}}, \qquad (4.13)$$

Under conditions of quantum–limited noise due to photon statistics (see chapter 3), the uncertainty in this value (per root repetition) is equal to the square root of the effective number of photons, $N_{eff} \equiv \mathcal{N}\int_0^\infty W(t_d)dt_d \cong \mathcal{N}T_{1_{on}}$. The signal–to–noise ratio S/N is then

$$S/N = \frac{S_{max}(\omega)}{\sqrt{N_{eff}}} = -(\frac{3\sqrt{3}}{8})\,\rho_0\,(\frac{1}{1+A})\,(\frac{d(\omega)B_n}{\Delta B})\,\sqrt{\mathcal{N}T_{1_{on}}}. \qquad (4.14)$$

The data of Figure 4.18 illustrate the optimization of B_0^d. Fig. 4.18 shows a stack plot of a series of ^{71}Ga CW–TSONMR experiments of sample 4 for different

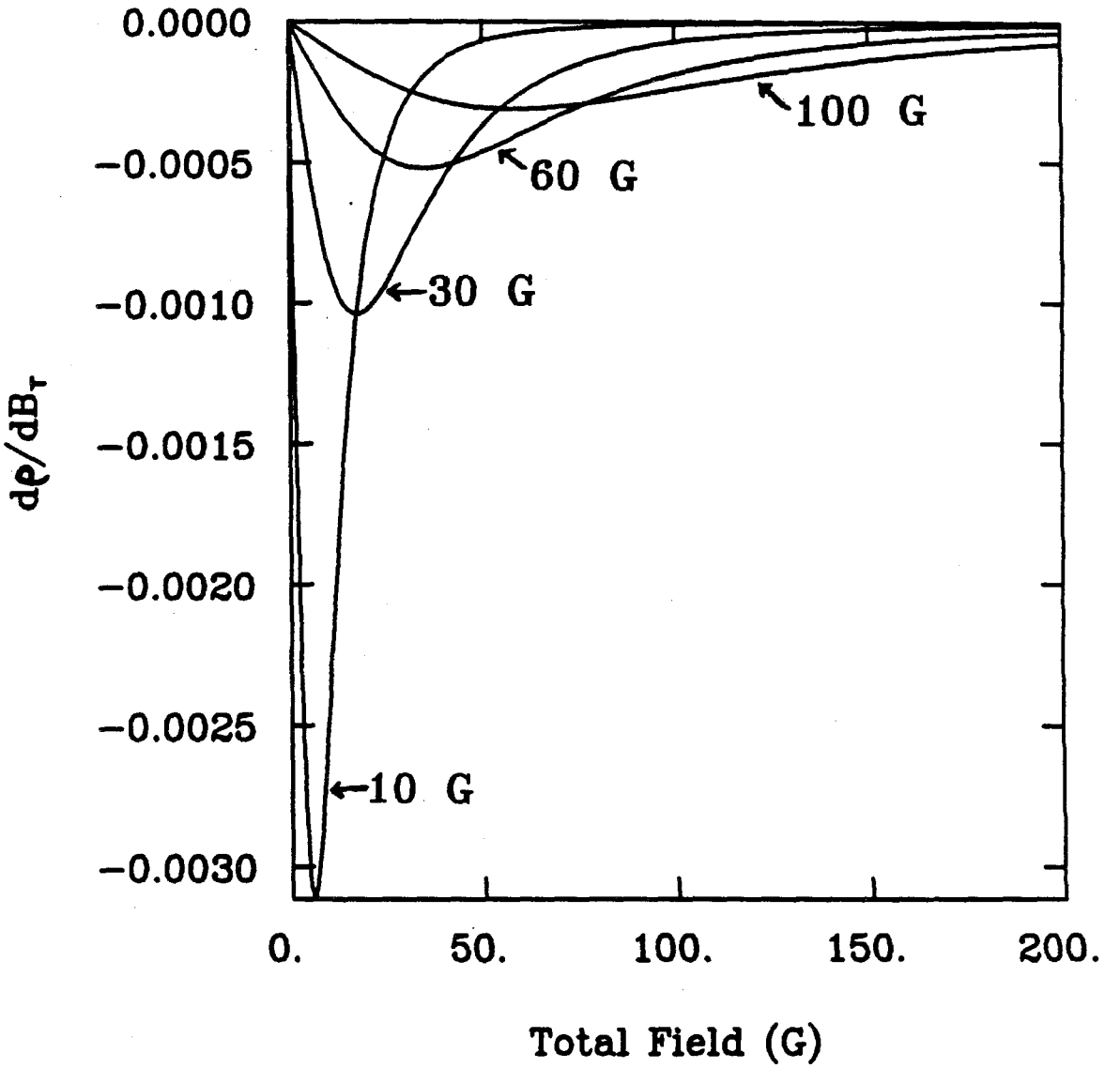

Figure 4.17: Hanle curve slope versus total field. The simulations assume $\rho_0 = C^2$. The sensitivity $d\rho/dB_T$ increases with decreasing Hanle width as expected. The curve relevant to our experiments is $\Delta B = 60$ G.

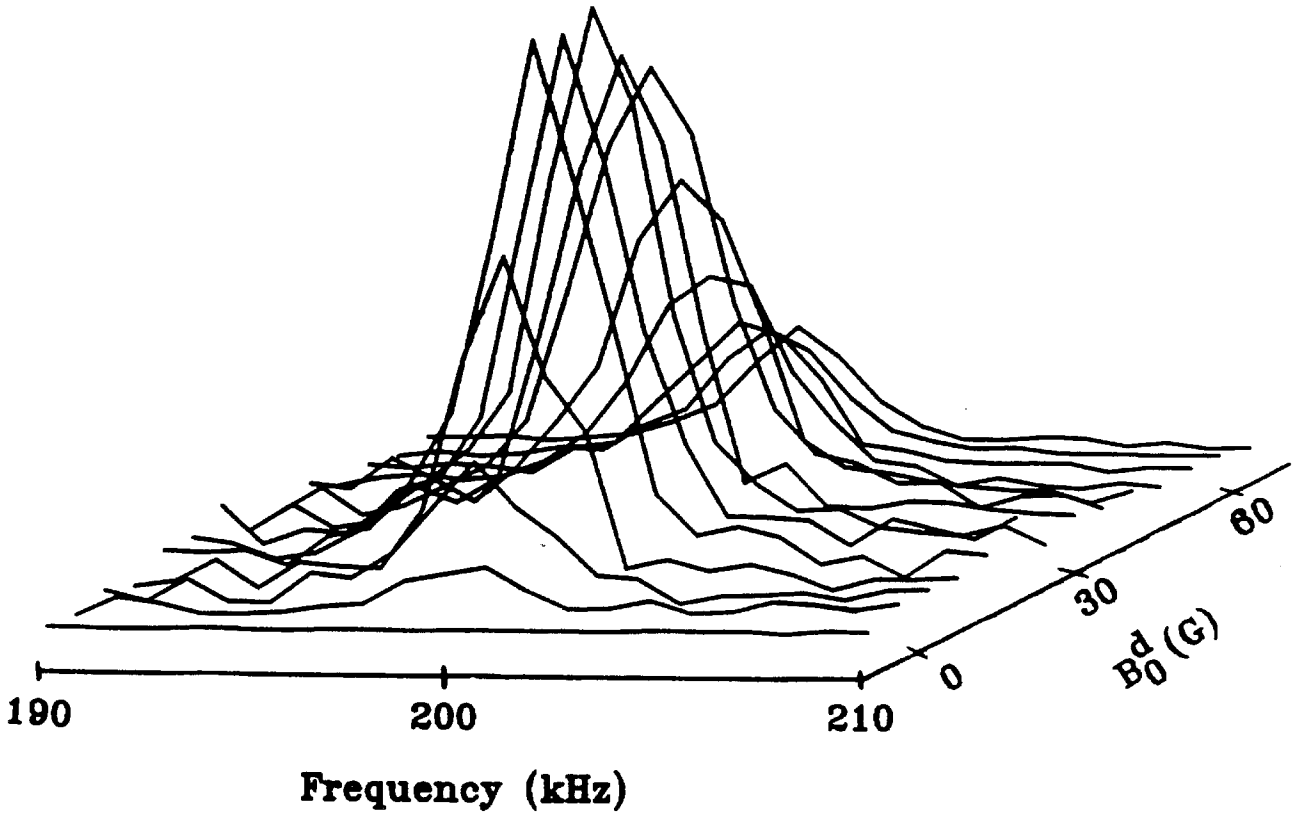

Figure 4.18: ^{71}Ga cw–TSONMR signal versus B_0^d. This data is from sample 4. Each spectrum was taken with antiparallel ONP in $B_0^p = -155$ G. The rf field of 0.01 G was applied for 100 ms for each point. The rf frequency was incremented 0.5 kHz/pt and each spectrum is an accumulation of 10 averages. The maximum signal is obtained for $B_0^d = 30$ G.

B_0^d. Each experiment was performed in the antiparallel geometry. The maximum signal occurs for $B_0^d = 30$ G. Using $B_n = 100$ G and A = 4 yields $B_T' \simeq 20$ G which is a factor of 0.6 of the theoretical prediction. For the case of parallel ONP the maximum signal occurred at $B_T' \simeq 35$ G which is approximately $1/\sqrt{3}\ \Delta B$, but the experimental sensitivity here was a factor of three smaller than obtained for the antiparallel geometry. This is because the time–dependent detection field assumed in the derivation of Eq. 4.14 was not implemented. Under this condition, the antiparallel geometry in which both flanks of the Lorentzian Hanle curve are traversed during t_d is preferable to the parallel geometry where only one flank is traversed.

The material parameters appearing in our sensitivity analysis for the time–sequenced experiment have been measured for samples used in quasi steady–state ODNMR experiments, [8,16,19,20] allowing the potential signal–to–noise for other systems to be estimated. The most striking observation in this regard is that in samples for which the less sensitive quasi steady–state ODNMR experiments have been demonstrated [6–8,10] nuclear fields up to several tesla have been cited. Thus the time–sequenced experiments succeeded with two to three orders of magnitude smaller nuclear field. This small value is not unexpected, as a decrease in nuclear field with acceptor concentration in p–type GaAs is well–known. [6,8,12] Evaluating Eq. 4.14 with literature values for both donor–compensated p–type and quantum well samples indicates that optimum TSONMR experiments on these samples would be approximately four orders of magnitude more sensitive then on the present samples.

In the present experiments the detection of ρ is not shot–noise limited, but is dominated by thermal noise in the detector (see section 3.9). At higher photon fluxes or with better detectors, this limit can be reached. Our early results with photon counting at reduced photon fluxes illustrates this limit. [21]

4.4.2 The ω_1 Dependence of CW–TSONMR

Figure 4.19 shows the CW–TSONMR spectrum of sample 4 using an rf field of 0.8 G. The spectrum not only shows resonances for all three major isotopes, but also shows several overtone resonances. The probability of these transitions arises from the dipolar Hamiltonian $\mathscr{H}_D$ [22]

$$H_D = \frac{\gamma_1 \gamma_2 h}{r^3} (A + B + C + D + E + F) \qquad (4.15)$$

where r is the internuclear distance. The terms of the dipolar alphabet A, B, C, D, E, and F expressed in spherical coordinates are:

$$A = I_{1z} I_{2z} (1 - 3\cos^2\theta)$$
$$B = -\frac{1}{4} (I_{1+} I_{2-} + I_{1-} I_{2+}) (1 - 3\cos^2\theta)$$
$$C = -\frac{3}{2} (I_{1+} I_{2z} + I_{1z} I_{2+}) \sin\theta \cos\theta \, e^{-i\varphi}$$
$$D = -\frac{3}{2} (I_{1-} I_{2z} + I_{1z} I_{2-}) \sin\theta \cos\theta \, e^{i\varphi}$$
$$E = -\frac{3}{4} I_{1+} I_{2+} \sin^2\theta \, e^{-i2\varphi}$$
$$F = -\frac{3}{4} I_{1-} I_{2-} \sin^2\theta \, e^{i2\varphi}.$$

The terms E and F give rise to intensity at the overtone transition (both spins flipping up or down). The probability of this transition calculated by considering H_D as a perturbation of H_Z goes as $(\omega_1^2 B_L/B_0)$ where B_0 is the applied static field. In our static field of 155 G the ratio $B_L/B_0 \simeq 1/50$, and the rf power of 0.8 G is sufficiently high to produce a detectable change in B_n at the overtone frequencies shown in Fig. 4.19.

The spectrum of Fig. 4.19 is a testament to the sensitivity of the TSONMR technique since the overtone transitions were not detected in the quasi steady–state experiment shown in Fig. 4.6 performed at the same rf field strength. If the rf field strength is lowered well below B_L, the expected linear–response spectrum is as

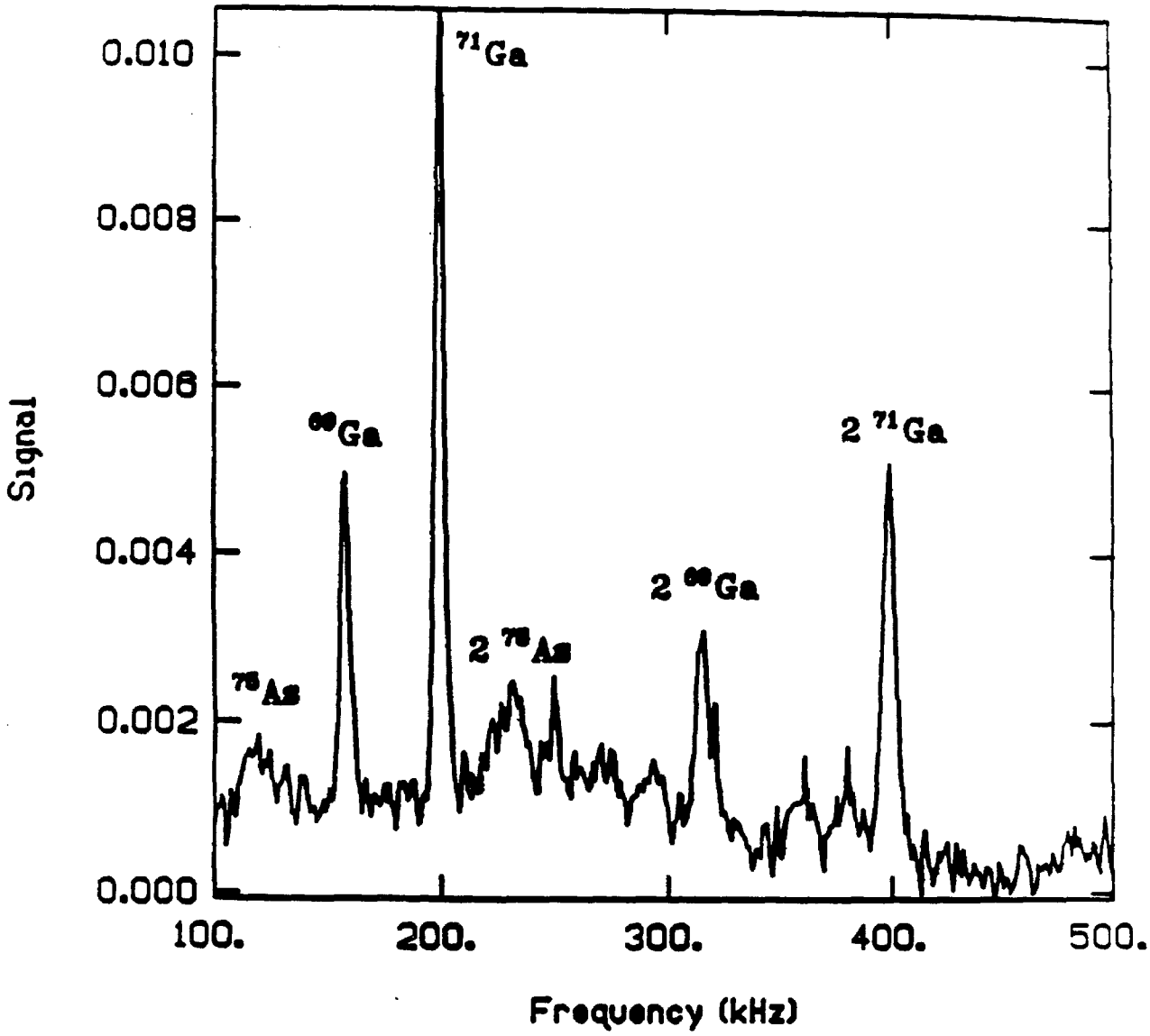

Figure 4.19: Nonlinear TSONMR spectroscopy. This data is from sample 4. The magnetic fields were: $B_0^d = -155$ G, $B_1 = 0.8$ G, and $B_0^d = 30$ G. The rf was applied for 100 ms and was incremented 3.0 kHz/pt. A total of 10 repetitions were averaged. The peak assignments are shown in the figure. Intensity at the two–spin transitions is due to a combination of the small applied field B_0^p, the large rf field B_1, and the high sensitivity of TSONMR.

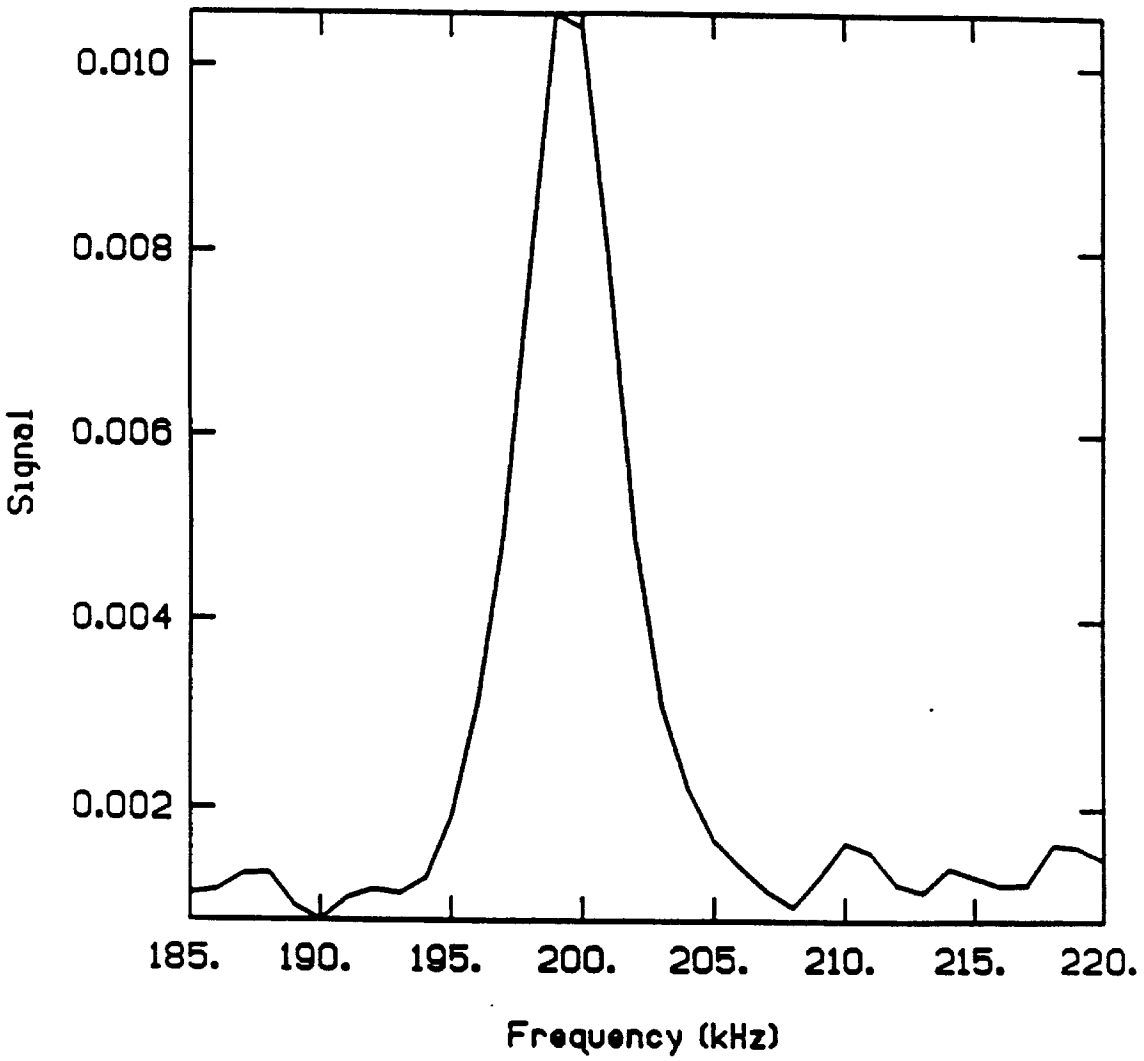

Figure 4.20: ^{71}**Ga CW–TSONMR.** The data is from sample 4. The magnetic fields used were: $B_0^p = -155$ G, $B_1 = 0.01$ G, and $B_0^d = 30$ G. The rf was applied for 100 ms and was incremented 1.0 kHz/pt. A total of 10 repetitions were averaged. The observed linewidth ($\simeq$ 3 kHz) is that expected from spin–spin couplings. [22,23] No two–spin transitions were observed at this rf field strength.

shown for the ^{71}Ga resonance of sample 4 in Figure 4.20. The linewidth obtained in this spectrum as that expected from spin–spin couplings alone [23,24] (see also Fig. 2.10), indicating that the CW–TSONMR signal is dominated by spins with the symmetry of the bulk crystal lattice. A more detailed discussion concerning the detected nuclear sites is given in chapter 5.

In the CW–TSONMR experiment the rf is applied as a long low–power pulse (100 ms) at frequancy ω. As was noted in subsection 2.4.2, small rf perturbations can still produce nonlinear effects (partial saturation) if applied for a time sufficient for the spin system to reach equilibrium in the rotating frame. [18] In order to insure that our experiments were done under conditions of linear response we performed a series of ^{71}Ga CW–TSONMR experiments with different rf irradiation times. Figure 4.21 shows the results of these experiments. At the rf field strength used for CW–TSONMR and a 100 ms rf pulse, the spin system is still in the linear response regime.

4.5 Conclusions

In this chapter the experimental foundations for TSONMR have been described. Nuclear field effects on the steady–state curves $\rho(B_0^p)$ and $\rho(B_0^d)$ are seen, and these simple experiments are used as a gauge for the nuclear fields of different samples.

Of the samples tested, the moderately–doped ($10^{16} - 10^{17}/cm^3$) p–type samples showed the strongest nuclear effects. An important point to note concerning these samples is that there was no intentional compensation with donors (the ORD's). The donor concentration is estimated to be quite small in high–quality uncompensated material ($10^{14} - 10^{15}/cm^3$) and highly dependent on the growth conditions. [4,11] If the hypothesis of nuclear polarization near the ORD [8,11] (in a

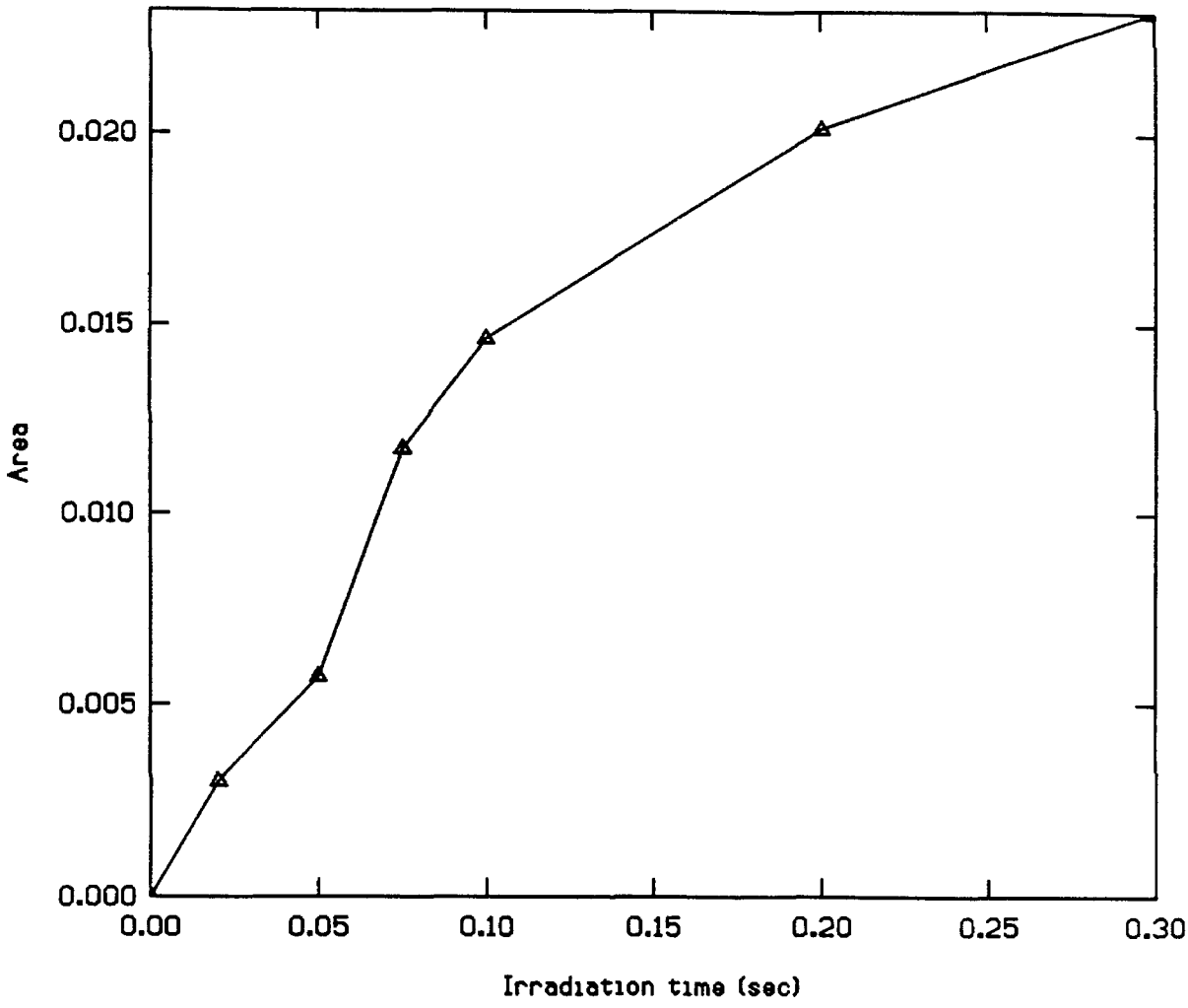

Figure 4.21: ^{71}Ga CW–TSONMR signal versus rf irradiation time. The data is from sample 4. The magnetic fields were: $B_0^p = -155$ G, $B_1 = 0.01$ G, and $B_0^d = 30$ G. An entire spectrum was acquired (30 pts, 1.0 kHz/pt, 10 scans) for irradiation time. The integrated signal is plotted as the y–axis. The signal is linear up to approximately 100 ms.

volume of approximately $[2a_0^*]^3$) holds, then the nuclear polarization (neglecting spin diffision) is achieved for only a small number of nuclei ($10^{11} - 10^{12}$). If spin diffusion is important to establishing a steady–state B_n, then this number will be higher. Spin diffusion effects will be discussed in depth in chapter 5. The chemical identity of the ORD in these samples is unknown, and the possibility of using TSONMR to discover its identity will be addressed in chapter 5.

The highly–doped ($10^{18} - 10^{19}/cm^3$) p–type samples showed strong luminescence and favorable ρ_0, but did not show any evidence of nuclear polarization. As mentioned, this result is in agreement with results of a previous optical pumping study of p–type GaAs, [12] where the absence of nuclear polarization is attributed to a small donor occupation probability Γ_t. In these samples the luminescence is dominated by the free carrier to acceptor level transition which has a lifetime 10 times faster than the lifetime of the donor to acceptor transition. The Hanle widths measured for the samples of reference [12] were on the order of 10 kG which is also consistent with our results that no change in ρ was seen in the small range of B_0^d swept. It should also be noted that donor compensation of highly–doped p–type samples (donors/acceptors $\simeq$ 0.3) results in an order of magnitude decrease in ΔB and large nuclear effects. [8]

The transient subsequent to field reorientation by 90° was shown to be an effective means of detecting B_n and was incorporated into the detection period of a TSONMR experiment. In the pointwise TSONMR experiment each point was given as the weighted difference between the detected transient $\rho(t_d)$ and the null transient $\rho_{null}(t_d)$ integrated over the detection time t_d. The signal–to–noise ratio of a TSONMR experiment was derived and depended on measurable material parameters which allowed comparisons between different samples.

The TSONMR technique achieves extreme sensitivity, without sacrificing resolution. In the present experiments, with relatively unfavorable samples, the

active volume is approximately 10^5 times smaller than conventional high–field NMR would require for the same S/N on the bulk resonances. Sites of reduced symmetry near dilute defects ($\lesssim$ 100 ppb) have also been detected by our method (described in chapter 5). This is about three orders of magnitude more sensitive than would be possible with conventional NMR. The technique is also general to any conceivable NMR experiment such as the modern time–domain experiments prevalent in conventional NMR (multiple–pulse, 2D, double resonance, etc.). In the next chapter, the application of both CW and time–domain TSONMR to the study of the ORD's of samples 4 and 5 is described.

4.6 References

[1] T.D. Harris, M.S. Skolnick, J.M. Parsey, Jr., and R. Bhat, Appl. Phys. Lett. **52**, 389 (1988).

[2] S.G. Bishop, in *Gallium Arsenide Technology Vol. 2* ed. D.K. Ferry (Howard W. Sams, Carmel, IN 1990) chp. 11.

[3] D.A. Fraser, *The Physics of Semiconductor Devices 4th Ed.* (Oxford, Oxford 1986) chp. 2.

[4] M.A. Herman and H. Sitter, *Molecular Beam Epitaxy: Fundamentals and Current Status* (Springer–Verlag, Berlin 1989) chp. 1.

[5] D.A. Fraser, *The Physics of Semiconductor Devices 4th Ed.* (Oxford, Oxford 1986) chp. 2.

[6] V.L. Berkovits, A.I. Ekimov, and V.I. Safarov, Zh. Eksp. Teor. Fiz. **65**, 346 (1973) [Sov. Phys.–JETP **38**, 169 (1974)].

[7] M.I. D'yakonov, V. I. Perel', V.L. Berkovits and V.I. Safarov, Zh. Eksp. Teor. Fiz. **67**, 1912 (1974) [Sov. Phys.–JETP **40**, 950 (1975)].

[8] D. Paget, G. Lampel, B. Sapoval, and V.I. Safarov, Phys. Rev. B **15**, 5780 (1977).

[9] V.G. Fleisher and I.A. Merkulov in *Optical Orientation* ed. F. Meier and B.P. Zakharchenya (North Holland, Amsterdam, 1984) chp. 5.

[10] A.I. Ekimov and V.I. Safarov, ZhETF Pis. Red. **15**, 453 (1972) [JETP Lett. **15**, 319 (1972)].

[11] D. Paget, Phys. Rev. B **24**, 3776 (1981).

[12] G. Fishman and G. Lampel, Phys. Rev. B **16**, 820 (1977).

[13] B.P. Zakharchenya, V.K. Kalevich, V.D. Kul'kov, and V.G. Fleisher, Fiz. Tverd. Tela **23**, 1387 (1981) [Sov. Phys. Solid State **23**, 810 (1981)].

[14] V.K. Kalevich, V.D. Kul'kov, and V.G. Fleisher, Pis'ma Zh. Eksp. Teor. Fiz. **35**, 17 (1982) [JETP Lett. **35**, 20 (1982)].

[15] D.T. Edmonds, Phys. Reports **29**, 233 (1977).

[16] M.I. D'yakonov and V.I. Perel', Zh. Eksp. Teor. Fiz. **65**, 362 (1973) [Sov. Phys.–JETP **38**, 177 (1974)].

[17] G.E. Pikus and A.N. Titkov in: *Optical Orientation* ed. F. Meier and B.P. Zakharchenya (North Holland, Amsterdam, 1984) chp. 3.

[18] M. Goldman, *Spin Temperature and Nuclear Magnetic Resonance in Solids* (Oxford, London, 1970).

[19] G.P. Flinn, R.T. Harley, M.J. Snelling, A.C. Tropper, and T.M. Kerr, J. of Lumines. **45**, 218 (1990).

[20] G.P. Flinn, R.T. Harley, M.J. Snelling, A.C. Tropper, and T.M. Kerr, Semicond. Sci. Technol. **5**, 533 (1990).

[21] S.K. Buratto, D.N. Shykind, and D.P. Weitekamp, Phys. Rev. B **44**, 9035 (1991).

[22] C.P. Slichter, *Principles of Magnetic Resonance 3rd Ed.* (Springer–Verlag, Berlin, 1990), Chp. 3.

[23] R.G. Shulman, B.J. Wyluda, and H.J. Hrotowski, Phys. Rev. **109**, 808 (1958).

[24] O.H. Han, H.K.C. Timken, and E. Oldfield, J. Chem. Phys. **89**, 6046 (1988).

Chapter 5

Application of TSONMR to GaAs Materials

In this chapter the application of various TSONMR experiments to two different p–type GaAs samples (numbers 4 and 5 from chapter 4) is described. Each sample is Zn–doped at a concentration of $10^{17}/cm^3$, but more importantly, as will become clear throughout the discussion, they are both uncompensated. As a result, the precise donor (ORD) identity and concentration is unknown for each sample. For high–quality MBE samples the concentration of undoped impurities is kept on the order of $10^{15} - 10^{16}/cm^3$ (0.1 – 1.0 ppm). [1] Although the precise number of nuclei detected by TSONMR will depend on the efficiency of spin diffusion to carry polarization to and from the optically–detected volume (≈ a sphere of radius 10 nm about the ORD), the number of nuclei contributing to the signal is quite small ($10^{12} - 10^{14}$ nuclei).

The structural information obtainable through TSONMR can be inferred by considering the spin Hamiltonian (in frequency units) for each nucleus in GaAs,

$$\mathcal{H} = \mathcal{H}_Z + \mathcal{H}_D + \mathcal{H}_Q \tag{5.1}$$

where the $\mathcal{H}_Z$ represents the Zeeman interaction $\mathcal{H}_Z = \gamma(B_0^p + B_e)I_z$ and $\mathcal{H}_D$ represents the dipole–dipole interaction defined in Eq. 4.15. $\mathcal{H}_Q$ represents the quadrupole interaction [2]

$$\mathcal{H}_Q = \frac{\omega_Q}{2I(2I-1)}[(3I_{z'}^2 - I^2) + \eta(I_{x'}^2 - I_{y'}^2)] \tag{5.2}$$

where $\omega_Q = e^2qQ/2$, (x′, y′, z′) are the coordinate axes of the principal axis

system (PAS) of the electric field gradient tensor V, eq = $V_{z'z'}$, $\eta = (V_{x'x'} - V_{y'y'})/V_{z'z'}$, and Q is the quadrupole moment. The Zeeman interaction is different for NMR of the valence band (light off during NMR) and for NMR of the conduction band (light on during NMR) due to the presence of the electron hyperfine field B_e which is absent when the light is off. Conduction band TSONMR has shown the effects of B_e as an optical Knight shift of the resonance frequency (see Fig. 2.8). The projected use of the distribution of hyperfine couplings to resolve different sites in heterostructure samples is the subject of section 5.4.

The most useful structural information comes from the quadrupole interaction of Eq. 5.2. Even though each major isotope in GaAs (^{69}Ga, ^{71}Ga, ^{75}As) is I = 3/2, the electric field gradient vanishes for each site due to the cubic symmetry. The nuclear sites surrounding a defect or near the surface, however, have reduced symmetry and nonzero quadrupole couplings. In our p–type samples this occurs in three places, near a Zn atom, near an unknown impurity (such as the ORD), and near the surface.

In order to illustrate the effect of the quadrupole interaction on the NMR spectrum two limiting cases can be considered, $\mathcal{H}_Q >> \mathcal{H}_Z$ illustrated in Figure 5.1, and $\mathcal{H}_Q << \mathcal{H}_Z$ illustrated in Figure 5.2. In the case of $\mathcal{H}_Q >> \mathcal{H}_Z$ the Zeeman interaction is considered a perturbation on the quadrupole interaction, and the $+ 1/2 \longrightarrow - 1/2$ transition is a narrow line (width due to spin–spin couplings) and highly dependent on the relative orientation of the PAS and the applied field B_0^p [2]. In the case of $\mathcal{H}_Q << \mathcal{H}_Z$ the quadrupole interaction is a perturbation of the Zeeman interaction, and the spectrum consists of three transitions as shown with the $+ 1/2 \longrightarrow - 1/2$ unshifted in first order. The position of the satellite transitions, $- 1/2 \longrightarrow - 3/2$ and $+ 3/2 \longrightarrow + 1/2$, are dependent on the orientation of the PAS with respect to the applied field B_0^p [3], but often fall outside the rf excitation bandwidth.

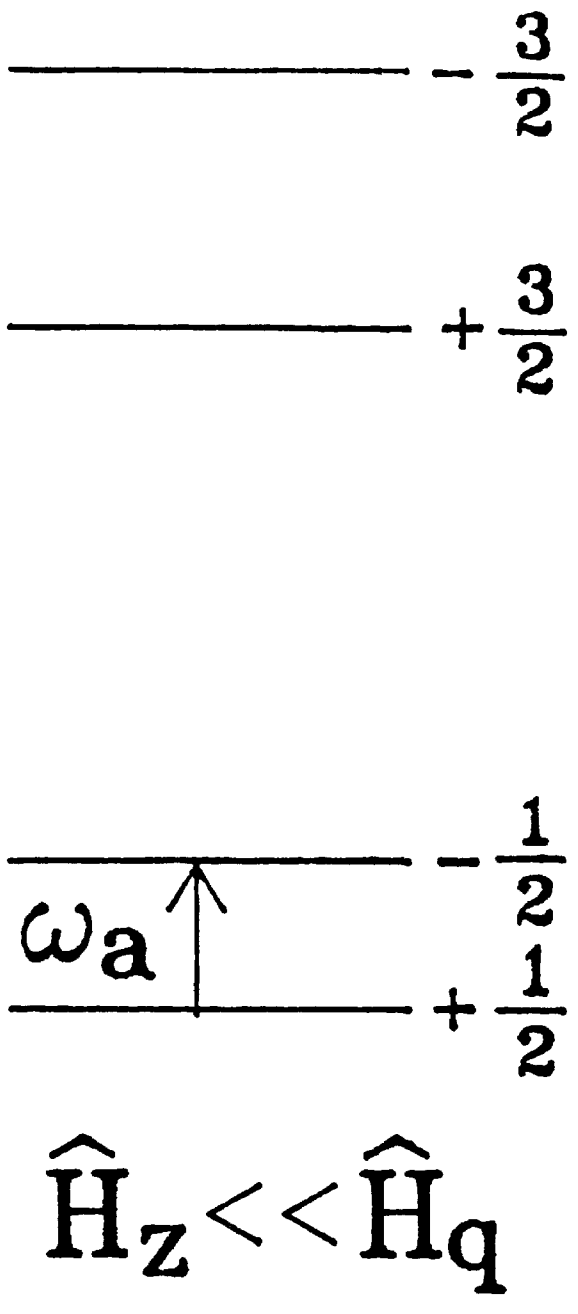

Figure 5.1: The strong quadrupole coupling limit. The central transition + 1/2 ⟶ 1/2 consists of a narrow line (width determined by spin–spin couplings) at frequency ω_a that is highly dependent on crystal orientation.

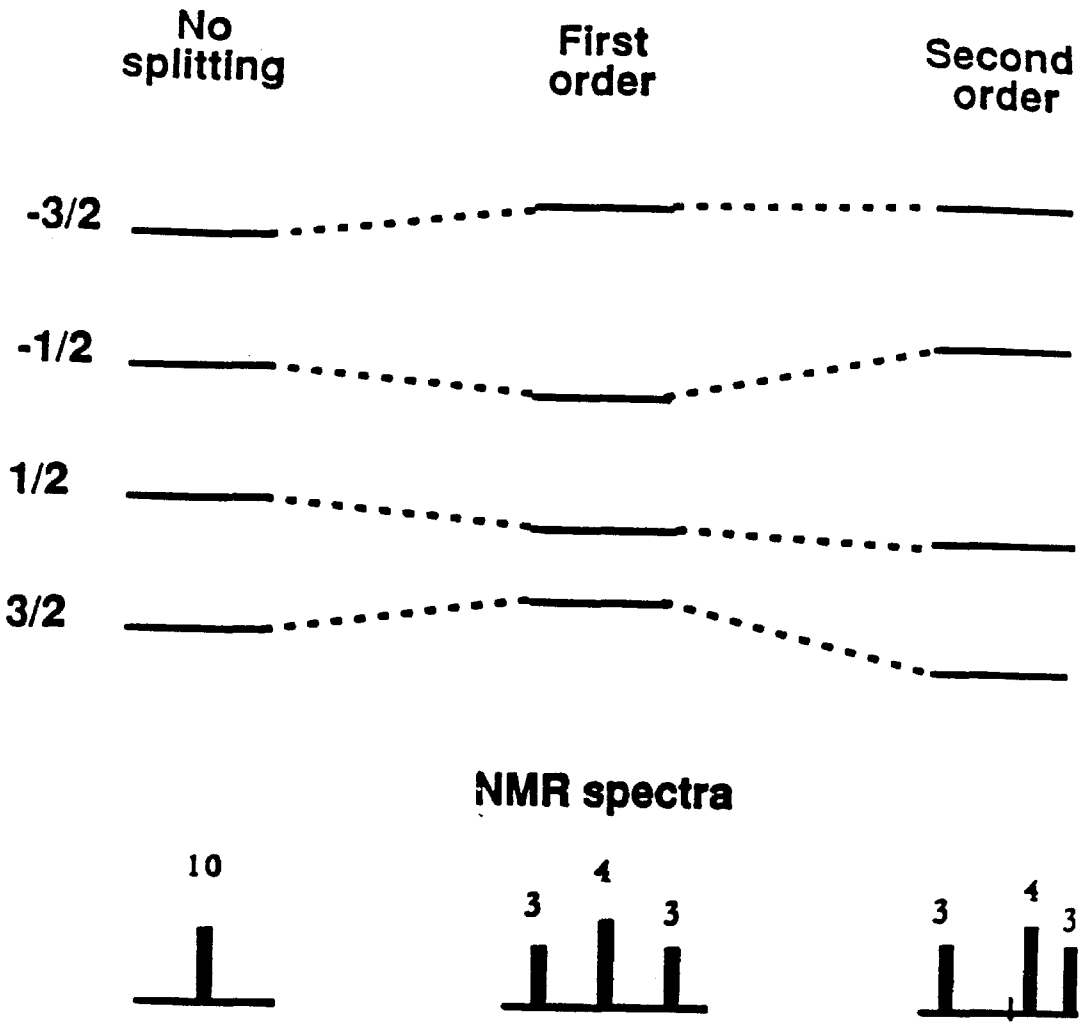

Figure 5.2: The weak quadrupole coupling limit. If $\mathscr{H}_Q = 0$ (left), the spectrum consists of a single line at the Larmor frequency ω_0. If $\mathscr{H}_Q$ is a weak perturbation (middle) the $+3/2 \longrightarrow +1/2$ and $-1/2 \longrightarrow -3/2$ transitions are split from the central transition which remains unchanged. The splitting is orientation dependent. If $\mathscr{H}_Q$ perturbs $\mathscr{H}_Z$ to second order (right) then all three transitions are shifted, and the magnitudes of the shifts are orientation dependent. The relative intensity of the three transitions is given on the bottom of the figure.

The results of this chapter show that the continuous wave (CW) and Fourier transform (FT) variants of the TSONMR experiment probe different sites. CW–TSONMR is sensitive to the bulk spins far from the ORD, while FT–TSONMR is sensitive to quadrupole perturbed sites near the ORD describable in the limit $\mathscr{H}_Z > \mathscr{H}_Q$. The two types of sites are linked by spin diffusion. Optical Knight shifts are seen and shown to vary with proximity to the ORD. The range of the hyperfine interaction is shown to be greater than that of the quadrupole interaction. Finally, an rf–optical multiple–pulse TSONMR experiment to measure the distribution of Knight shifts in GaAs/$Ga_{1-x}Al_xAs$ wells is described and estimates of the results of such an experiment are given.

5.1 Continuous Wave TSONMR

The CW variant of the TSONMR experiment has been previously introduced in sections 2.5 and 4.4. This experiment uses the timing–sequence shown in Figure 2.5 with a 100 ms pulse of rf frequency ω (usually $B_1 \simeq 0.02$ G to insure linear response) during the NMR part of the experiment. Figures 2.8 – 2.10, and 4.18 – 4.20 are examples of CW–TSONMR applied to sample 4. We have seen in section 4.4 that if the rf field strength is high ($B_1 > 0.1$ G), then overtone transitions are seen as well as significant power broadening of the lineshapes (Fig. 4.19). When the rf power is low ($B_1 < 0.1$ G), however, the CW–TSONMR experiment attains high resolution as indicated in Figs. 2.9, 2.10, and 4.20. The resulting lineshape is equal to that expected from spin–spin couplings alone. [4,5] The assignment of these high resolution spectra to bulk nuclear sites will be described later.

Figures 5.3 and 5.4 show the full CW–TSONMR spectra for samples 4 and 5, respectively. The spectra for the two samples are very similar (allowing for the smaller field B_0^p in the case of sample 5) and contain two noteworthy features. First,

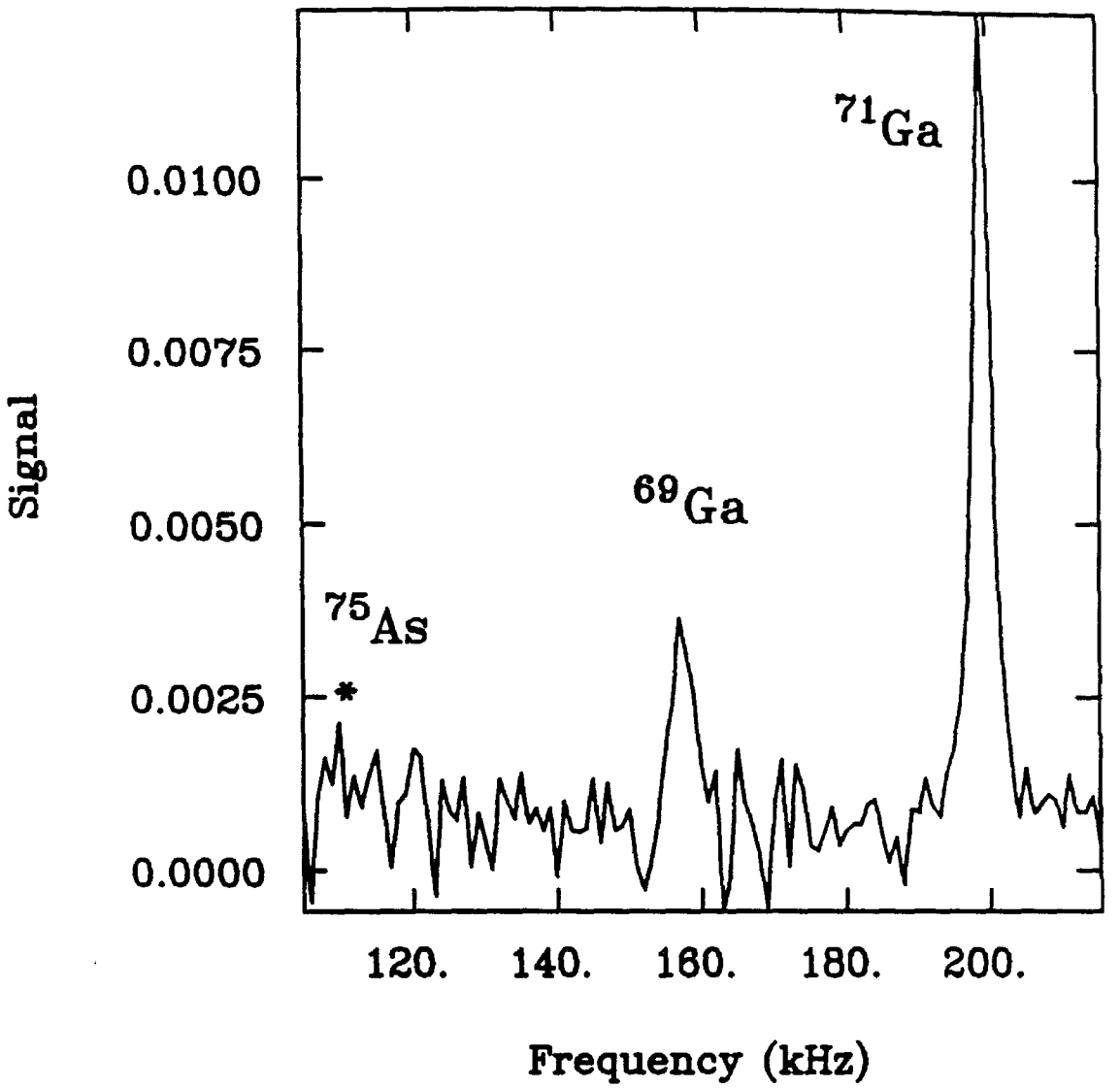

Figure 5.3: CW–TSONMR spectrum of sample 4. The applied field $B_0^p = -155$ G and the rf field $B_1 \simeq 0.02$ G. The resonances of the two gallium isotopes (^{69}Ga and ^{71}Ga) are indicated on the figure. No signal is observed for ^{75}As due to its small nuclear field. The linewidths are equal to linewidths of bulk sites.

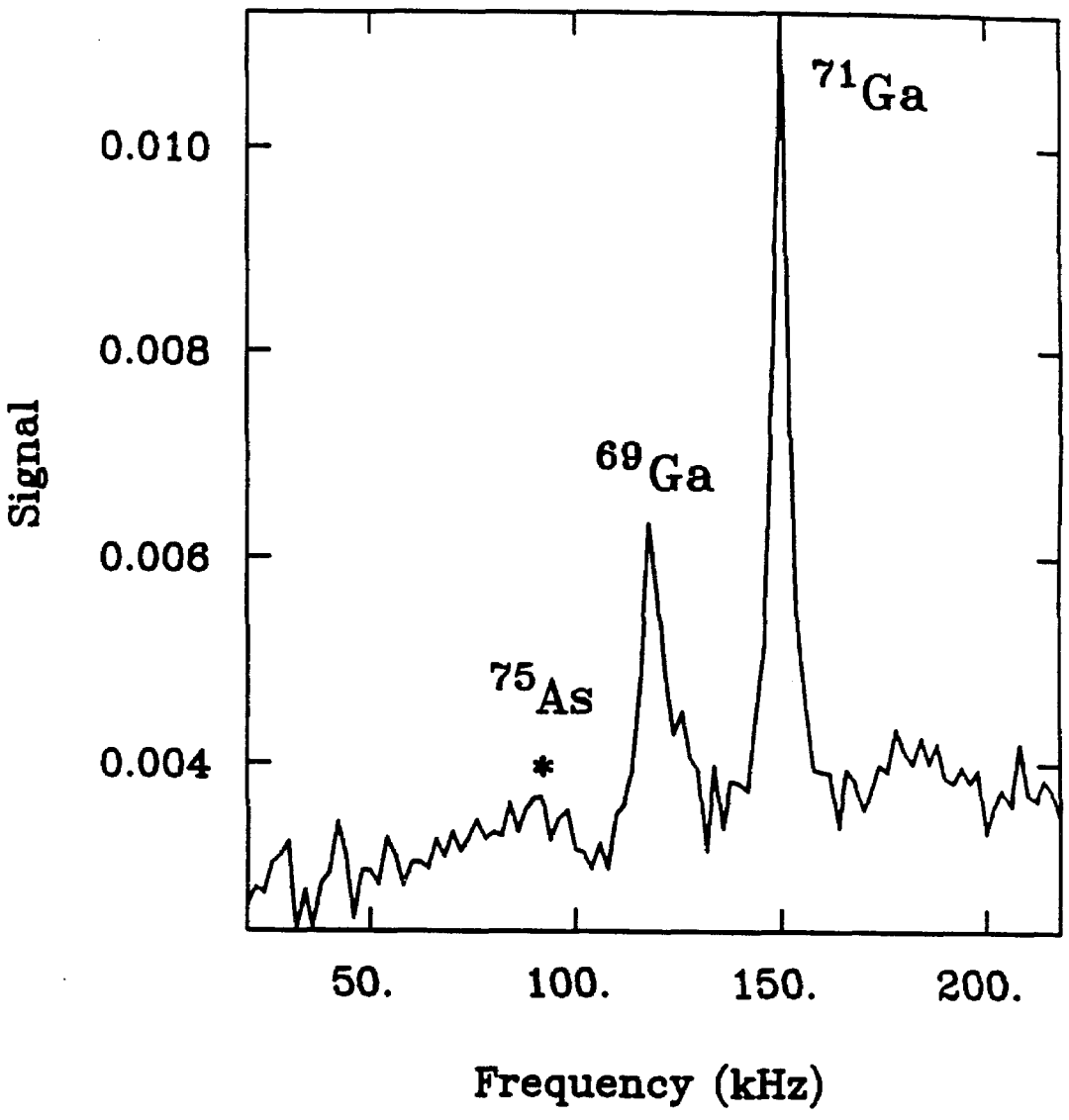

Figure 5.4: CW–TSONMR spectrum of sample 5. The applied field $B_0^p = -120$ G and the rf field $B_1 \simeq 0.02$ G. The spectrum is very similar to the spectrum of sample 4. Again, no signal for ^{75}As is observed.

there is a conspicuous absence of an ^{75}As resonance in each spectrum. The star (*) in each figure indicates the expected position of the ^{75}As resonance. The intensity ratio of the two gallium isotope resonances (^{69}Ga/^{71}Ga) is also unexpected. From the theory of reference [6], the intensities for the transitions of the major isotopes should be opposite of what is observed in Figs. 5.3 and 5.4. The largest signal should be due to the ^{75}As resonance and the smallest signal should be due to the ^{71}Ga resonance.

5.1.1 The ^{75}As Resonance

The ^{75}As resonance can be observed if the rf field strength is increased by a factor of five as seen by the dashed trace of Figure 5.5. The solid trace in Fig. 5.5 is from an experiment designed to enhance the ^{75}As signal. As seen from Figs. 5.3 and 5.4, the ^{71}Ga spin reservoir dominates the nuclear field. At 155 G this spin reservoir is isolated from the other nuclear spin reservoirs (see discussion in section 2.3), and each spin reservoir is described by a different spin temperature θ_a. If, however, the applied field is brought to zero adiabatically, then the nuclear cooling obtained during ONP is transferred to dipolar order [7]. The nuclei from different spin reservoirs then interact through the heteronuclear dipolar couplings, reaching a common spin temperature 0. If the applied field is then ramped adiabatically back to 155 G, the spin temperature 0 is conserved for each nuclear reservoir. Through the process of adiabatic demagnetization, the colder ^{71}Ga reservoir interacts with the warmer ^{75}As reservoir resulting in a net cooling of the ^{75}As reservoir and a net heating of the ^{71}Ga reservoir. After adiabatic remagnetization, the ^{75}As nuclear field is enhanced and its nuclear resonance signal gets larger.

The experiment described in the previous paragraph was accomplished in practice by switching the current in the z–field coils to zero. The field strength

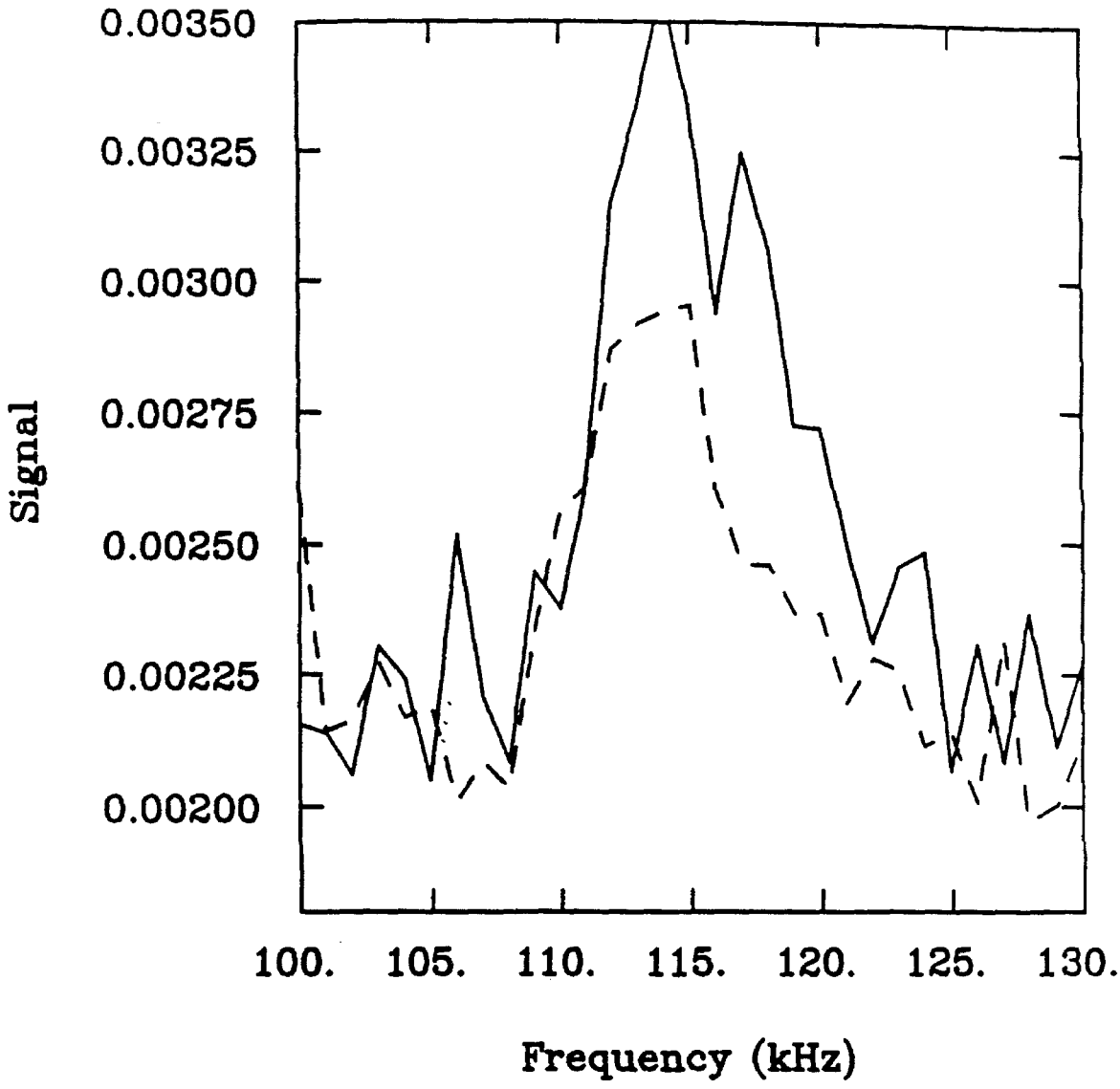

Figure 5.5: ^{75}As CW–TSONMR. The applied field $B_0^p = -155$ G and the rf field $B_1 \simeq 0.1$ G. The dashed trace shows signal obtained by ordinary CW–TSONMR, and the solid trace shows the enhancement from a 500 ms delay in zero field before NMR.

decayed from the value $B_0^p = -155$ G to zero field in approximately 100 ms. It is also important to note that no compensation for parasitic fields (such as the earth's field) was attempted. We have seen that when no current is in either magnet (B_0^p or B_0^d) the field along **z** could not be measured (≤ 0.01 G), and the field along **x** was approximately 0.4 G. The solid trace in Fig. 5.5 shows the result of the experiment described above for a delay of 500 ms in zero field. The observed enhancement was approximately a factor of 1.5. An accompanying loss in ^{71}Ga signal by a factor of 3 was also observed. We attempted the same experiment for several different time delays in zero field, and a delay time of 500 ms resulted in the maximum enhancement.

An important consequence of this experiment is that initiating thermal contact (by adiabatic demagnetization) between two reservoirs of different spin temperatures results in a transfer of spin order that is optically–detected. This transfer of order is the heart of double resonance TSONMR which is discussed in section 5.3.

5.1.2 The ^{69}Ga/^{71}Ga Intensity Ratio

As previously noted, relative intensities of the ^{69}Ga and ^{71}Ga resonances is unexpected based on previous theory. [6] The theory of reference [6] assumed that the leakage factors for each nuclear species was the same. In this subsection this theory is amended to include the possibility of different leakage factors for the three major isotopes are different. If it is assumed that the major mechanism for leakage is relaxation through the quadrupole interaction T_{1_q}, then the leakage factor $f_\alpha \leq 1$ of nuclear species α is given by,

$$f_\alpha = \frac{T_{1_q}^{\alpha}}{T_{1_q}^{\alpha} + T_{1_{hf}}^{\alpha}}. \tag{5.3}$$

Since we observe experimentally that $f_a << 1$ for each nuclear species a, $T_{1_{hf}} >> T_{1_q}$ and Eq. 5.3 simplifies to

$$f_a \approx \frac{T_{1_q}^{a}}{T_{1_{hf}}^{a}}. \tag{5.4}$$

If we assume that both the resonance frequency ω_0 and the rf field strength ω_1 are held constant experimentally for each nucleus, then the ratio of their TSONMR signals will be equal to the ratio of their nuclear fields. The ratio of the nuclear fields $B_n^{^{69}Ga}/B_n^{^{71}Ga}$ is given by (see Eq. 2.22) [6]

$$\frac{B_n^{^{69}Ga}}{B_n^{^{71}Ga}} = \left(\frac{f_{^{69}Ga}}{f_{^{71}Ga}}\right)\left(\frac{\gamma_{^{69}Ga}}{\gamma_{^{71}Ga}}\right)\left(\frac{\chi_{^{69}Ga}}{\chi_{^{71}Ga}}\right). \tag{5.5}$$

Inserting the expression for f_a given in Eq. 5.4, Eq. 5.5 becomes

$$\frac{B_n^{^{69}Ga}}{B_n^{^{71}Ga}} = \left(\frac{T_{1_q}^{^{69}Ga}}{T_{1_q}^{^{71}Ga}}\right)\left(\frac{T_{1_{hf}}^{^{71}Ga}}{T_{1_{hf}}^{^{69}Ga}}\right)\left(\frac{\gamma_{^{69}Ga}}{\gamma_{^{71}Ga}}\right)\left(\frac{\chi_{^{69}Ga}}{\chi_{^{71}Ga}}\right). \tag{5.6}$$

Relaxation due to the quadrupole interaction is proportional to ω_Q^2 [8],

$$\frac{1}{T_{1_q}} \propto \omega_Q^2, \tag{5.7}$$

and relaxation due to localized electrons at the ORD is proportional to γ^2 [6,9],

$$\frac{1}{T_{1_{hf}}} \propto \gamma^2. \tag{5.8}$$

Subsituting Eqs. 5.7 and 5.8 into Eq. 5.6 we have,

$$\frac{B_n^{^{69}Ga}}{B_n^{^{71}Ga}} = \left(\frac{\omega_Q^{^{71}Ga}}{\omega_Q^{^{69}Ga}}\right)^2\left(\frac{\gamma_{^{69}Ga}}{\gamma_{^{71}Ga}}\right)^3\left(\frac{\chi_{^{69}Ga}}{\chi_{^{71}Ga}}\right) \tag{5.9}$$

Using the values [10],

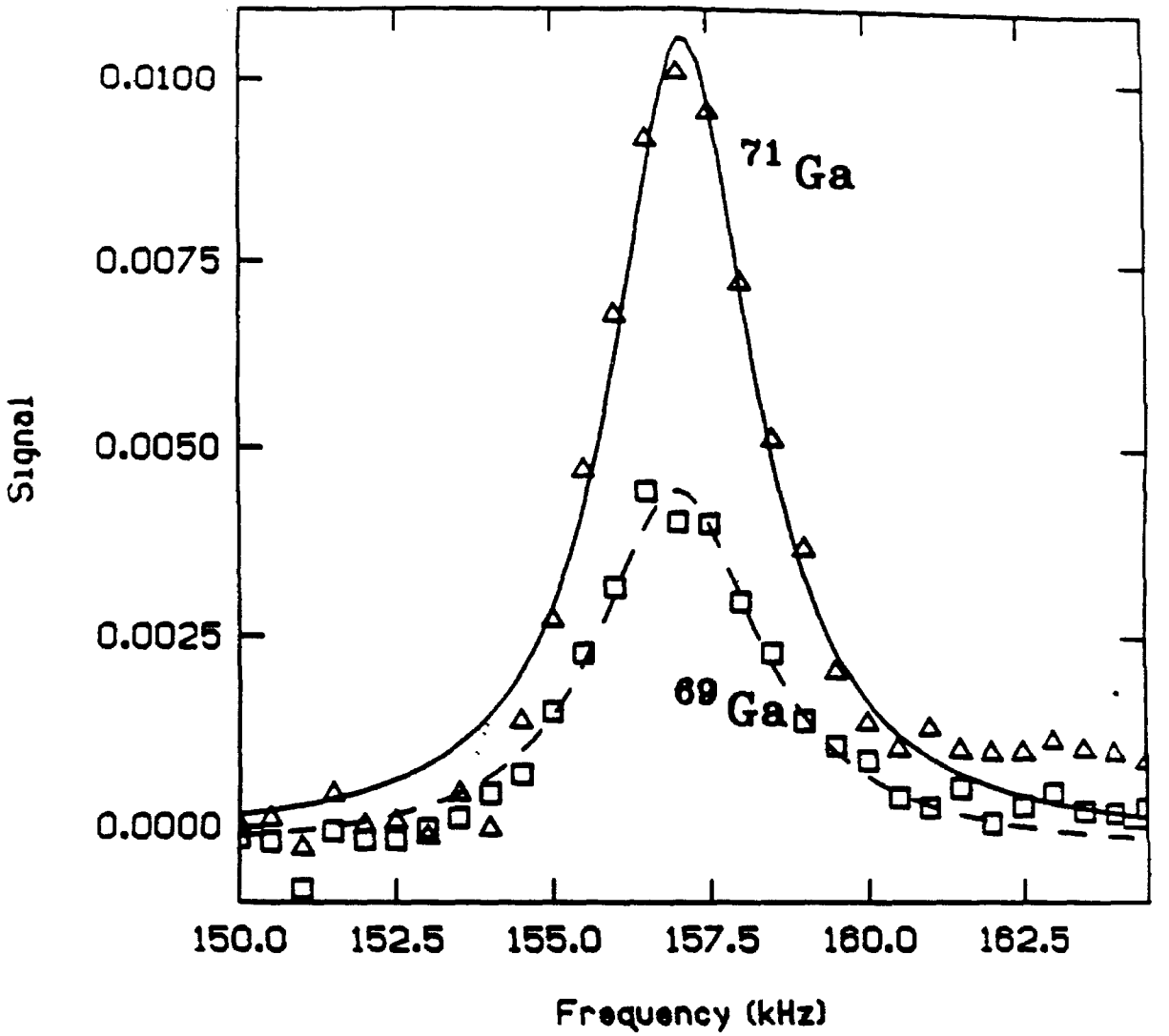

Figure 5.6: $^{69}Ga/^{71}Ga$ CW–TSONMR signal ratio. The data is from sample 4. The resonances were recorded at the same resonance frequency and the same rf field strength. The resonances were fitted to a Lorentzian lineshape, and integration of the two signals yielded the ratio $B_n^{^{69}Ga}/B_n^{^{71}Ga} = 0.495$.

$$\left(\frac{\omega_Q^{71Ga}}{\omega_Q^{69Ga}}\right) = 0.629, \quad \left(\frac{\gamma_{71Ga}}{\gamma_{69Ga}}\right) = 1.27, \text{ and } \left(\frac{\chi_{69Ga}}{\chi_{71Ga}}\right) = 1.53,$$

we obtain a value of 0.296 for the ratio of the intensities of the ^{69}Ga and ^{71}Ga resonances. Performing the same calculation for the ratio B_n^{75As}/B_n^{71Ga} yields a value of 0.062.

The conditions of equal frequencies ω_0 and ω_1 for the ^{71}Ga and ^{69}Ga isotopes, are realized quite easily with TSONMR. First the CW–TSONMR experiment is performed for the ^{69}Ga resonance in a static field B_0^p using an rf field strength of ω_1. The ^{71}Ga resonance is then recorded by adiabatically switching B_0^p to a field B_0^n after ONP and before NMR such that $B_0^n = (\gamma_{69Ga} / \gamma_{71Ga})\, B_0^p$, and attenuating the rf field B_1 by the same factor of $(\gamma_{69Ga} / \gamma_{71Ga})$. Figure 5.6 shows the results of this experiment. The conditions for resonance of ^{69}Ga were $B_0^p = -$ 155 G and $B_1 = 0.02$ G, and the conditions for resonance of ^{71}Ga were $B_0^n = -122$ G, and $B_1 = 0.016$ G. Each resonance was fitted to a Lorentzian lineshape (which gave a marginally better fit than a Gaussian), and the ratio of the areas (^{69}Ga/^{71}Ga) was 0.495. This observed value is larger than the previously calculated ratio of 0.296 and much smaller than the 1.17 ratio predicted by the theory of reference [6].

The same experiment was attempted for the ^{75}As and ^{71}Ga resonances but no signal could be observed for the ^{75}As resonance in the linear response regime.

5.1.3 Spin–Lattice Relaxation Studies

The CW–TSONMR technique can also be used to measure relaxation times, $T_{1_{off}}$. For the CW experiment the spin–lattice relaxation is measured by waiting a time t_1 in the dark after the rf irradiation and then cycling the field for detection.

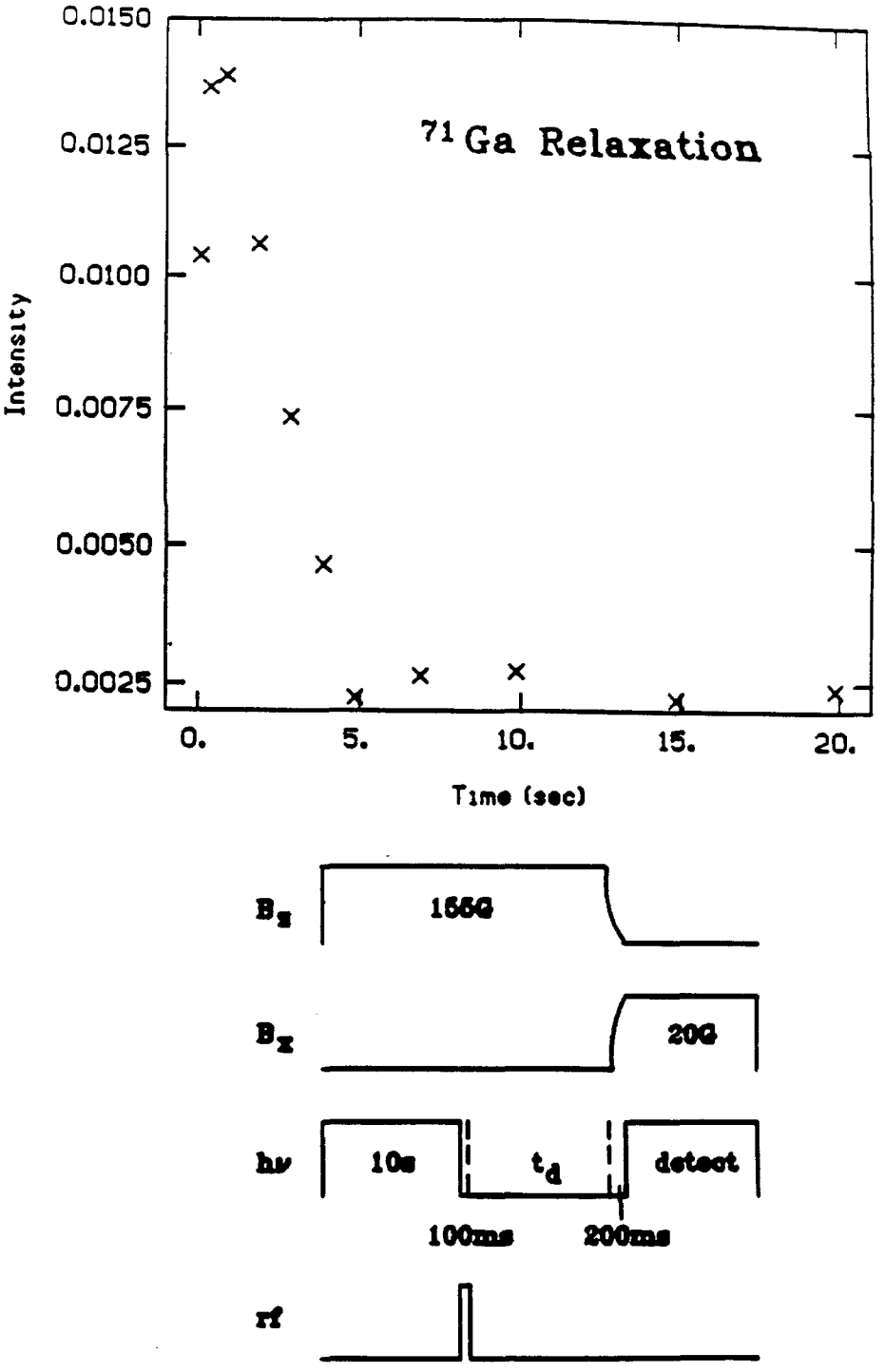

Figure 5.7: ^{71}Ga spin–lattice relaxation of sample 4 by CW–TSONMR. The timing sequence for the experiment is shown below the data. The rise in the initial points is due to bulk sites influencing the optically–detected signal through spin diffusion. The signal completely decays in 6 s.

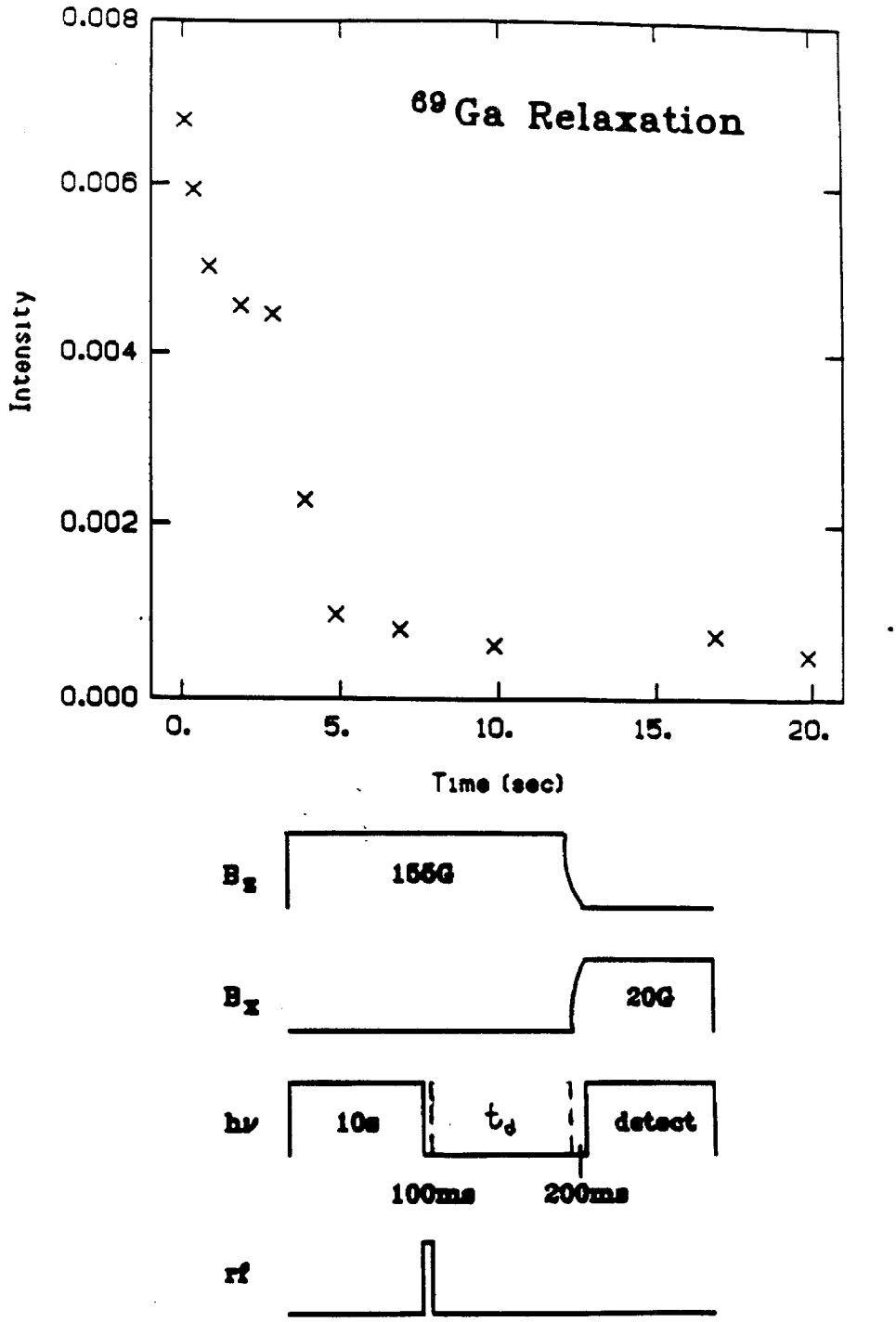

Figure 5.8: ^{69}Ga spin–lattice relaxation of sample 4 by CW–TSONMR. The timing sequence is the same as given in Fig. 5.7. The behavior of points 3 – 5 is due to spin diffusion from bulk sites. The effects of spin diffusion are not as strong as in the case of ^{71}Ga. As with ^{71}Ga, the signal completely decays in 6 s.

The magnetization is monitored using TSONMR as it diminishes along the z axis toward the small equilibrium value as a function of the delay time t_1. The $T_{1_{off}}$ measurements for both the ^{71}Ga and ^{69}Ga isotopes of sample 4 are shown in Figures 5.7. and 5.8, respectively. The data for the ^{71}Ga isotope shows an unexpected rise in the first two points. The signal completely decays in a time of approximately 6 s. The data for the ^{69}Ga isotope does not show the same rise as the ^{71}Ga data, but the signal at early times is clearly non–exponential. There is a plateau near 2 s which is due to spin diffusion effects. The signal in Fig. 5.8 also completely decays in 6 s.

5.1.4 Optical Knight Shifts

The optical Knight shift occurs if the light is kept on during NMR as illustrated in Figure 2.8. The shift arises from the average electron hyperfine field B_e discussed in section 2.2 [6,11]. Since the hyperfine interaction between the lattice nuclei and the conduction electrons is dominated by the electrons localized at the ORD's, the optical Knight shift should be spatially varying as indicated by Eq. 2.19. We have shown by spin–echo (a technique described in the next section) that this spatial inhomogeneity is responsible for the broadening in the "light on" resonance of Fig. 2.8.

The data in Fig. 2.8 was obtained via photon counting for the ^{69}Ga resonance of sample 4. In order to ensure that the count rate was below 800 kHz we were forced to attenuate the signal with neutral density filters. When the capability for synchronous detection using lock–in amplifiers was realized the full photoluminescence was detected. We then repeated the experiment of Fig. 2.8 using the lock–in detection scheme described in section 3.5. The result is presented in Figure 5.9. The observed optical Knight shift is reduced by a factor of 6, and there

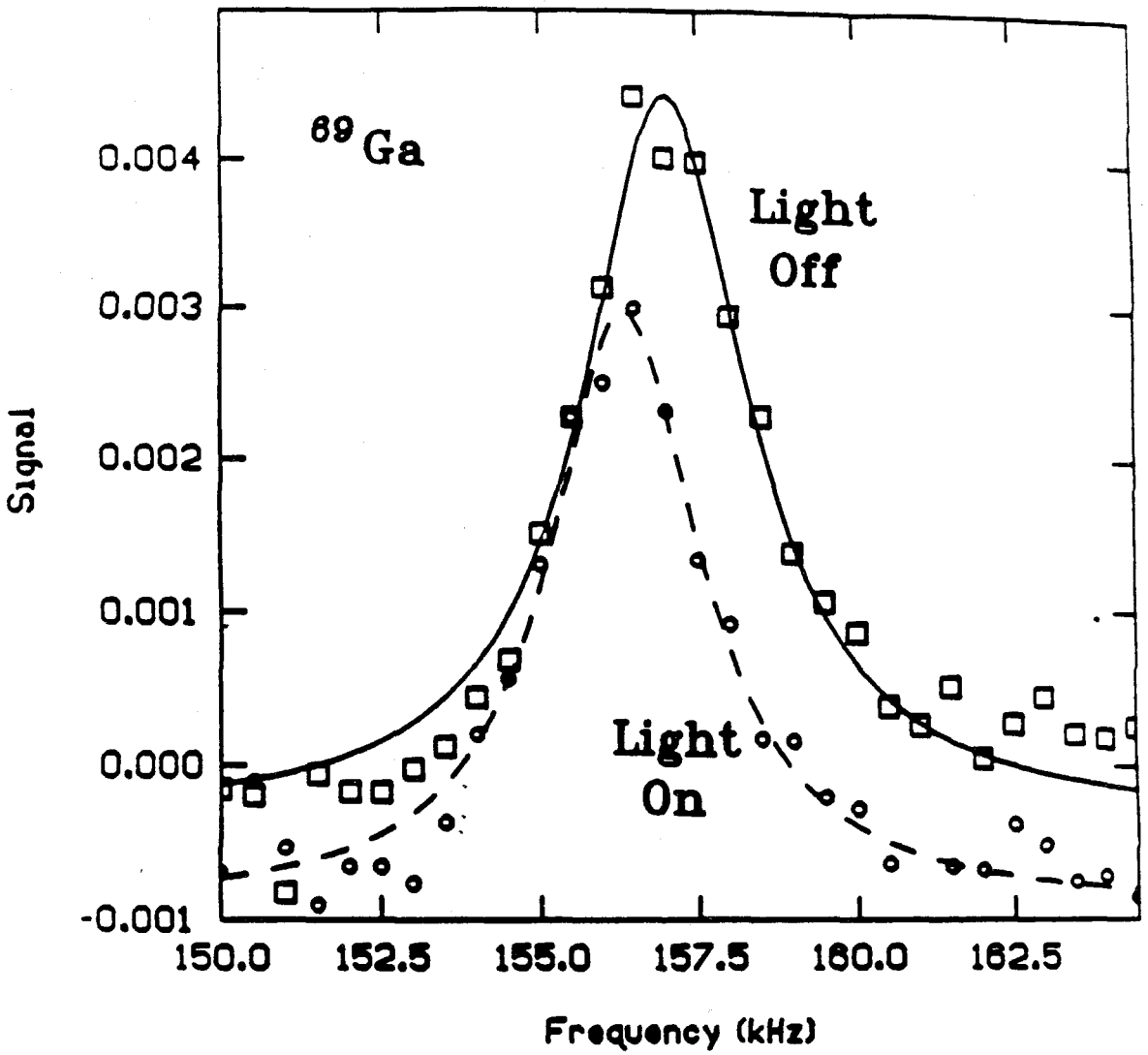

Figure 5.9: ^{69}Ga optical Knight shift. The data is from sample 4 and was detected using lock–in detection. The shift is approximately 700 Hz, and only a small broadening ($\simeq$ 0.5 kHz) is observed for the light on resonance. This observation contrasts with the 6 kHz shift of Fig. 2.8 which was detected using gated photon counting.

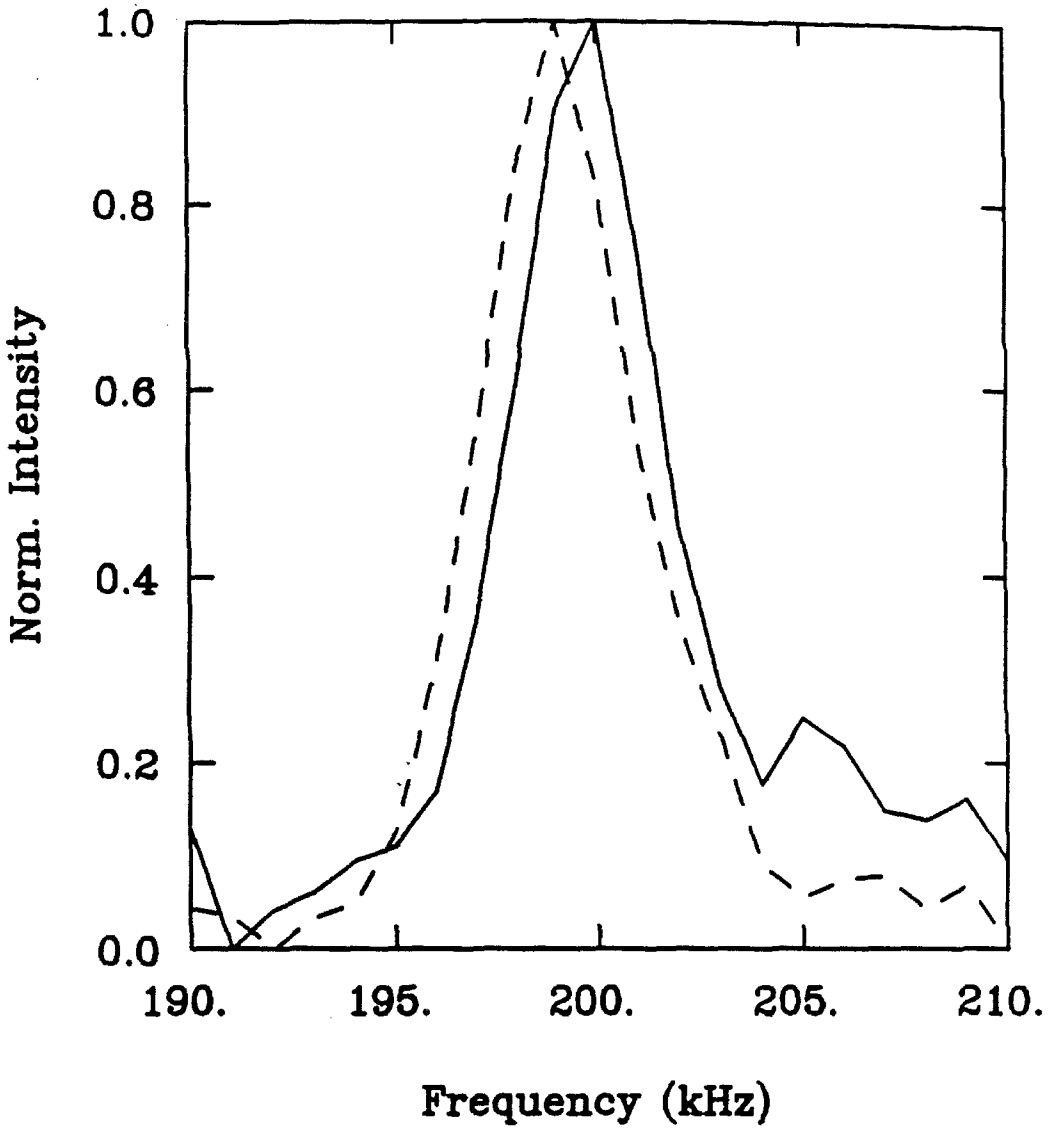

Figure 5.10: ^{71}Ga optical Knight shift. The data is from sample 4 and lock–in detection. The observed shift is 900 Hz with a broadening of the light on resonance of 1.6 kHz.

is only a slight broadening of the "light on" resonance. Figure 5.10 shows the same experiment for the ^{71}Ga isotope of sample 4. The observed Knight shift is 1.1 kHz with a slight broadening of the shifted line by $\simeq$ 0.7 kHz. When the circular polarization of the exciting light was changed from right to left the shift reversed sign which proved that the effect was an optical Knight shift rather than a chemical shift.

We hypothesized several reasons for the reduction in the Knight shift of sample 4. First, we attempted to focus the laser spot more tightly, on the assumption that the focus was lost when the apparatus was changed to accommodate lock–in detection. We observed the same shifts shown in Figs. 5.9 and 5.10 in all cases where the focus was altered. The shift also remained the same when the location of the laser spot on the sample was changed. One significant change in the apparatus that was made to accomodate lock–in detection was the addition of an optical chopper in the excitation optics (see Fig. 3.8). The chopper was inserted to allow detection of the total luminescence ($I_+ + I_-$), and was not required for gated photon counting. Because of this change, the total time that the laser hits the sample during NMR in the "light on" experiment is cut in half. In order to test whether this affected the observed shift, we moved the chopper to the detection side, in front of the detector. Again the shift was unchanged. A final possibility is that by attenuating the luminescence we observe a different site with a larger Knight shift than if the total luminescence is detected.

5.1.5 Discussion

The narrow linewidths of the CW–TSONMR spectrum imply that either the observed sites are $-1/2 \longrightarrow +1/2$ transitions in the limit $\mathscr{H}_Q >> \mathscr{H}_Z$, or the observed sites are unperturbed. If the former hypothesis is correct then the line

position would be orientation dependent [2]. We performed the CW–TSONMR experiment over a range of angles spanning 30°, and no change in position was seen. Thus, the sites observed by CW–TSONMR are sites far enough from the ORD to feel a negligible quadrupole interaction, but close enough to influence the optically–detected signal.

The observation of bulk sites is an important result. This result indicates that the technique of CW–TSONMR is not relegated to the study of the ORD even though it is the locus of the ONP and OD processes. Thus, any randomly distributed site can be detected by CW–TSONMR.

It was also determined that the spins outside the optically–detected volume contribute to the signals in Figs. 5.3 and 5.4. It is known from previous quasi–steady–state ODNMR results [12] that sites which are distant ($\geq$ 10 nm) from the ORD can influence the optically–detected spins by spin diffusion with time constants, typically, on the order of seconds. The data of Figure 5.7 indicate that spins outside the optically–detected volume do contribute to the CW–TSONMR signal since for early time points there is an increase in the measured signal. The initial rise of the T_1 data of Figure 5.7 is attributed to the response of the bulk spins to resonant irradiation measured as a time–delayed effect on the nuclei in the optically detected volume. A maximum in the signal intensity is seen after an 800 ms delay in the dark after irradiation with rf. At times greater than 800 ms the signal is dominated by these numerous spins and their return to equilibrium accounts for the decay.

The ratios of the contributions to the nuclear field of each of the major isotopes is due to efficient spin–lattice relaxation through the quadrupole interaction. The theory of reference [6], which does not take into account relaxation through the quadrupole interaction, is clearly inadequate for our samples, even failing to predict the right trend. By including the effects of relaxation through the

quadrupole interaction as the cause of leakage, it is possible to achieve the same qualitative result observed ($B_n^{^{71}Ga} > B_n^{^{69}Ga} > B_n^{^{75}As}$), but the calculation fails to reproduce the experiment quantitatively. The intensity ratio is higher than predicted by the calculation. It is possible that in our small applied fields (120 – 155 G) that the three Zeeman reservoirs are not completely isolated from one another, and some ^{71}Ga polarization is transferred to ^{69}Ga. Increasing the applied field strength would help sort out the behaviour of the three spin reservoirs under ONP conditions. This improvement to the apparatus is currently under way.

Although it appears that the effect of relaxation through the quadrupole interaction is not as severe as predicted, it is still undermining the ONP enough such that a signal for ^{75}As could not be observed in conditions of linear response. A signal for ^{75}As nuclei was, however, detected using time–domain TSONMR which has a higher sensitivity as demonstrated in section 5.2.

The optical Knight shift results show effects of a spatially varying hyperfine interaction. Since the entire resonance shifts, even in the case of the smaller shifts, the signal is dominated substantially by sites sufficiently close to the ORD to experience the electron polarization as a hyperfine field. Thus, the hyperfine interaction has a greater range of influence than the quadrupole interaction which is not observed by CW–TSONMR.

5.2 Time–Domain TSONMR

In order to further develop the TSONMR technique as a powerful and versatile spectroscopy, we have extended our method to include time–domain experiments. Not only will this extension provide larger signal due to the full modulation of the resonant spin's nuclear field, but it will also allow the more sophisticated multiple–pulse and two–dimensional techniques, common in

conventional NMR, to be used in conjunction with TSONMR. Such an extension is not possible with the quasi steady–state ODNMR technique.

In this section a variety of time–domain TSONMR experiments are demonstrated on samples 4 and 5. It will be shown that the Fourier transform (FT) TSONMR is sensitive to the spins near defects which are the locus for optical NMR (the ORD), in contrast to the CW–TSONMR experiment which is sensitive to the more numerous sites far from the ORD. The two experiments can be reconciled by allowing for and manipulating nuclear spin diffusion.

5.2.1 FT–TSONMR

A Fourier transform TSONMR (FT–TSONMR) experiment consists of a simple two–pulse experiment using the sequence

$$\theta_x - t_1 - \theta_x$$

during the NMR part of the experiment. The initial θ_x pulse rotates the nuclear magnetization into the yz plane of the rotating frame by an angle $\theta_x = \gamma B_1 t_p = \omega_1 t_p$ (for resonance offset $<< \omega_1$) and initiates a period of free evolution during t_1, just as in conventional FTNMR. Once the free–evolution period finishes, a second θ_x pulse returns the remaining magnetization to the z–axis. The second θ_x is required because the optical detection period is optimized for nuclear magnetization proportional to I_z prior to field reorientation. The signal $S(t_1)$,

$$S(t_1) = \mathcal{N} \int_0^\infty [\rho(t_1,t_d) - \rho_{null}(t_d)]\, W(t_d)\, dt_d, \qquad (5.10)$$

is analogous to an FID observed in a conventional NMR experiment except the contribution of a given spin is to the nuclear field rather than the nuclear magnetization. These differ only slightly within approximately a_0^* of the ORD as described in chapter 2.

Figure 5.11 shows an FID of ^{71}Ga nuclei obtained by FT–TSONMR of

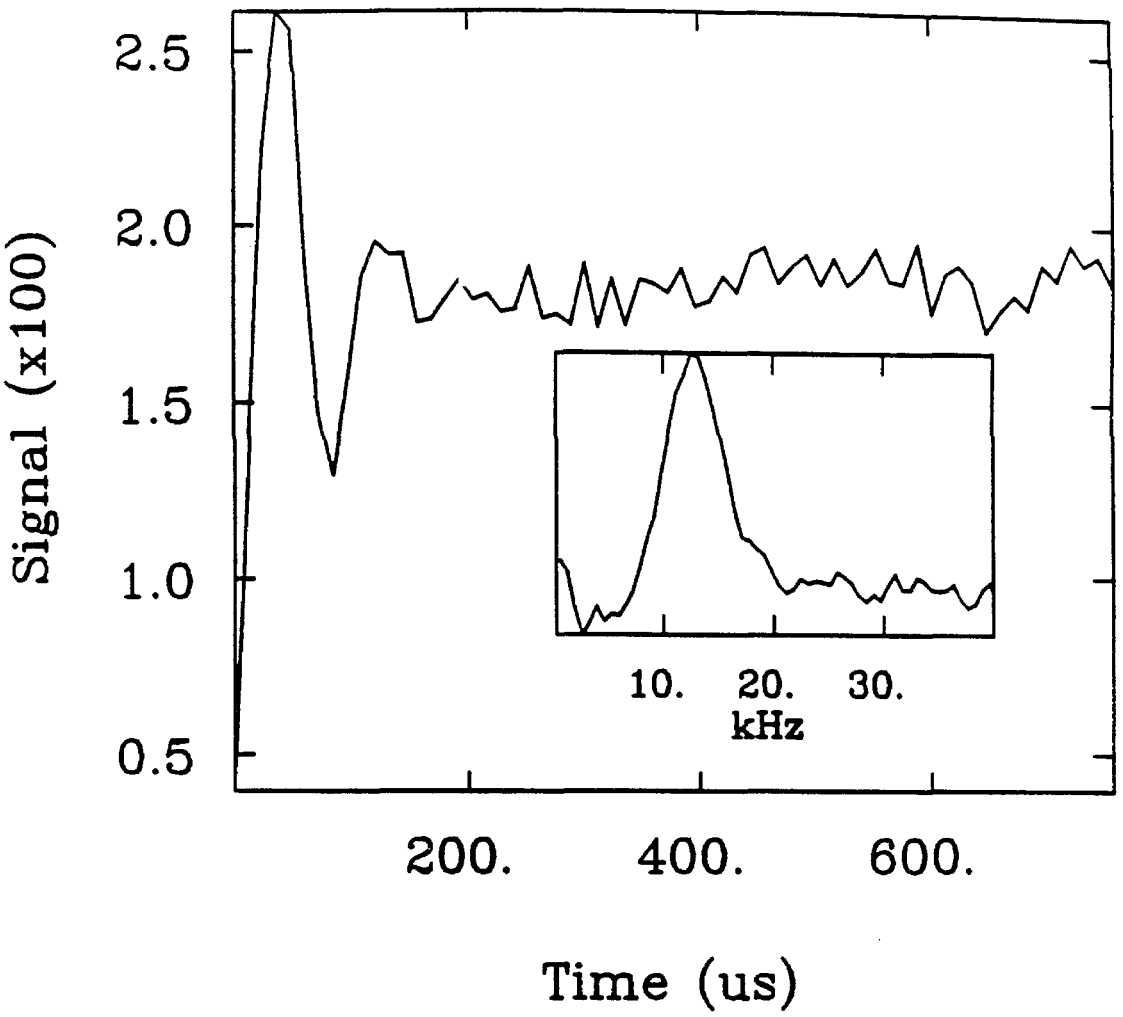

Figure 5.11: ^{71}Ga TSONMR free induction decay of sample 4. The FT–TSONMR spectrum is shown in the inset. The linewidth is 3.7 kHz which is a factor of 1.6 times larger than the CW–TSONMR linewidth indicating the presence of quadrupole perturbed sites.

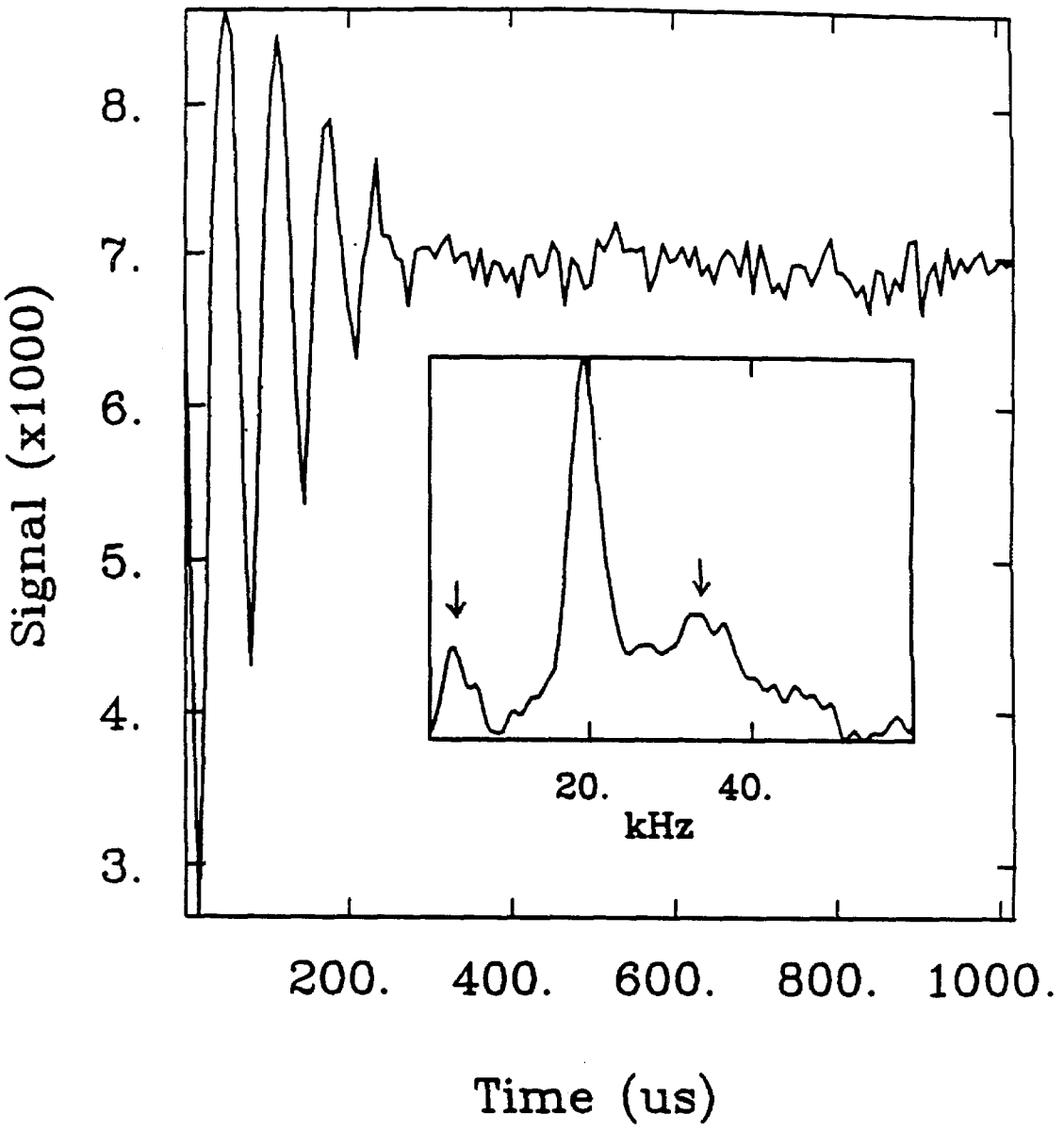

Figure 5.12: ^{71}Ga TSONMR free induction decay of sample 5. The FT–TSONMR spectrum appears in the inset. The largest resonance has a linewidth of 6 kHz. The broadening is due to unresolved quadrupole couplings. The two resonances on either side of the central peak are second order shifts of the central transition.

sample 4. The rf carrier frequency was offset from the resonance frequency by 12 kHz and both pulse lengths were set to 12.0 μs for an effective $\theta_x = \pi/2$ pulse angle at this offset. The inset in the figure shows the Fourier transform of the FID. The resonance line was fitted to a Lorentzian lineshape (which gives a nominally better fit than a Gaussian lineshape in all cases) with a linewidth of 3.7 kHz. This linewidth is 1.6 times larger than that observed for the CW–TSONMR and conventional NMR experiments, which indicates that the FT–TSONMR experiment probes sites different from its CW counterpart.

The ^{71}Ga FT–TSONMR spectrum of sample 5 shown in Figure 5.12 is even more striking in this regard. Not only is the central resonance broader than the CW–TSONMR spectrum of this sample, but structure appears (as indicated by the arrows) on each side of the central resonance. Another interesting observation concerning the FT–TSONMR spectrum of sample 5 is that the resonance frequency for the central transition is shifted from the resonance frequency of the CW–TSONMR spectrum as seen in Figure 5.13.

The assignment of the broadening in the FT–TSONMR spectra of samples 4 and 5 as well as the structure observed in the spectrum of sample 5 can be accomplished with a Hahn spin–echo experiment. [13]

5.2.2 The Hahn Spin–Echo and TSONMR

Through the use of a Hahn spin–echo we were able to show that the broadening in our FT–TSONMR experiment is not a Zeeman or second–order quadrupole effect and must be due to first–order quadrupolar effects which are not refocused. [13] The echo experiment is done by using a three–pulse sequence

$$\frac{\pi}{2}_x - t_1 - \pi_x - t_1 - \frac{\pi}{2}_x .$$

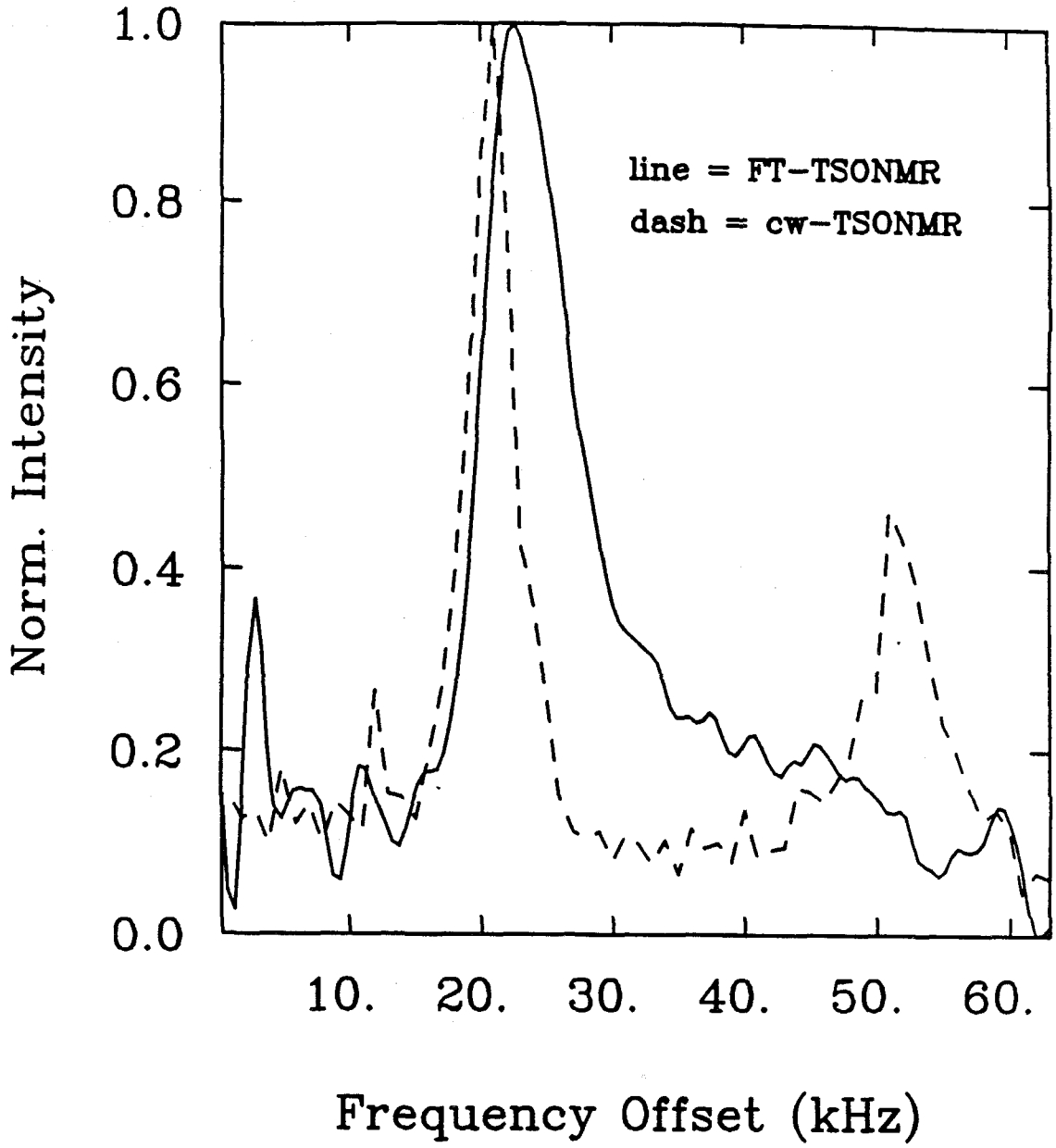

Figure 5.13: ^{71}Ga FT–TSONMR versus CW–TSONMR of sample 5. The FT–TSONMR spectrum has a different lineshape than the CW–TSONMR spectrum indicating that the two techniques are sensitive to different sites. The difference in resonance frequency is 1.5 kHz. The peak at ≃ 51 kHz offset in the CW spectrum is the ^{69}Ga resonance which is not in the excitation bandwidth of the FT experiment.

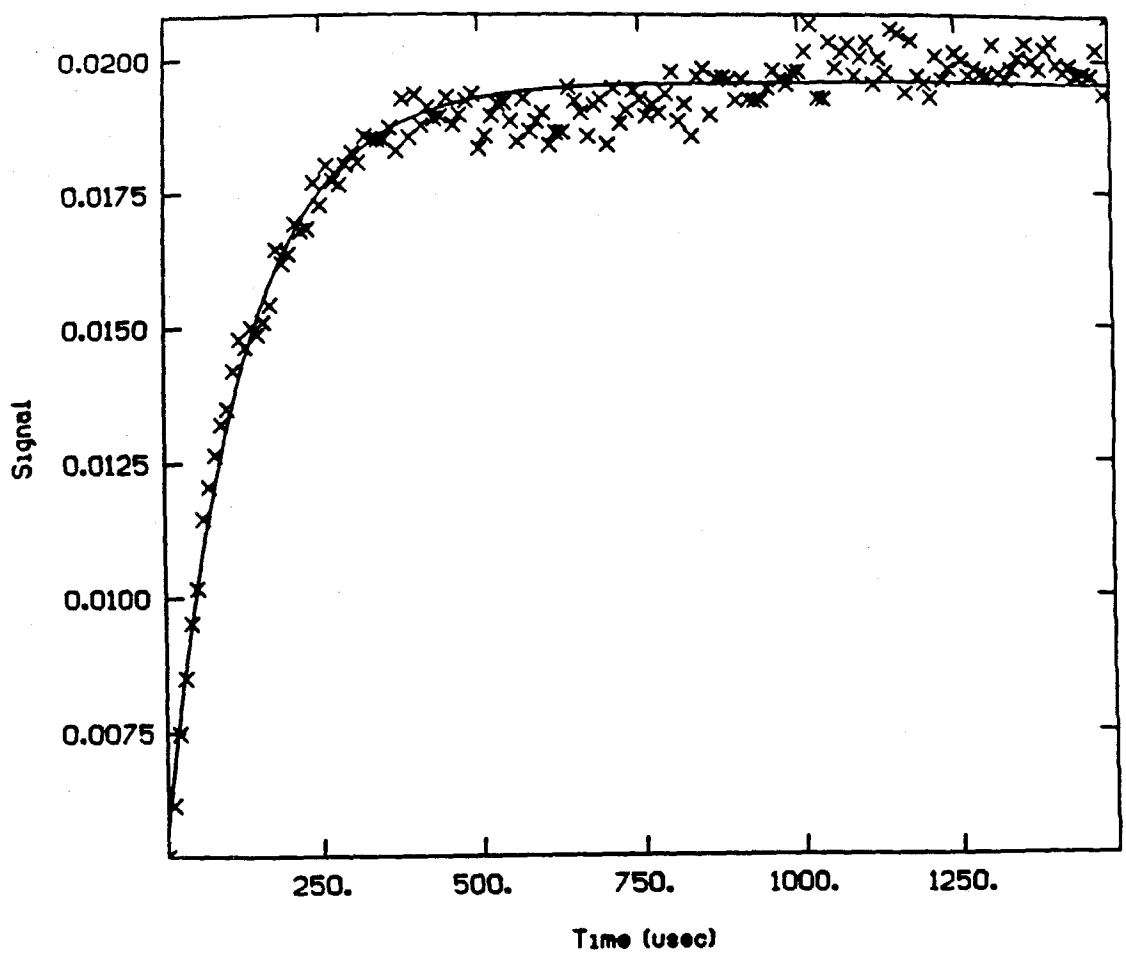

Figure 5.14: ^{71}Ga Hahn spin–echo TSONMR of sample 4. The echo envelope decays with time constant $T_2 = 130\ \mu s$ ($1/\pi T_2 \simeq 2.5$ kHz) indicating that most of the broadening is not refocused by the π_x pulse in the echo sequence. This residual broadening must, therefore, be unresolved first–order quadrupole satellite transitions.

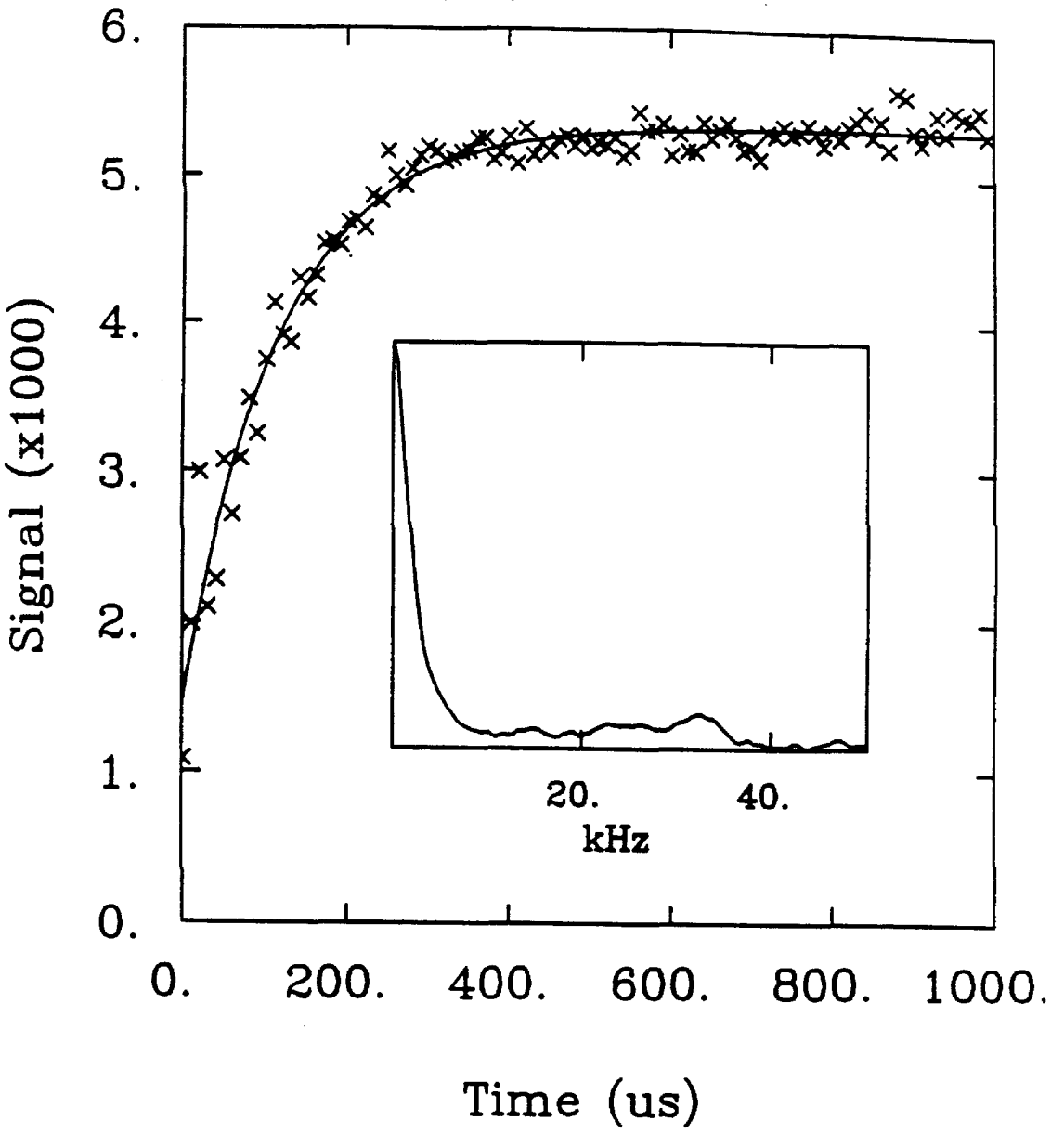

Figure 5.15: ^{71}Ga Hahn spin–echo TSONMR of sample 5. The echo envelope decays with time constant $T_2 = 110\ \mu s$ ($1/\pi T_2 = 2.9$ kHz) indicating that half of the broadening is removed by the echo sequence. The Fourier transform of the echo envelope does not show the structure of Fig. 5.12 indicating that the structure is due to second–order shifts of the central transition. The small resonance at 35 kHz is due to ^{69}Ga spins which fall within the excitation bandwidth at the low applied field $B_0^p = -120$ G.

The first two pulses $\pi/2_x - t_1 - \pi_x$ produce the echo at time $2t_1$ at which point the third pulse $\pi/2_x$ transfers the refocused magnetization into magnetization which is optically–detectable. The data is presented as echo amplitude versus t_1, and the results of the spin–echo experiments on both samples 4 and 5 are shown in Figures 5.14 and 5.15, respectively.

The spin–echo pulse sequence removes inhomogeneous broadening of the free evolution signal by refocusing terms in the spin Hamiltonian of odd order in I_z. In the Hamiltonian of Eq. 5.1, the resonance offset, heteronuclear dipolar couplings, and the second–order shift of the quadrupole interaction are refocused by the spin–echo sequence. The first–order quadrupole interaction and the homonuclear dipolar couplings which are bilinear in I_z are not refocused by the spin–echo sequence. The data of Figs. 5.14 and 5.15 show that most of the linewidth remains after the spin–echo indicating that this broadening is due to unresolved first–order quadrupole interactions. Another important observation from the data of Fig. 5.15 is that the Fourier transform of the echo envelope (inset of Fig. 5.15) shows no structure. If the transitions indicated by the arrows in Fig. 5.12 were first–order satellites then they would appear in the Fourier transform of the spin–echo. Thus, the resolved splittings in Fig. 5.12 can be assigned as second–order shifts of the central $(+ 1/2 \longrightarrow - 1/2)$ transition.

5.2.3 Nutation TSONMR

Transient nutation phenomena, also known as Torrey oscillations, [14] occur when rf radiation is suddenly turned on at or near resonance. It can be visualized in the rotating frame as the precession of the magnetization around the effective field with frequency

$$\omega_e = (\Delta\omega^2 + \omega_1^2)^{1/2}, \tag{5.11}$$

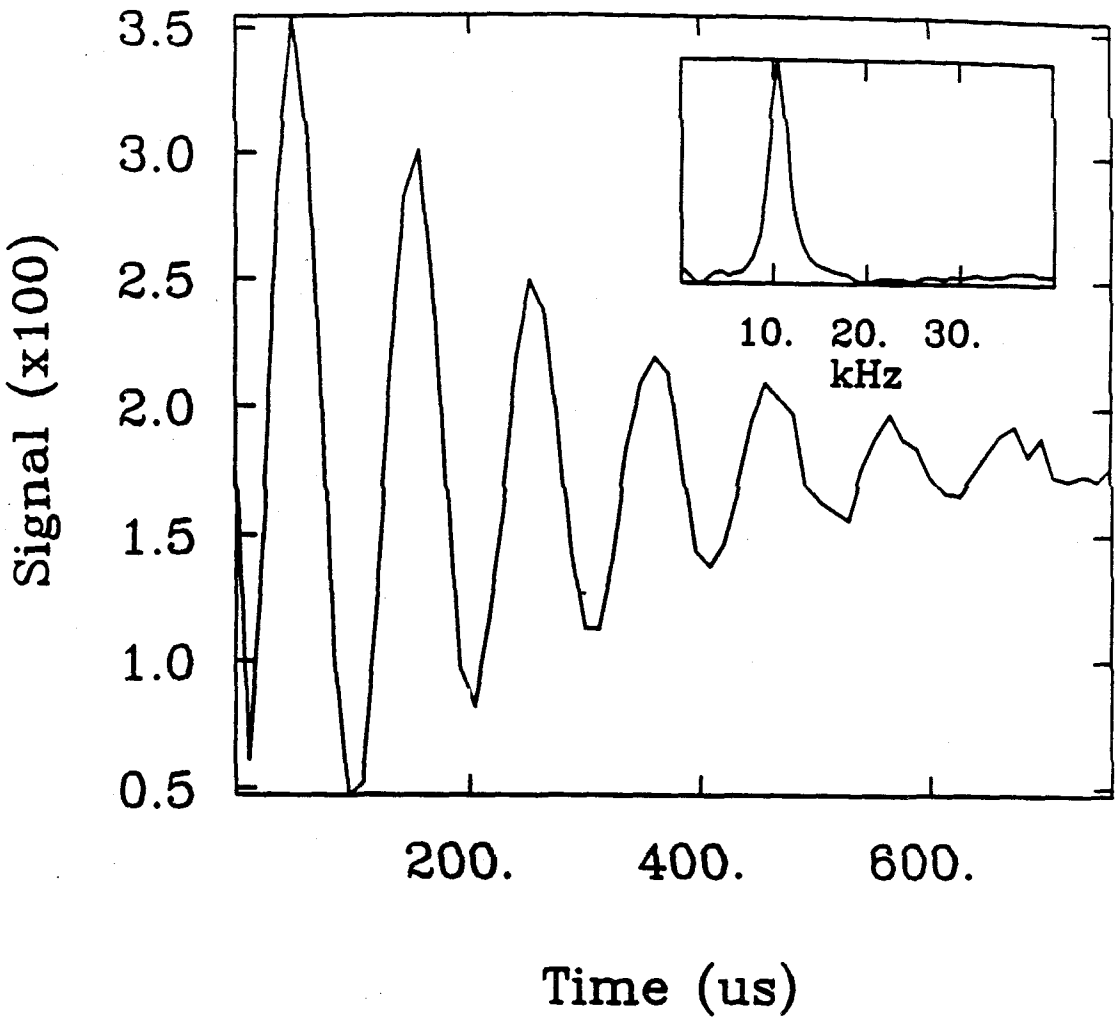

Figure 5.16: ^{71}Ga Nutation TSONMR of sample 4. The frequency spectrum is shown in the inset. Only one Fourier component at $\omega_1 = 12$ kHz is observed indicating that the quadrupole couplings observed in the FT–TSONMR spectrum are much smaller than 12 kHz.

where $\omega_1 = \gamma B_1$ is the strength of the driving field and $\Delta\omega = \omega - \omega_0$ is the frequency offset of the driving field from the resonance frequency. The nutation pulse sequence consists of a single pulse of length t_1 that is incremented for each point in the spectrum. A nutation–TSONMR experiment on the ^{71}Ga resonance of sample 4 is presented in Figure 5.16. The Fourier transform of this data is provided as an inset. An important point to note about our nutation experiment is that due to our relatively small static field of 155 G a significant Bloch–Siegert shift is seen. [15] This shift is due to the counter–rotating component of our linearly–polarized rf field. The shift is equal to $(\omega_1^2/4\omega_0) = 0.840$ kHz, and is measured experimentally as the difference in ^{71}Ga resonance frequency between the CW–TSONMR and nutation TSONMR experiments.

A nutation experiment provides the means of checking the strength of the quadrupole couplings relative to the strength of the rf field. [16,17] If the quadrupole coupling is sufficiently small that all three single–quantum transitions are within the bandwidth of $\sim \omega_1$, then the corresponding Torrey oscillations (for each of the three transitions) occur at a single frequency ω_1 for the case of on–resonance excitation. If, however, there are non–zero electric field gradient perturbations then other frequencies are present in the nutation experiment. The limiting case where $\omega_Q >> \omega_1$ is illustrated in Figure 5.17 for a nuclear spin I = 3/2. In this limit only the central transition is excited and its nutation frequency occurs at $2\omega_1$. [16] In the intermediate region where the quadrupole splitting and the rf field strength are comparable the nutation spectrum contains frequencies between zero and $2\omega_1$ and is highly dependent on the orientation of the PAS of the EFG tensor with respect to the applied rf field.

Whereas the data of Fig. 5.16 shows only one frequency component at ω_1 indicating that the range of quadrupole frequencies detected in sample 4 are much smaller than 12 kHz, two frequencies are seen in the nutation TSONMR spectrum of

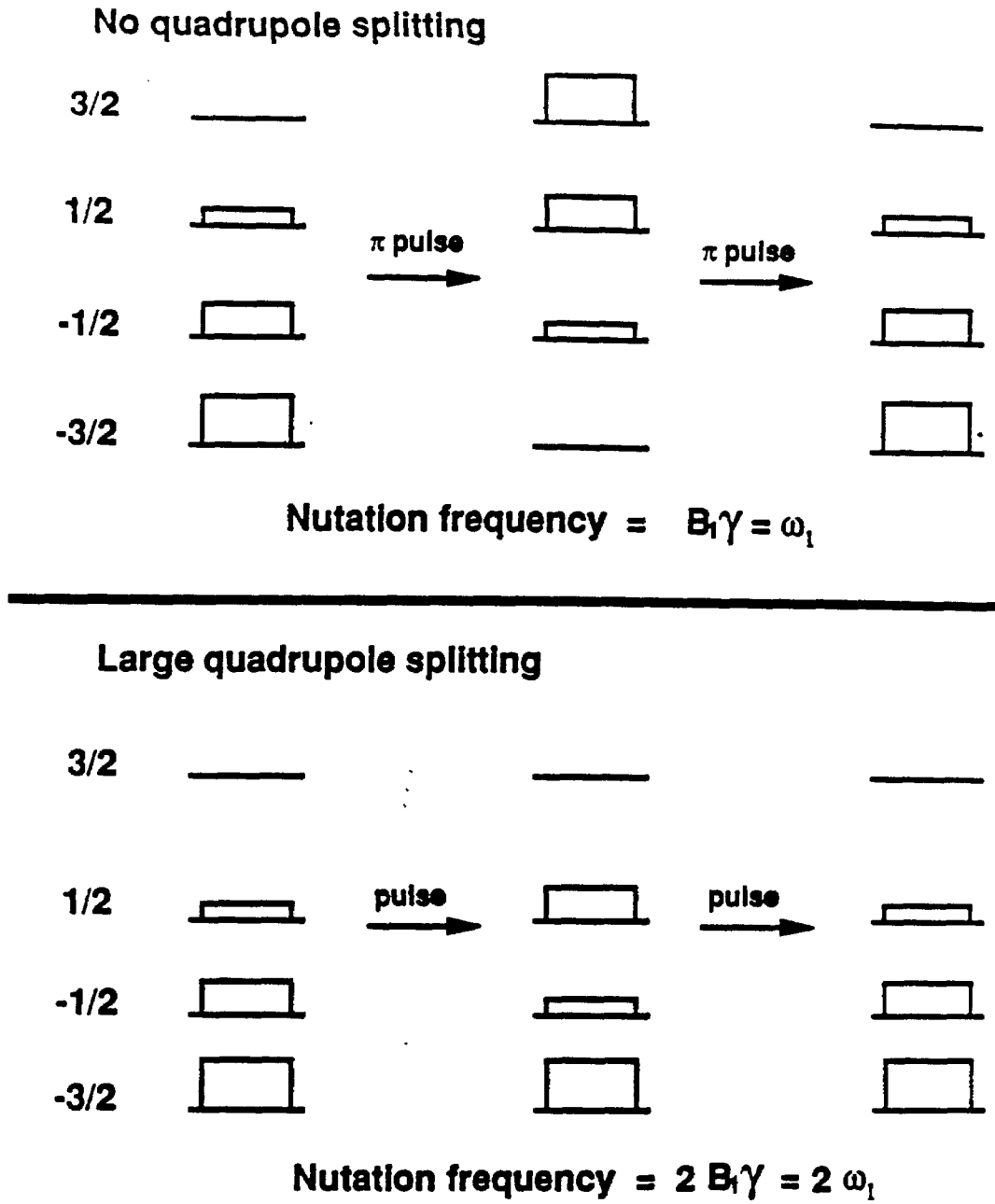

Figure 5.17: Nutation frequencies for a spin I = 3/2. With no quadrupole splitting (upper diagram) the rf field excites all three allowed transitions and the nutation frequency is equal to ω_1. In the limit $\omega_Q >> \omega_1$ (lower diagram), only the central transition is excited by the rf field and the observed nutation frequency is $2\omega_1$.

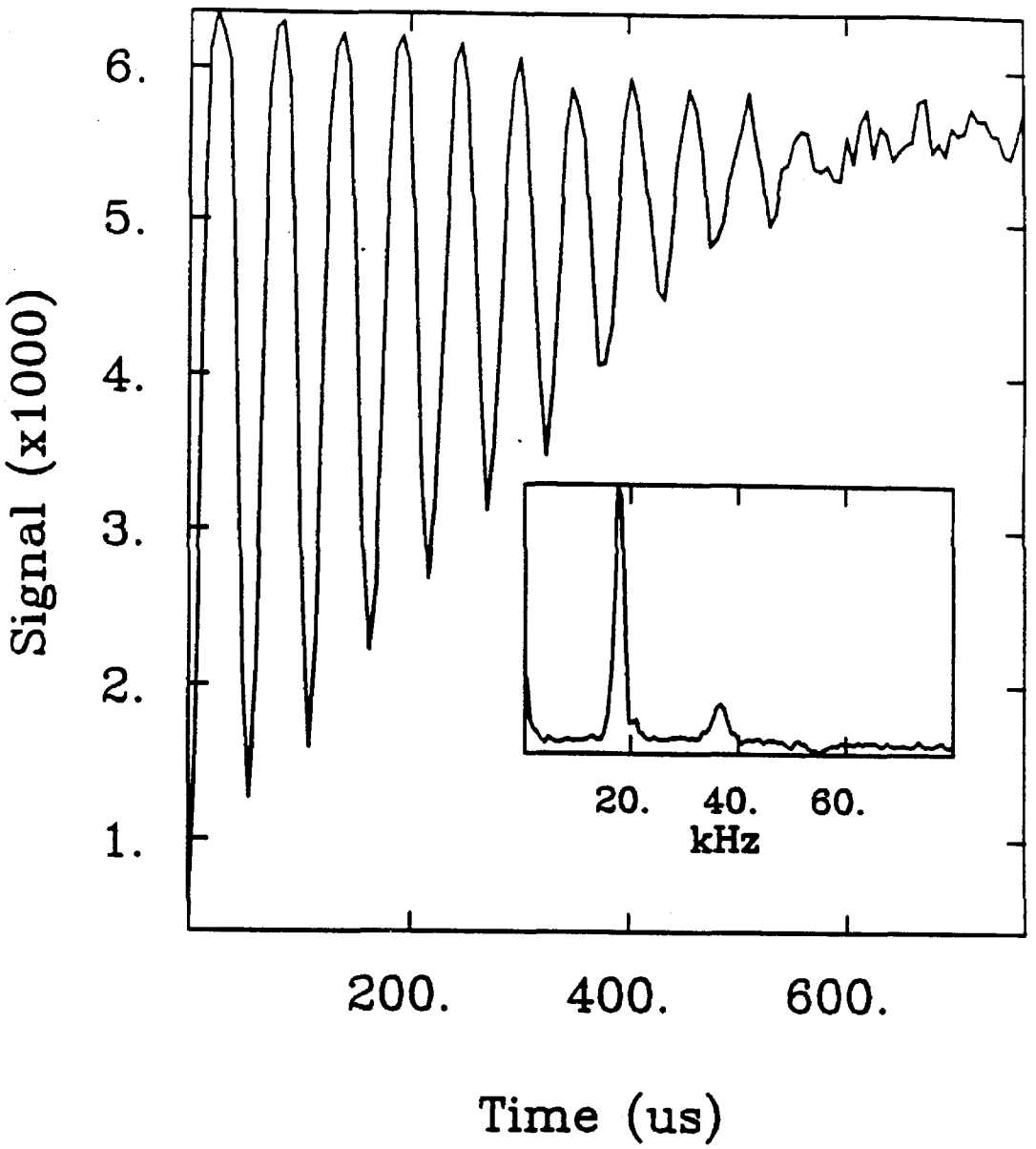

Figure 5.18: ^{71}Ga Nutation TSONMR of sample 5. The frequency spectrum (inset) shows nutation at ω_1 = 18 kHz and $2\omega_1$ = 36 kHz indicating the presence of strong electric field gradient perturbations (ω_Q >> 18 kHz).

sample 5 shown in Figure 5.18. For this experiment, nutation frequencies were detected at ω_1 = 18 kHz and $2\omega_1$ = 36 kHz indicating electric field perturbations far in excess of 18 kHz. Both of these results are consistent with the results of the FT–TSONMR experiments on samples 4 and 5 which did not show resolved splittings in the case of sample 4 but did show splittings in the case of sample 5.

There have been few quantitative results for the quadrupole perturbations in GaAs semiconductors. In conventional NMR experiments performed on an isovalently–doped GaAs sample with an In concentration of $10^{19}/cm^3$, the second shell of As atoms showed a quadrupole coupling of approximately 1 MHz. The first As shell resonances have not been found in these samples presumably because of the low number of atoms and their large splittings. The quadrupole splittings of the first shell of As atoms have been measured to be 16 MHz using steady–state ODNMR on a p–type $Ga_{1-x}Al_xAs$ (x = 0.3) sample. [19] The exact splittings certainly depend on the defect responsible for reducing the symmetry, but using these numbers as a guide the splittings detected in our FT–TSONMR experiment must be from spins well removed from the defect.

5.2.4 Two–Dimensional TSONMR

The observation of a nutation frequency of $2\omega_1$ in the ^{71}Ga nutation TSONMR spectrum of sample 5 affords the possibility of using two–dimensional nutation spectroscopy to separate the resonances of the strongly perturbed sites from those of the bulk sites. [16,17] The 2D nutation experiment is performed in the following manner: (i) a nutation pulse of length t_1 is applied, (ii) a period of free evolution at the end of t_1 for a time t_2, and (iii) restoration of the transverse magnetization to longitudinal magnetization for optical detection. The rf pulse sequence for 2D nutation is given in Figure 5.19.

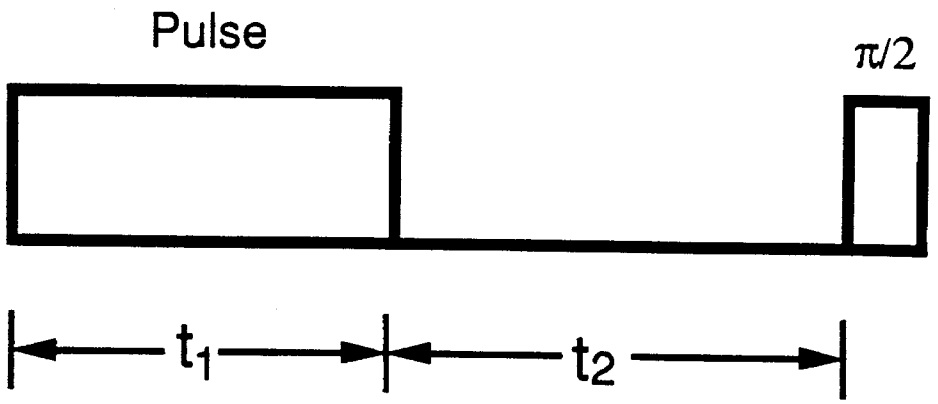

Figure 5.19: 2D nutation TSONMR spectroscopy. The pulse sequence in the figure is applied in the NMR part of the time–sequenced experiment. The nutation spectrum is encoded in the t_1 dimension and the free evolution spectrum is encoded in the t_2 dimension. The spectrum is recorded in a 3D fashion because of the pointwise nature of the FT–TSONMR technique. An entire TSONMR FID is acquired for each increment in t_1.

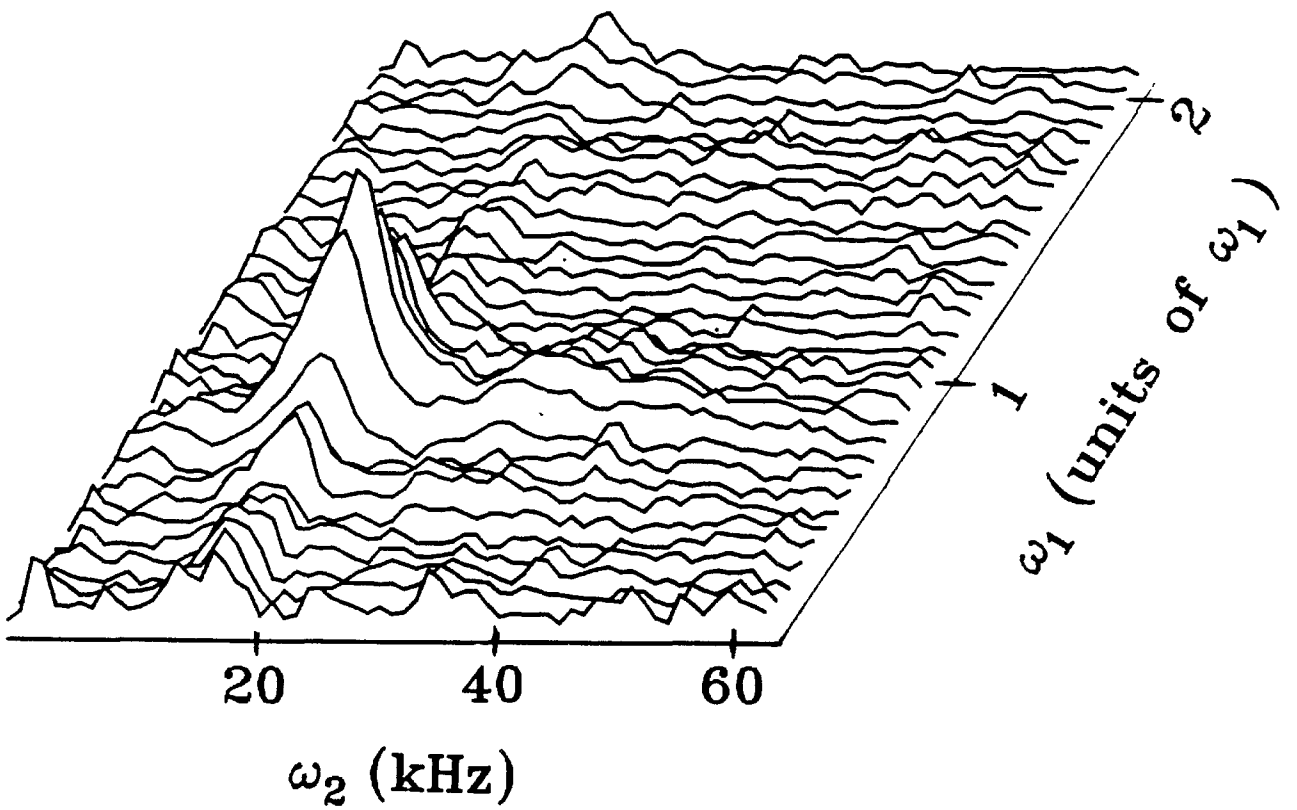

Figure 5.20: ^{71}Ga 2D Nutation TSONMR of sample 5. The two sites are separated in the ω_1 dimension. The second–order shifts in the free evolution (ω_2) dimension are buried in the noise. The data is an accumulation of 2 averages and was recorded over 12 hrs. The spectrum contains 64 t_1 points and 32 t_2 points.

The 2D nutation TSONMR experiment is analogous to a three–dimensional NMR experiment since a full pointwise FT–TSONMR spectrum was recorded for each nutation pulse length t_1. The result of this experiment on the ^{71}Ga resonance of sample 5 is shown in Figure 5.20. The spectrum took 12 hrs to acquire for an accumulation of 2 averages. The 2D signal $S(t_1,t_2)$ is Fourier transformed with respect to both t_1 and t_2 to yield the spectrum of Fig. 5.20. The ω_1 dimension represents nutation, and a projection along this axis should yield the same spectrum seen in Fig. 5.18. The ω_2 dimension represents free evolution, and a projection onto this axis yields the same spectrum seen in Fig. 5.12. The full 2D data set shows two sets of resonances separated in the ω_1 dimension, one at frequency ω_1 which represents the resonance of the bulk sites, and one at frequency $2\omega_1$ which represents the resonance of the perturbed sites.

5.2.5 Time–Domain Relaxation Measurements

In addition to the NMR spectral information which can be found from FT–TSONMR and TSONMR nutation experiments, the time–sequenced technique can also measure NMR relaxation times.

The $T_{1_{off}}$ measurement by FT–TSONMR is done with a suitable adaptation of the inversion–recovery experiment widely used in conventional NMR. The spins are inverted by a $\theta_x = \pi$ pulse followed by a recovery delay t_1 which is incremented for each point on the decay curve. The spin–lattice relaxation curve from this experiment for ^{71}Ga nuclei in sample 4 is presented in Figure 5.21. The data is fitted to a single exponential decay with a T_1 time constant of 2.4 seconds. None of the spin diffusion effects are seen in the measurement of T_1 by time–domain techniques. This observation is consistent with the hypothesis that the time–domain experiments are sensitive to different sites than the CW experiment. Spin diffusion

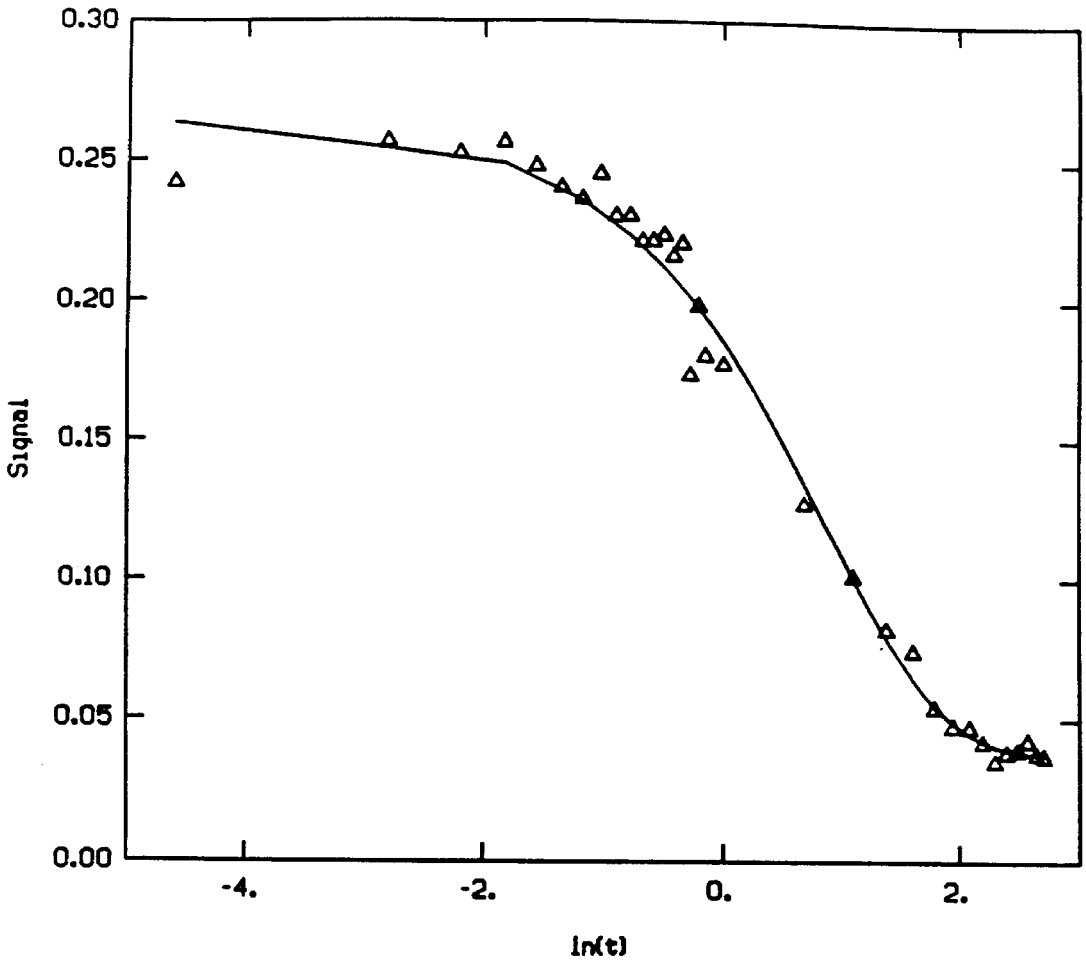

Figure 5.21: ^{71}Ga spin–lattice relaxation of sample 4 by time–domain TSONMR. The data shows none of the spin diffusion effects seen in the CW variant of the experiment. The single exponential time constant $T_{1_{off}} = 2.4$ s corresponds to the fitted solid line.

does not occur in this case because the strong rf pulse excites both the perturbed and unperturbed spins alike, and very little spin temperature difference between the two sites exists. Spin diffusion processes will be examined in detail in the next subsection.

5.2.6 Spin Diffusion Effects

In previous quasi steady–state ODNMR experiments spin diffusion has been shown to be a link between the bulk nuclear spins and the nuclear spins which are optically polarized and detected (in a sphere of radius 10 nm about the ORD).[6] These more distant spins influence the optically detected NMR signal by coupling to the near nuclei through nuclear dipole–dipole interactions. The diffusion constant and the diffusion radius for ^{75}As in high–purity GaAs have been previously determined experimentally. [12] The effect of spin diffusion was noted previously (subsection 5.1.3) in the $T_{1_{off}}$ data of ^{71}Ga and ^{69}Ga obtained from measurements using CW–TSONMR. In this subsection it will be shown that spin diffusion links the two groups of sites seen by CW–TSONMR and FT–TSONMR, respectively.

The difference between the CW and FT TSONMR experiments can be qualitatively understood in terms of three populations of nuclei at increasing distance from the ORD as illustrated in Figure 5.22. For the nearest several shells only the central transition is within the pulse bandwidth, giving rise to the $2\omega_1$ nutation components. These sites are not observed in sample 4. Outside these nuclei are less perturbed sites whose quadrupole satellites lie within the pulse bandwidth. These sites are responsible for the broadening in the FT–TSONMR resonance. Still further distant are the most abundant sites, those with undetectable perturbation by the ORD. These three populations interact through spin diffusion. In the CW experiment, the perturbed sites are not seen despite their dominant contribution to

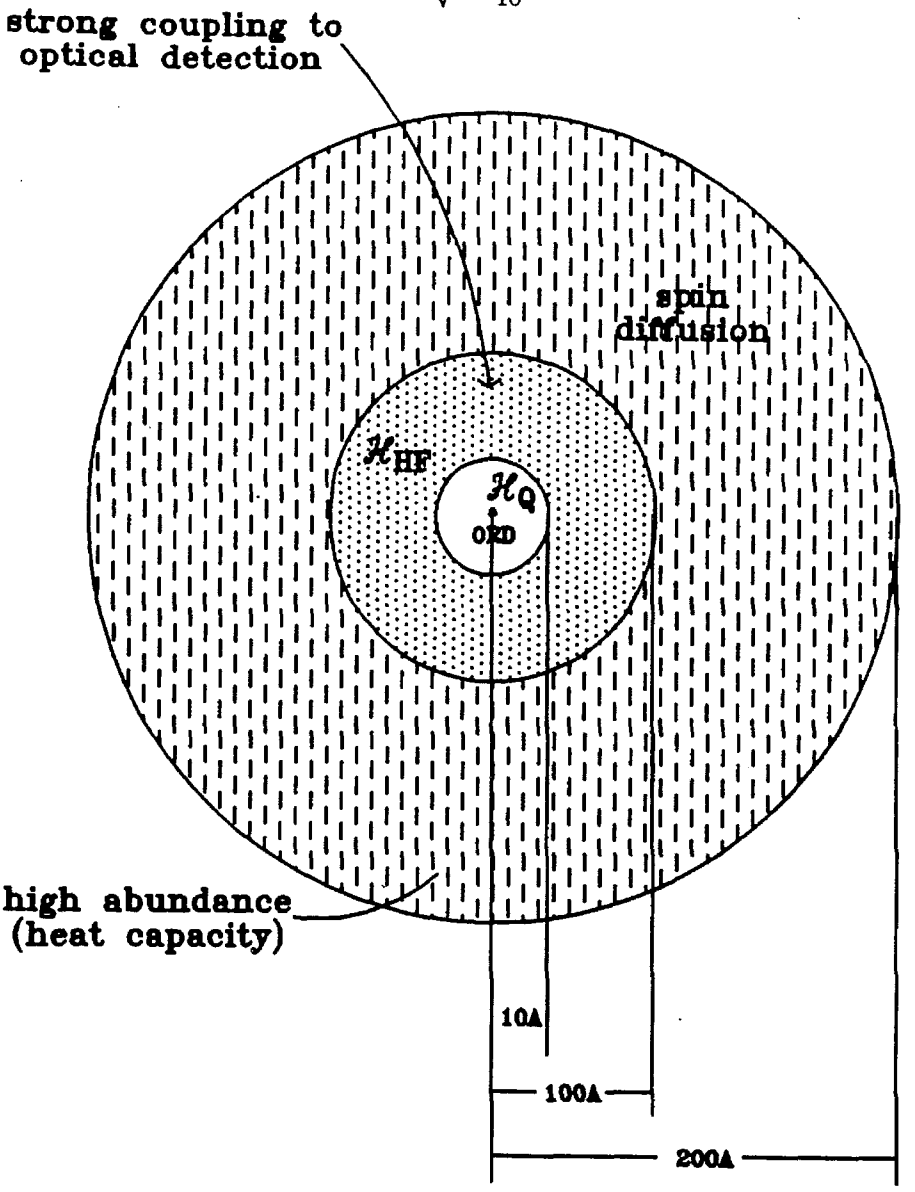

Figure 5.22: The influence of the ORD. The nuclei nearest the ORD (unhatched region) not only feel a strong hyperfine coupling, but also a strong quadrupole coupling. At a somewhat farther distance distance from the ORD (dotted region) the nuclei still feel a hyperfine interaction, but experience a much weaker quadrupole coupling. The numerous bulk sites farther than 100 Å from the ORD do not directly couple to the optical detection, and can only influence the TSONMR spectrum by spin diffusion.

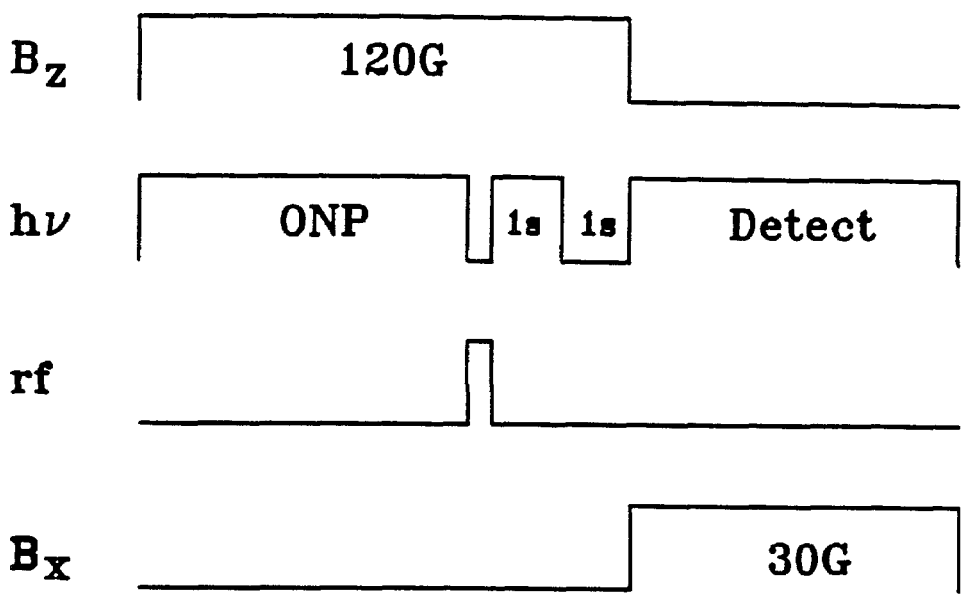

Figure 5.23: Timing sequence for manipulating spin diffusion. The FT–TSONMR two–pulse sequence is applied during the NMR part of the experiment. The extra ONP after the rf pulses nullifies the contribution of the spins near the ORD. The dark time allows the signal from the bulk sites to couple to the optical detection through spin diffusion.

the optically–detectable nuclear field because any small resonant perturbation of their spin–temperature is erased by contact with the cold and numerous distant spins. In the FT and nutation experiments this suppression is ineffective because of the greater modulation of the nuclear field and the smaller spin–temperature difference.

We have engineered an experiment to test the spin diffusion link between the different spin populations. The timing sequence for this experiment is given in Figure 5.23. The NMR part of the experiment consists of the same $\pi/2_x - t_1 - \pi/2_x$ pulse sequence used in FT–TSONMR. Once the rf pulse sequence is complete the exciting light is restored, nullifying the contribution of the sites near the ORD (with nonzero quadrupole couplings) by repolarizing them. After the extra ONP time, a delay in the dark is initiated to allow distant spins to couple to the optical detection by spin diffusion. The expected result of this experiment is a lineshape similar to the CW–TSONMR lineshape since the contribution of the perturbed sites to the signal was erased by the extra ONP.

The dashed trace of Figure 5.24 shows the result of the experiment described above for the ^{71}Ga resonance of sample 4. The experiment represented by the dashed trace probes the same sites as the CW–TSONMR experiment (dotted trace) as indicated by the smaller linewidth than the FT–TSONMR experiment (solid trace). Figure 5.25 shows the result of the same experiment applied to sample 5. While there is a narrowing of the central transition (from ~ 5.5 kHz to ~ 3.2 kHz) and removal of most of the structure by extra ONP and spin diffusion (dashed trace), the sites probed by this experiment are still different than the sites probed by CW–TSONMR (dotted line) as indicated by the resonance shift.

The narrowing of the line by manipulating spin diffusion is illustrated more effectively by a spin–echo experiment. The timing sequence for this experiment is the same as shown in Fig. 5.23 except that the spin–echo sequence is used as the

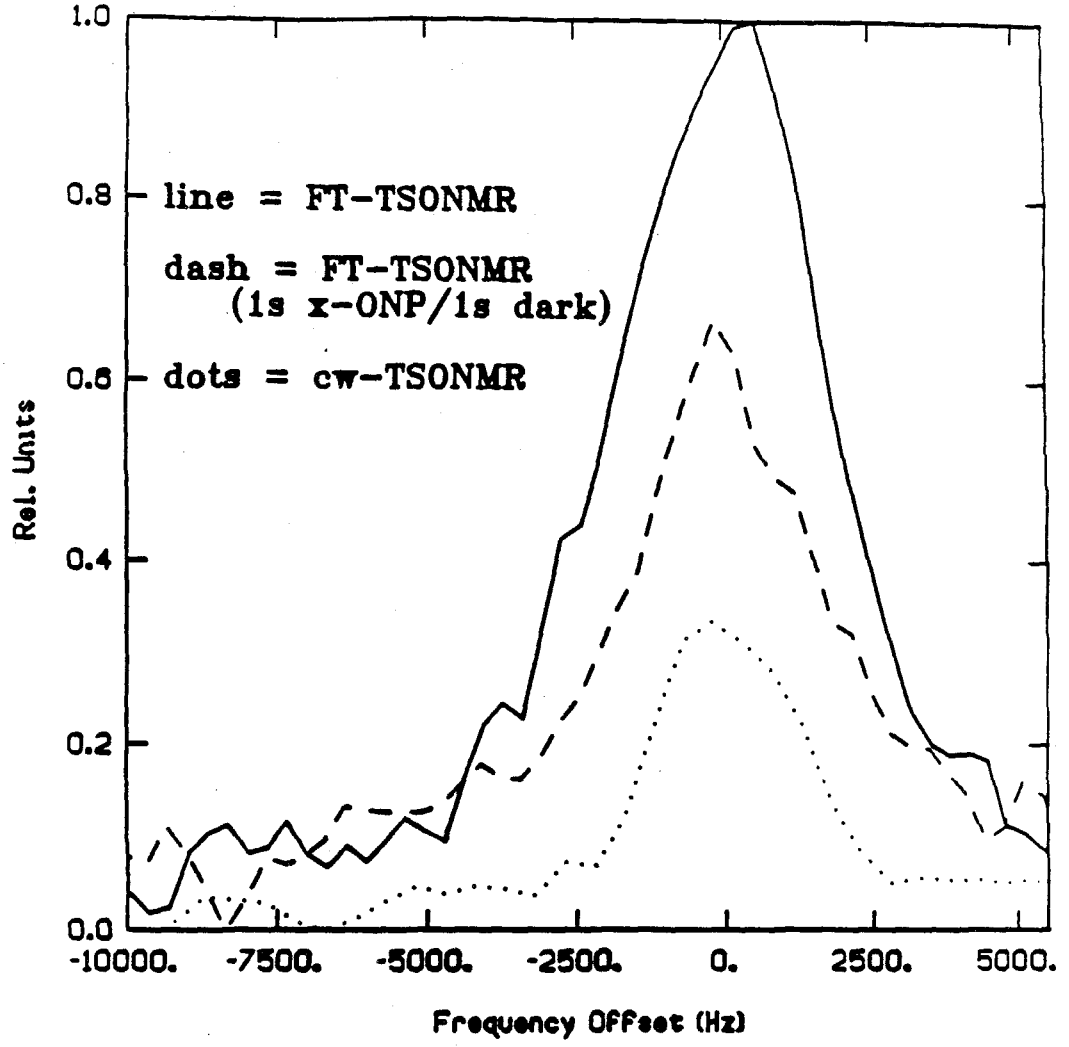

Figure 5.24: Manipulating spin diffusion in sample 4. The data is from the ^{71}Ga resonance. The experiment involving extra ONP and spin diffusion (dashed trace) probes the same sites as the CW–TSONMR experiment (dotted trace) as indicated by the smaller linewidth than the FT–TSONMR experiment (solid trace).

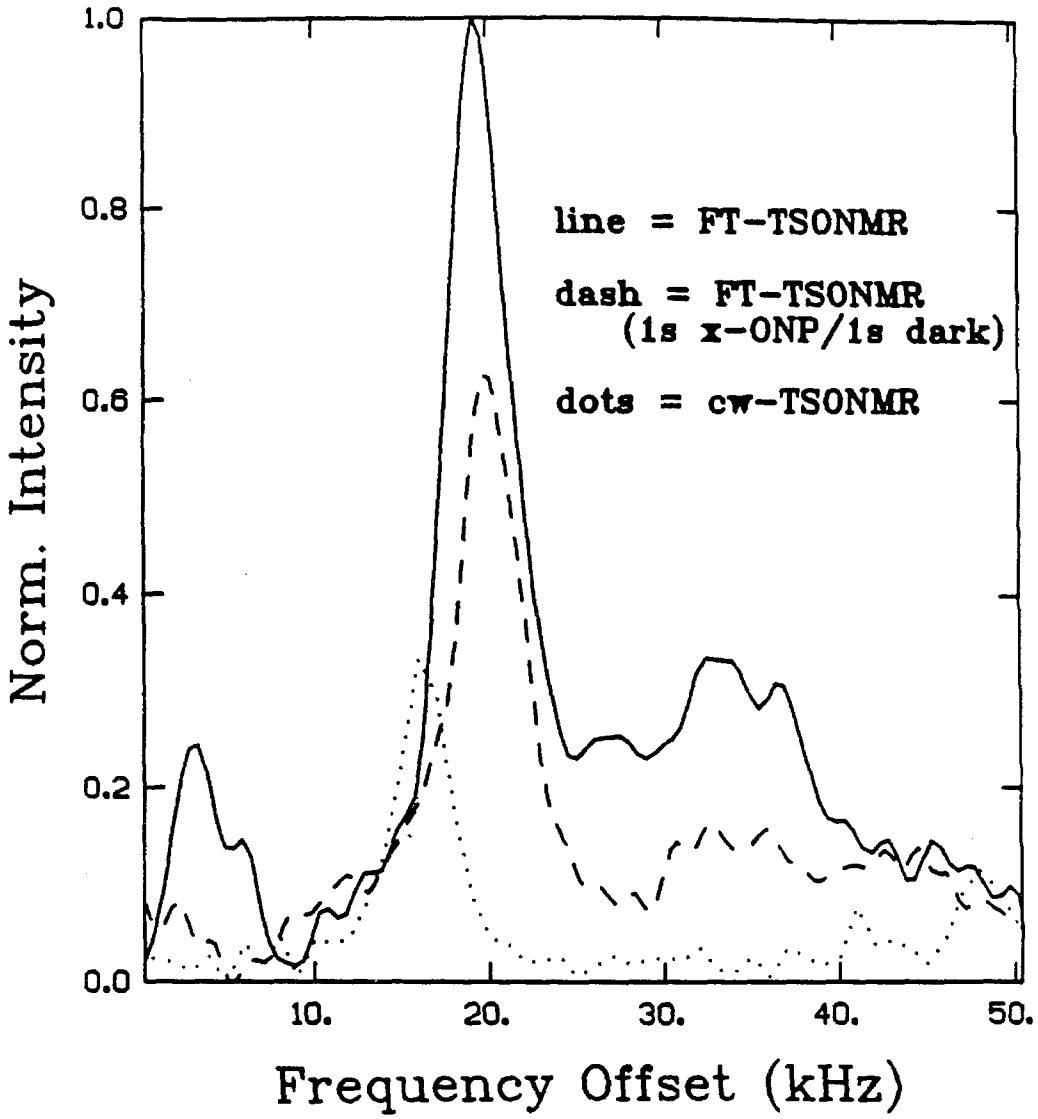

Figure 5.25: Manipulating spin diffusion in sample 5. The data is from the ^{71}Ga resonance. The experiment involving extra ONP and spin diffusion (dashed trace) removes the structure seen in the FT–TSONMR experiment (solid trace) and has a smaller linewidth, but the experiment does not reproduce the same resonance frequency as the CW–TSONMR experiment (dotted trace).

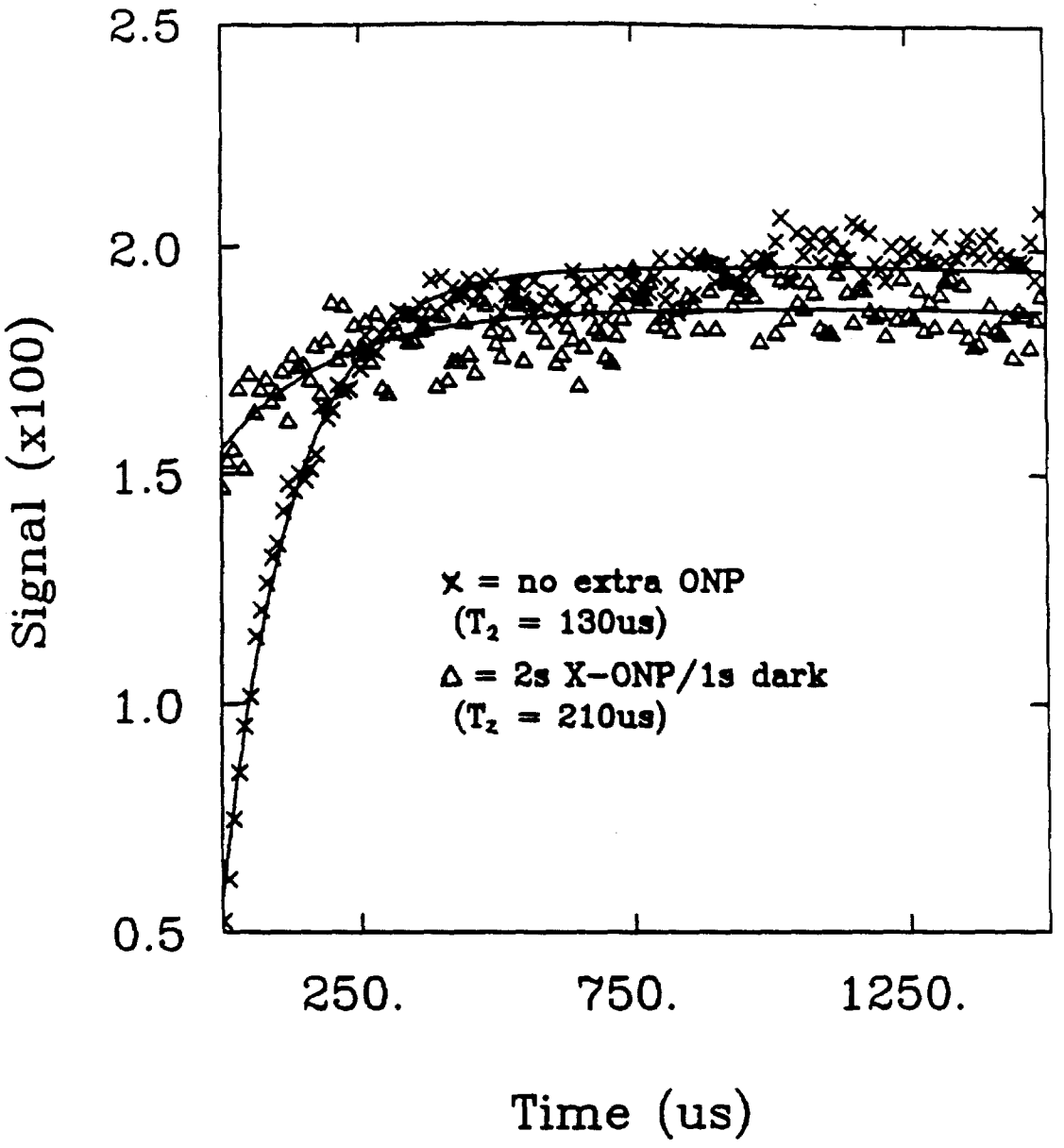

Figure 5.26: Manipulating spin diffusion in Hahn spin–echo TSONMR of sample 4. The data is for the ^{71}Ga resonance. The effect of the extra ONP followed by spin diffusion (triangles) is seen as an increase in T_2. The other data set (x) is the same as in the Hahn spin–echo of Fig. 5.14.

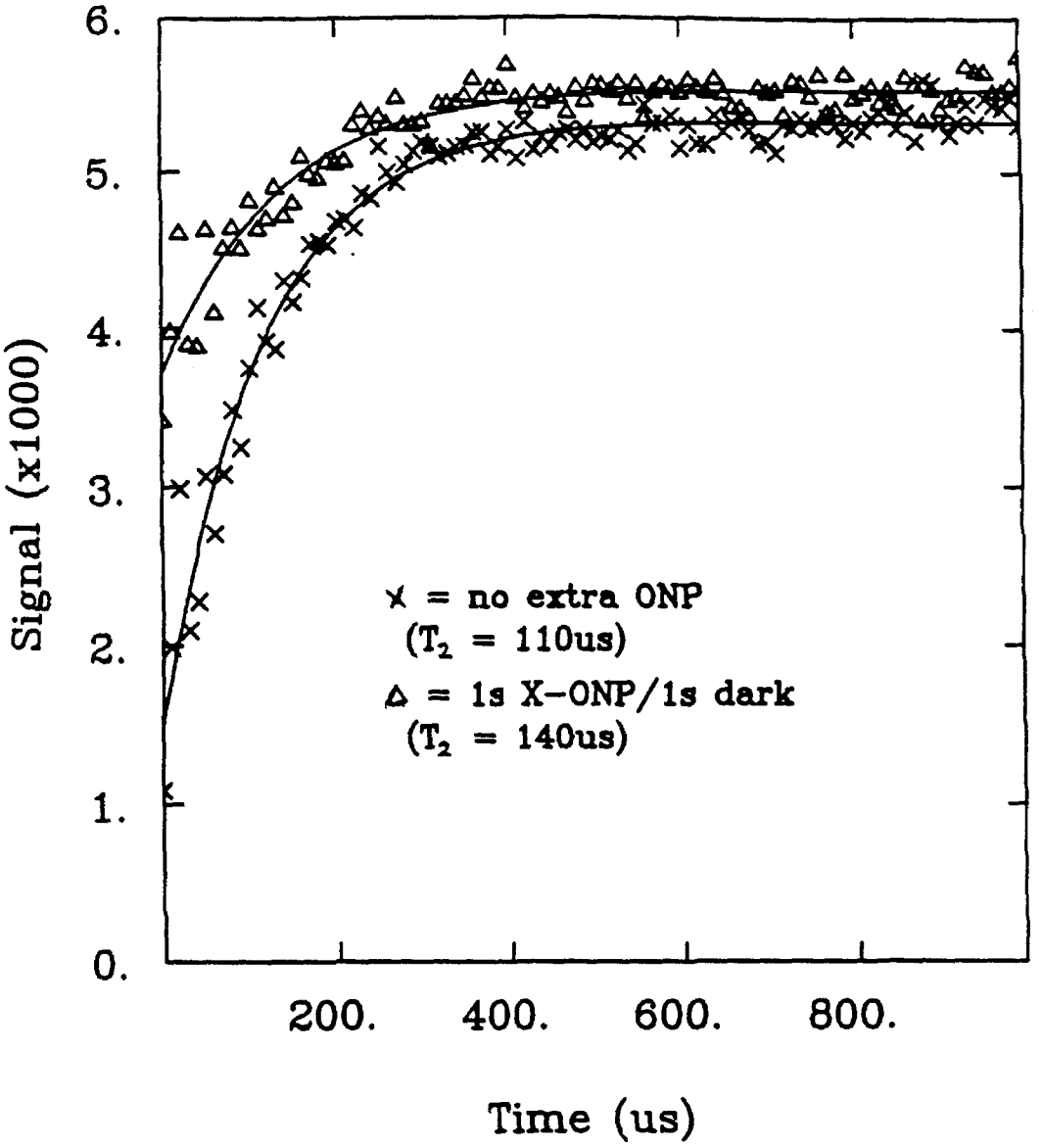

Figure 5.27: Manipulating spin diffusion in Hahn spin–echo TSONMR of sample 5. The effect of the extra ONP time and spin diffusion is not as dramatic as the effect on sample 4. The time constant increases marginally over the time constant from the data of Fig. 5.15.

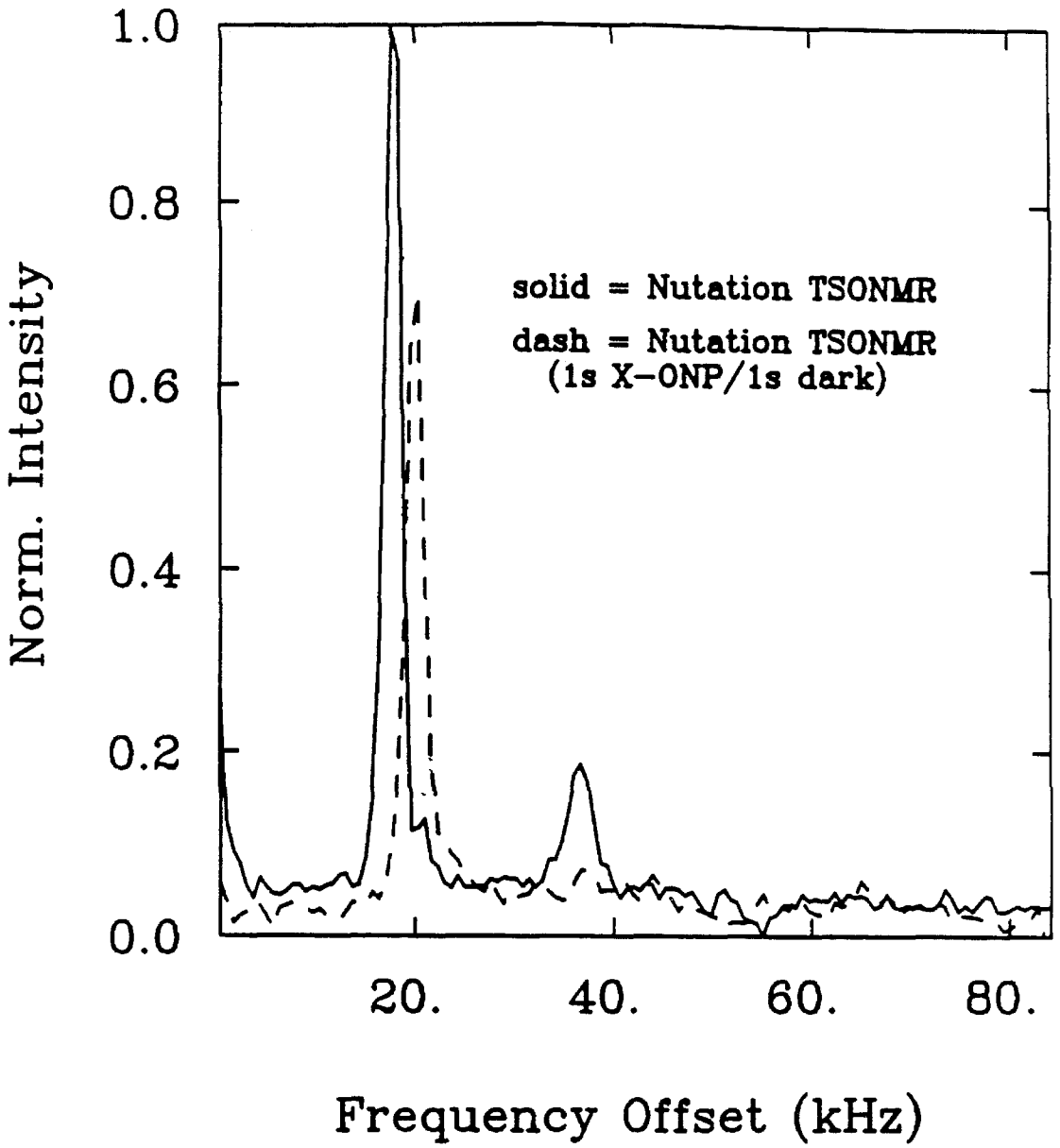

Figure 5.28: Manipulating spin diffusion in nutation TSONMR of sample 5. The experiment involving extra ONP and spin diffusion (dashed trace) shows an anomalous shift in nutation frequency. The peak at $2\omega_1$ is absent in the dashed trace.

NMR part of the experiment. Figures 5.26 and 5.27 show the results of this experiment for samples 4 and 5, respectively. In each case the echo amplitude decays more slowly for the extra ONP/spin diffusion experiment indicating that this technique removes the contribution of the quadrupole–perturbed sites to the line broadening.

We have also performed the nutation variant of the extra ONP/spin diffusion technique on sample 5. Figure 5.28 shows the results of this experiment. An anomalous shift in the nutation frequency is seen in the extra ONP/spin diffusion experiment as well as the expected elimination of the peak at $2\omega_1$.

5.2.7 Multiple–pulse line–narrowing and TSONMR

The ability to perform time–domain TSONMR experiments makes the use of multiple–pulse line–narrowing pulse sequences in the NMR part of the experiment possible. We have performed line–narrowing experiments using the two pulse sequences shown in Figure 5.29. The data in Figure 5.30 is from the WAHUHA [20] four–pulse sequence (Fig. 5.29a) performed on sample 5. This pulse sequence averages away the homonuclear spin–spin coupling and first–order quadrupole contributions to the linewidth. The linewidth of the trace of Fig. 5.30 is approximately 350 Hz, an order–of–magnitude narrower than the FT–TSONMR linewidth. The lineshape is noteworthy. The WAHUHA sequence does not average the second–order quadrupole interaction to zero, but scales it down by a factor of $\sqrt{3}$. The peaks occuring in the wings of the line–narrowed spectrum could possibly be due to second–order quadrupole shifts unresolved in the FT–TSONMR spectrum.

Figure 5.31 shows the application of the 16–pulse sequence (Fig. 5.29b) to sample 5. This 16–pulse sequence [21–24], common in solid–state imaging

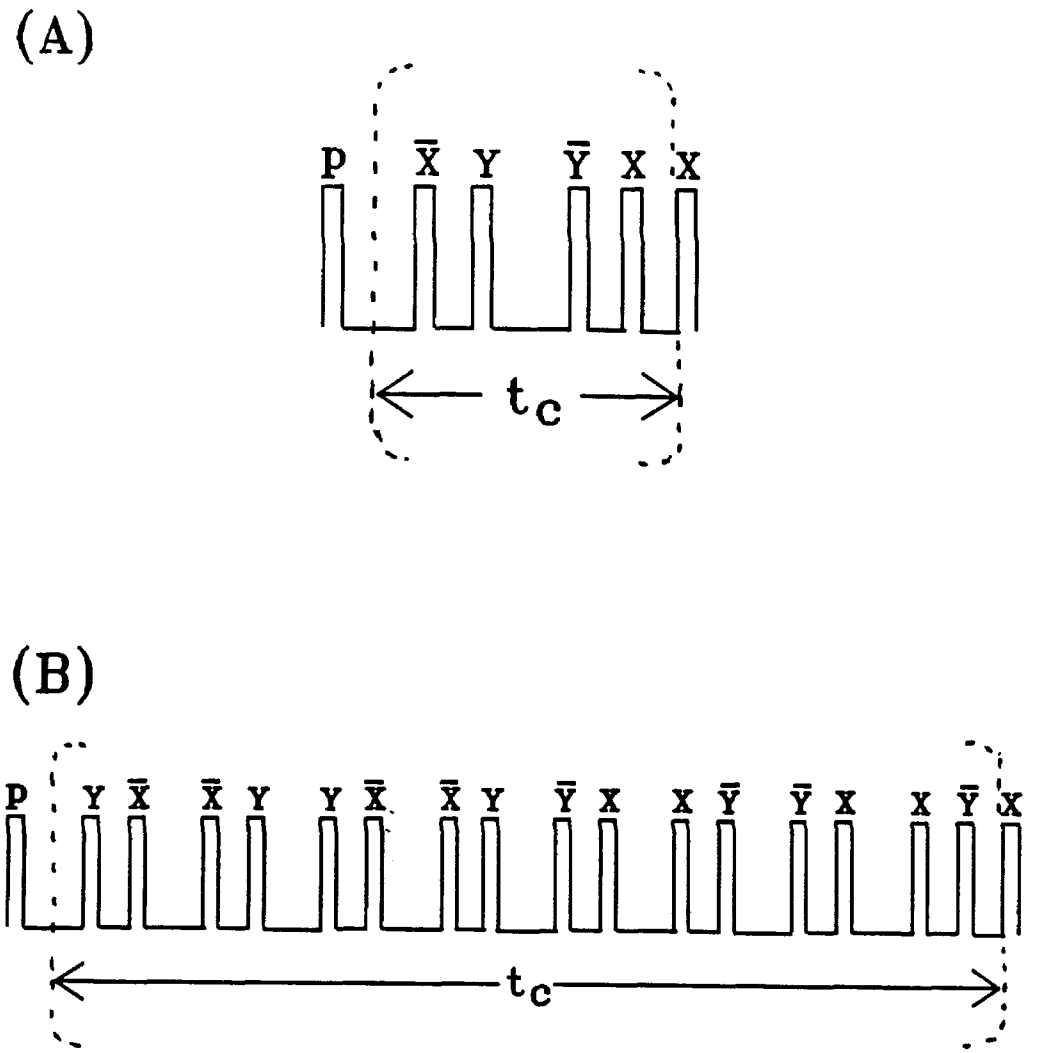

Figure 5.29: (A) WAHUHA four–pulse sequence and (B) 16–pulse sequence. Each sequence begins with a preparation pulse P. The pulse cycle is enclosed in parentheses and the number of cycles is incremented for each iteration of the TSONMR timing sequence. The cycle time is denoted by t_c. The sequence of part (A) averages terms bilinear in I_z (homonuclear dipolar couplings and first–order quadrupole couplings) to zero and scales terms linear in I_z by $1/\sqrt{3}$. The sequence in part (B) averages all dipolar couplings (heteronuclear and homonuclear) and quadrupole couplings to zero as well as removing the resonance offset.

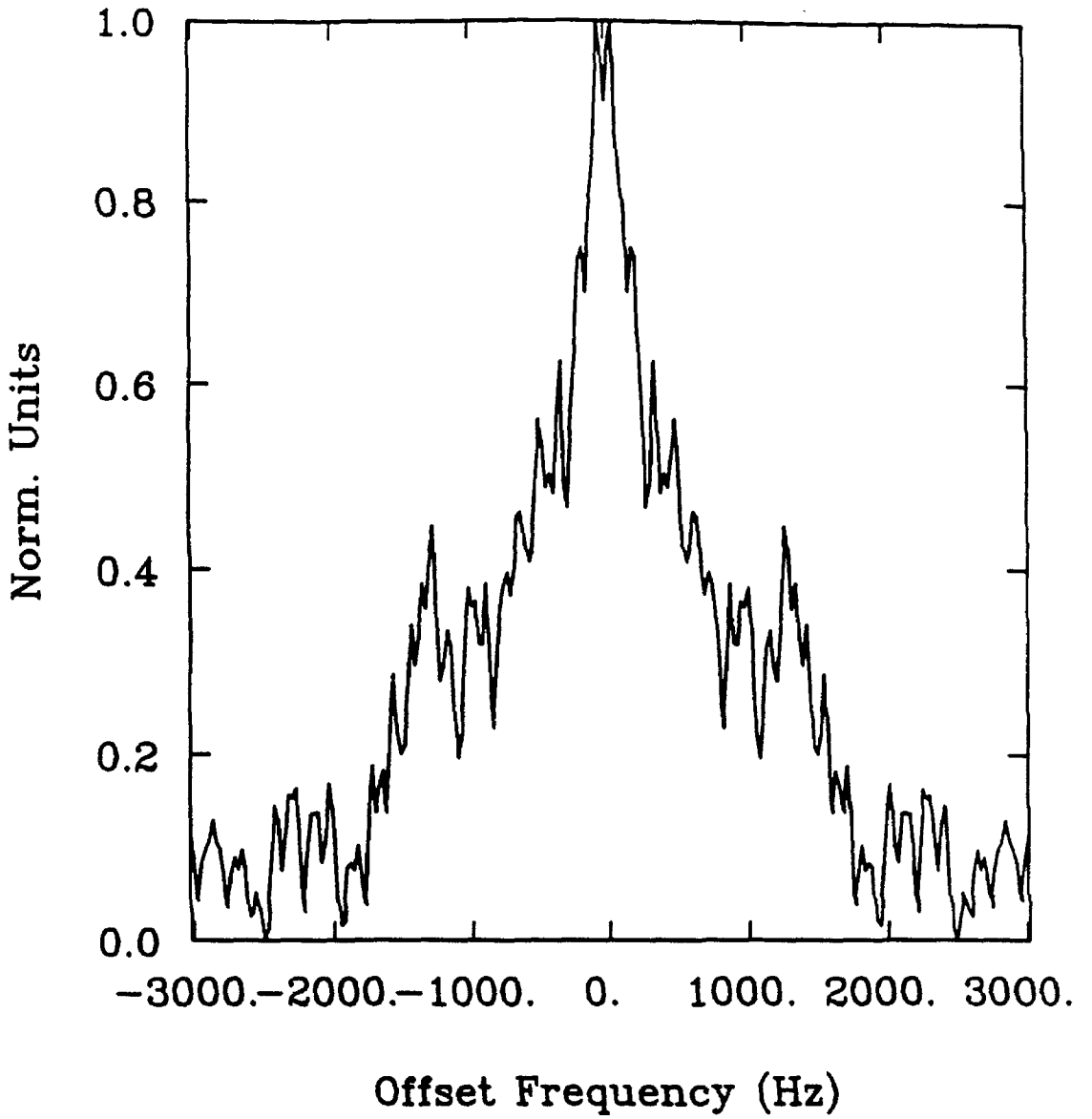

Figure 5.30: ^{71}Ga Line–narrowing TSONMR of sample 5 using the WAHUHA sequence. The preparation pulse was a $\pi/4_x$ pulse. The cycle time was 152 μs and the $\pi/2$ pulse widths were 19.0 μs. The total linewidth is approximately 350 Hz, and structure appears in the wings which could be second–order shifts which are not averaged by the sequence. The data is a mirror image about zero offset because only one channel is detected (see text).

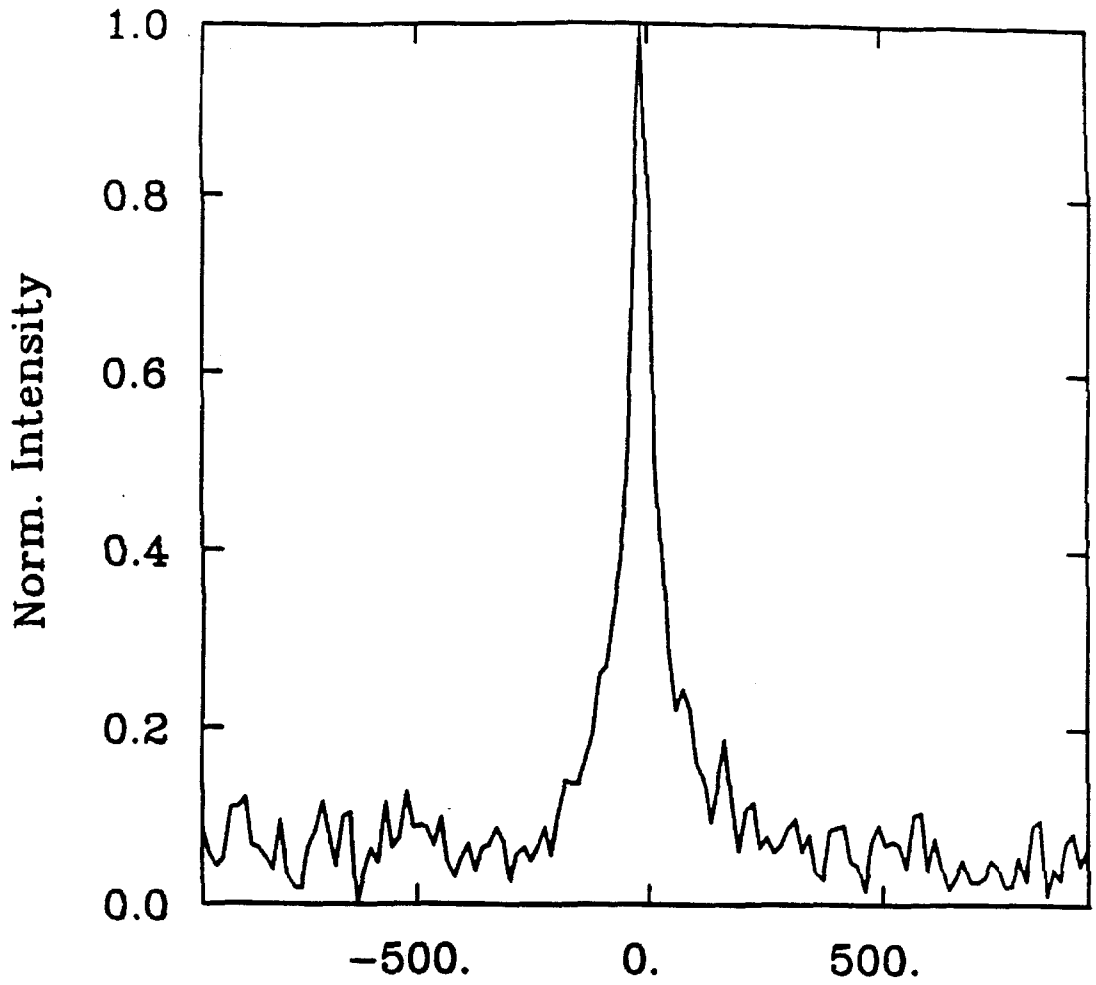

Figure 5.31: ^{71}Ga Line–narrowing TSONMR of sample 5 using a 16–pulse sequence. This experiment was performed using the 16–pulse sequence of Fig. 5.29b. In this experiment both channels were detected by performing two experiments: one with a finishing pulse of $\pi/2_x$ and the other with a finishing pulse of $\pi/2_y$. The cycle time was 550 μs and the $\pi/2$ pulse widths were 19.0 μs. The linewidth is approximately 100 Hz.

experiments, is designed to average the heteronuclear and homonuclear dipolar interactions and the quadrupole interaction to zero as well as to remove the resonance offset. The line–narrowing performs much better in this case yielding a single line of width approximately 100 Hz. The use of multiple–pulse line–narrowing TSONMR experiments in resolving optical Knight shifts will be addressed later in this chapter.

5.2.8 Discussion

Two important results are seen from the time–domain TSONMR data of this chapter. First, the FT–TSONMR experiment probed sites that are different from those detected by CW–TSONMR. Through the use of a spin–echo, the mechanism of the broadening was determined. The broadening in the central transition was due to unresolved first–order quadrupole couplings, while the structure observed in sample 5 was due to second–order effects. The nutation experiment provided the strength of the couplings relative to the rf field strength ω_1. For sample 4 the couplings were much smaller than the 12 kHz rf field, but sample 5 showed sites with couplings much larger than the 18 kHz rf field used. The sites observed by CW–TSONMR can be observed by FT–TSONMR by controlling spin–diffusion between the far away spins and the optically–detected volume. This experiment reconciled the results from both FT–TSONMR and CW–TSONMR.

The second observation is the dramatic difference in the FT–TSONMR spectra of samples 4 and 5. The quadrupole effects in sample 5 are much greater than those in sample 4. This result indicates that although the two samples are electrically–equivalent (p–type with 10^{17} Zn atoms/cm^3) their ORD's are much different. This result raises the question of how growth conditions determine the ORD. This question could be answered by obtaining a series of samples grown under

controlled conditions and comparing their time–domain TSONMR spectra.

The difference in resonance frequency between the FT–TSONMR and CW–TSONMR spectra of sample 5 is still unexplained as is the shift in nutation frequency with extra ONP and spin diffusion. It cannot be a chemical shift or a second–order quadrupole effect as we have shown that it does not change measurably with a 25% change in B_0^p. One possible explanation is that it is the direct effect of the highl nuclear polarization on the magnetic field seen by the detected spins. This would be absent in the FT experiment since this polarization is in the transverse plane, but present in the CW experiment where the polarization is weekly perturbed. This polarization effect is currently under investigation.

We have demonstrated the capability of both 2D and multiple–pulse TSONMR experiments. In each case the experiment needs to be optimized to fully understand the results. In the 2D nutation experiment peaks are seen separated in the ω_1 dimension, but the structure present in Fig. 5.12 could not be observed above the noise in the ω_2 dimension. This experiment is inherently difficult because of its 3D nature. More averages would be required to interpret the data, but the cost in time would be enormous. An improvement in signal by increasing B_0^p or by lowering the temperature is possible.

The multiple–pulse line–narrowing experiments show promise in selectively averaging spin interactions to uncover new resonances. In the case of the four–pulse sequence [20] structure is observed in the wings which can be interpreted as second–order shifts not resolved in the FT–TSONMR experiment. Because of the low rf field strength, the pulse widths were long and the windows had to be made short in order to keep the cycle time down. By increasing the rf power the pulses would be made short compared to the windows and the averaging would become more efficient. [20] The 16–pulse sequence [21–24], although more robust than its

four–pulse counterpart, would also benefit from shorter pulse widths and longer windows.

5.3 Nuclear Double Resonance and TSONMR

So far the applications of CW–TSONMR and FT–TSONMR have concentrated on the nuclei surrounding an unknown ORD. In this section TSONMR techniques designed to measure the NMR spectrum of the ORD will be discussed. As mentioned, the concentration of these defects is very small in our MBE–grown samples ($10^{15} - 10^{16}/cm^3$). Therefore, in our irradiated volume of 10^{-7} cm^3 there are only $10^8 - 10^9$ ORD's! In order to measure the spectrum of these dilute nuclei, an even greater enhancement in sensitivity than is presently realized with TSONMR is needed. Fortunately, enhancements of up to 10^5 have been observed by employing nuclear double resonance (also called cross polarization or indirect detection) methods long established in conventional NMR [25–27]. Using these double resonance methods in conjunction with TSONMR should result in an extremely high–sensitivity technique.

It will be shown in this section that double resonance TSONMR is feasible based on measurements of the important relaxation parameters that govern the success of cross polarization.

5.3.1 Introduction to Nuclear Double Resonance

In order to obtain the highest possible sensitivity for detecting dilute species in GaAs it will be neccesary to employ cross polarization methods. [25–27] The cross polarization involves a contact between the spins of the dilute species and the spins of the abundant species. Two of the ways to initiate the contact between the

two spins are by spin–locking with matched nutation frequencies (the Hartmann–Hahn experiment) [25] or by a common spin reservoir of dipolar order in zero field (the Slusher–Hahn experiment) [26] or high field (the Lurie–Slichter experiment). [27] Cross polarization methods are easily understood using thermodynamic analogies. The dilute spins are at a higher temperature than the abundant spins (^{69}Ga, ^{71}Ga, or ^{75}As), and a contact is made between the spin systems such that the dilute spins heat the abundant spins. This heating causes the polarization of the abundant spins to decrease which decreases the spin system's contribution to the optically–detected nuclear field and we detect this decrease optically.

The key to the success of cross polarization methods is that the dipolar couplings have time to transfer spin order between the species. The feasibility of this transfer can be shown using measured rate parameters. We have measured a number of these parameters, and the results are described in the next subsection.

5.3.2 Relevant Relaxation Parameters

The important relaxation parameters for double resonance are: the spin–lattice relaxation rate in the dark $1/T_{1_{off}}$, the spin–lattice relaxation rate in the rotating frame $1/T_{1\rho}$, and the spin–lattice relaxation rate for dipolar order $1/T_{1d}$. The time constants $T_{1_{off}}$, and T_{1d} in zero field have been previously measured to be on the order of seconds (see section 4.3). Here we present measurements of the relaxation times $T_{1\rho}$ by spin–locking [28] and T_{1d} by adiabatic demagnetization in the rotating frame (ADRF). [27,28]

Figure 5.32 shows the decay of the spin–locked ^{71}Ga magnetization of sample 4. The spin–locking pulse sequence used in the NMR part of this experiment was

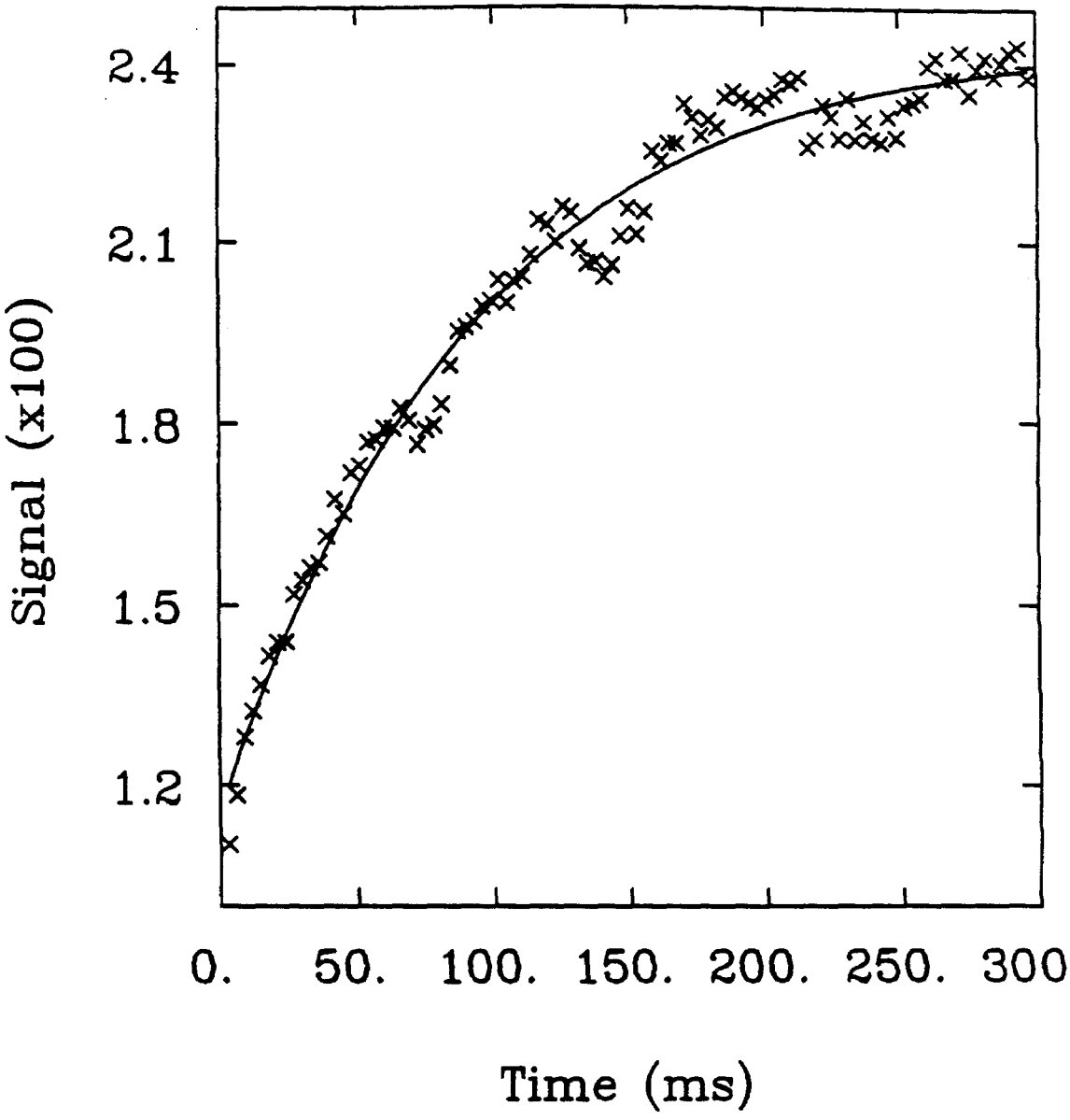

Figure 5.32: ^{71}Ga spin–locking TSONMR of sample 4. The spin–locking was performed off–resonance with the pulse sequence described in the text. The data was fitted to a single exponential yielding $T_{1\rho}$ = 100 ms.

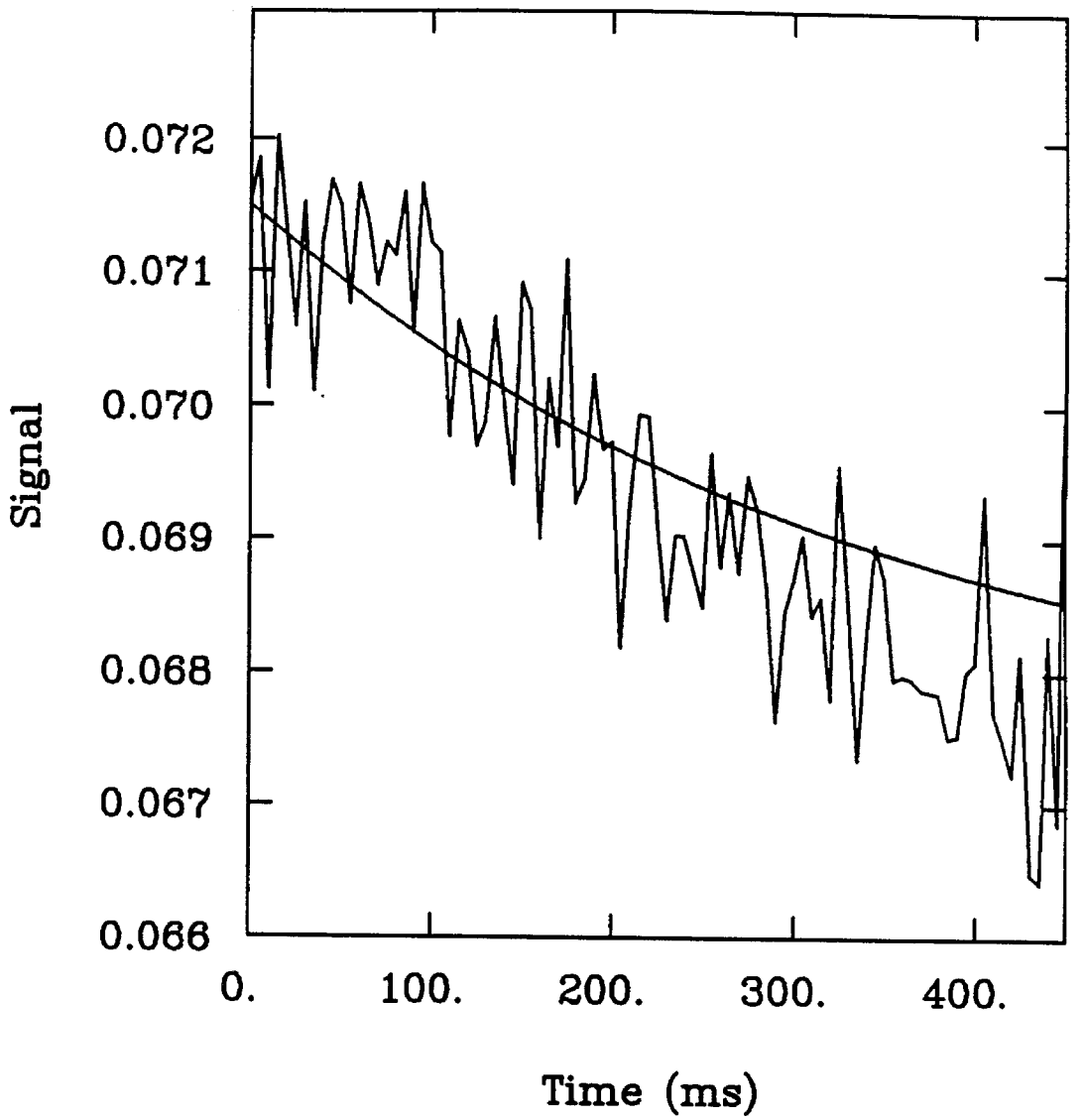

Figure 5.33: ^{71}Ga spin–locking TSONMR of sample 5. The spin–locking was performed on–resonance using the standard $\pi/2_x - \theta_y$ sequence. At the end of the y–pulse another $\pi/2_x$ pulse is given to allow optical detection. The signal starts at the maximum value because the second $\pi/2_x$ pulse inverts the magnetization which corresponds to the largest signal in TSONMR. The signal is still decaying at t_1 = 450 ms, and the time constant $T_{1\rho}$ is $\simeq$ 300 ms.

$$\frac{\pi}{2}_{x} - \tau - (\text{x–pulse of length } t_1) - \tau - \frac{\pi}{2}_{x},$$

where the carrier frequency was set such that $\Delta\omega = \omega_1$, and the delay time τ was set such that $(\Delta\omega)\tau = \pi/4$. Note that the $\pi/2_x$ pulse is calculated for the effective field defined by ω_1 and $\Delta\omega$ (see Eq. 5.11). The above sequence was necessary since at the time of the experiment we had not implemented a quadrature rf source. The data is presented as a function of the length of the spin–locking pulse t_1 and a fit yields $T_{1\rho} = 100$ ms. Figure 5.33 measures $T_{1\rho}$ for sample 5 ($T_{1\rho} \simeq 300$ ms) using a more conventional $\pi/2_x - (\text{y–pulse of length } t_1) - \pi/2_x$. In each case the values for $T_{1\rho}$ are encouraging for the use of double resonance.

We have performed an ADRF experiment [26,28] for sample 5. The rf pulse sequence is shown in Figure 5.34a. In this experiment the magnetization is first spin–locked along the effective field in the rotating frame, and then the spin–locking pulse is ramped adiabatically to zero. During the adiabatic demagnetization the ^{71}Ga magnetization is transformed to dipolar order. [28] The dipolar order then decays during the time t_1 (see Fig. 5.34a) and is remagnetized by adiabatically restoring the spin–locking pulse. Finally, a $\pi/2_x$ pulse is given to store the spin–locked magnetization into magnetization that is optically–detectable. The data of Fig. 5.34b shows the result of this ADRF experiment on sample 5 yielding $T_{1d} = 2.0$ s which is quite favorable for double resonance.

5.3.3 Discussion

The relaxation parameters $T_{1_{off}}$, $T_{1\rho}$, and T_{1d} are all favorable for double resonance. Given the sensitivity of TSONMR, a contact between the dilute spin and the abundant spin of a few seconds will destroy enough nuclear polarization to be optically–detected. It is possible to use parameters from the literature to obtain an

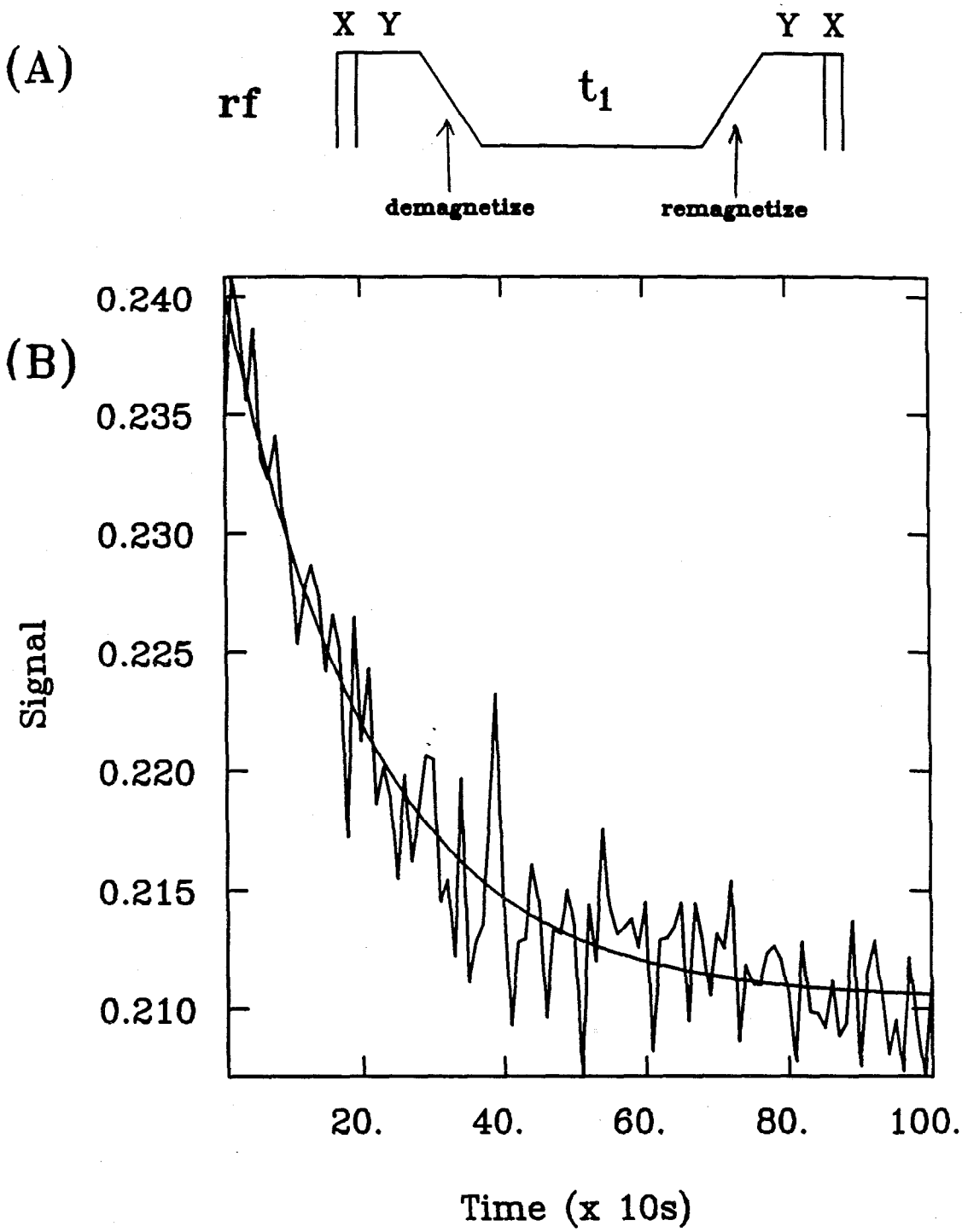

Figure 5.34: ^{71}Ga adiabatic demagnetization in the rotating frame (ADRF) TSONMR of sample 5. The pulse sequence is given in part (A). The data is fitted to a single exponential to yield T_{1d} = 2.0 s.

estimate of the effect of double resonance on the ^{75}As spin reservoir.

In the GaAs lattice (Fig. 1.1) a defect site can never be more than 4Å from any ^{75}As nucleus. Consequently, the cross relaxation times expected between a defect nucleus and an ^{75}As nucleus (10^{-4} to 10^{-2}sec) are much shorter than the T_1 times given above. Through spin diffusion, an ^{75}As nucleus depolarized by contact with a defect nucleus can depolarize an area of radius $\simeq (10^{-13} \text{ x } 10 \text{ cm}^2)^{1/2}$ in ten seconds. [6] If the dilute species were present at a concentration of $10^{17}/\text{cm}^3$ ($\simeq$ 10ppm), all of the sample would fall within such a radius and the depolarization of the ^{75}As nuclei would be complete. Since only a small fraction of the nuclear field needs to be depolarized, the impurity concentration can be much lower than $10^{17}/\text{cm}^3$, perhaps as low as $10^{14}/\text{cm}^3$.

5.4 Resolving Sites by Optical Knight Shifts

In the final section of this chapter, the possibility of applying TSONMR experiments to GaAs heterostructures is examined. The extension of the quasi steady–state ODNMR method to such structures has already been realized [30–32], albeit with the same limitations of the technique discussed in chapter 2. With the use of TSONMR, the possibility of obtaining extreme spectral resolution by means of selective averaging with rf–optical multiple–pulse techniques is discussed. The aim of such an experiment would be to isolate the site–specific changes in the spin Hamiltonian associated with excitation to localized states of the conduction band. Simulations are presented to evaluate the approach proposed. It is concluded that such experiments are capable of the sensitivity and resolution necessary to resolve individual epitaxial layers in high–quality quantum well structures and would provide unprecedented detail on the electronic structure and its uniformity by way of spin–averaged hyperfine interactions.

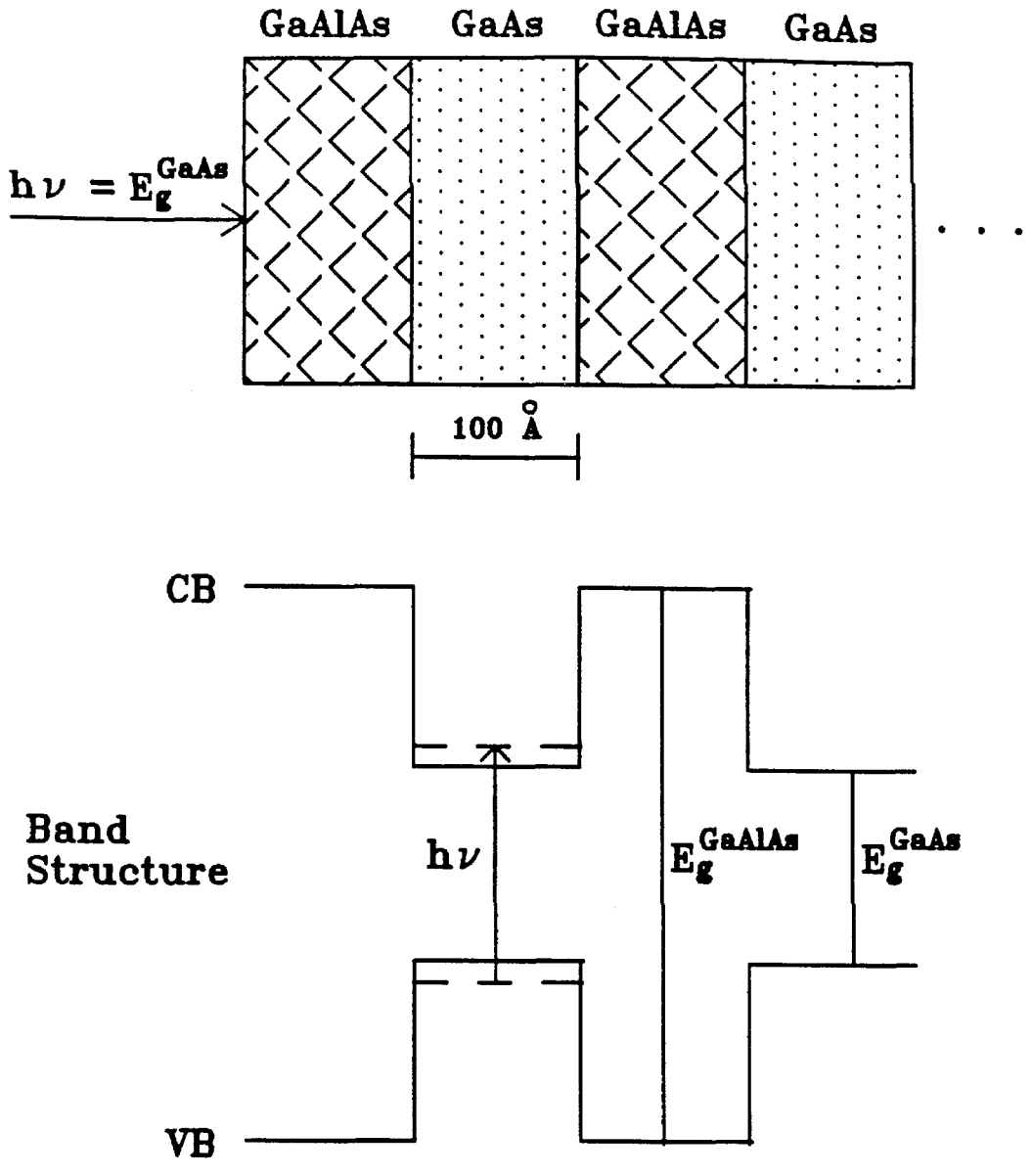

Figure 5.35: GaAs/$Ga_{1-x}Al_xAs$ quantum well. The band offset forms a one–dimensional square–well potential (in the growth direction) for the carriers in the GaAs layer. The optical absorption is quantized by the particle–in–a–1D–box energy levels. The n=1 excitation is shown. The spin–polarized electrons in a quantum well have been shown to produce large nuclear fields (see refs. [30,31]).

Before proceeding to the description of the proposed experiment and the estimates of the results for quantum wells, a brief introduction to these structures is given.

5.4.1 Introduction to Epitaxial Structures

The type of samples considered in this section are of the type with built–in localization such as the GaAs/$Ga_{1-x}Al_xAs$ ($x \simeq 0.3$) quantum well depicted in Figure 5.35. The band structure along the growth direction is completely analogous to a 1D square–well due to the band offset of the two semiconductors. [33,34] A photocarrier generated in the GaAs layer is confined to two dimensions by this offset. The absorption spectrum of a quantum well is quantized with the energy levels of a particle–in–a–1D–box for excitation normal to the growth direction. [33,34] Optical excitation from the n=1 level is shown in Fig. 5.35.

Another important consequence of the quantum well structure is that the inherent strain of the structure (which is due to the different lattice constants of GaAs and $Ga_{1-x}Al_xAs$) breaks the degeneracy of the light and heavy holes (see Fig. 2.1). [34] It is possible to select only the n=1 heavy hole absorption and obtain 100 % electron spin polarization. In the previous optical NMR study of quantum wells, the electron polarization was observed to be 80 % due to non–negligible electron spin relaxation. [30,31] The nuclear field for this sample was estimated to be on the order of 10^4 G and was attributed to efficient ONP by way of the electron localization inherent in the structure.

5.4.2 Resolution of Knight Shifts with 2D Localization

As was seen in section 5.1.4, the optical Knight shift in bulk GaAs is

dominated by localized electrons, and the magnitude of the shift varies spatially as the square of the donor state wavefunction. A similar situation is expected for electrons localized in quantum wells, where the Knight shift is modulated according to the eigenfunctions of the appropriate 1D square–well potential.

The Knight shift measurement has apparently not yet been attempted in a GaAs/$Ga_{1-x}Al_xAs$ quantum well, but has been observed in a p–channel $Al_xGa_{1-x}As$/GaAs heterojunction (x = 0.36). [32] In the heterojunction the Knight shift was attributed to electrons localized in the interface since the luminescence was detected on a line originating from the interfacial region. [35] The region of localization was estimated to be ~ 50 nm. [35] Spin exchange with the localized electrons, common in bulk GaAs [11], was ruled out in this case because a difference in the electron spin polarization was seen for different luminescence lines. The Knight shift here was found to be 4.4kHz for the ^{75}As nuclei with $\langle S_z \rangle = 0.4$. [32] Given this interpretation, this value for the Knight shift could be taken as a lower bound for that due to electrons experiencing 2D localization in a 10 nm quantum well, which has a narrower localization width and a higher spin polarization. By detecting the luminescence on a line due to 2D electrons in the quantum well it should be possible to measure the resulting Knight shift for the n = 1 level. The Knight shift for this case is expected to be [33,34]

$$\gamma_\alpha B_e^\alpha(z) = \gamma_\alpha b_e^\alpha(0) \langle S_z \rangle \cos^2(\pi z/d) \qquad (5.12)$$

where d (= 10 nm) is the well width.

Figure 5.36 shows a pulse sequence and simulation of a TSONMR experiment designed to resolve individual layers of ^{75}As atoms in a 10 nm quantum well. This experiment takes advantage of a multiple–pulse line–narrowing sequence shown in Fig. 5.29b designed to average the dipolar and quadrupole interactions to zero as

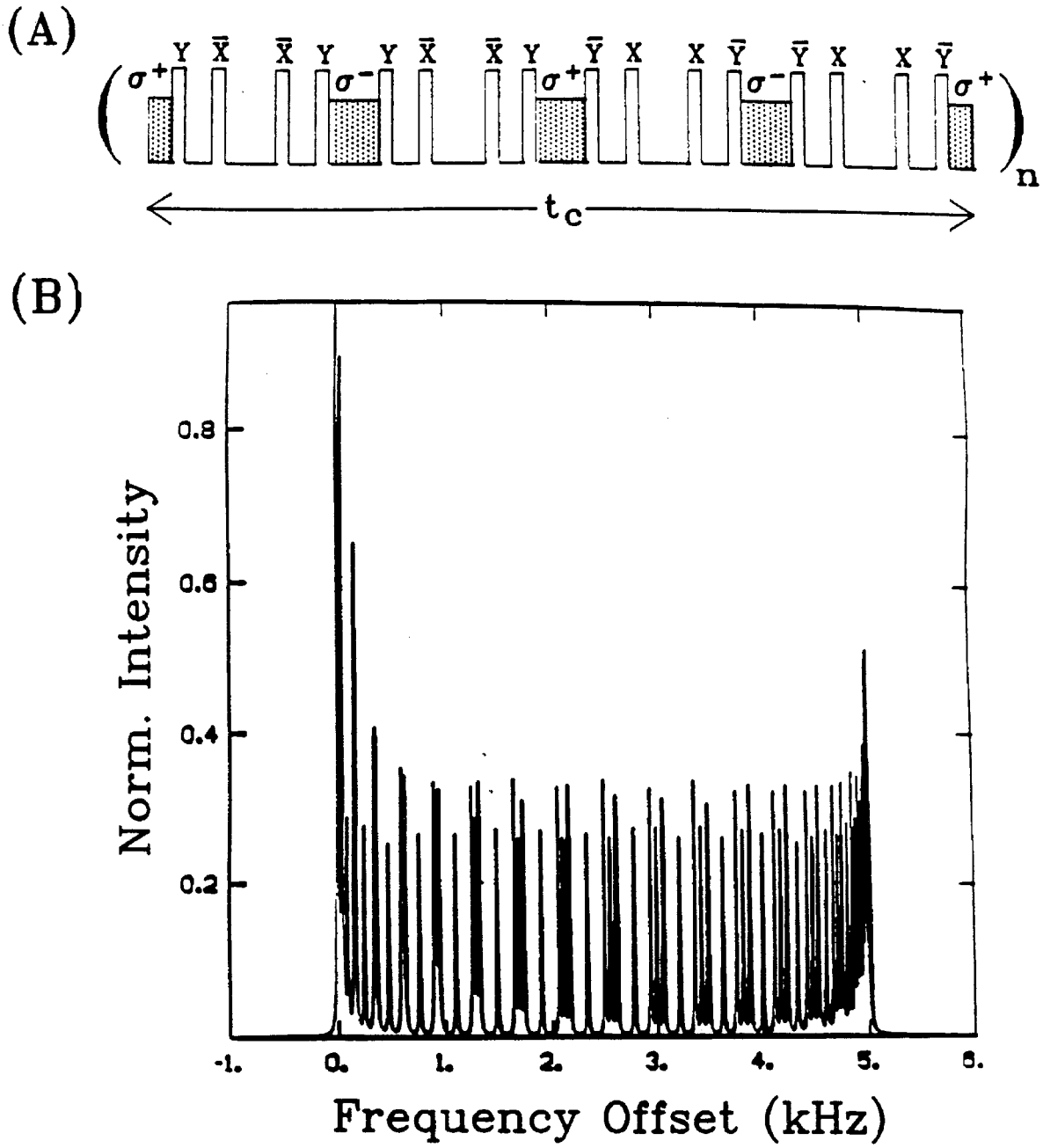

Figure 5.36: Resolving atomic layers in a quantum well. Simulation of the optical Knight shift in a quantum well using the line–narrowing pulse sequence in part (A) with light pulses in the windows as shown. The Knight shift at the center of the well is assumed to be 15 kHz, and the narrowed linewidth is assumed to be 10 Hz. The simulation in part (B) is for a well width of ≃ 10 nm ± 1 monolayer. Only at the center of the well (5 kHz) and the interface (0 kHz) remain unresolved.

well as to remove the resonance offset. The result of this sequence applied to sample 5 is shown in Fig. 5.31 and results in a line at zero offset with a width of ~ 100 Hz. The Knight shift information is obtained by turning the light on during the windows of the line–narrowing sequence as illustrated in Figure 5.36a. This type of experiment is most closely analogous to a solid–state NMR imaging experiment where DC gradient pulses are given in the windows to encode the spatial dependence of the gradient, [21,23] but uses a 16 pulse rf line–narrowing sequence used for rf gradient imaging. [22,24] The success of the line–narrowing experiment depends on the amount of nuclear spin relaxation that occurs during the length of the pulse sequence. The relaxation time of interest is spin–lattice relaxation in the rotating frame $T_{1\rho}$ which has been measured to be $\geq$ 100 ms for bulk GaAs (see subsection 5.3.2). The line–narrowing optical–pulse sequence of Fig. 5.36a scales the Knight shift by a factor of 1/3. If the well contains 36 layers of As atoms arranged symmetrically about the center and each layer is assumed to contribute equally to the spectrum, then only 18 lines are expected. If the As atoms are arranged asymmetrically about the center of the well then all 36 lines are expected. Figure 5.37b shows a simulation for a realistic sample (d $\simeq$ 10nm $\pm$ 1 monolayer). [33,34] Line–narrowing to 10 Hz is assumed (by optimizing the sequence used in Fig. 5.31), and the center shift is estimated to be $b_e^{\alpha}(0)\langle S_z\rangle$ = 15 kHz. The spectrum is a superposition of equal amounts of three different well widths. Nearly all atomic layers are resolved, except the layers near the surface and near the center of the well.

By using the hyperfine interaction as a way of distinguishing different sites in a GaAs epitaxial layer, valuable information about the structure as well as the excited electronic states can be obtained. The more sophisticated multiple–pulse and 2D NMR techniques now accesible with optical methods make TSONMR an informative tool for studying GaAs semiconductors.

5.5 References

[1] M.A. Herman and H. Sitter, *Molecular Beam Epitaxy: Fundamentals and Current Status* (Springer–Verlag, Berlin 1989) chp. 1.

[2] T.P. Das and E.L. Hahn, *Solid State* Physics, edited by, H. Ehrenreich, F. Seitz, and D. Turnbull (Academic Press, New York, 1958).

[3] C.P. Slichter, *Principles of Magnetic Resonance 3rd Ed.* (Springer–Verlag, Berlin, 1990), Chp. 10.

[4] R.G. Shulman, B.J. Wyluda, and H.J. Hrotowski, Phys. Rev. **109**, 808 (1958).

[5] O.H. Han, H.K.C. Timken, and E. Oldfield, J. Chem. Phys. **89**, 6046 (1988).

[6] D. Paget, G. Lampel, B. Sapoval, and V.I. Safarov, Phys. Rev. B **15**, 5780 (1977).

[7] M. Goldman, *Spin Temperature and Nuclear Magnetic Resonance in Solids* (Oxford, London, 1970).

[8] A. Abragam, *Principles of Nuclear Magnetism* (Oxford, Oxford, 1961).

[9] M.I. D'yakonov and V.I. Perel', Zh. Eksp. Teor. Fiz. **65**, 362 (1973) [Sov. Phys.–JETP **38**, 177 (1974)].

[10] B.C. Gerstein and C.R. Dybowski, *Transient Techniques in NMR of Solids: An Introduction to Theory and Practice* (Academic Press, Orlando, 1985) pp. 8–11.

[11] D. Paget, Phys. Rev. B **24**, 3776 (1981).

[12] D. Paget, Phys. Rev. B **25**, 4444 (1982).

[13] E.L. Hahn, Phys. Rev. **80**, 580 (1950).

[14] H.C. Torrey, Phys. Rev. **76**, 1059 (1949).

[15] F. Bloch and A. Siegert, Phys Rev. **57**, 522 (1940).

[16] A. Samoson and E. Lippmaa, Chem. Phys. Lett. **100**, 205 (1983).

[17] R. Janssen and W.S. Veeman, J. Chem. Soc. Faraday Trans. 1 **84**, 3747 (1988).

[18] J.Y. Hwang, H.M. Cho, and D.P. Weitekamp, in preparation.

[19] V.L. Berkovits and V.I. Safarov, Fiz. Tverd. Tela **20**, 2536 (1978) [Sov. Phys. Solid State **20**, 1468 (1978)].

[20] U. Haeberlen, *High Resolution NMR in Solids: Selective Averaging* (Academic Press, New York, 1976).

[21] P. Mansfield and P.K. Grannell, Phys. Rev. B **12**, 3618 (1975).

[22] H.M. Cho, C.J. Lee, D.N. Shykind, and D.P. Weitekamp, Phys. Rev. Lett. **55**, 1923 (1985).

[23] D.G. Cory, J.B. Miller, and A.N. Garroway, J. Magn. Reson. **87**, 202 (1990).

[24] M. H. Werner, Ph.D. Thesis, California Institute of Technology, Pasadena, CA 1992.

[25] S.R. Hartmann and E.L. Hahn, Phys. Rev. **128**, 2042 (1962).

[26] F.M. Lurie and C.P. Slichter, Phys. Rev. **133**, A1109 (1964).

[27] R.E. Slusher and E.L. Hahn, Phys. Rev. **166**, 332 (1968).

[28] C.P. Slichter, *Principles of Magnetic Resonance 3rd Ed.* (Springer–Verlag, Berlin, 1990), Chp. 5.

[29] A.G. Redfield, Rhys. Rev. **98**, 1787 (1955).

[30] G.P. Flinn, R.T. Harley, M.J. Snelling, A.C. Tropper, and T.M. Kerr, J. of Lumines. **45**, 218 (1990).

[31] G.P. Flinn, R.T. Harley, M.J. Snelling, A.C. Tropper, and T.M. Kerr, Semicond. Sci. Technol. **5**, 533 (1990).

[32] M. Krapf, G. Denninger, H. Pascher, G. Weimann, and W. Schlapp, Solid State Comm. **78**, 459 (1991).

[33] K. Ploog and G.H. Döhler, Adv. Phys. **32**, 285 (1983).

[34] C. Weisbuch and B. Vinter, *Quantum Semiconductor Structures* (Academic Press, San Diego 1991) chp. III.

[35] Y.R. Yuan, M.A.A. Pudensi, G.A. Vawter, and J.L. Merz, J. Appl. Phys. **58**, 397 (1985).

Appendix A

Interfacing and Software

This appendix presents a detailed description of interfacing the various instruments of the TSONMR spectrometer (see chapter 3) to the IBM PS/2 model 80 computer. Both IEEE–488 (GPIB) and parallel digital input/output (DIO) types of interfacing were used. The GPIB bus serviced five devices, the SR400 photon counter, the SR530 lock–in amplifier, the ITI word generator, the HP frequency synthesizer, and the PTS frequency synthesizer, and the DIO board serviced the shutter controller.

The data acquisition program was written entirely in the C programming language and was compiled using the Microsoft C version 5.0 compiler. A description of the program was presented previously in section 3.8. The source code for the program TSONMR.C can be found in section A.4. The GPIB function calls are defined in the MCIBL.OBJ object file, and the DIO board function calls are defined in the MCLABDRV.LIB library. Each of these files were included in the link list.

A.1 GPIB Protocol

This section is designed as a general description of interfacing the various instruments using GPIB. Each of the instruments is configured using the IBCONF setup program supplied with the National Instruments board. In order to use the GPIB bus, the board must be addressed by the CONFIG.SYS file executed when booting the computer. The GPIB bus is addressed by including the statement

DEVICE = GPIB.COM in the CONFIG.SYS file. When IBCONF is run, each device is given a series of GPIB parameters. Of these parameters, the ones that are most important for our applications are the primary address, the end–of–string (EOS) byte, and the timeout setting.

TABLE A.1: GPIB Attributes

Device	Primary GPIB Address	EOS Byte (ASCII)	Timeout (ms)
SR400	23	carriage return	10
SR530	27	carriage return	10
HPSYNTH	4	none	10
PTS	24	carriage return	10
ITI	1	!	10

Each of these parameters is described below and the values for these parameters for each of the devices are listed in Table A.1.

(1) The Primary Address: This is important for addressing the device with software. When the IBFIND function is called it looks for the device at the primary address. Once the device is found, its listen address (in decimal) is established as (primary address + 32), and the talk address is established as (primary address + 64). The GPIB bus is given primary address 0.

(2) The EOS Byte: The EOS byte for a particular device is what separates data records when the device is the listener or the talker. For example, when the SR400 photon counter is sent the command to set its analog port P1 to zero volts, "PL1,0.000", it must be appended with (or followed by) the EOS byte, a carriage return ("\r" in the C language), in order for the command to be executed. The character string set across the bus is then "PL1,0.000\r" (or equivalently, "PL1,0.000" followed by "\r"). The EOS byte is also sent as the last byte of data from the device. The HP synthesizer does not use an EOS byte, and the commands

are terminated with the last byte sent. This can create problems if data records are sent too fast for the HP synthesizer. Before writing to the HP synthesizer, the interface must be cleared to ensure proper data transfer.

(3) The Timeout Setting: This parameter limits the time that the bus waits for the device to send or receive data. If this time is exceeded during data transfer, then a GPIB error occurs. In practice the timeout setting is set to 10 ms which is ample time for data transfers for all devices.

A.2 GPIB Function Calls

The functions most commonly used in interfacing with the GPIB bus are described below (all examples are written in C). When a GPIB function call is executed a 7–bit status byte is updated to keep track of addressed devices and boards as well as errors. Each bit of the status byte is given a name defined in the object file MCIBL.OBJ.

(1) ibfind (bd): The parameter 'bd' is either a device or a board. This function finds a device or board and returns an integer pointer. For example,

```
sr530 = ibfind ("SR530");
```

finds the SR530 lock–in amplifier and the integer pointer sr530 is used to address the device.

(2) ibsic (bd): Clears the GPIB bus defined by 'bd'. For example,

```
ibsic (gpib0);
```

clears the GPIB interface for the board gpib0. The argument of this function must be a board and not a device.

(3) ibclr (dev): Clears a specific device defined by 'dev'. For example,

```
ibclr (iti);
```

clears the ITI word generator. Care must be taken when using this function since

clearing the SR400, SR530 and HP synthesizer results in placing the device in its default setting which is, in general, not the setting in which it is used. Clearing the ITI is necessary before modifying sequences or tables, but is not necessary in between triggers. In practice, the IBCLR function call is used only for the ITI word generator, and only when necessary. Clearing the interface is more readily accomplished using IBSIC.

(4) ibwrt (dev, string, cnt): Writes a specific number of bytes to a device. The IBWRT function performs several tasks. First, it sets up the GPIB bus as the talker and the device as the listener. Second, it sends the n bytes of data (usually an ASCII string) to the listen address of the device. Finally, it sends the unlisten command (ASCII "?") to all devices and the untalk command (ASCII "_") to the talk address of the board. An example of a write statement is given below:

```
ibwrt (iti, "trg!", 4);
```

This statement writes the string "trg!" of length 4 bytes to the ITI word generator. The command TRG triggers the ITI word generator, and the character "!" is the EOS for the ITI.

(4) ibwait (bd, mask): The parameter 'bd' specifies a device or board, and 'mask' specifies a bit mask of the status word. This functions executes a delay until the events selected in the bit mask occur or the timeout flag is set. Consider the set of statements,

```
ibwrt (sr530, "q1\r", 3);
ibwait (sr530, CMPL);
```

The IBWRT function sends the string "q1\r" to the SR530, and the IBWAIT function delays the bus until the CMPL bit of the status byte is set, which signifies completion of the ibwrt statement.

(5) ibrd (dev, rd, cnt): The parameter 'dev' is a specific device, 'rd' is the storage buffer for the data, and 'cnt' is the number of bytes sent. This function

sends data from a device to a string buffer via the GPIB bus. The IBRD function does the tasks of addressing the device to talk and the board to listen, sends the data to the board, and unaddresses the board and all devices. The board writes the data to the storage buffer defined in the function call. The use of IBRD is always preceded by an IBWRT function call to poll the device for its data. For example, the statement

```
ibwrt (sr530, "q1\r", 3);
```

polls the SR530 for the output of the A channel. The SR530 digitizes the A channel and loads the result into its memory stack. The statement

```
ibrd (sr530, temp, 50);
```

then reads the result into the character array TEMP. It is important to note that the number of bytes specified (50) is much greater than the data record sent by the SR530 (5 in this case). The IBRD function terminates when the EOS of the SR530 (a carriage return) is sent. The data in the character array TEMP is converted to a double precision variable in C by removing the EOS byte from the record.

A.3 DIO Software

The DIO board is used essentially as a computer–controlled TTL source. In the C language the board is initialized by calling the function

```
Init_DA_Brds (3,8);
```

which initializes the DIO board located at address 3 in the physical slot number 8 of the PS/2. The function

```
DIG_Prt_Config (3,0,0,1);
```

configures the 16 lines of channel A as output ports only. The first parameter of the function addresses the board, the second parameter addresses the 16–bit A channel, the third parameter sets the read flag to zero, and the fourth parameter sets the

write flag high. A particular bit of the 16–bit A channel is set high or low by the function

DIG_Out_Line (3,0,0,1);

which, in this case, sets bit 0 of channel A high. The shutter is controlled by bits 0 and 1 of the A channel. Bit 0 opens the shutter when it is pulled high, and bit 1 closes the shutter when it is pulled high. Once bit 0 or 1 is set, it must be pulled low before it can be used to open or close the shutter again.

A.4 Source code for TSONMR.C

```
#include <types.h>
#include <timeb.h>
#include <stdio.h>
#include <time.h>
#include <decl.h>
#include <math.h>
#include "doslbdrv.h"

double mag[300], null[300];
double factor;

/*@@@@@@@@@@@@@@@@@@@@@@@@@@@@@@@@@@@@@@@@@@@@@@@@@@@@@@@@@@@@@@@@@@@@*/
/* This function uses the PC clock to set a delay for a
period of seconds determined by the parameter delay_time (0
to 60 seconds delay) */

delay_sec (delay_time)
int delay_time;
{
  struct timeb timebuffer;
  char *timeline;
  int min, sec, millsec;
  int min_new, sec_new, flag;
  char smin[3];
  char ssec[3];

  ftime(&timebuffer);                    /* reads the PC clock
*/
  timeline = ctime(&(timebuffer.time));  /* enters the time
to a character */
  millsec = (int) timebuffer.millitm;    /* the values of
milliseconds */

/* extract the minutes from the character timeline */
  smin[0] = timeline[14];
  smin[1] = timeline[15];
  smin[2] = '\0';

/* extract the seconds from the character timeline */
  ssec[0] = timeline[17];
  ssec[1] = timeline[18];
  ssec[2] = '\0';

/* convert minutes and seconds to integers */
  sscanf(smin,"%d",&min);
  sscanf(ssec,"%d",&sec);

  sec_new = sec + delay_time;
  flag = 0;
```

```
  if (sec_new < 60) {
    do         /* keep reading the clock until delay is
complete */
      {
     ftime(&timebuffer);
     timeline = ctime(&(timebuffer.time));

     millsec = (int) timebuffer.millitm;
     ssec[0] = timeline[17];
     ssec[1] = timeline[18];
     ssec[2] = '\0';

     sscanf(ssec,"%d",&sec);

     if (sec_new <= sec)
       flag = 1;
     else
       flag = 0;
      }
    while (flag != 1);}

  else {    /* for new_sec > 60 need to wrap around the
minutes */
    min_new = min + 1;
    if (min_new == 60) min_new = 0;
    sec_new = sec_new - 60;

    do         /* reads clock until delay is complete */
      {
      ftime(&timebuffer);
      timeline = ctime(&(timebuffer.time));

      millsec = (int) timebuffer.millitm;
      smin[0] = timeline[14];
      smin[1] = timeline[15];
      smin[2] = '\0';
      ssec[0] = timeline[17];
      ssec[1] = timeline[18];
      ssec[2] = '\0';

      sscanf(smin,"%d",&min);
      sscanf(ssec,"%d",&sec);

      if (sec_new <= sec && min_new == min)
        flag = 1;
      else
        flag = 0;
      }
    while (flag != 1);}
}
/*@@@@@@@@@@@@@@@@@@@@@@@@@@@@@@@@@@@@@@@@@@@@@@@@@@@@@@@@*/

/*%%%%%%%%%%%%%%%%%%%%%%%%%%%%%%%%%%%%%%%%%%%%%%%%%%%%%%%%*/
/* This function acts exactly the same as delay_sec except
```

```
the delay is now for a period of milliseconds instead of
seconds (0 to 100 msec). */

delay_millsec (delay_time)
int delay_time;
{
  struct timeb timebuffer;
  char *timeline;
  int sec, millsec;
  int new_sec, new_millsec, flag;
  char ssec[3];

  ftime(&timebuffer);
  timeline = ctime(&(timebuffer.time));

  millsec = (int) timebuffer.millitm;
  ssec[0] = timeline[17];
  ssec[1] = timeline[18];
  ssec[2] = '\0';

  sscanf(ssec,"%d",&sec);

  new_millsec = millsec + delay_time;

  if (new_millsec < 1000){
    do
      {
     ftime(&timebuffer);
     timeline = ctime(&(timebuffer.time));

     millsec = (int) timebuffer.millitm;
     ssec[0] = timeline[17];
     ssec[1] = timeline[18];
     ssec[2] = '\0';

     sscanf(ssec,"%d",&sec);

     if (new_millsec <= millsec)
       flag = 1;
     else
       flag = 0;
      }
    while (flag != 1);}

  else {
    new_sec = sec + 1;
    if (new_sec == 60) new_sec = 0;
    new_millsec = new_millsec - 1000;
    do
      {
     ftime(&timebuffer);
     timeline = ctime(&(timebuffer.time));

     millsec = (int) timebuffer.millitm;
```

```
      ssec[0] = timeline[17];
      ssec[1] = timeline[18];
      ssec[2] = '\0';

      sscanf(ssec,"%d",&sec);

      if (new_millsec <= millsec && new_sec == sec)
        flag = 1;
      else
        flag = 0;
       }
     while (flag != 1);}
}
/*%%%%%%%%%%%%%%%%%%%%%%%%%%%%%%%%%%%%%%%%%%%%%%%%%%%%%%%%%%%%%%%%%%%%%%%%*/


/*&&&&&&&&&&&&&&&&&&&&&&&&&&&&&&&&&&&&&&&&&&&&&&&&&&&&&&&&&&&&&&&&&&&&&&&&*/
/* This function checks for a digital output error using the
error codes returned by the DOS LabDriver functions. If an
error occurs, the error code is displayed on the terminal.
*/

error (n)
int n;
{
   if (n != 0){
     printf ("A digital output error has occurred %d\n",n);
     exit ();}
}
/*&&&&&&&&&&&&&&&&&&&&&&&&&&&&&&&&&&&&&&&&&&&&&&&&&&&&&&&&&&&&&&&&&&&&&&&&*/

/*KKKKKKKKKKKKKKKKKKKKKKKKKKKKKKKKKKKKKKKKKKKKKKKKKKKKKKKKKKKKKKKKKKKKKKKK*/
/* This function counts the number of characters in a
character string */
int string_length (string)
  char string[];
  {
     char cmnd[80];
     int count = 0;
     sprintf (cmnd, "%s\r", string);
     do
       {
       ++count;
       }
     while (cmnd[count] != '\r');
     return (count);
  }
/*KKKKKKKKKKKKKKKKKKKKKKKKKKKKKKKKKKKKKKKKKKKKKKKKKKKKKKKKKKKKKKKKKKKKKKKK*/

/*$$$$$$$$$$$$$$$$$$$$$$$$$$$$$$$$$$$$$$$$$$$$$$$$$$$$$$$$$$$$$$$$$$$$$$$$*/
/* This function sends setup commands to the lock-in */

gpibli (sr530)
int sr530;
```

```
{
  char IEEE_file[25], junk[25];
  FILE *in_file, *fopen ();
  int flag, data, c;

/* get sr530 parameters from the appropriate gpib command
file (*.txt) */
  printf ("Enter the name of the SR530 setup file:\n");
  scanf ("%s", IEEE_file);

    in_file = fopen(IEEE_file, "r");

    if (in_file == NULL)
      printf ("Couldn't open %s for reading.\n",IEEE_file);
    else{
      flag = 0;
      while (flag != 1)
     {
       if ( feof (in_file) )
         flag = 1;
       fscanf (in_file, "%s", junk);
       if (junk[0] >= 97 && junk[0] <= 122){
         data = string_length (junk);
         ibwrt (sr530, junk, data);
         ibwrt (sr530, "\r", 1);
         }
     }
     }
}

/*$$$$$$$$$$$$$$$$$$$$$$$$$$$$$$$$$$$$$$$$$$$$$$$$$$$$$$$$$$$$$$$$*/

/*$$$$$$$$$$$$$$$$$$$$$$$$$$$$$$$$$$$$$$$$$$$$$$$$$$$$$$$$$$$$$$$$*/
/* This function sends setup commands to the ITI */

gpibwg (iti)
int iti;
 {
   char IEEE_file[25], junk[80];
   FILE *in_file, *fopen ();
   int flag, data, c;

/* get ITI parameters from the appropriate gpib command file
(*.txt) */
   printf ("Enter the name of the ITI setup file:\n");
   scanf ("%s", IEEE_file);

     in_file = fopen(IEEE_file, "r");

     if (in_file == NULL)
       printf ("Couldn't open %s for reading.\n",IEEE_file);
     else{
       ibclr (iti);
       flag = 0;
```

```
       while (flag != 1)
      {
        if ( feof (in_file) )
          flag = 1;
        fscanf (in_file, "%s", junk);
        if (junk[0] >= 97 && junk[0] <= 122){
          data = string_length (junk);
          ibwrt (iti, junk, data);
          ibwrt (iti, "!", 1);
          ibwait (iti, CMPL|TIMO);
          }
      }
      }
 }

/*$$$$$$$$$$$$$$$$$$$$$$$$$$$$$$$$$$$$$$$$$$$$$$$$$$$$$$$$*/


/*||||||||||||||||||||||||||||||||||||||||||||||||||||||||*/
/* This function reports an error during data transfers to
and from sr530 */
err ()
  {
     printf ("GPIB function call error:\n");
     printf ("ibsta = 0x%x, iberr = 0x%x,", ibsta, iberr);
     printf ("ibcnt = 0x%x\n", ibcnt);
     exit();
  }
/*||||||||||||||||||||||||||||||||||||||||||||||||||||||||*/

/*||||||||||||||||||||||||||||||||||||||||||||||||||||||||*/
/* This function reports an error of sr530 */
srerr ()
  {
     printf ("SR530 error:\n");
     exit();
  }
/*||||||||||||||||||||||||||||||||||||||||||||||||||||||||*/

/*||||||||||||||||||||||||||||||||||||||||||||||||||||||||*/
/* This function gets data from the sr530 */
double get_data_point (sr530)
  int sr530;
  {
     double data;
     char temp[80];
     strcpy (temp, "                     ");
     if (ibrd(sr530,temp,56)&ERR) err();
     sscanf (temp, "%lE", &data);
     return (data);
  }
/*||||||||||||||||||||||||||||||||||||||||||||||||||||||||*/
```

```
/*OOOOOOOOOOOOOOOOOOOOOOOOOOOOOOOOOOOOOOOOOOOOOOOOOOOOOOOOOOOOO*/
/* This function dumps the scan if rho > 1 */
dump ()
 {
   printf ("RHO WAS GREATER THAN 1!!!\n");
   exit ();
 }
/*OOOOOOOOOOOOOOOOOOOOOOOOOOOOOOOOOOOOOOOOOOOOOOOOOOOOOOOOOOOOO*/

/*MMMMMMMMMMMMMMMMMMMMMMMMMMMMMMMMMMMMMMMMMMMMMMMMMMMMMMMMMMMMM*/
/* This function obtains data from the sr530 */
data (sr530)
int sr530;
{
  double junk1, junk2, rho;
  int n;
/* get data from sr530 */
    for (n=1; n<=102; ++n)
    {
       ibwrt (sr530, "q1;x1\r", 6);
       if (ibsta & ERR) err();
       if (ibwait (sr530, TIMO|RQS)&(ERR|TIMO)) err();
       if (ibrsp(sr530,spr)&ERR) err();
       if (spr != 0) srerr();
       junk1 = get_data_point (sr530);
       if (junk1 > 1.0E-2) dump();
       junk2 = get_data_point (sr530);
       if (junk2 == 0.0000) {
      rho = 1.000;}
       else {
      rho = junk1/(junk2*factor);}
       mag[n] = mag[n] + rho;
    }
}
/*MMMMMMMMMMMMMMMMMMMMMMMMMMMMMMMMMMMMMMMMMMMMMMMMMMMMMMMMMMMMM*/

/*##################################################*/
main ()
{

   int err_num,
       *board_code;
   int delay1, answer1, answer2, delay2, delay3, ans;
   int gpib0, sr530, sr400, n_scans, m, s, iti, query;
   int n_expts, z, l, hpsynth, n1, q, zero_delay,
zero_delay2;
   float port_val1, init_freq, freq, step_size;
   float port_val2;
   double weight[100], asymp, asymp2, diff, junk_pt,
data_point;
   char outfile[25], cmnd[25], prefix[25];
   FILE *out_file, *fopen ();

/* get program parameters */
```

```
   printf ("Input the main field voltage.\n");
   scanf ("%f", &port_val1);
   printf ("Input the Hanle field voltage.\n");
   scanf ("%f", &port_val2);
   printf ("Input the initial rf frequency in kHz.\n");
   scanf ("%f", &init_freq);
   printf ("Input the rf frequency step size in kHz.\n");
   scanf ("%f", &step_size);
   printf ("Is this the NMR done with the light on or
off?\n");
   printf ("1=off, 2=on\n");
   scanf ("%d", &answer1);
   printf ("Do you wish to delay in zero field? (1=yes)\n");
   scanf ("%d", &answer2);
   if (answer2 == 1)
     {
     printf ("Do you wish a delay after ONP (1), after NMR
(2),");
     printf ("or both (3).\n");
     scanf ("%d", &query);
     if (query == 3) {
     printf ("Input zero field delay after ONP in
milliseconds.\n");
     scanf ("%d", &zero_delay2);
     printf ("Input the delay after NMR in
milliseconds.\n");
     scanf ("%d", &zero_delay);}
     else if (query == 1) {
     printf ("Input zero field delay after ONP in
milliseconds.\n");
     scanf ("%d", &zero_delay2);}
     else {
     printf ("Input the delay after NMR in
milliseconds.\n");
     scanf ("%d", &zero_delay);}
     }
   printf ("Is the time the iti needs to work > 1sec
(1=yes).\n");
   scanf ("%d", &ans);
   if (ans == 1) {
     printf ("Input the time iti needs to work in
seconds.\n");
     scanf ("%d", &delay3);}
   else {
     printf ("Input the time iti needs to work in
milliseconds.\n");
     scanf ("%d", &delay3);}
   printf ("Input the ONP time.\n");
   scanf ("%d", &delay1);
   printf ("Input the number of points in the spectrum.\n");
   scanf ("%d", &n_expts);
   printf ("Input the number of scans.\n");
   scanf ("%d", &n_scans);
   printf ("Input the multiplication factor for the
```

```
denominator.\n");
   scanf ("%lE", &factor);
   printf ("Input the name of the output file.\n");
   scanf ("%s", outfile);

   *board_code = 8;

/* initialize gpib board */
   gpib0 = ibfind ("GPIB0");
   ibsic (gpib0);

/* initialize sr530 */
   sr530 = ibfind ("SR530");
   if (sr530 < 0)
     printf ("Didn't find sr530!\n");

/* initialize sr400 */
   sr400 = ibfind ("SR400");
   if (sr400 < 0)
     printf ("Didn't find sr400!\n");

/* initialize hp synthesizer */
   hpsynth = ibfind ("HPSYNTH");
   if (hpsynth < 0)
     printf ("Didn't find hpsynth!\n");

/* initialize ITI pulse programmer */
   iti = ibfind ("ITI");
   if (iti < 0)
     printf ("Didn't find iti!\n");

/* load lock-in amplifier and pulse programmer */
   gpibli (sr530);
   gpibwg (iti);

/* Initialize the DIO board and configure port A as a write
port */
   err_num = Init_DA_Brds(3,board_code);
   error (err_num);
   err_num = DIG_Prt_Config(3,0,0,1);
   error (err_num);
   err_num = DIG_Out_Line(3,0,0,0);
   error (err_num);
   err_num = DIG_Out_Line(3,0,1,0);

/* obtain the null data */
   for (q = 1; q <= 200; ++q){
      null[q] = 0.000;
      mag[q] = 0.000;}

   for (m=1; m <= n_scans; ++m) {

   printf ("NULL EXPERIMENT:");
   printf ("SCAN %d OF %d\n", m, n_scans);
```

```
/* set the ONP fields */
   ibwrt (sr400, "pl2,0.000\r", 10);
   if (ibcnt != 10) {
     ibwrt (sr400, "\r", 1);
     ibwrt (sr400, cmnd, 10);}

   sprintf (cmnd, "pl1,%.3f\r", port_val1);
   ibwrt (sr400, cmnd, 10);
   if (ibcnt != 10) {
     ibwrt (sr400, "\r", 1);
     ibwrt (sr400, cmnd, 10);}

/* Open shutter and delay ONP time */
   delay_millsec (200);
   err_num = DIG_Out_Line(3,0,0,1);
   error (err_num);
   err_num = DIG_Out_Line(3,0,0,0);
   error (err_num);

   delay_sec (delay1);

/* close the shutter */
   err_num = DIG_Out_Line(3,0,1,1);
   error (err_num);
   err_num = DIG_Out_Line(3,0,1,0);
   error (err_num);

/* delay in zero field if desired */
   if (answer2 == 1)
   {
     ibwrt (sr400, "pl1,0.000\r", 10);
     if (ibcnt != 10) {
       ibwrt (sr400, "\r", 1);
       ibwrt (sr400, "pl1,0.000\r", 10);}
     if (query == 3) {
     delay_millsec (zero_delay);
     delay_millsec (zero_delay2);}
     else if (query == 1) {
     delay_millsec (zero_delay2);}
     else {delay_millsec (zero_delay);}
   }

/* field cycle */
   sprintf (cmnd, "pl2,%.3f\r", port_val2);
   ibwrt (sr400, cmnd, 10);
   if (ibcnt != 10) {
     ibwrt (sr400, "\r", 1);
     ibwrt (sr400, cmnd, 10);}

   ibwrt (sr400, "pl1,0.000\r", 10);
   if (ibcnt != 10) {
     ibwrt (sr400, "\r", 1);
     ibwrt (sr400, "pl1,0.000\r", 10);}
```

```
/* open shutter and take the data */
   delay_millsec (60);
   err_num = DIG_Out_Line(3,0,0,1);
   err_num = DIG_Out_Line(3,0,0,0);

   data (sr530);

/* close the shutter */
   err_num = DIG_Out_Line(3,0,1,1);
   error (err_num);
   err_num = DIG_Out_Line(3,0,1,0);
   error (err_num);

   }

/* set Hanle field back to zero */
   ibwrt (sr400, "pl2,0.000\r", 10);
   if (ibcnt != 10) {
     ibwrt (sr400, "\r", 1);
     ibwrt (sr400, "pl2,0.000\r", 10);}

/* divide by # of scans */
   for (m=4; m<=102; ++m){
      null[m] = mag[m]/n_scans;}

/* get the null asymptote */
   asymp = 0.000;
   for (q=78; q<=102; ++q) {
      asymp = asymp + null[q];}
   asymp = asymp/25.0;

/* calculate the weighting function */
   for (q=4; q<=75; ++q) {
      weight[q] = (asymp - null[q])/(asymp - null[1]);}

/* initialize rf frequency */
   freq = init_freq;
   sprintf (cmnd, "F%.3fK", freq);
   n1 = string_length (cmnd);
   do {
   ibwrt (hpsynth, cmnd, n1);}
   while (ibsta & ERR);

/* Open the output file */
   out_file = fopen (outfile, "w");

   for (z=1; z<=n_expts; ++z){

   printf ("POINT %d OF %d IN PROGRESS\n", z, n_expts);

   for (q = 1; q <= 200; ++q){
      mag[q] = 0.000;}
```

```
   for (m=1; m <= n_scans; ++m) {

   printf ("SCAN %d OF %d\n", m, n_scans);

/* set the ONP fields */
   ibwrt (sr400, "pl2,0.000\r", 10);
   if (ibcnt != 10) {
     ibwrt (sr400, "\r", 1);
     ibwrt (sr400, cmnd, 10);}

   sprintf (cmnd, "pl1,%.3f\r", port_val1);
   ibwrt (sr400, cmnd, 10);
   if (ibcnt != 10) {
     ibwrt (sr400, "\r", 1);
     ibwrt (sr400, cmnd, 10);}

/* Open shutter and delay ONP time */
   delay_millsec (200);
   err_num = DIG_Out_Line(3,0,0,1);
   error (err_num);
   err_num = DIG_Out_Line(3,0,0,0);
   error (err_num);

   delay_sec (delay1);


/* perform NMR */

   if (answer1 == 1){
   err_num = DIG_Out_Line(3,0,1,1);
   error (err_num);
   err_num = DIG_Out_Line(3,0,1,0);
   error (err_num);}

/* delay in zero field if desired */
   if (answer2 == 1 && (query == 1 || query == 3))
   {
     ibwrt (sr400, "pl1,0.000\r", 10);
     if (ibcnt != 10) {
       ibwrt (sr400, "\r", 1);
       ibwrt (sr400, "pl1,0.000\r", 10);}
     delay_millsec (zero_delay2);
     sprintf (cmnd, "pl1,%.3f\r", port_val1);
     ibwrt (sr400, cmnd, 10);
     if (ibcnt != 10) {
       ibwrt (sr400, "\r", 1);
       ibwrt (sr400, cmnd, 10);}
   }

/* use ITI to control rf irradiation */
   ibwrt (iti, "trg!", 4);

/* delay program while ITI does its thing */
   if (ans == 1) {delay_sec (delay3);}
```

```
   else {
   delay_millsec (delay3);}

/* delay in zero field if desired */
   if (answer2 == 1 && (query == 2 || query == 3))
   {
     ibwrt (sr400, "pl1,0.000\r", 10);
     if (ibcnt != 10) {
       ibwrt (sr400, "\r", 1);
       ibwrt (sr400, "pl1,0.000\r", 10);}
     delay_millsec (zero_delay);
   }

   if (answer1 == 2){
   err_num = DIG_Out_Line(3,0,1,1);
   error (err_num);
   err_num = DIG_Out_Line(3,0,1,0);
   error (err_num);}

/* field cycle */
   sprintf (cmnd, "pl2,%.3f\r", port_val2);
   ibwrt (sr400, cmnd, 10);
   if (ibcnt != 10) {
     ibwrt (sr400, "\r", 1);
     ibwrt (sr400, cmnd, 10);}

   ibwrt (sr400, "pl1,0.000\r", 10);
   if (ibcnt != 10) {
     ibwrt (sr400, "\r", 1);
     ibwrt (sr400, "pl1,0.000\r", 10);}

/* open shutter and take the data */
   delay_millsec (60);
   err_num = DIG_Out_Line(3,0,0,1);
   error (err_num);
   err_num = DIG_Out_Line(3,0,0,0);
   error (err_num);

   data (sr530);

/* close the shutter */
   err_num = DIG_Out_Line(3,0,1,1);
   error (err_num);
   err_num = DIG_Out_Line(3,0,1,0);
   error (err_num);

   }

/* set Hanle field back to zero */
   ibwrt (sr400, "pl2,0.000\r", 10);
   if (ibcnt != 10) {
     ibwrt (sr400, "\r", 1);
     ibwrt (sr400, "pl2,0.000\r", 10);}
```

```
   delay_millsec (60);
   err_num = DIG_Out_Line(3,0,0,1);
   error (err_num);
   err_num = DIG_Out_Line(3,0,0,0);
   error (err_num);

/* divide by the number of scans */
   for (m=4; m<=102; ++m) {
      mag[m] = mag[m]/n_scans;}

/* calculate the data point from the transient stored in mag
array */
   asymp2 = 0.000;
   for (q=78; q<=102; ++q) {
      asymp2 = asymp2 + mag[q];}
   asymp2 = asymp2/25.0;
   diff = asymp - asymp2;

   data_point = 0.000;
   for (q=4; q<=75; ++q) {
      mag[q] = mag[q] + diff;        /* asymptote adjustment
*/
      junk_pt = (mag[q] - null[q])*weight[q];
      junk_pt = fabs(junk_pt);
      data_point = data_point + junk_pt;}


/* load data point into the output file */
      fprintf (out_file, "%f %lE ", freq, data_point);
      fprintf (out_file, "\n");

/* step rf frequency for next transient */
   freq = freq + step_size;
   sprintf (cmnd, "F%.3fK", freq);
   n1 = string_length (cmnd);
   do {
   ibwrt (hpsynth, cmnd, n1);}
   while (ibsta & ERR);

   }

   fclose (out_file);
}
/*#####################################################*/
```